

Investigation of flexoelectricity and ionic contamination in nematic liquid crystals

CHRISTOPHE LIONEL TRABI

A thesis submitted in partial fulfilment of
the requirements of
Nottingham Trent University
for the degree of Doctor of Philosophy

August 2009

This work is the intellectual property of the author, and may also be owned by the research sponsor(s) and/or Nottingham Trent University. You may copy up to 5% of this work for private study, or personal, non-commercial research. Any reuse of the information contained within this document should be fully referenced, quoting the author, title, university, degree level and pagination. Queries or requests for any other use, or if a more substantial copy is required, should be directed in the first instance to the author.

“The important thing in science is not so much to obtain new facts as to discover new ways of thinking about them”

Sir William Bragg, 1968

*To my grand parents, Djelloul & Fatma Trabi, René & Andrée Devillette,
my parents, Ahmed & Claudine Trabi,
my sisters and brother, Marie-Agnès, Catherine & David*

Acknowledgements

First would like to thank my supervisors, Prof. Carl V. Brown, Prof. Glen Mchale and Dr. Michael I. Newton for their support, encouragement and advices they have given to me during the period of my PhD. I would like to include people who I have been continuously questioned along my journey, the lecturers Dr. David Fairhurst and Dr. Martin Bensick, the physics technicians Steve Elliot and Dave Parker, and my colleagues Dr. Andrew A.T. Smith, Dr James Hind, Dr. Paul Roach, Dr. Carl Evans, Dr. Simon Stanley, Dr. Neil Shirtcliffe, Robert Morris, David Willmer, Gary Wells, Nicola Doy, Shaun Atherton and Sam Lawman.

I would like to show a sincere gratitude to the person would help me to extend my knowledge in liquid crystals during formal or informal meeting, Prof. Nigel J. Mottram, Andrew J. Davidson, Sharon A. Jewell and the members of the British Liquid Crystals Society (B.L.C.S.). I would like to thank K. Turner for proof read and spellcheck my work. Finally I would like also to mention Mr. Y. Lapouge and Mr. J.C. Garcia (respectively former head of “Traitement des Eaux” and former headmaster of “Lycee R. Dautry”) who gave me the opportunity to explore multi-disciplinary in study.

Abstract

The work presented is a study of nematic liquid crystal physical properties. One of the phenomenon investigated is the bistability or in other words, the ability of the director of the material to rest in different orientations as function of the geometry of the sidewall. The main core of this research is the study of flexoelectric effect and ionic contamination within the nematic layer. This can be split into three approaches. In the first part, the flexoelectric coefficients are determined from the distortion of a nematic liquid crystal in response to non uniform electric fields created using an interdigitated electrode architecture. The distortion was deduced from the fringes movement in a Mach-Zhender interferometer built especially for this investigation. In the second part, the transient capacitance technique is used to measure the permittivity response of two homogeneous nematic materials subjected to different electric signal waveforms. The results remain to be fitted in order to give an alternative method to deduce the flexoelectric coefficients values and a better understanding of the effect of ionic contamination. The last part of the work relates to the determination of the flexoelectricity coefficients and ionic contamination and their effects on the Fréedericksz transition in homogeneous nematic liquid crystal using magnetic fields. The Mach-Zhender interferometer was also used to investigate two other phenomena, the first one is electrophoresis and the second is the resonance mode of insects.

Contents

1	Introduction	1
1.1	Liquid crystals	2
1.2	Different type of liquid crystals	3
1.3	Calamitic liquid crystals	4
1.4	Nematic liquid crystal order parameter	4
1.5	Physical properties of nematic liquid crystals and anisotropy . . .	6
1.5.1	Birefringence in crystals	6
1.5.2	Refractive index and birefringence in liquid crystals	8
1.5.3	Permittivities	12
1.5.4	Magnetic susceptibility	19
1.5.5	Continuum theory, elastic constants and Fréedericksz effect	20
1.5.6	Flexoelectricity	25
1.5.7	2 frequency materials	26
1.6	Diffraction optical devices	27
1.6.1	Diffraction	27
1.6.2	Diffraction efficiency	29
1.6.3	Nematic phase gratings	30
1.7	Preview of the work	31
1.7.1	Previous work	31
1.7.2	Outline of the work	32

2	Experimental Methods	33
2.1	Phase grating device fabrication	34
2.1.1	Introduction	34
2.1.2	Electrode fabrication	34
2.1.3	Design of mask	36
2.1.4	Surface alignment and device assembly	38
2.1.5	Measurement of cell gap	40
2.1.6	Data interpretation for thickness determination	41
2.2	Capacitance measurements	41
2.2.1	Sample detail (earth ring)	41
2.2.2	Static measurements	42
2.2.3	Dynamic measurements	43
2.3	Fréedericksz transition measurement	46
2.3.1	Dielectric measurement	46
2.3.2	Optical measurement	47
2.3.3	Magnetic measurement	49
2.4	Mach-Zenhder interferometer	52
2.4.1	Principle	52
2.4.2	Description and specificities	53
3	Investigation of the flexoelectric polarisation in nematic phase grating structures	54
3.1	Introduction	55
3.2	Device geometry and data acquisition	56
3.2.1	Construction of a cell	56
3.2.2	Image processing	57
3.2.3	Extraction of results	59
3.3	Experimental results on a dual frequency material	61
3.4	Nematic continuum theory in 2 dimensions	62

3.5	Experimental results on a non-dispersive nematic liquid crystal (E7)	68
3.5.1	Thick cell with antiparallel alignment	68
3.5.2	Thick cell with parallel Alignment	68
3.5.3	Cell thickness dependence	69
3.6	Implementation of the model	74
3.6.1	Assumption in the numerical modelling	74
3.6.2	Transient capacitance measurements and simulations	74
3.7	Optical diffraction measurements	78
3.7.1	Sample and processing details	78
3.7.2	Diffraction measurements	79
3.7.3	Static optical diffraction patterns	79
3.7.4	Time dependent optical diffraction patterns	80
3.8	Fit to experimental data using the continuum theory model	82
3.9	Conclusion	84
4	Transient capacitance in the presence of ionic contamination	86
4.1	Introduction	87
4.2	Experimental results	91
4.2.1	Results from the amplitude modulation signal (A.M.)	91
4.2.2	Investigation of the ionic contamination and effects	97
4.2.3	Investigation of the flexoelectric effect in E7 and TL216	102
4.2.4	Other observations during the transient capacitance investigation	105
4.3	Modelling and fitting	106
4.4	Conclusion	106
5	Effects of ionic contamination and flexoelectricity on the Fréedericksz transition	108
5.1	Principle	109

5.2	Experimental setup	110
5.2.1	Magnetic field experiment	110
5.2.2	Electric field experiment	112
5.2.3	Experimental parameters	114
5.3	Experimental results	115
5.3.1	Magnetic determination of elastic constants	115
5.3.2	Electric determination of elastic constants	117
5.3.3	Analysis and comparison of K_{33}/K_{11} from different methods	119
5.4	Model results	121
5.5	Discussion and further work	123
6	Bistability in nematic liquid crystals controlled by sidewall morphology	124
6.1	Principle of bistability	125
6.2	Geometries of test cells	125
6.3	Different type of director orientation across the cell	128
6.4	Observations and results	131
6.4.1	Observations	131
6.4.2	Statistic and results	132
6.5	Conclusion	136
7	Other investigations using interferometric methods	137
7.1	Foreword	138
7.2	Liquid dielectrophoresis	138
7.2.1	Principle	138
7.2.2	Preliminary investigation and data	139
7.2.3	Experimental results and conclusion	140
7.3	Investigation of resonance modes in insects	145
7.3.1	Introduction on honeybees and the <i>Varroa destructor</i> mite	145
7.3.2	Outline of the investigation	146

7.3.3	Preliminary study to validate the method	148
7.3.4	Investigation of resonance of a large insect: <i>Carabus prob-</i> <i>lematicus</i>	149
7.3.5	Investigation on the <i>Varroa destructor</i>	151
7.3.6	Conclusion	152
8	Conclusion	153
8.1	Ionic contamination	154
8.1.1	Effects on the Fréedericksz transition	154
8.1.2	Transient capacitance measures	154
8.2	Bistability	155
8.3	Flexoelectricity	156
8.4	Other studies	156
8.5	Further Works	157
A	Appendix	159
A.1	Interdigitated electrodes model	160
A.2	Regression analysis for the spectrometer data	171
A.3	Regression analysis for determination of the calibration factor of the electromagnet	172
A.4	Regression analysis for the $\ln(A/V^2)$ vs. h/d	172

List of Figures

1.1	Different states of water at atmospheric pressure	2
1.2	Schematic representation of liquid crystal molecules	3
1.3	Different states of MBBA	4
1.4	Illustration of nematic liquid crystal “rod like”	5
1.5	Representation of the variation of the order parameter as a function of the critical temperature (T_c)	7
1.6	Double refraction as manifestation of birefringence	7
1.7	Anisotropic properties: Refractive index and polarisabilities	8
1.8	Refractive index in 5CB as a function of temperature	11
1.9	Refractive index in 5CB as function of wavelength	12
1.10	Illustration of the Langevin function	14
1.11	Representation of the anisotropic properties: permittivities	16
1.12	Permittivity anisotropy for 5CB as function of temperature	19
1.13	Illustration of splay, twist and bend distortions in nematic liquid crystals	22
1.14	Evolution of the orientation of the director as a function of the applied voltage	22
1.15	Different types of distortion relative to the orientation of the mag- netic field and the type of cell	23
1.16	Ideal curve of permittivity measure as function of applied voltage	25
1.17	Example of flexoelectricity created by distortion in liquid crystals	25

1.18	Evolution of permittivity anisotropy as a function of frequency for MLC2048	26
1.19	Schematic representation of a diffraction grating system	30
1.20	Schematic representation of a binary phase grating	31
2.1	Different stages of the optical lithography process	34
2.2	Schematic view of interdigitated electrodes	36
2.3	Photolithographic mask for production of interdigitated electrodes substrates	37
2.4	Detail of the photolithographic mask to underline the “Snake” electrode pattern.	37
2.5	Cross section of an interdigitated cell	38
2.6	Different alignments and rubbing process	39
2.7	Results from the UV/vis spectrometer, plot of absorbance as a function of the wavelength	40
2.8	Plotting of n vs. $\frac{1}{\lambda}$ to determine the thickness d of the cell	41
2.9	Detail of ring electrodes	42
2.10	Electric fields across the test cell with (bottom) and without (top) earth ring	43
2.11	Setup for dynamic measurement (Courtesy of Mr. T Muller) . . .	44
2.12	Schematic diagram of the experimental apparatus for dynamic measurement	44
2.13	Simple representation of the transmission experimental setup . . .	48
2.14	Ideal curve of transmission measure	48
2.15	Representation of the different setup for magnetic measurement .	50
2.16	Schematic representation of the setup for the Mach-Zenhder interferometer	52
3.1	Cross-section of an assembled, filled and connected cell	57
3.2	Observation of interdigitated electrodes under microscope	57

3.3	Picture observed from the CCD camera in the interferometer . . .	58
3.4	Picture of raw data (left) and threshold data (right) from interferometer observations	59
3.5	3D plot of the distortion across the cell and as a function of time	60
3.6	Plots of the distortion across the cell and as a function of time . .	60
3.7	Fringe movement induce by 2-frequency material when different frequencies signals are applied	61
3.8	Schematic cross-section of the cell with nematic liquid crystal used for modelling	62
3.9	Illustration of the effects from the parameter used for the fitting (A: pretilt; B: flexoelectricity and C: ions)	67
3.10	Maximum distortion during positive applied signal (squares) and negative applied signal (diamonds) for the antiparallel thick geometry and the model data represented by the line. With 0 representing the centre of the electrode where the signal is applied. . .	69
3.11	(a) The filled circles show experimental data for the relative fringe movement as a function of time at the position $x=15\mu\text{m}$. (b) The applied voltage wave form is shown as the dotted line. The solid line shows the voltage waveform that was used to obtain the fit to the data shown by the solid line in (a).	70
3.12	Contour plot of the relative fringe movement with time as a function of the distance in the x-direction across cell CLT08-07A. From 0.0-2.5 and 5.0-7.5 s +1.17V is applied to the central electrode, and from 2.5-5.0 and 7.5-10.0 s the applied voltage is -1.17V	71
3.13	Results of the relative fringe movement as a function of time in a parallel alignment cell	71
3.14	Maximum distortion during positive applied signal (circles) and negative applied signal (squares) in a parallel alignment cell . . .	72

3.15	Results of the relative fringe movement as a function of time in thin antiparallel alignment cell	73
3.16	Maximum distortion during positive and negative applied signal for the thin antiparallel geometry cell	73
3.17	Transient capacitance response of a $22\ \mu m$ planar layer of the nematic liquid crystal E7 to an applied squarewave voltage waveform with frequency 0.2 Hz and amplitude between 1.02 V and 1.86 V.	76
3.18	Theoretical prediction of the transient capacitance in response to a squarewave voltage waveform with frequency 0.2 Hz and amplitude 1.5 V with concentration of charged mobile ionic species shown in the legend.	76
3.19	Theoretical predictions for the electric field in the centre of the cell multiplied by the cell thickness corresponding to the transient capacitance curves shown in the previous figure.	77
3.20	Schematic representation of the setup for the diffraction experiment	79
3.21	Diffraction pattern induced by the $40\ \mu m$ interdigitated electrode sample with a signal of $1.16V_{rms}$ and $1kHz$	80
3.22	Time dependent observation of the diffraction pattern induced by the $40\ \mu m$ interdigitated electrode sample (negative signal from 0 to 2.5 seconds and positive signal from 2.5 to 5 seconds)	81
3.23	(a) and (b) show the time dependent intensity of different orders in the far field diffraction pattern. (c) shows the displacement of fringes in a Mach-Zehnder interferometer as a function of time.	83
4.1	Illustration of the Amplitude Modulation (A.M.) signal sample used in this investigation	88
4.2	Illustration of the Square signal sample (S.Q.) used in this investigation	89

4.3	Illustration of the combined positive, zero and negative signal sample (PoNo) used in this investigation	89
4.4	Measure of permittivity in the thick planar E7 cell with the AM signal as a function of temperature (top) and as function of the applied voltage (bottom)	92
4.5	Measure of permittivity in the thin planar E7 cell with the AM signal as a function of temperature (top) and as function of the applied voltage (bottom)	93
4.6	Measure of permittivity in the thin HAN E7 cell with the AM signal as a function of temperature (top) and as function of the applied voltage (bottom)	94
4.7	Measure of permittivity in the thin planar TL216 cell with the AM signal as a function of temperature (top) and as function of the applied voltage (bottom)	94
4.8	Measure of permittivity in the thin HAN TL216 cell with the AM signal as a function of temperature (top) and as function of the applied voltage (bottom)	95
4.9	Measure of permittivity in the thick planar E7 cell with the SQ signal as a function of temperature (top) and as function of the applied voltage (bottom)	96
4.10	Measure of permittivity in the thick planar E7 cell with the PoNo signal as a function of temperature (top) and as function of the applied voltage (bottom)	96
4.11	Measure of permittivity in the thin planar E7 cell with the SQ signal as a function of temperature (top) and as function of the applied voltage (bottom)	99
4.12	Measure of permittivity in the thin planar E7 cell with the PoNo signal as a function of temperature (top) and as function of the applied voltage (bottom)	99

4.13	Measure of permittivity in the thin planar TL216 cell with the SQ signal as a function of temperature (top) and as function of the applied voltage (bottom)	100
4.14	Measure of permittivity in the thin planar TL216 cell with the PoNo signal as a function of temperature (top) and as function of the applied voltage (bottom)	101
4.15	Measure of permittivity in the thin HAN E7 cell with the SQ signal as a function of temperature (top) and as function of the applied voltage (bottom)	102
4.16	Measure of permittivity in the thin HAN E7 cell with the PoNo signal as a function of temperature (top) and as function of the applied voltage (bottom)	103
4.17	Measure of permittivity in the thin HAN TL216 cell with the SQ signal as a function of temperature (top) and as function of the applied voltage (bottom)	104
4.18	Measure of permittivity in the thin HAN TL216 cell with the PoNo signal as a function of temperature (top) and as function of the applied voltage (bottom)	104
4.19	Results for the investigation of the evolution of the ion effect at low temperatures on a thick ionic planar cell	105
5.1	Experimental setup for the magnetic measure of bend distortion .	110
5.2	Experimental setup for the magnetic measure of splay distortion .	111
5.3	Idealised results for permittivity measurements	113
5.4	Experimental results for K_{11} determination	115
5.5	Experimental results for K_{33} determination	116
5.6	Permittivity comparison between old and new sample and different thickness'	117

5.7	Permittivity comparison between old (latest measurement) and new (earlier measurement) sample of $22\mu\text{m}$, the solid line is the fit for each cell	118
5.8	Permittivity (solid line) and loss (dashed line) as a function of the signal frequency for E7 material in old (later) and new (earlier) cell	119
5.9	Theoretical results for the magnetic experiment highlighting the effect of flexoelectricity and ions on the Fréedericksz transition . . .	122
6.1	Schematic cross-section of sawtooth sample	126
6.2	Schematic top view of anti-phase sawtooth sample	126
6.3	Schematic top view of in-phase sawtooth sample	127
6.4	Schematic top view of sawtooth flat sample	127
6.5	Schematic cross-section of sawtooth/flat samples (A: anti-phase, B: In-phase and C: sawtooth/flat)	128
6.6	Theoretical optical textures across the cell of the different states in samples	129
6.7	Experimental observations of the different states in samples from theoretical predictions shown in Figure 6.6	130
6.8	Microscope observations of a bend defect in an anti-phase sample under crossed polarised light at different angles from $+45^\circ$ (left) to -45° (right) by steps of 15°	131
6.9	Microscope control before and after annealing for defects not occurring at different position	132
6.10	Statistical results of presence of bend and planar states in the anti-phase sample as a function of the pitch	133
6.11	Statistical results of presence of bend and planar states in the in-phase sample as a function of the pitch	134
6.12	Statistical results of presence of bend, planar and Pi states in the flat/sawtooth sample as a function of the pitch	135

7.1	Schematic cross-section of dielectrophoresis sample	139
7.2	Observation of the fringe movement related to thickness variation across the oil layer, the size of the electrodes and the voltage applied	141
7.3	Results for $20\mu\text{m}$ electrodes with $2.85\mu\text{m}$ thick oil layer	142
7.4	Results for $40\mu\text{m}$ electrodes with $4.83\mu\text{m}$ and $7.79\mu\text{m}$ thick oil layers	142
7.5	Results for $80\mu\text{m}$ electrodes for different oil layer thickness	143
7.6	Results for $120\mu\text{m}$ electrodes for different oil layer thickness	143
7.7	Plot of the relation between $\ln(A/V^2)$ vs. h/d	145
7.8	Pictures of <i>Varroa destructor</i>	145
7.9	Schematic representation of the Michelson interferometer setup	147
7.10	Experimental setup for interferometry and accelerometer data ac- quisition	148
7.11	Comparison between interferometry (high) and accelerometer (low) results	149
7.12	View of the <i>Carabus problematicus</i>	150
7.13	Results from the Optical Coherence Tomography	151
A.1	Schematic cross-section of a planar alignment interdigitated cell with nematic liquid crystal	160
A.2	Regression analysis from the spectrometer data for the determina- tion of the sample thickness	171
A.3	Calibration curve for the magnetic field as function of the current in the coils	172
A.4	Regression analysis for the determination of the factor between the current in the coils and the magnetic field generated	173
A.5	Regression analysis for the $\ln(A/V^2)$ vs. h/d	174

List of Tables

1.1	Order of magnitude of the different parameters	15
3.1	Characteristics of cells used during interferometric investigations of the sum of flexoelectric coefficients ($e_1 + e_3$)	68
3.2	Parameters obtained from the fit to the interferometric data for the phase grating device with parallel and anti parallel alignment	84
4.1	Characteristics of the liquid crystal materials used in the transient capacitance experiment.	90
4.2	Characteristics of cells used for transient capacitance experiments	91
5.1	Results of fitting parameter for E7 material illustrated in Figure 5.7121	
7.1	Results of fringe distortion as a function of electrodes size and oil thickness	144

Chapter 1

Introduction

1.1 Liquid crystals

Surrounding matter is usually divided into three distinct states. The first is the solid state, with a high degree of order; the next is the liquid state with a greater degree of freedom; the final one with no order is the gas or vapour state. The best example of these three states can be observed with water (see Figure 1.1) which is solid under atmospheric pressure at a temperature below 0°C , liquid from 0°C up to 100°C , and then transforms to water vapour at temperatures higher than 100°C .

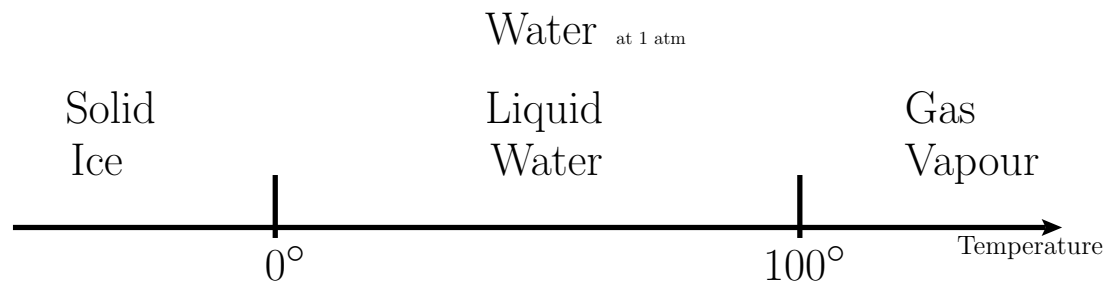


Figure 1.1: Different states of water at atmospheric pressure

But there also exists states of matter which can not be classified in any of these three states: plasma, super-critical fluid and liquid crystals. This last intermediate state of matter is called “*mesophase*” or “*mesomorphic phase*” [1]. Liquid crystals were discovered during the second half of the 19th century. Friedrich Reinitzer observed the strange behaviour of organic substances “*cholesteryl acetate*” and “*cholesteryl benzoate*”, while studying cholesterol in plants [2–4]. The name “Liquid Crystals” was coined by Otto Lehmann [2]. It is only in the last 40 years (since the 1970’s) that electronic displays have been developed, enabled by the synthesis of the first room temperature nematic liquid crystal in the late 1960s [4].

1.2 Different type of liquid crystals

A distinction can also be made by the composition; if the material is pure and its properties depend on the temperature, it will be “*Thermotropic*”. Where as if it has a mix of various components and its properties depends on the concentration, it is a “*Lyotropic*” liquid crystal material. The most common example of the lyotropic phase is soap [1, 5]. It can be a “*racemic*” liquid, where the concentration of *Levorotatory* and *Dextrorotatory* molecules are equal. Racemic type is also the most common material in liquid crystal [1] but also can be a single molecule or non chiral mixture.

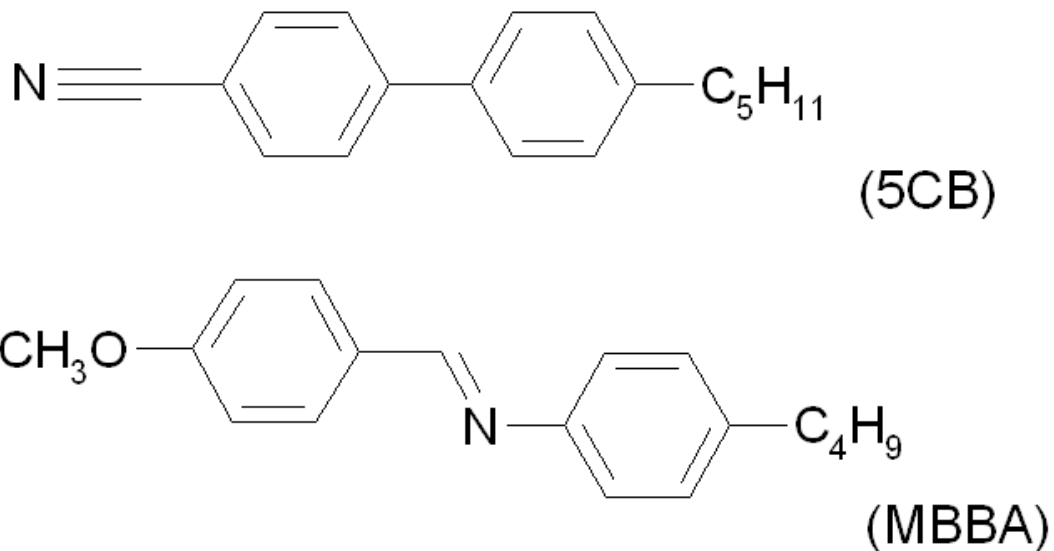


Figure 1.2: Schematic representation of liquid crystal molecules

Liquid crystals are composed mainly of carbon and hydrogen. They are characterised by a long apolar alkyl group at one end (C_5H_{11} or C_4H_9) and at the other end by a short and polar methoxy- (CH_3O) or cyano-group ($C \equiv N$). An example of the two most studied liquid crystals molecules (5CB and MBBA) [6, 7] can be observed in Figure 1.2. 4-MethoxyBenzylidene-4'-n-ButylAniline (or MBBA) is the typical example of nematic liquid crystal. At room temperature ($20^\circ C$) it is solid. At $22^\circ C$ the solid melts and it transforms into a cloudy liquid, another

change occurs at 47°C when the liquid turns clear [2]. The cloudy phase is called “liquid crystal” (see Figure 1.3).

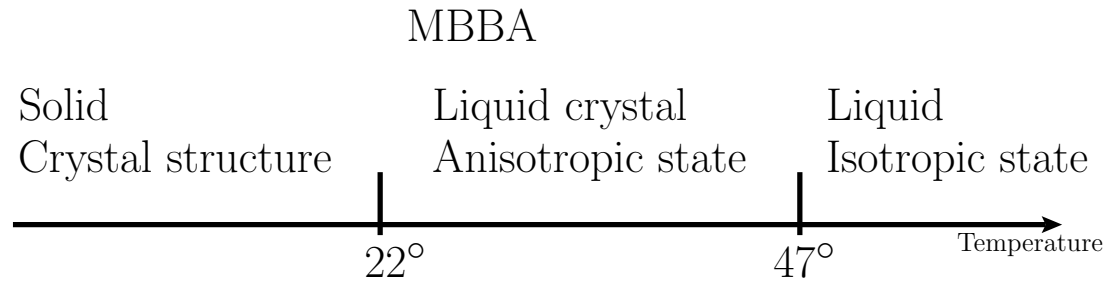


Figure 1.3: Different states of MBBA

The shape of the solid in the liquid crystal determines the family in which it is classified. There are 3 main groups: Nematic, Smectic and Discotic (or Columnar) liquid crystals. The main groups are composed of many subdivisions and other smaller groups such as Smectic B, Smectic C, etc.

1.3 Calamitic liquid crystals

This is the most common type of liquid crystal, the molecules are “rod like”; the ratio between their length and their diameter is large. The main difference between the isotropic phase and the liquid crystal phase is that the molecules which compose the second state tend to point in a certain orientational order. Calamitic liquid crystal can be divided into several subgroups according to the level of organisation. If the compound possesses positional and orientational ordering it is called the “*Smectic phase*” which is itself subdivided according to the specific orientation and symmetry. If the material possesses orientational but not positional ordering the phase is called the “*Nematic phase*” [4].

1.4 Nematic liquid crystal order parameter

The nematic phase is the simplest type of liquid crystal possessing only orientational order [8]. The nematic liquid crystals tend to align to a preferred

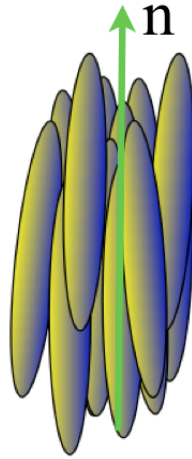


Figure 1.4: Illustration of nematic liquid crystal “rod like”

orientation (\mathbf{n}), with the molecules being quasi-parallel to each other. The nematic material does not possess positional ordering. The average direction of the molecule is called the director (\mathbf{n}). The director can be either an average over time at a point in space or an average over space at a defined time [1, 9]. The state of the director, in the absence of electric or magnetic forces, can not be distinguished, $\vec{n} = -\vec{n}$. The nematic order parameter (S) is an average of the second Legendre polynomial defined as:

$$S = \frac{1}{2} \langle 3 \cos^2 \theta - 1 \rangle \equiv \frac{\int \frac{1}{2} f(\theta) (3 \cos^2 \theta - 1) d\Omega}{\int \frac{1}{2} f(\theta) d\Omega} \quad (1.1)$$

Where the distribution function $f(\theta, \phi) d\Omega$ is the probability of finding the nematic molecule pointing in a small solid angle $d\Omega$ around the direction (θ, ϕ) . (θ) and (ϕ) are respectively the inclination and the azimuth into spherical coordinate system. As the nematic molecules have a complete cylindrical symmetry about \mathbf{n} [1], the distribution function only depends upon the inclination angle ($f(\theta, \phi) = f(\theta)$). As the direction \mathbf{n} and $-\mathbf{n}$ can not be distinguished ($\vec{n} = -\vec{n}$) it creates another symmetry ($f(\theta) \equiv f(\theta - \pi)$). For perfect ordering, when all the molecules are pointing in the same direction, the distribution function, this angle even when the angle is rotated in the opposite direction, is equal to one. The distribution

function for any other angles is null ($f(\theta) = 1$ for $\theta = 0$ and $\theta = \pi$, but $f(\theta) = 0$ when $0 < \theta < \pi$). This leads to an order parameter also equal to one by using the left part of Equation 1.1 and replacing θ by π .

$$S \sim \frac{1}{2} \langle 3 \cos^2 \pi - 1 \rangle = 1 \quad (1.2)$$

In the opposite case, a non ordered system, or in other words an isotropic system, the distribution function is equal to one regardless of the angle the molecule is pointing at ($f(\theta) = 1$ for $0 \leq \theta \leq \pi$). This leads the order parameter to be equal to zero.

$$S \sim \int_0^{2\pi} d\phi \int_0^\pi \frac{1}{2} (3 \cos^2 \theta - 1) \sin \theta d\theta = 0 \quad (1.3)$$

The nematic order parameter is also dependant on the temperature. The typical value of (S) at the nematic-isotropic transition or critical temperature (or critical temperature T_c) is around 0.3 to 0.4 which is a weak first order transition. The order parameter increases as the temperature is lowered as represented in Figure 1.5 [2, 9]. The combination of molecular order and anisotropic molecules leads to anisotropic physical properties such as dielectric anisotropy $\Delta\epsilon$ and refractive index anisotropy Δn .

1.5 Physical properties of nematic liquid crystals and anisotropy

1.5.1 Birefringence in crystals

Materials such as glass have an isotropic refractive index, but calcite is a material which behaves differently. According to Snell law's the angle of a refracted beam of light depends on the index of the material and the angle of incidence. For calcite with polarised light, double refraction occurs where the angle has different values according to the orientation of the sample (see Figure 1.6) [10–14].

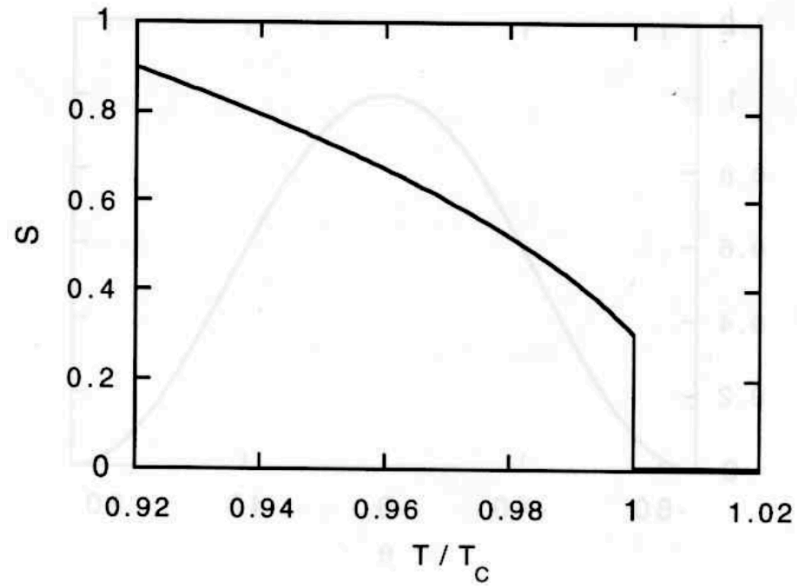


Figure 1.5: Representation of the variation of the order parameter as a function of the critical temperature (T_c)

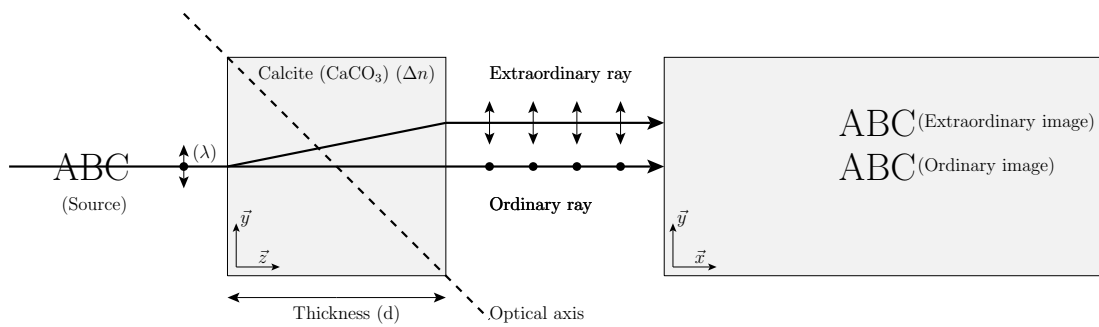


Figure 1.6: Double refraction as manifestation of birefringence

Calcite CaCO_3 has two different refractive indices according to direction of propagation. One called ordinary which follow normal laws of refraction perpendicular to the axis of anisotropy, is $n_o=1.658$. The other one called extraordinary which depends on the direction in the crystal parallel to the axis of anisotropy, is $n_e=1.486$ [15, 16]. Birefringence is determined as the difference between these two refractive indices.

$$\Delta n = n_e - n_o \quad (1.4)$$

1.5.2 Refractive index and birefringence in liquid crystals

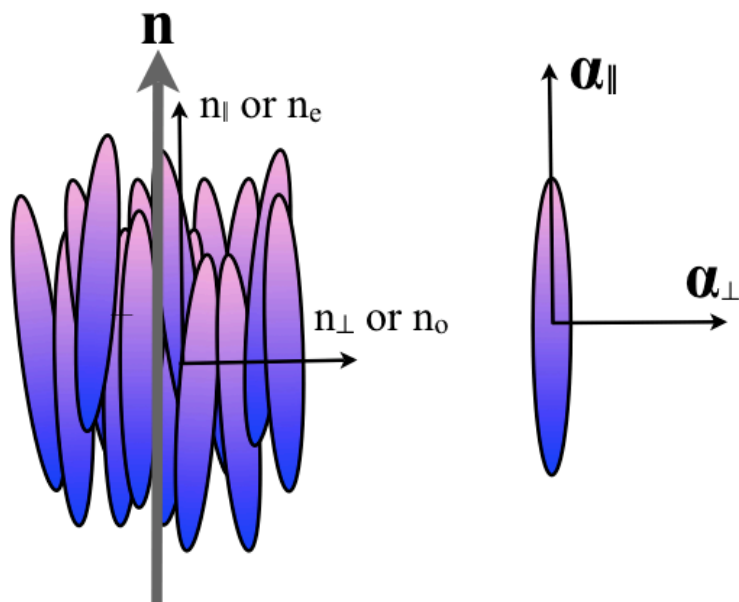


Figure 1.7: Anisotropic properties: Refractive index and polarisabilities

In the case of liquid crystals, polarisability (α) is the induced dipole moment per unit field. This induced moment is related to the delocalisation of the electron cloud in the phenyl ring in the liquid crystal molecule (see Figures 1.2 and 1.7) [7, 14]. In the case of 5CB, the two approximately coplanar rings give a large parallel polarisability ($\alpha_{||}$) relatively to the perpendicular one (α_{\perp}). This configuration

generates a polarisability anisotropy (see Equation 1.5).

$$\Delta\alpha = \alpha_{\parallel} - \alpha_{\perp} \quad (1.5)$$

The refractive index of a non-magnetic medium is defined as the ratio of the speed of light in vacuum divided by the speed of light in the medium (see Equation 1.6).

$$n = \frac{c_{vacuum}}{\nu_{medium}} = \sqrt{\epsilon_r} \quad (1.6)$$

The interaction of light on the delocalised electronic cloud is null. Light which is an electro-magnetic wave at a frequency of few hundreds of terahertz (10^{12}Hz) [14]. The change of electro-magnetic orientation is too fast to generate an electronic migration. At these frequencies, dipole moments per molecule are defined parallel to the director as:

$$m_{\parallel} \propto \left(\bar{\alpha} + \frac{2}{3}\Delta\alpha S \right) E \quad (1.7)$$

And perpendicular to the director as:

$$m_{\perp} \propto \left(\bar{\alpha} - \frac{1}{3}\Delta\alpha S \right) E \quad (1.8)$$

Where (S) is the nematic order parameter and (E) is the strength of the electro-magnetic excitation.

From the molecule moment, the polarisation of the bulk containing N dipoles per unit volume, can be calculated as:

$$P = Nm = \epsilon_0(\epsilon_r - 1)E \quad (1.9)$$

From the Equation 1.9, the permittivity (ϵ_r) and the refractive index (n) can be calculated from the dipole moment using the Equations 1.6, 1.7, 1.8 and 1.9

where:

$$\bar{\alpha} = \frac{1}{3}(\alpha_{\parallel} + 2\alpha_{\perp}) \quad (1.10)$$

The relationship between the nematic order parameter (S), the polarisability and the polarisability anisotropy (α and $\Delta\alpha$) and the refractive index is given by:

$$\frac{S\Delta\alpha}{\alpha} = \frac{n_{\parallel}^2 - n_{\perp}^2}{n^2 - 1} \quad (1.11)$$

From the Equation 1.11, the birefringence can be defined as:

$$\Delta n = n_{\parallel} - n_{\perp} \sim S\Delta\alpha \quad (1.12)$$

The refractive index is a parameter which depends on the temperature. The nematic order parameter dominates the temperature dependence. Each refractive index can be related to the polarisability and the order parameter as:

$$n_{\parallel} \propto \left(1 + \bar{\alpha} + \frac{2}{3}\Delta\alpha S\right)^{1/2} \quad (1.13)$$

$$n_{\perp} \propto \left(1 + \bar{\alpha} - \frac{1}{3}\Delta\alpha S\right)^{1/2} \quad (1.14)$$

Figure 1.8 [17] shows the variation of both refractive indices as a function of temperature for 5CB (see Figure 1.2), it also shows the fact that the isotropic phase possesses only one refractive index compared to two in the nematic phase. The refractive index also varies as a function of wavelength (λ), it increases near to an absorption. For 5CB, an absorption peak is located at a wavelength of 275nm, this gives larger refractive index at the lower end of the visible range as shown in Figure 1.9 [7, 17]. The different refractive indices act on the different components of the polarisation which are therefore subject to different phase shifts. The light then recombines to give linear, circular or elliptical polarisation depending on the wavelength (λ), the thickness (d) and the birefringence of the medium (Δn) (see

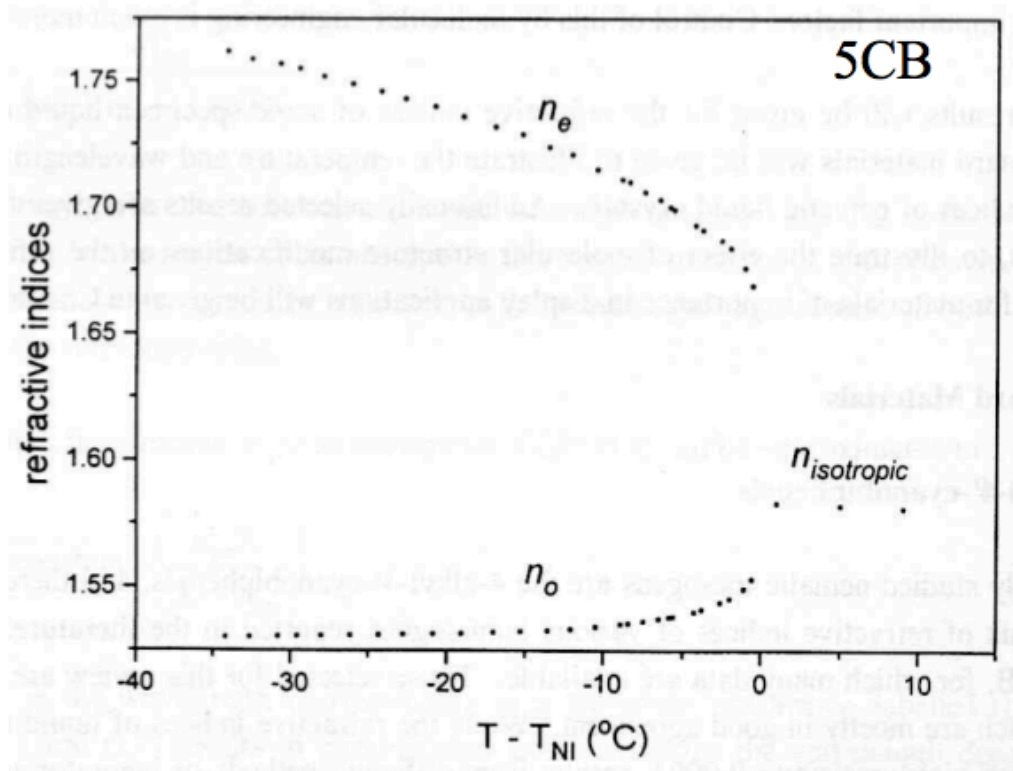


Figure 1.8: Refractive index in 5CB as a function of temperature

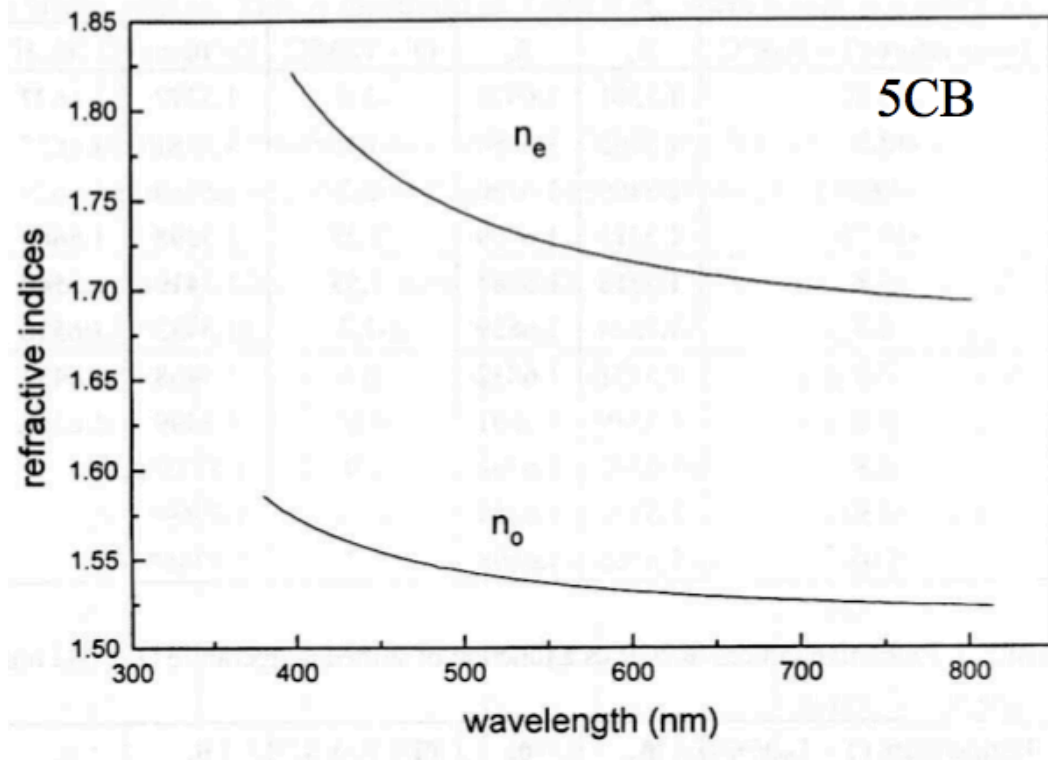


Figure 1.9: Refractive index in 5CB as function of wavelength

Figure 1.6).

1.5.3 Permittivities

Langevin theory for an isotropic fluid

Considering a plate capacitor with the capacitance being equal to C_0 when empty and a constant voltage V_0 is applied across the plates. Introducing a polarisable medium between the capacitor plates with the voltage kept constant, the capacitance is now C . The dielectric permittivity (ϵ_r) of the medium can be calculated as the ration C/C_0 . A medium with polarised charge in free space, with permittivity ϵ_0 , is described by replacing the charge by a region of permittivity $\epsilon_r\epsilon_0$. ϵ_r is defined in Equation 1.15 with P being the polarisation (or dipole moment per unit volume) defined in Equation 1.16 where N is the number of dipoles per unit volume, μ the dipole moment, Q is the charge in the dipole and l the separation

of the positive and negative charge in the dipole.

$$\varepsilon_r = 1 + \frac{P}{\varepsilon_0 E} \quad (1.15)$$

$$P = n\mu = NQl \quad (1.16)$$

Taking a fluid with molecules possessing a permanent dipole, the molecules are in constant thermal motion each one having an energy per classical degree of freedom given by:

$$\frac{1}{2}k_B T \quad (1.17)$$

There is no dipole moment of the fluid due to nematic symmetry. If now an electric field is applied to the fluid, the applied force tries to align the dipoles but is frustrated by the thermal motion of the molecules. The potential energy in an electric field (E) pointing in a direction making an angle (θ) with the director of the dipole moment, is given by:

$$\varepsilon = -\vec{\mu} \cdot \vec{E} = -\mu E \cos \theta \quad (1.18)$$

Whereas the thermal energy of molecules is given by:

$$\varepsilon \sim k_B T \quad (1.19)$$

Under these condition the probability that the dipole will be pointing at angle θ , $p(\theta)$, is given by the *Boltzmann factor*:

$$p(\theta) \sim \exp -\frac{\varepsilon}{k_B T} = \exp \left(\frac{\mu E \cos \theta}{k_B T} \right) \quad (1.20)$$

To determine the polarisation, the average number of dipoles aligned along the electric field need to be known and this is calculate by:

$$\bar{\mu} = \langle \mu \cos \theta \rangle \Rightarrow \frac{\bar{\mu}}{\mu} = \langle \cos \theta \rangle \quad (1.21)$$

Where:

$$\langle \cos \theta \rangle = \frac{\int \rho(\theta) \cos \theta d\Omega}{\int \rho(\theta) d\Omega} \quad (1.22)$$

The integral over all possible directions and over all solid angles, is:

$$\frac{d\Omega}{\Omega} = \frac{r \sin \theta . r d\theta . 2\pi}{4\pi r^2} = \frac{1}{2} \sin \theta d\theta \quad (1.23)$$

Using the results of Equations 1.22 and 1.23, the right hand side of Equation 1.21 becomes:

$$\frac{\bar{\mu}}{\mu} = \frac{\int_0^\pi \exp\left(\frac{\mu E \cos \theta}{k_B T}\right) \cos \theta . \sin \theta d\theta}{\int_0^\pi \exp\left(\frac{\mu E \cos \theta}{k_B T}\right) \sin \theta d\theta} \quad (1.24)$$

The integral of Equation 1.24 gives an analytical solution:

$$\frac{\bar{\mu}}{\mu} = \coth\left(\frac{\mu E}{k_B T}\right) - \frac{1}{\frac{\mu E}{k_B T}} \quad (1.25)$$

The theory gives a function for the result of $\frac{\bar{\mu}}{\mu}$, called the *Langevin function* as shown on Figure 1.10.

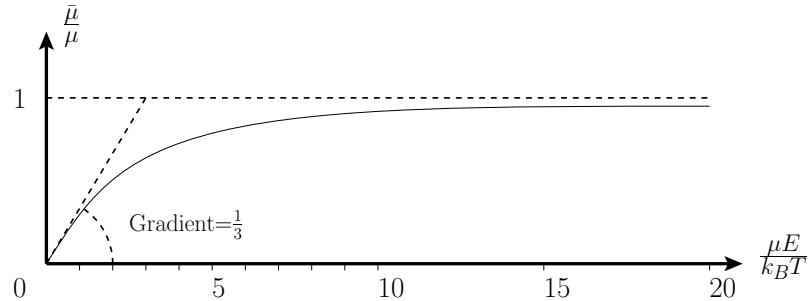


Figure 1.10: Illustration of the Langevin function

From the last line of Table 1.1, the parameter $\frac{\mu E}{k_B T}$ is well in the region of the

Table 1.1: Order of magnitude of the different parameters

μ	\sim few Debye	$\sim 1.10^{-29}$ C.m	maximum dipole moment
E	~ 10 V. μm^{-1}	$\sim 10^7$ V.m $^{-1}$	maximum electric field
T	$\sim 27^\circ\text{C}$	~ 300 K	room temperature
$k_B T$	$\sim 1.38 \times 10^{-23} \times 300$	$\sim 4 \times 10^{-21}$ J	thermal energy
$\frac{\mu E}{k_B T}$	~ 0.025	$\ll 1$	

curve where there is a constant gradient of $\frac{1}{3}$, which leads to:

$$\frac{\bar{\mu}}{\mu} \simeq \frac{\mu E}{3k_B T} \quad (1.26)$$

The equation for the polarisation:

$$P = N\bar{\mu} \quad (1.27)$$

Becomes:

$$P = \frac{N\mu^2}{3k_B T} E \quad (1.28)$$

Equation 1.28 is the mathematical expression for the Langevin theory for an isotropic fluid. Liquid crystals, as explained in Section 1.4, are anisotropic fluids, the permittivity properties depends on the direction as shown in Figure1.11 [17].

Onsager relation and Maier and Meier equations

Langevin theory considers that the electric field applied is not affected by the material. Also the surrounding permanent dipole exerts a local force. The applied field (E_d) exerting a force on the permanent dipoles is distinct from the local field (E_{loc}).

$$P = N\alpha E_{loc} + \frac{N\mu_d^2}{3K_B T} E_d \quad (1.29)$$

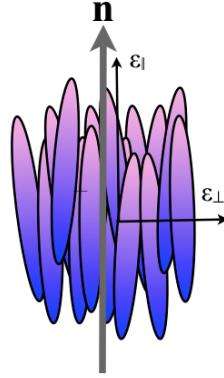


Figure 1.11: Representation of the anisotropic properties: permittivities

$$\frac{\varepsilon_r - 1}{\varepsilon_r + 2} = \frac{N}{3\varepsilon_0} \left(\alpha + \frac{\mu_d^2}{3K_B T} \right) \quad (1.30)$$

The debye equation takes into account the induced (first term on RHS in Equation 1.29) and permanent dipoles (second term on RHS in Equation 1.29). But this relationship only works for low density gases.

$$\varepsilon - 1 = \frac{NhF}{\varepsilon_0} \left(\alpha + \frac{F\mu_d^2}{3K_B T} \right) \quad (1.31)$$

$$F = \frac{1}{1 - \alpha f} \quad (1.32)$$

Where:

$$f = \frac{2N}{3\varepsilon_0} \left(\frac{\varepsilon - 1}{2\varepsilon + 1} \right) \quad (1.33)$$

$$h = \frac{3\varepsilon}{2\varepsilon + 1} \quad (1.34)$$

To apply the local field to condensed matter, the Onsager relation (Equation 1.31) uses a reaction field factor (Equation 1.32) and a cavity field factor (Equation 1.34), but this is still restricted to rigid unassociated molecules in simple liquids. To take into account the dependance of the field with the interaction of a molecule with its environment, it required a generalisation of the Onsager expression to

anisotropic fluids. This leads to Maier and Meier equations.

$$\bar{\mu}_{\parallel} = (\bar{\alpha} + \frac{2}{3}\Delta\alpha S)FhE_{\parallel} \quad (1.35)$$

$$\bar{\mu}_{\perp} = (\bar{\alpha} + \frac{1}{3}\Delta\alpha S)FhE_{\perp} \quad (1.36)$$

Where:

$$\bar{\alpha} = \frac{1}{3}(\alpha_{\parallel} + 2\alpha_{\perp}) \quad (1.37)$$

And:

$$\Delta\alpha = \alpha_{\parallel} - \alpha_{\perp} \quad (1.38)$$

The induced dipole moments per molecule (see Equations 1.35 and 1.36), are now defined for anisotropic material. With Langevin analysis (First part of Section 1.5.3) and Maier-Saupe mean field approximation (LHS of equation 1.1) for the order parameter S , an expression for $(\varepsilon_{\parallel})$ and (ε_{\perp}) can be written; The Maier-Meier equations (Equations 1.39 and 1.40) for uniaxial liquid crystals with the dipole along the axis.

$$\bar{\varepsilon} = \frac{1}{3}(\varepsilon_{\parallel} + 2\varepsilon_{\perp}) = 1 + \frac{NhF}{\varepsilon_0} \left(\bar{\alpha} + \frac{F\mu^2}{3K_B T} \right) \quad (1.39)$$

$$\Delta\varepsilon = \varepsilon_{\parallel} - \varepsilon_{\perp} = \frac{NhF}{\varepsilon_0} \left(\Delta\alpha + \frac{F\mu^2}{2K_B T} (1 - 3\cos^2\beta) \right) S \quad (1.40)$$

If the dipole in the liquid crystal is off axis and makes an angle β with it, Equation 1.40 becomes:

$$\Delta\varepsilon = \varepsilon_{\parallel} - \varepsilon_{\perp} = \frac{NhF}{\varepsilon_0} \left[\Delta\alpha + \frac{F\mu}{2K_B T} \left(\mu_{\parallel}^2 - \frac{\mu_{\perp}^2}{2} \right) \right] S \quad (1.41)$$

With μ_{\parallel} and μ_{\perp} defined as:

$$\mu_{\parallel} = \mu\cos\beta \quad (1.42)$$

$$\mu_{\perp} = \mu\sin\beta \quad (1.43)$$

With respect to:

$$\mu^2 = \mu_{\parallel}^2 + \mu_{\perp}^2 \quad (1.44)$$

Permittivity in nematic liquid crystals

Liquid crystal molecules are asymmetrical and their end groups (eg: $-\text{C}\equiv\text{N}$ or C_xH_y type groups) possess different electronegativities [14]. To achieve high values of parallel dipole (μ_{\parallel}), the molecule should possess a cyanobiphenyl group at one end, as can be seen in 5CB material on schematic representation in Figure 1.2. For a very large parallel dipole moment, the Equation 1.40 can be approximated as:

$$\Delta\varepsilon \simeq \frac{\mu_{\parallel}^2 S}{T} \quad (1.45)$$

However having high electronegative groups at the end tends to make the molecule dissociate into ions. Nematic material have been developed with values of permittivity anisotropy ($\Delta\varepsilon$) between -10 and 50. To create large negative values of the permittivity anisotropy the perpendicular dipole moment needs to be large with the consequence of reducing significantly the free rotation around the molecular axis. The permittivity anisotropy is a factor dependent on the temperature (see Figure 1.12). It can also be dependent on the frequency of the applied field and creating a specific type of nematic material called 2-frequencies with a specific frequency where the anisotropy goes from being positive to negative.

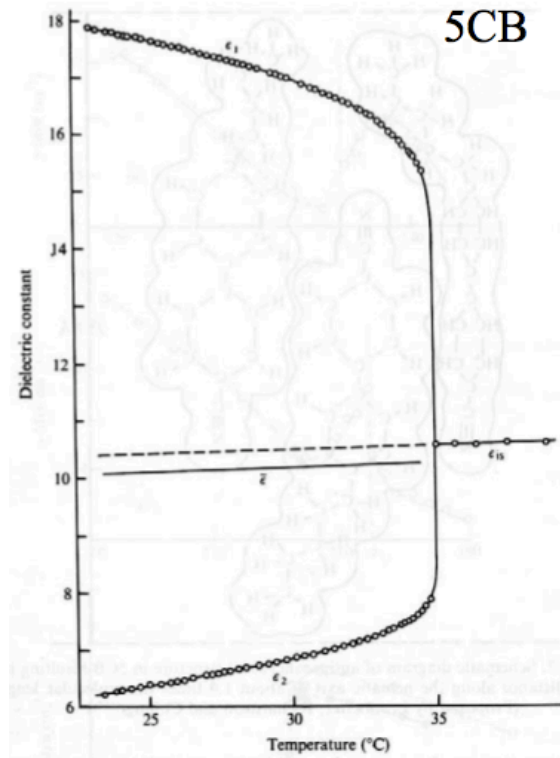


Figure 1.12: Permittivity anisotropy for 5CB as function of temperature

1.5.4 Magnetic susceptibility

To understand magnetic susceptibility, an analogy can be made with electric susceptibility or permittivity. If an electric field is applied to a liquid crystal sample, it creates a bulk polarisation (\vec{P}); a magnetic field (\vec{H}) will create a bulk magnetisation (\vec{M}) or magnetic dipole moment per unit volume of the liquid crystal sample. Due to the aromatic ring (phenyl) in the liquid crystal molecular structure, it is diamagnetic, creating an induced molecular magnetic moment in the opposite direction to the applied magnetic field. Due to the anisotropy, liquid crystal molecules tend to align either perpendicular or parallel to the magnetic field. The relation between the applied magnetic field (H) and the induced magnetisation (M) has the form as below:

$$M = Nm = \chi_m \cdot H \quad (1.46)$$

This relation can be extended to both directions as it is also an anisotropic property.

For the parallel direction:

$$M_{\parallel} = \chi_{m\parallel} \cdot H_{\parallel} \quad (1.47)$$

and for the perpendicular:

$$M_{\perp} = \chi_{m\perp} \cdot H_{\perp} \quad (1.48)$$

Where H_{\parallel} is for the magnetic field component parallel to the director n and H_{\perp} is for the perpendicular one; the coefficients $\chi_{m\parallel}$ and $\chi_{m\perp}$ are the diamagnetic susceptibilities parallel and perpendicular respectively to the director.

$$\Delta\chi = \chi_{m\parallel} - \chi_{m\perp} \quad (1.49)$$

$\Delta\chi$ is referred to as magnetic anisotropy; Positive $\Delta\chi$ gives an orientation along the magnetic fields, a negative one gives a perpendicular orientation but it is generally positive for most nematic liquid crystals [1]. The advantage of using magnetic fields is that they do not interact with ions which might be present in the liquid crystal sample. Generally the value of $\Delta\chi$ is small which removes the need to solve Maxwell's equation for the magnetic field in the sample.

1.5.5 Continuum theory, elastic constants and Fréedericksz effect

Introduction to the continuum theory

This is mainly based on the work in the early 20th century by Oseen [18, 19] and Zocher [20] later formulated by Frank in the mid 20th century [21]. Ericksen confined the theory in a mechanical framework and generalised the interpretation of static theory [5, 22]. This theory is based upon the director (n) and its possible distortions. One primordial characteristic of liquid crystals is the Fréedericksz

transition, which manifests itself when a constricted sample of liquid crystal is subject to an applied electric or magnetic field. The orientation of the director (\mathbf{n}) within a sample may be affected by a sufficient external applied field to generate a reorientation. The reorganisation competes with the alignment at the boundary surfaces.

Elastic constants

In a confined sample of liquid crystal the director orientation is dictated by the conditions at the boundaries surfaces in the absence of any external fields. Distortion can be caused, as explained in the introduction of continuum theory, by magnetic or electric fields. In the sample, the free energy per unit volume relative to the state of uniform orientation is also called “*Frank-Oseen elastic energy*” (see Equation 1.50) [23]. It applies to general distortion in a director field in a chiral nematic.

$$\delta F = \frac{1}{2}K_{11} \left(\frac{\partial n_x}{\partial x} \right)^2 + \frac{1}{2}K_{22} \left(\frac{\partial n_y}{\partial y} \right)^2 + \frac{1}{2}K_{33} \left(\frac{\partial n_z}{\partial z} \right)^2 \quad (1.50)$$

It can also be expressed as:

$$F_v = \frac{1}{2}K_{11}(\nabla \cdot \vec{n})^2 + \frac{1}{2}K_{22}(\vec{n} \cdot \nabla \times \vec{n})^2 + \frac{1}{2}K_{33}(\vec{n} \times \nabla \times \vec{n})^2 \quad (1.51)$$

Where \mathbf{n} is the unit vector of the director orientation, and $\partial n_x/\partial x$ is the splay deformation, $\partial n_y/\partial y$ is the twist deformation and $\partial n_z/\partial z$ the bend deformation component of curvature defined in a right-handed Cartesian coordinate system XYZ with Z being parallel to the director orientation as illustrated in Figure 1.13 [5, 24]. K_{11} , K_{22} and K_{33} are Frank elastic constants specific to the material [8].

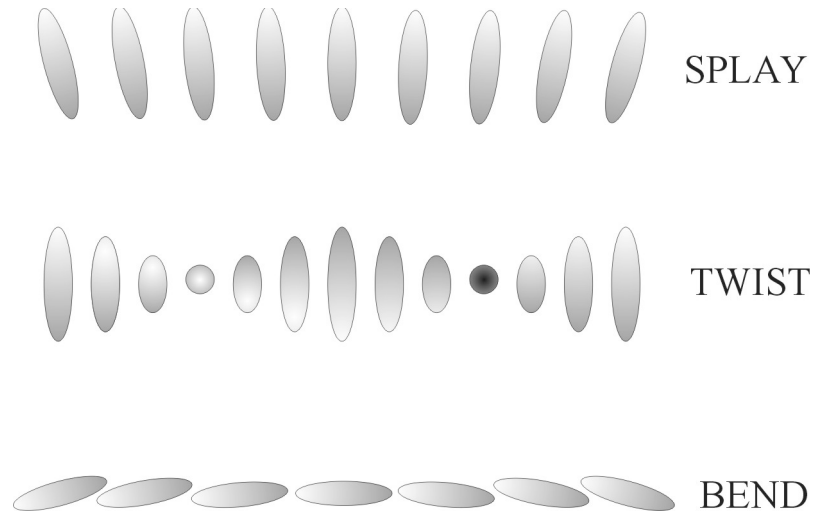


Figure 1.13: Illustration of splay, twist and bend distortions in nematic liquid crystals

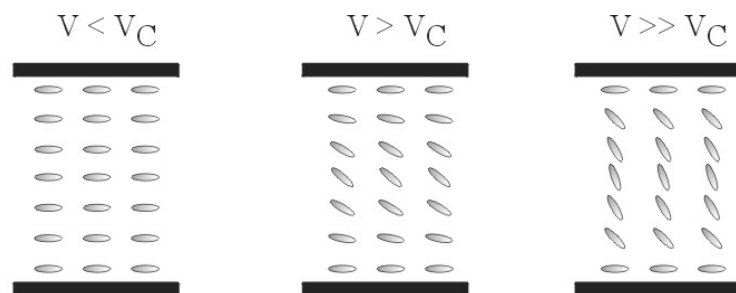


Figure 1.14: Evolution of the orientation of the director as a function of the applied voltage

Fréedericksz effect

The Fréedericksz transition is the result of the competition between the anchoring at the surface of the liquid crystal cell (shown on the left of Figure 1.14) and the force induced by the applied field, electric or magnetic. The transition occurs when the field goes above a threshold value referred to as “*critical field strength*” and starts reorientating the director \vec{n} from its resting position induced by the surface anchoring (illustrated on the middle and right side of Figure 1.14)[1, 5, 25, 26].

Measures types: Magnetic field

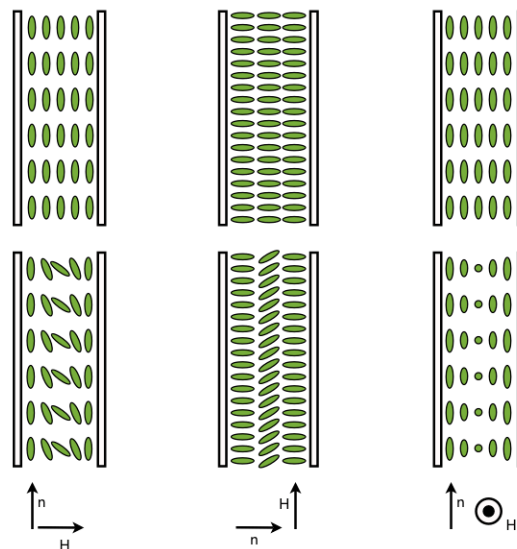


Figure 1.15: Different types of distortion relative to the orientation of the magnetic field and the type of cell

The Fréedericksz transition and threshold can be characterised by applying a magnetic field to a liquid crystal sample. The geometry of the sample and the orientation of the field determine the type of deformations; from splay (left side of Figure 1.15), twist (middle of Figure 1.15) or bend (right side of Figure 1.15) deformations [5]. The elastic constants can be deduced from these experiments

respectively by these equations:

$$H_{C(s)} = (\pi/d) \sqrt{\frac{K_{11}}{\Delta\chi}} \quad (1.52)$$

$$H_{C(t)} = (\pi/d) \sqrt{\frac{K_{22}}{\Delta\chi}} \quad (1.53)$$

$$H_{C(b)} = (\pi/d) \sqrt{\frac{K_{33}}{\Delta\chi}} \quad (1.54)$$

For the magnetic determination of Fréedericksz transition, the thickness (d) is a determining factor (see Equation 1.52, 1.53 and 1.54) [5].

Measures types: Electric field

The same type of experiment can be done using an electric field rather than a magnetic one and the Fréedericksz threshold can be related to the elastic constants by:

$$V_{C(s)} = \pi \sqrt{\frac{K_{11}}{\varepsilon_0 \Delta\varepsilon}} \quad (1.55)$$

$$V_{C(t)} = \pi \sqrt{\frac{K_{22}}{\varepsilon_0 \Delta\varepsilon}} \quad (1.56)$$

$$V_{C(b)} = \pi \sqrt{\frac{K_{33}}{\varepsilon_0 \Delta\varepsilon}} \quad (1.57)$$

Determining the Fréedericksz threshold using an electric field is not dependent upon the thickness (d) (see Equation 1.55, 1.56 and 1.57). $H_{C(s)}$ or $V_{C(s)}$ for a splay distortion, $H_{C(t)}$ or $V_{C(t)}$ for a twist distortion, $H_{C(b)}$ or $V_{C(b)}$ for a bend distortion. Measuring the permittivity of a sample using the electric field induced Fréedericksz transition has been used as a standard method to determine the elastic constants K_{11} and K_{33} , and the ordinary and extraordinary permittivity. From a typical curve of measure (see Figure 1.16), V_c can be used to determine the value of K_{11} using Equation 1.55. The gradient after the threshold gives the ratio between K_{33} and K_{11} . ε_{\perp} is deduced for the value of permittivity below the

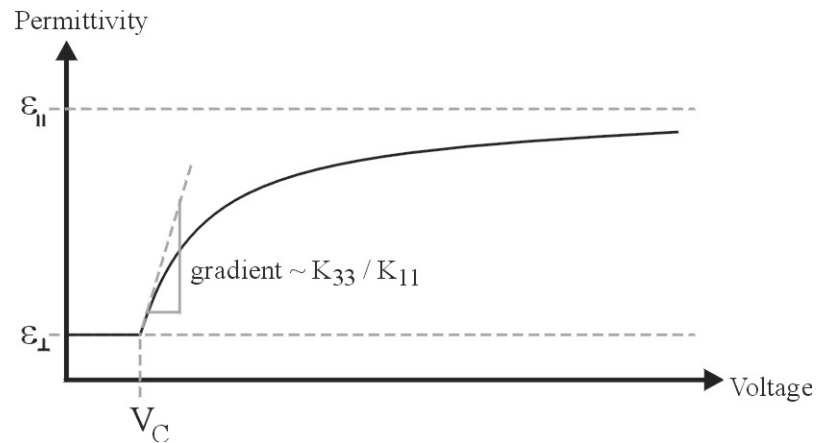


Figure 1.16: Ideal curve of permittivity measure as function of applied voltage

threshold and ϵ_{\parallel} is found from an extrapolation to $\frac{1}{V} \rightarrow 0$ of ϵ vs. $\frac{1}{V}$ [17].

1.5.6 Flexoelectricity

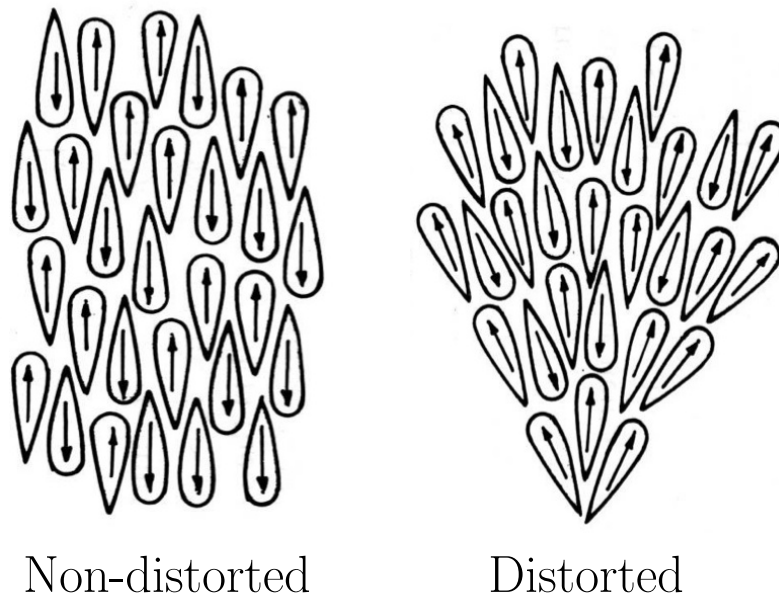


Figure 1.17: Example of flexoelectricity created by distortion in liquid crystals

If a force is applied to certain ionic crystals, it results in polarisation, this effect is called piezoelectricity. An analogy can be made with liquid crystals which show a polarisation effect for a bend or a splay distortion. This effect is called flexoelectricity [1, 27]. In a non deformed nematic liquid crystal, it can be assumed

that molecules are randomly oriented parallel or anti-parallel with respect to the director. On average the sample presents no net polarisation. If a splay distortion is applied to a sample with pear shaped molecules, it appears that the molecules rearrange with a preferred orientation and a net polarisation appears along the new director orientation (see Figure 1.17). The same phenomenon happens for a bent deformation with banana-shaped molecules which leads to the polarisation direction being perpendicular to the director orientation [1, 27–32].

1.5.7 2 frequency materials

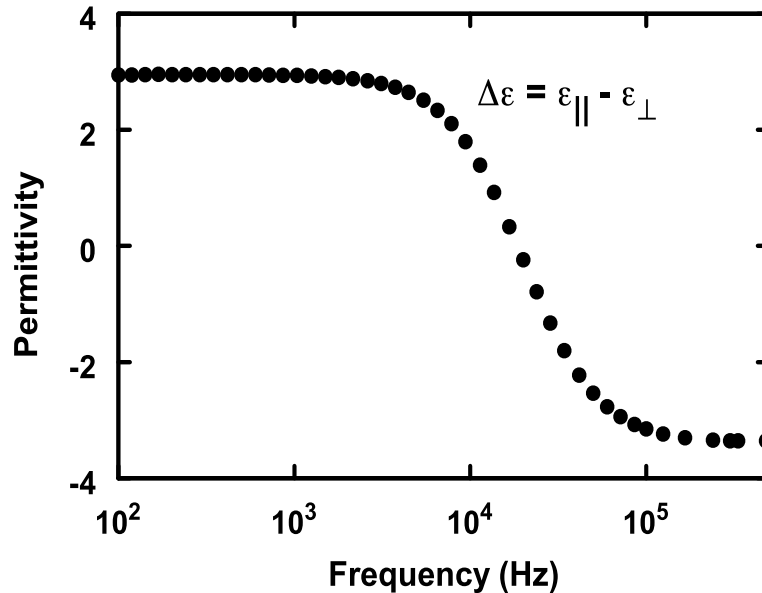


Figure 1.18: Evolution of permittivity anisotropy as a function of frequency for MLC2048

When an electric field is applied to a liquid crystal material, it generates an induced bulk polarisation via several mechanisms. At the atom level, an electronic polarisation which can also be observed at a molecular scale and also a re-orientation of the permanent molecular dipoles. The speeds at which they occur, are different and they appear at different time-scales. Liquid crystals are molecules containing permanent dipoles and the induced bulk polarisation is related to a partial re-orientation of these permanent dipoles. Due to the viscosity

of the fluid, there is a time difference for the re-orientation of the dipoles. A low relaxation frequency is often observed in calamitic nematic liquid crystals, when the electric field is applied parallel to the director compared to when the field is applied perpendicular to the director. The rotation around the long molecular axis being easier than the one around the short axis. Typical values for relaxation of the dielectric susceptibility (χ_{\parallel}) along the director, are above $10^5 Hz$ and are above $10^7 Hz$ for relaxation in the dielectric susceptibility perpendicular to the director (χ_{\perp}). In some liquid crystal materials, the relaxation in χ_{\parallel} happens at lower frequencies in the order of $10^3 Hz$ at room temperature. These kind of liquid crystals are called “dual frequencies” or “2f” materials. When the frequency of the applied signal is under the critical frequency (f_c), the dielectric susceptibility anisotropy $\Delta\chi = \chi_{\parallel} - \chi_{\perp}$ is positive, whereas for applied signals with a frequency well above f_c , the dielectric susceptibility is negative. The liquid crystal will align parallel to the electric field lines at a low frequency and perpendicular to the lines at high frequency. This effect has already been used to create fast switching displays by voltage addressing systems. One down side of this kind of material is a high temperature dependence of f_c . In Figure 1.18, the liquid crystal MLC2048 [33] measured at $25^{\circ}C$ and $0.1 V_{rms}$ excitation voltage shows a variation of permittivity anisotropy, the difference is equal to zero for a signal frequency around 18 kHz [34].

1.6 Diffractive optical devices

1.6.1 Diffraction

Huygens principle states that every point on a propagating wave-front serves as a source of spherical secondary wavelets, and that the wave-front at some later time is the envelope of these wavelets. If the propagating wave has a frequency ν , and is transmitted through the medium at a speed v_t , the secondary wavelets have that

same frequency and speed [11]. Young's experiment is the first to demonstrate interference of light. If light from a monochromatic source passes through two pinholes, these two pinholes can be considered as secondary monochromatic point sources [13]. In Young's experiment, the pinholes are replaced by two slits, and the principle of superposition can be applied to the monochromatic wave from the secondary sources. The electromagnetic waves equations can be written as:

$$E_1 = E_a \cos(k s_a - \omega t + \varphi_a) \quad (1.58)$$

$$E_2 = E_b \cos(k s_b - \omega t + \varphi_b) \quad (1.59)$$

The phase φ of both waves is considered to be zero at time $t=0$. s_a and s_b are the distances from the slits a and b respectively. The constant phase expression $\alpha = ks + \varphi$ can be introduced to simplify the expressions which become:

$$E_1 = E_a \cos(\alpha_a - \omega t) \quad (1.60)$$

$$E_2 = E_b \cos(\alpha_b - \omega t) \quad (1.61)$$

Considering wave propagation in the direction normal to the plane containing both slits. The waves, intersecting at a point P, have a phase difference of:

$$\alpha_b - \alpha_a = k(s_b - s_a) + (\varphi_b - \varphi_a) \quad (1.62)$$

The resultant equation of the superposition can be now written for the point P as:

$$E_r = E_1 + E_2 = E_a \cos(\alpha_a - \omega t) + E_b \cos(\alpha_b - \omega t) \quad (1.63)$$

In this equation if the difference of phase $(b-a)=2m\pi$ where m is an integer, the beams are called "in phase", there is a constructive interference and the intensity

is the sum of the intensity of the two beams.

$$E_r = E_1 + E_2 = E_a \cos(\alpha_a - \omega t) + E_b \cos(\alpha_a + 2m\pi - \omega t) = (E_a + E_b) \cos(\alpha_a - \omega t) \quad (1.64)$$

Contrastingly, if the difference is equal to $(2m+1)\pi$, the beams in an opposite phase, there is a destructive interference, the intensity resultant is zero if the intensity of the two beams are the same [10].

$$E_r = E_a \cos(\alpha_a - \omega t) + E_b \cos(\alpha_a + (2m + 1)\pi - \omega t) = (E_a - E_b) \cos(\alpha_a - \omega t) \quad (1.65)$$

For an array of slits and an arbitrary angle (θ) away from the normal, this approach can be extended for maximum diffraction as:

$$\Delta L = d \sin \theta = \pm N \lambda \quad (1.66)$$

For the minimum as:

$$\Delta L = d \sin \theta = \pm \left(N + \frac{1}{2} \right) \lambda \quad (1.67)$$

1.6.2 Diffraction efficiency

The transmission coefficient (γ_m^t) is the ratio between the power of the outgoing (m^{th}) order beam going through the device and the power from the incoming beam. The reflection coefficient (γ_m^r) is the ratio between the (m^{th}) order reflected beam and the total incoming intensity. Knowing these coefficients the diffraction efficiencies can be determined according to the angle and order of diffraction. At a distance where the different orders are distinct, the expression for the diffraction efficiencies can be written as:

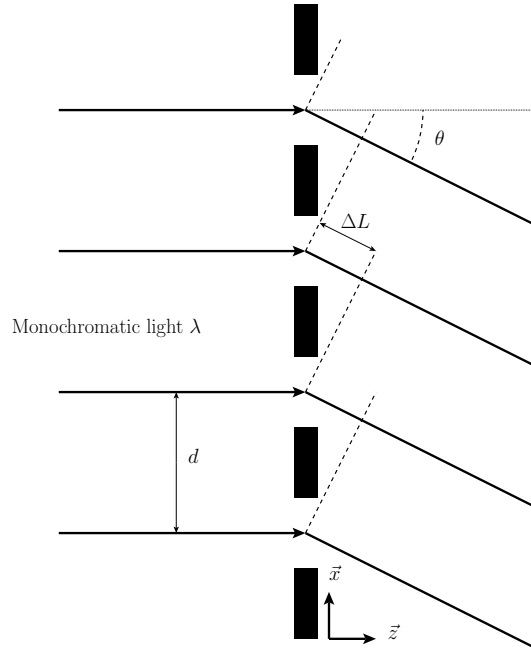


Figure 1.19: Schematic representation of a diffraction grating system

For transmission:

$$\gamma_m^T = \frac{n_t \cos \theta_m}{n \cos \theta_i} |T_m|^2 \quad (1.68)$$

For reflection:

$$\gamma_m^R = \frac{\cos \theta_m}{\cos \theta_i} |R_m|^2 \quad (1.69)$$

Where (n_T) is the refractive index of the diffractive medium, (n) the refractive index of material on the incidence side, (θ_m) the emergence angle and (θ_i) the incidence angle [35, 36]. The sum of all the efficiencies must obey:

$$\sum_m \gamma_m^T + \sum_m \gamma_m^R = 1 \quad (1.70)$$

1.6.3 Nematic phase gratings

Phase gratings consist of a succession of two different refractive index materials. When an incident beam passes through the system, it exits it with different phases according to the materials it passed through. The ideal phase grating system using liquid crystal is a structure made of a linear array of perpendicular

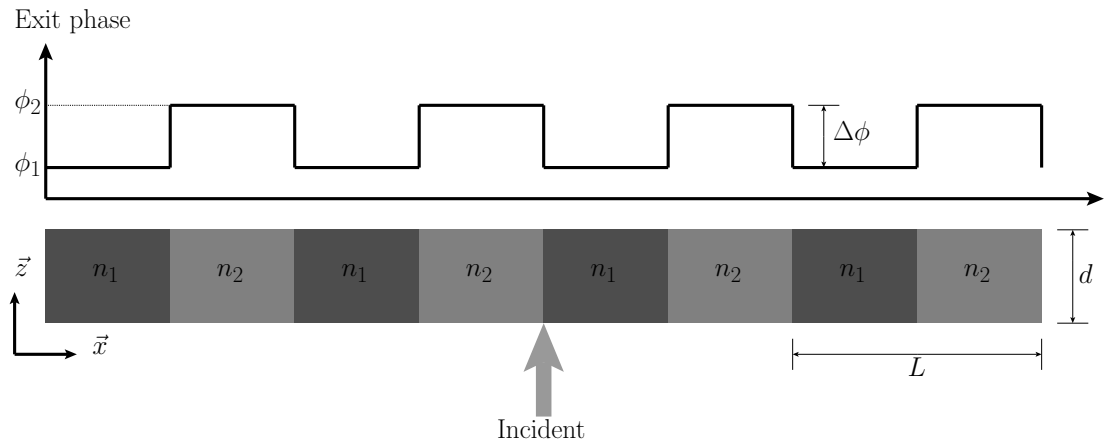


Figure 1.20: Schematic representation of a binary phase grating

and parallel refractive index repeating regularly in one direction (see Figure 1.20). To obtain this configuration, a nematic liquid crystal can theoretically be used in alternating stripes of planar and homeotropic orientation. The transition from one refractive index to the other will not be sudden, but smooth, mainly due to the elastic constants driven by the Frank-Oseen equation. Reducing the size of the transition zone can improve the efficiency of a liquid crystal phase grating system [35, 36].

1.7 Preview of the work

1.7.1 Previous work

Early applications of liquid crystals include watch displays, but the last 20 years has seen the development of LCD technologies and the rise of optical communications. The recent development of optical applications of liquid crystal has been made possible by a better understanding of the material properties. Research has been undertaken to try to reduce the pitch (down to micrometrical scale) of the LCD or the grating systems which lead to an improvement of these systems [36–38].

1.7.2 Outline of the work

Chapter 2 presents an introduction of the different methods and techniques used during the different investigations undertaken for this PhD. This chapter includes details of the process followed to produce patterned samples using photolithography techniques. Different methods for characterising (capacitance and Fréedericksz transition) samples are then detailed. Finally in this chapter, there is a detailed review of the Mach-Zhender interferometer system.

In Chapter 3, the investigation of flexoelectricity in a nematic liquid crystal phase grating system will be detailed. To extract the value of the flexoelectric polarisation in the samples, a numerical model has been generated. Another part of the investigation will look at static and dynamic diffraction patterns.

Using the transient capacitance technique, Chapter 4 highlights the influence and behaviour of free charge carriers. The investigation followed two paths, the first using different nematic materials submitted to different signals to reveal the influences of ionic contamination, the second looking at the evolution of measures of the first at different temperatures.

Continuing the investigation of ionic contamination and flexoelectricity in nematic liquid Crystal materials, Chapter 5 considers their effects on the Fréedericksz transition.

As described previously, nematic materials tend to align along the director \vec{n} . The orientation of the director can be dictated by the geometry of the sidewall structure of a well, this work is detailed in Chapter 6.

Chapter 7 describes related studies using interferometry techniques, here being applied to electrophoresis and resonance in insects generated by sound waves.

Chapter 2

Experimental Methods

2.1. Phase grating device fabrication

pieces go through a cleaning process which involves immersion in a series of warm solutions of decreasing detergent (Decon[®]90 from Decon Laboratories Limited) concentrations from 5% to 0.5% then only in de-ionised water. To improve the efficiency of the cleaning each solution is heated up to around 60°C and then placed into an ultrasonic bath for 10 minutes. At the end of this first stage, the pieces are dipped in Isopropyl Alcohol (IPA) at 40°C and then blow dried to remove any traces of water. This is a degreasing stage (Part 1 in Figure 2.1). The dry pieces are then spin-coated with the photoresist (MicropositTM S1813TM G2 Positive photoresist from Rhom and Haas Electronic Materials) on the ITO side (Part 2 in Figure 2.1). The speed of rotation and the duration determines the resultant thickness of the photoresist. The spin program was composed of two stages (achieved with the spin coating model WS-6505-6NPP/A2/AR2 from Laurell Technologies Corporation). The first one, 5 seconds at 500 rpm to remove any excess of photoresist. The second, 30 seconds long at 3000 rpm to get a uniform layer of photoresist. After that the resin is cured by removing part of the solvent contained in the photoresist. This is done with a pre-bake of 75 sec at 105°C before being exposed to a mask under U.V. light for 1.7 sec in the mask aligner (Model MJ54 from SUSS Microtec) using soft contact (Part 3 in Figure 2.1). To reveal the pattern in the photoresist, the sample is put into a 50/50 water-developer solution (MicropositTM developer concentrate from Rhom and Haas Electronic Materials). When the developing step is complete the samples are blow-dried with dry nitrogen gas and then hardened with another baking at 105°C stage for 10 min (Part 4 in Figure 2.1). The final part of the process is the etching stage. The samples are placed into a stirred solution of oxalic acid (Prepared from Oxalic acid $C_2H_2O_4$ anhydrous 98% from Acros organics, M.W.: 90.04 g.mol⁻¹) at 0.5 M for 10 minutes, this dissolves the unprotected layer of ITO (Part 5 in Figure 2.1). To stop the process, the sample is put into a water bath. The remaining photo-resist is then removed with acetone and the sample is cleared of any trace of solvent using an IPA bath followed by a blow-dry with

nitrogen (Part 6 in Figure 2.1). The patterned samples are now ready to be used to construct the liquid crystal cells.

2.1.3 Design of mask

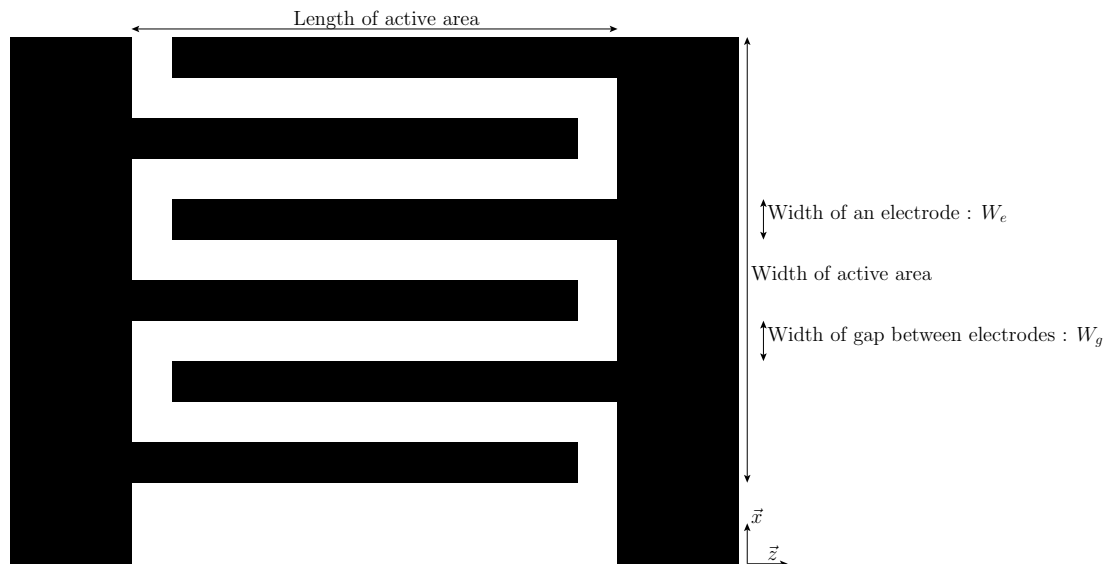


Figure 2.2: Schematic view of interdigitated electrodes

The technique used to produce the sample is etching, and uses a positive photo-resist, S1813 as described in Section 2.1.2. The mask needs to be an exact positive copy of the required electrodes pattern. The features of the mask are composed of an array of areas; a 5 by 5 mm interdigitated electrode pattern as shown in Figure 2.2. It is a 100 by 100 mm bright chrome on glass 1.5 mm thick provided by Qudos Technology LTD. The characteristics of these electrodes, which can vary, are the size of the electrodes (W_e) and also the size of the gap (W_g) which separates them. There were 14 different areas as shown in Figure 2.3, with the size of electrodes (W_e) going from $5\mu\text{m}$ up to $200\mu\text{m}$ with $W_e = W_g$, $W_e = \frac{1}{2}W_g$ and $W_e = \frac{1}{4}W_g$. Also two areas were designed with a third stripe connected to an electrode which is running between the interdigitated electrodes with the same size and spacing (see Figure 2.4). This allows every third stripe on an array to be biased at the same voltage.

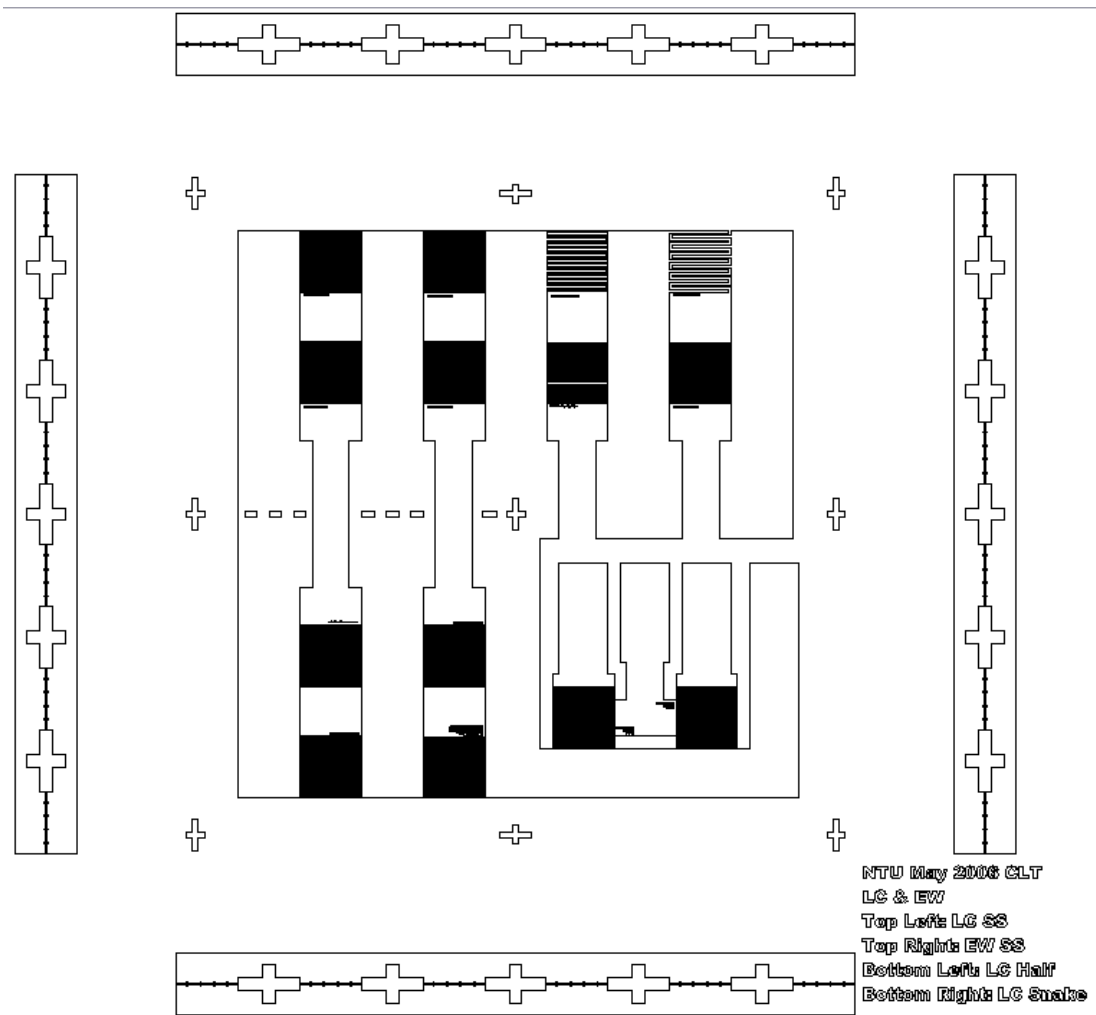


Figure 2.3: Photolithographic mask for production of interdigitated electrodes substrates

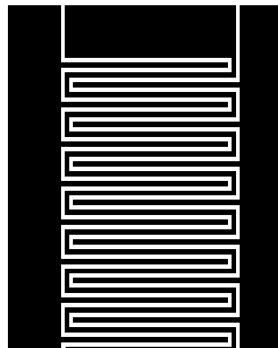


Figure 2.4: Detail of the photolithographic mask to underline the “Snake” electrode pattern.

2.1.4 Surface alignment and device assembly

The sample is made of two glass plates coated with a transparent layer of conducting Indium-Tin Oxide (ITO). The two plates are separated by spacers which are strip of Mylar[®] which determine the thickness of the cell. One of the glass slides was patterned using the photolithography technique outlined in Section 2.1.2 to produce a pad of interdigitated striped electrodes; the opposite plate was a continuous earth plane. Both glass substrates were coated with a polymer to give the planar orientation. For this cell, the polymer used is Polyvinyl Alcohol (PVA: Mw>9000 from Aldrich) which is rubbed to determine the direction of the orientation of the director at the surfaces [40–42].

After using the same cleaning process for the plane electrode plate, the two

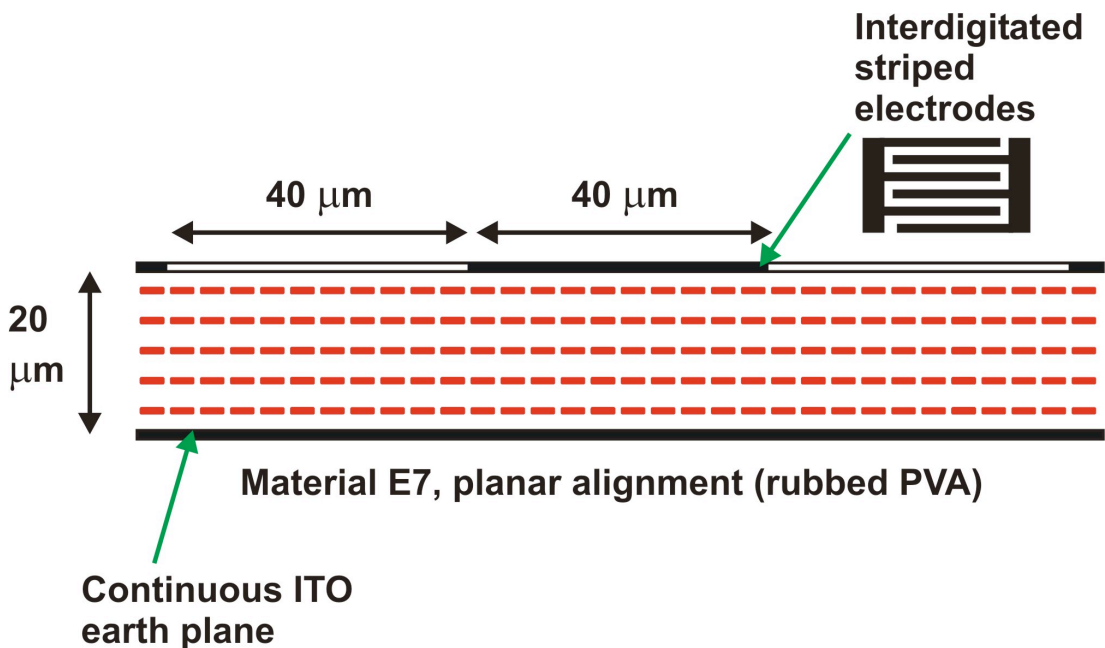


Figure 2.5: Cross section of an interdigitated cell

pieces are immersed in a 1% solution of PVA in DI water and then removed and left to dry in a slanted orientation at room temperature. The residue is a film of the polymer which is rubbed in a specific direction on both the substrates as shown in Figure 2.6. The substrates are put together separated by strips of Mylar[®] spacer and glued at the edges with epoxy resin. After the resin is cured

the thickness is measured using a spectrometer. The cell is capillary filled with the nematic liquid crystal material at a temperature just above the isotropic-nematic transition. Connections are soldered using indium metal and finally the cell is sealed with epoxy resin to prevent leakage.

Alignment geometries

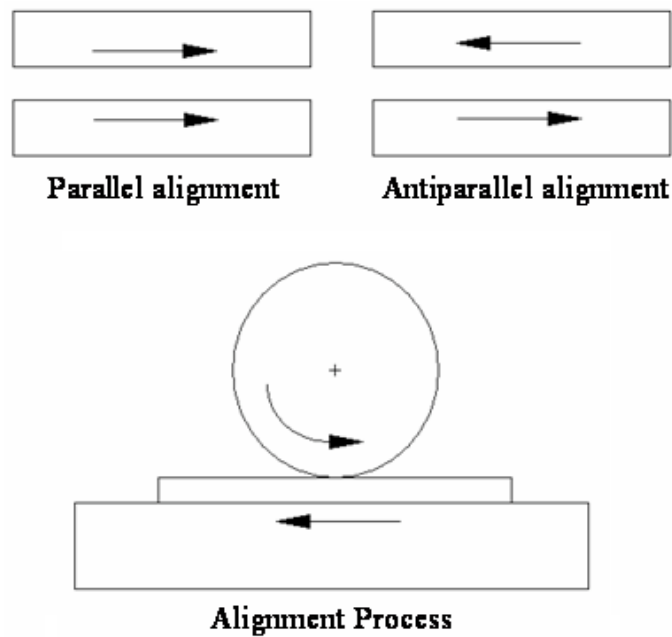


Figure 2.6: Different alignments and rubbing process

Each surface can be planar, tilted or homeotropic [6]. The rubbed PVA process produces tilted planar alignment, rubbing determines the pretilt direction. The cell produce for interferometry study described in Chapter 3, can be built planar parallel (rubbed the same direction on the two substrates) or planar antiparallel (rubbed in opposite directions on the two substrates) as shown as shown in Figure 2.6. The alignment is achieved using a rubbing polishing cloth (from Selvyt) wrapped around a cylinder which is rotated while the substrate is passed in contact in the opposite direction underneath the cylinder as shown in Figure 2.6.

2.1.5 Measurement of cell gap

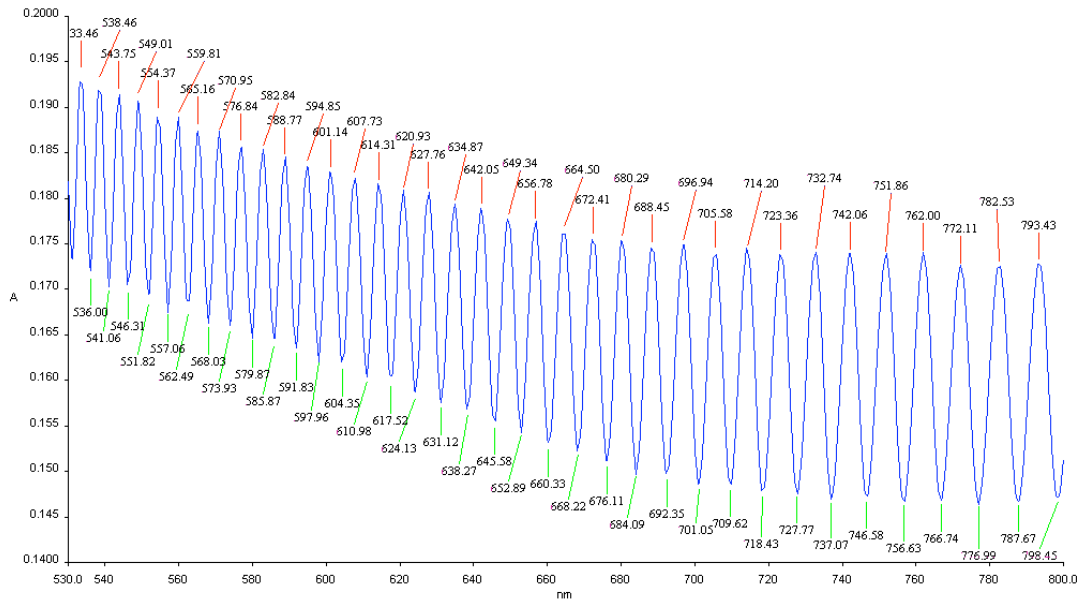


Figure 2.7: Results from the UV/vis spectrometer, plot of absorbance as a function of the wavelength

One of the most important characteristics of the cell prepared is the spacing of the plates which determines the thickness of the nematic liquid crystal layer. Accurate determination of this is achieved using a UV/vis spectrometer (Lambda 25 UV/vis spectrometer from Perkin Elmer Instruments or DU 70 Spectrophotometer from Beckman) with the sample measured in transmission. The interference will be destructive at a particular wavelength (λ) if the number of wavelengths contained is a integer plus a half.

$$d = n \frac{\lambda}{2} \quad (2.1)$$

To be able to scan continuously over a wide range of wavelengths, the spectrometer is used. The intensity of the signal at each wavelength is compared to a reference beam as a function of the wavelength. This results in the plot shown in Figure 2.7. From this plot (see Figure 2.7), the position of the maximum and minimum are determined.

2.1.6 Data interpretation for thickness determination

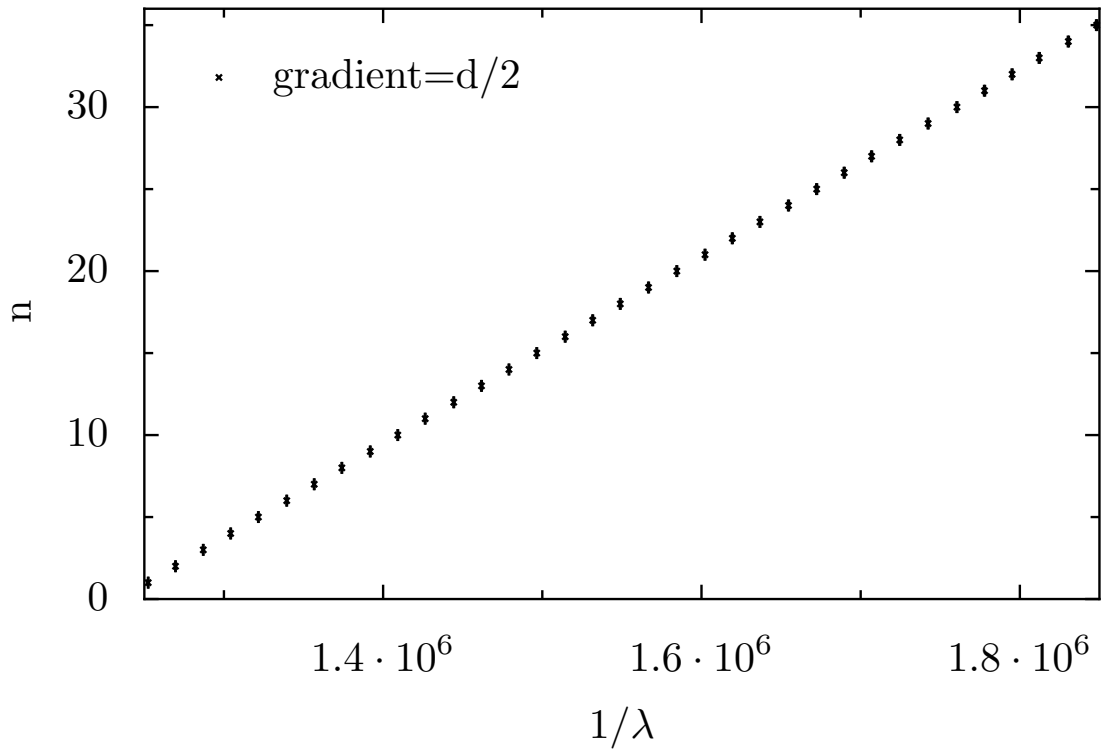


Figure 2.8: Plotting of n vs. $\frac{1}{\lambda}$ to determine the thickness d of the cell

For each of the minimums recorded an integer (n) is assigned to each which is incremented by one for each adjacent minimum. The index (n) of the minimum is plotted versus the reciprocal of the wavelength $\frac{1}{\lambda}$. The results follow a straight line of a gradient equal to half of the thickness $\frac{d}{2}$ of the sample measured. In Figure 2.8 has a gradient of $(57.04 \pm 0.02) \mu m$ which gives a thickness of $(28.52 \pm 0.01) \mu m$ for the sample. The regression analysis for the data can be seen in Section A.2

2.2 Capacitance measurements

2.2.1 Sample detail (earth ring)

The test cell for measuring the Fréedericksz effect needs to have a well defined active surface. The cell provides a circular one which is connected to the soldering

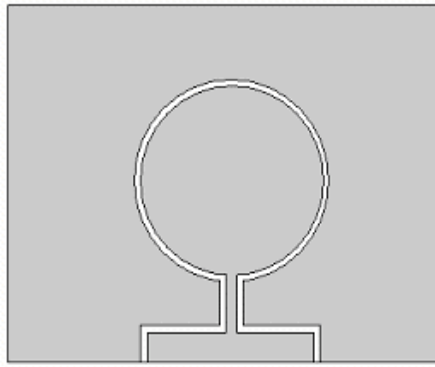


Figure 2.9: Detail of ring electrodes

pad by a thin electrode. The surrounding area is also connectible and usually linked with the earth to prevent any interference between the active area of well known surface area (1cm^2), as show in Figure 2.9. The cell is a sandwich, a liquid crystal material inside two coated and patterned ITO glass slides. The thickness of the cell is determined using the method described in Section 2.1.5. These empty test cells are not built on site but provided by Merck Ltd. The importance of the earth ring as illustrated in Figures 2.9 and 2.10, is to reduce errors on the determination of the permittivity of the material by reducing the fringing field. With the earth ring, the surface area of the active electrodes is known and only the material sandwiched between these two electrodes is included in the measure. Whereas in the absence of the earth ring, an extra volume of material included in the fringing field could reorient and reduce the accuracy of the measure.

2.2.2 Static measurements

Measuring the static capacitance of a liquid crystal cell is achieved using as Agilent 4284A LCR meter. The cell is placed into a temperature control device, Linkam LTS350, which is driven by the controller, Linkam TMS94, which allows precise control of the temperature at which the measures are achieved. The range of temperature runs from just under 0°C up to the nematic-isotropic transition temperature (over 100°C) of all the nematic liquid crystals used in the labora-

2.2. Capacitance measurements

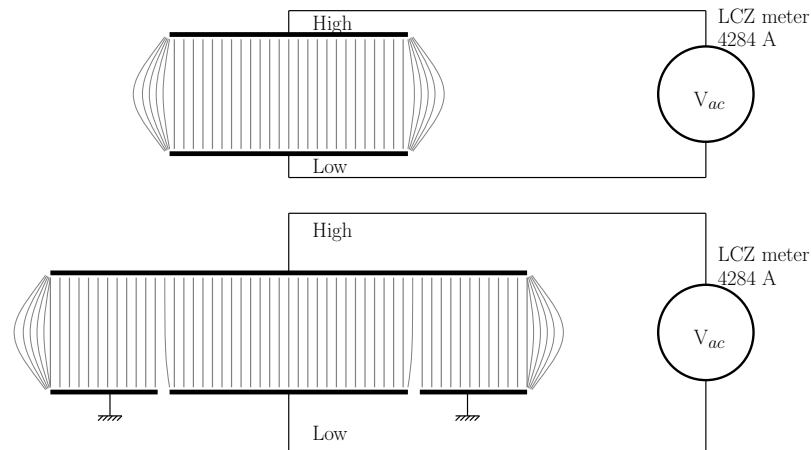


Figure 2.10: Electric fields across the test cell with (bottom) and without (top) earth ring

tory. The LCR meter is computer controlled with two measuring options, either at a set frequency where the only variable is the voltage applied to the sample or alternatively, the voltage can be set and only the frequency of the signal applied is varied.

2.2.3 Dynamic measurements

The dynamic measure of the capacitance provides information on the behaviour of the director of the liquid crystal material and if a change in direction occurs with the applied signal. To conduct this measure the cell is placed into a temperature control device, Linkam LTS350, as for the static experiment described in Section 2.2.2. As shown in Figures 2.11 and 2.12, the signal for dynamic measure of the capacitance is provided by a 4 channel waveform generator, TTI Arbitrary Waveform Generator TGA1244. This can be set to deliver different signals such as amplitude modulation (AM), square signal or any combination of four different signals which can be either summed or modulated. In addition to the signal delivered by the waveform generator a continuous sinusoidal signal, with a constant frequency of 10 kHz, high enough to avoid ionic migration but also low enough to avoid finite resistivity from the ITO electrodes is added. This extra

2.2. Capacitance measurements

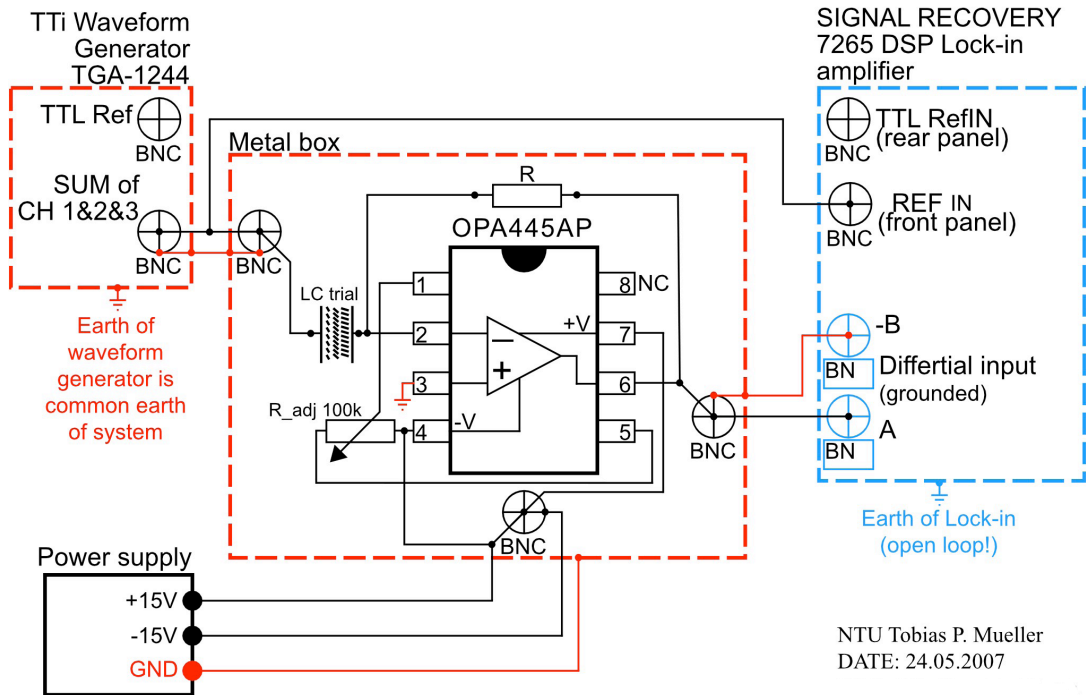


Figure 2.11: Setup for dynamic measurement (Courtesy of Mr. T Muller)

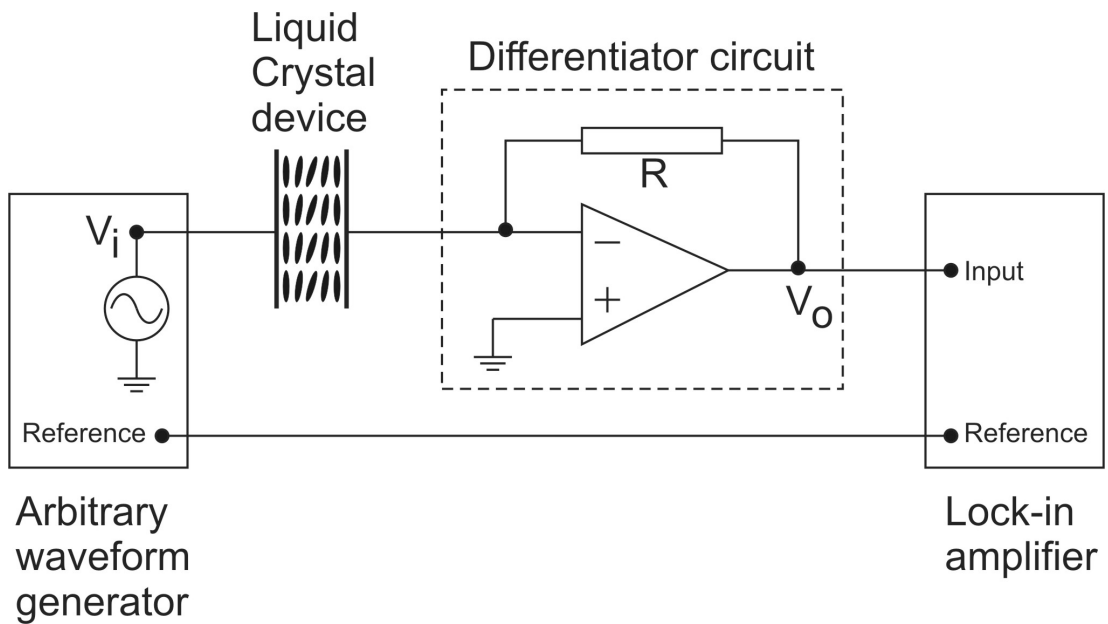


Figure 2.12: Schematic diagram of the experimental apparatus for dynamic measurement

2.2. Capacitance measurements

sinusoidal signal has a sub-threshold amplitude of 0.05 V rms. The cell is used as a capacitor in an amplifier circuit using an Operational Amplifier OPA445AP. The negative connector of the operational amplifier acts as a virtual earth and the liquid crystal cell experiences the full amplitude of the signal delivered by the waveform generator. The value of the resistor and of the capacitor in the circuit is used to determine the value of the output signal in relation to the input signal using the formulae:

$$V_{out} = R.C.\omega.V_{in} \quad (2.2)$$

where (R) is the value of the resistor as labelled in Figures 2.11 and 2.12, (C) is the capacitance of the liquid crystal cell and (V_i) is the voltage delivered by the waveform generator. The value of (ω) is defined by:

$$\omega = 2\pi.f \quad (2.3)$$

Where (f) is the frequency of the input signal. And the capacitance is related to the permittivity($\epsilon(t)$) by:

$$C = C_0.\epsilon(t) \quad (2.4)$$

With C_0 being the empty cell capacitance. The signal formulae become:

$$V_{out} = R.C_0.\epsilon(t).2\pi.f.V_{in} \quad (2.5)$$

The output signal goes into the Signal Recovery 7265DSP Lock-In Amplifier set to detect the 90° phase shift, where the phase shift between the reference signal and the output signal (see Figure 2.12) allows dynamic determination of the value of capacitance. The small sub-threshold signal finds its justification when signals applied to the LC cell do not carry a sinusoidal component or are null during an extended fraction of their periods. The signal generated by the lock-in amplifier is correlated to the capacitor value by the amplification factor [43]. The signal

can be measured, plotted and recorded from the oscilloscope AGILENT 54 622A. The data recorded needs to be analysed to retrieve the value of the capacitance with the formulae:

$$\varepsilon_{(t)} = \frac{V_{out}}{R.C_0.2\pi.f.V_{in}} \quad (2.6)$$

2.3 Fréedericksz transition measurement

2.3.1 Dielectric measurement

Equipment

The Fréedericksz effect occurs when there is reorientation of the director of liquid crystal submitted to a threshold value of voltage. As the Fréedericksz effect is related to reorientation, an indirect measure can be to use the properties of the liquid crystal which are orientation dependant. The setup of the experiment is the same as the one described in Section 2.2.2. The data is collected by the computer and can be post processed and then plotted. The curve is the permittivity versus the applied voltage, and it can also be the permittivity versus the frequency of the signal. On the ideal curve, V_c is the threshold voltage when the Fréedericksz effect occurs and the reorientation starts. From the value of the threshold and by fitting the curve, the elastic constants and permittivities can be determined.

Example of measures

To find the measure of permittivity allowing the determination of the critical voltage (V_c), increments of voltage are applied to the liquid crystal cell. When the value of voltage goes beyond the threshold value a step back in voltage is taken. Then the steps of voltage increment are reduced and the time for data acquisition extended. The precautions are for the critical slowing down which makes the measurement around the threshold values difficult. The typical curve obtained is shown in Figure 1.16.

Analysis

From the retrieved data, the characteristics of the liquid crystal can be calculated. From the plotted data (see Figure 1.16), the Fréedericksz threshold allows us to calculate the size of k_{11} . The formulae is:

$$V_c = \pi \sqrt{\frac{K_{xx}}{\epsilon_0 \Delta \epsilon}} \quad (2.7)$$

Increasing the signal makes the permittivity evolve, the slope just after the threshold value allows us to determine the ratio between elastic constants (see Figure 1.16). The value of permittivity tends to go close to the parallel permittivity (ϵ_{\parallel}) without reaching it at high value of applied voltage. It will take an infinite applied voltage to get to it. To determine this value, another plot can be done which involves plotting the permittivity as a function of the ratio $1/V_{(app)}$ for the high values of applied voltage. This plot (see Figure 1.16) is then extrapolated and the value of the parallel permittivity ϵ_{\parallel} is the constant part of the straight trend line equation. The value of the perpendicular permittivity (ϵ_{\perp}) is the value measured when the signal is under the Fréedericksz threshold $V_{app} > V_c$. The permittivity anisotropy $\Delta \epsilon$ is the difference between the two permittivities as explained in Equation 1.40 in Section 1.5.3. The whole curve is fitted using continuum theory.

2.3.2 Optical measurement

Equipment

The Fréedericksz transition can be measured using another characteristic of the liquid crystal which is depending of the direction. This characteristic is birefringence; using the variation of the refractive index to get constructive or destructive interference through the sample. The experiment is composed of a monochromatic coherent light source, a laser. The sample is positioned between two crossed polarisers with its rubbing direction at $\pm 45^\circ$ from the direction of

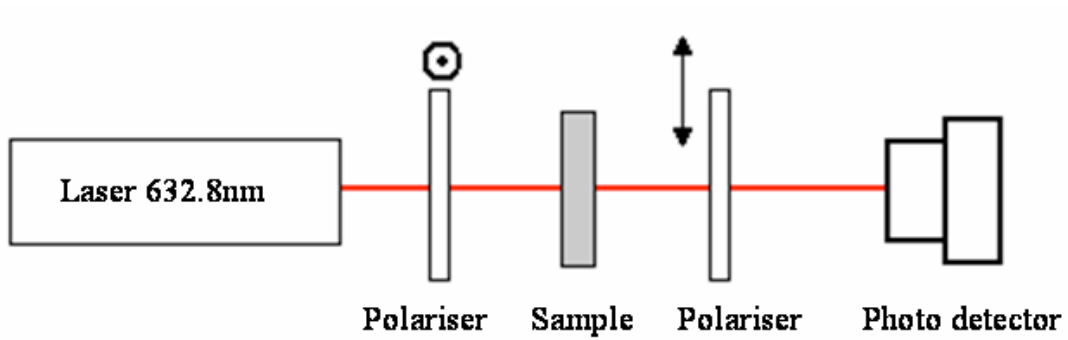


Figure 2.13: Simple representation of the transmission experimental setup

the first polariser. Then a photo-detector is placed on the other side of the light source to measure the intensity of light passing through the sample according to the signal applied. The signal applied to the sample is, as in the previous Section 2.3.1, an electric one.

Example of measures

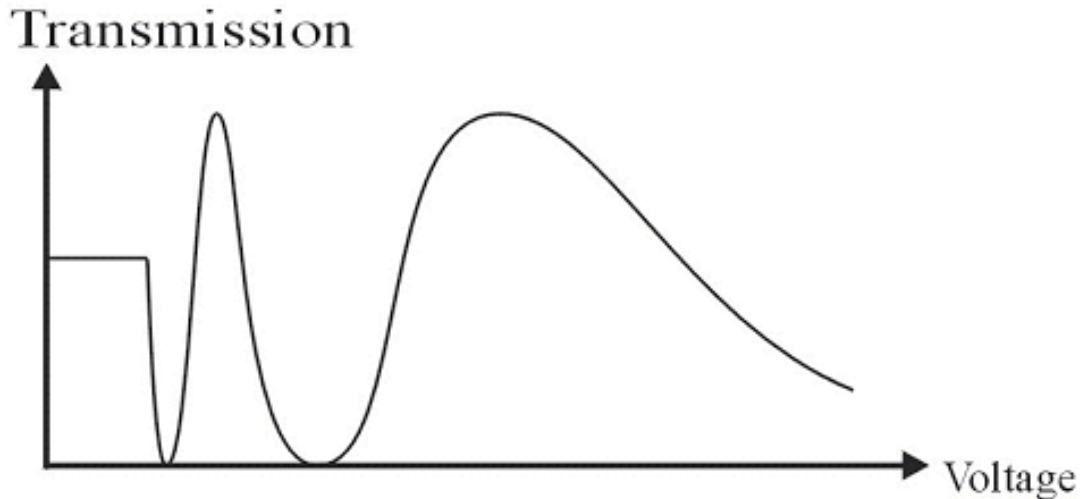


Figure 2.14: Ideal curve of transmission measure

The curve obtained from retrieving the data is composed of two parts. The first part is a constant straight line at voltage below the Fréedericksz voltage, corresponding to the transmission of the experimental setting when the strength of the electric field is not strong enough to reorientate the director. The value of

this transmission is related to the refractive index anisotropy of the liquid crystal material (Δn), the thickness of the sample (d) and the wavelength of the laser source (λ) by:

$$T \propto \frac{\Delta n \cdot d}{\lambda} \quad (2.8)$$

Then when the applied voltage reaches the Fréedericksz value (same as that in Section 2.3.1), the optical path changes due to the director reorientation. The exact value of the Fréedericksz voltage is determined at the change from the constant part to the sharp variation of the light intensity detected by the photo-detector as shown in Figures 2.13 and 2.14.

Analysis

The value of the Fréedericksz transition allows us to extract the value of the elastic constant k_{11} when using a planar cell. The formulae is the same as the equation 2.7. Optical experiments are another way to measure Fréedericksz threshold, but it is difficult to extract the elastic constant ratios from the results. This experiment is based on the same physical effect as the dielectric measure described in Section 2.3.1, it is achieved with the same process for the voltage settings.

2.3.3 Magnetic measurement

Equipment

Another way to measure the Fréedericksz transition value is to use an alternative source to reorient the liquid crystal. One of their characteristics is that they have an induced magnetic dipole when they are placed in an external magnetic field. The advantage of using a magnetic field compared to an electric one is that the ions which may be contained in the sample will not be excited by the magnetic field and do not create disturbances in the measurements and will not affect the results. To drive this experiment, a computer is used to set up the parameters. It also controls the value of the magnetic field between the two poles

2.3. Fréedericksz transition measurement

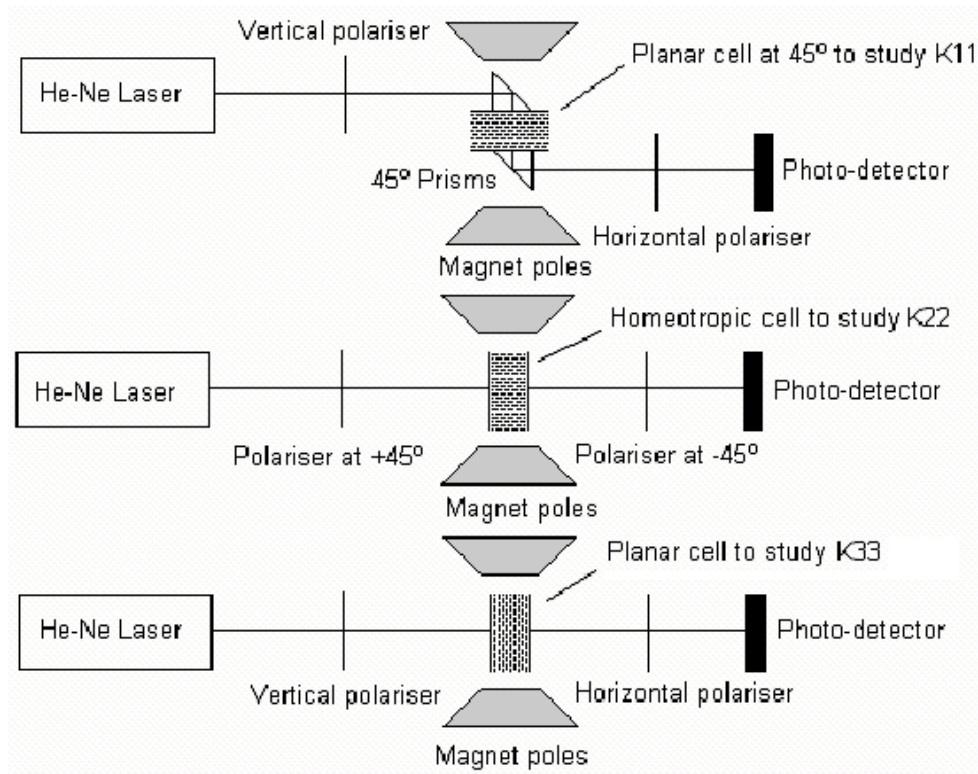


Figure 2.15: Representation of the different setup for magnetic measurement

of the electromagnet by controlling the intensity of the current which runs into the coils. A preliminary experiment has to be completed before achieving this in order to calibrate the value of the magnetic fields associated with the value of current. The setup of the experiment is composed of a laser source, two polarisers oriented crossed at an angle of 90° and a photo-detector. The sample is placed between the two polarisers with the direction of rubbing at an angle of 45° to the polarisers. This intensity value is saved on the computer. The data can then be plotted as a light intensity function of magnetic field magnitude.

This experiment setup has to be adapted dependant on which characteristics are investigated. If the characteristic studied is K_{11} the cell is tilted at an angle of 45° to the vertical and the two polarisers are vertical and horizontal. The planar cell is placed between the magnet poles, perpendicular to the field lines as represented in Figure 2.15.

Measuring the K_{22} constant, the same planar cell used previously is employed

but instead of getting the magnetic field perpendicular to the cell, its direction should be in-plane of the cell but perpendicular to the rubbing direction. When the strength of the field is high enough, a twist distortion occurs at the centre of the cell. The polarisers should be placed at a $\pm 45^\circ$ to the rubbing direction.

To determine the last of the principal elastic constants, K_{33} , which corresponds to a bend distortion, the planar cell from the previous experiments is substituted by an homeotropic one. The direction of the magnetic field is orientated as previously, in-plane of the cell. The orientation is independent of the rubbing direction. Above the Fréedericksz transition the liquid crystal molecules tend to reorient in a planar orientation and create a bend distortion.

Example of measures

The typical curves obtained for the determination of the Fréedericksz transition are function of magnet current. It can be related to the intensity of the magnetic field using the parameters determined in the preliminary experiment. The graph displays a constant part when the strength of the field that is too weak and a sharp transition when the field is strong enough to reorient the director of the liquid crystal molecules as illustrated in Figure 2.14. The intensity of the constant part is ruled by the experimental setup and the optical path with the liquid crystal cell.

Analysis

From the curve the elastic constant can be determined using the formulae 1.52, 1.53 or 1.54, according to the cell and the experimental setup used, the three major elastic constants K_{11} , K_{22} and K_{33} can be determined. Ionic charges can move in response to low frequency electric fields, using a magnetic field avoids these effects.

2.4 Mach-Zenhder interferometer

2.4.1 Principle

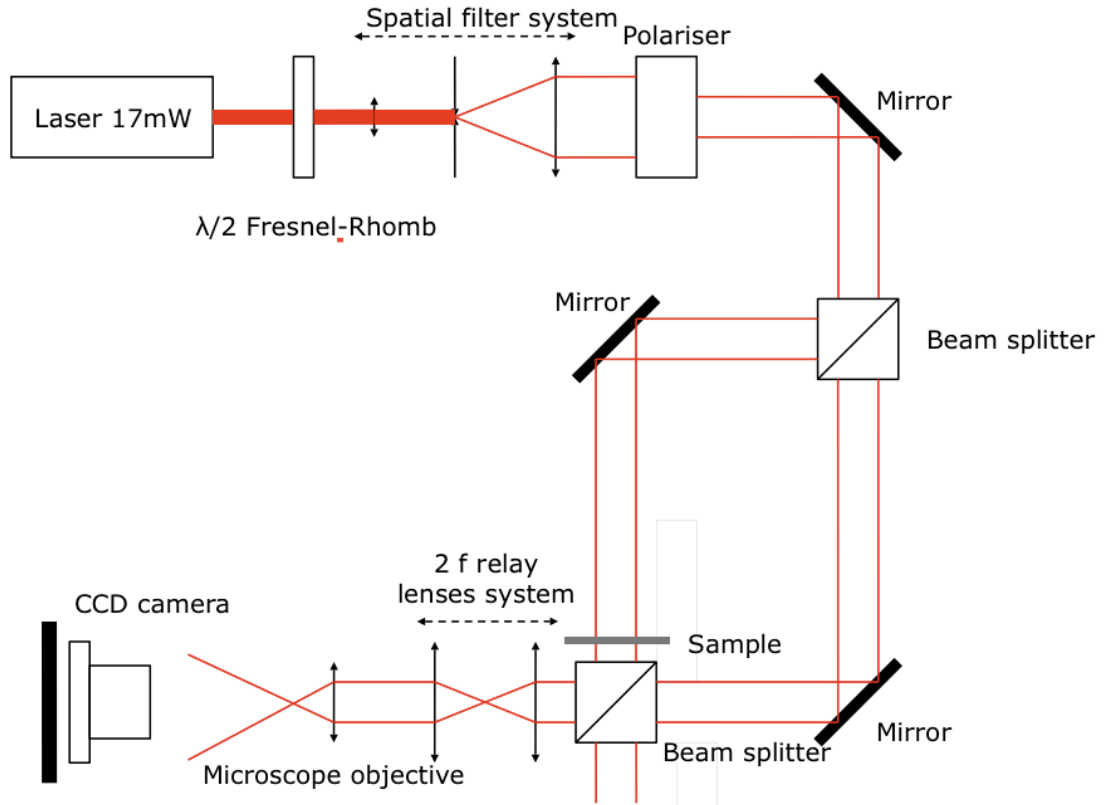


Figure 2.16: Schematic representation of the setup for the Mach-Zenhder interferometer

The Mach-Zenhder interferometer [44, 45] is composed of three different parts, the light source, the interferometer's main body and the image capture system. The light source, in this example is a coherent, collimated and monochromatic one produce by a He-Ne laser. The orientation of the polarisation is controlled by the half-wave plate($\lambda/2$), then the beam is cleaned and expanded by the spatial filter system, which gives a Gaussian intensity profile. The polarisation of the beam is controlled by the polariser. Then the beam goes to the interferometer's main body where it is divided by the beam splitter into a reference arm and a measure arm where the sample will be placed. The two beams are then recombined by the second beam splitter, it is here where the interference are created by the difference

of the optical path between the reference and measure arms. The image of the sample needs to be spatially transferred which is done by the relay lenses system [46] into the microscope objective which expand it to be observable by the CCD camera [37, 38, 47, 48]. The pictures are then acquired by computer software to be analysed afterwards.

2.4.2 Description and specificities

The laser used for the experiment is a 17mW He-Ne polarised laser. The spatial filter system is composed of an entry lens of short focal length, of a pinhole of $20\mu\text{m}$ and of an output lens of 100 mm focal length and 25 mm diameter. The beam exiting the lens, is 25 mm in diameter and has a Gaussian intensity profile, but the size of the beam is reduced to a square profile of 10 mm side length due to the polariser characteristics. The size of the observed spot is only a few hundreds of μm across; The light density can be considered as constant over all the area studied. An additional white light source is placed in the measure arm for focusing purposes. The image caption system is used as a microscope to place the sample in the focal plane and also allow us to choose which of its part will be observed. The interferometer creates fringes when one of its reflective mirrors is slightly tilted from 45° (see Figure 2.16), so the waveforms are slightly inclined with respect to one another. It also gives an interference pattern of a series of parallel linear fringes [49].

Chapter 3

Investigation of the flexoelectric polarisation in nematic phase grating structures

3.1 Introduction

Switchable liquid crystal diffraction gratings have applications for optical beamsteering in optical fibre based telecommunication systems [36, 50]. A number of devices have been demonstrated based on the switching of a layer of planar nematic liquid crystal to produce a periodic spatially varying phase profile [51–56]. When no voltages are applied the molecular director of the nematic liquid crystal through the layer is oriented along a direction pre-determined by uni-directional rubbing of the substrates. Switching is produced via a striped electrode array on one substrate opposite to a continuous earth plane on the opposite substrate. By applying a suitable periodically repeating pattern of voltages a blazed or sawtooth phase profile can be produced which allows efficient beamsteering for electromagnetic waves that are polarised along the surface rubbing direction. Under ideal circumstances there should be abrupt transitions between the linearly varying regions in the sawtooth phase profile, referred to as “fly-back” regions. The liquid crystal is unable to reproduce these abrupt transitions due to the inherent elasticity of the medium. This property, coupled with the effects of fringing electric fields at electrode edges, leads to smooth transitions in the phase profile and the widening of the fly-back regions. The aims were firstly to investigate the “fly-back” region in dual frequency material and to reduce its size to improve the efficiency of the diffractive system. Secondly the “fly-back” region was used to quantify the sum of flexoelectric coefficients (e_1+e_3) in a commercial nematic liquid crystal (E7) [57] using a Mach-Zhender interferometer [44, 45] to measure the time dependent periodic distortion using a planar aligned phase grating. It was proposed by Meyer [1, 27] that liquid crystal material whose molecules possess a shape asymmetry and a permanent dipole will, when distorted, present a flexoelectric polarisation (P_f) related to the n-director by the flexoelectric coefficients

e_1 and e_3 respectively related to splay and bend distortions via:

$$P_f = e_1(\nabla \cdot n)n + e_3(\nabla \times n) \times n \quad (3.1)$$

The first measurements of the sum of the coefficients ($e_1 + e_3$) were carried out by Prost and Pershan [58] on a homeotropically aligned nematic phase grating. In-plane fields were applied via an interdigitated electrode geometry in which voltages of alternating polarity were applied to alternate electrodes. The spatial period of the flexoelectric distortion in this geometry is twice the spatial period of the dielectric distortion and so optical diffraction was used to distinguish between the two. A number of groups have also subsequently used the hybrid aligned nematic (HAN) geometry to determine the value of ($e_1 + e_3$) [59–65]. In the HAN cell, one surface imparts homeotropic alignment to the nematic liquid crystal, and the other planar alignment. The in-built distortion gives rise to a flexoelectric polarization and an asymmetric response to the polarity of an applied field. Complications for HAN cell measurements include the presence of ionic contamination and the influence of the surface polarization at the homeotropic surface [59–61, 66–69]. A recent development of the HAN cell technique uses the pi-cell geometry to avoid the latter effect.

3.2 Device geometry and data acquisition

3.2.1 Construction of a cell

When one of the substrates is patterned and not short-circuited like the ones seen in Figure 3.2, it is paired with a plain electrode. Two stripes of Mylar[®] are placed on both of the non-connecting sides to separate the substrate at the desired distance. The cell is clamped; if the interference pattern is minimally visible when two flat pieces of glass are close enough, the construction is glued and left to cure for 24 hours. The sample is used if less than 3 white light interference, fringes

3.2. Device geometry and data acquisition

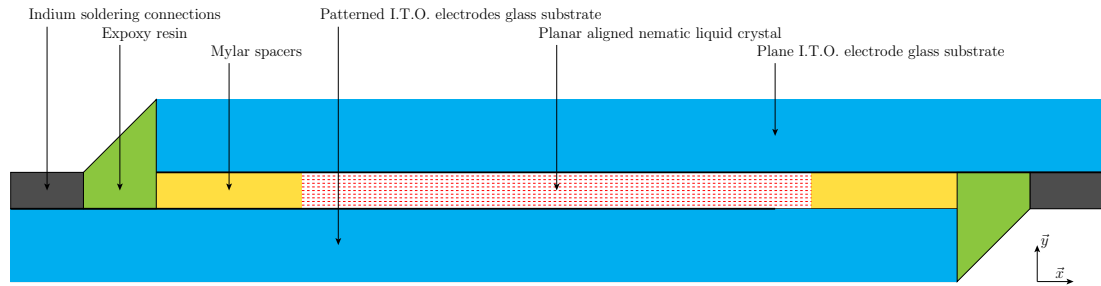


Figure 3.1: Cross-section of an assembled, filled and connected cell

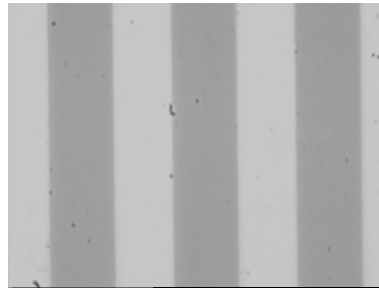


Figure 3.2: Observation of interdigitated electrodes under microscope

due to thickness changes, are seen over the active area and rejected if there are more than 3 visible fringes. This is the criterion to check that the thickness is uniform. After the epoxy resin is set, the thickness of the sample needs to be determined with precision this is achieved with a spectrometer, this technique is explained in the Section 2.1.5. When the characteristics of the sample are known, it is then filled with the desired material. The cell is heated up at the same time as the material in order that the cell may be capillary filled at just above the temperature of the nematic-isotropic transition of the liquid crystal. The cell is thermally annealed by cooling down to room temperature at less than 0.5°C per minute, then electric connections are added. The cell is finally sealed and the indium solder lumps covered with epoxy resin (see Figure 3.1).

3.2.2 Image processing

When the sample is ready, it undergoes the experiment in the interferometer. It is placed in one of the arms of the setup. If the interferometer is set up

correctly (as described in Section 2.4), the fringes will be located in the plane of the liquid crystal layer and tilt fringes will be observed by the CCD camera with coherent laser light. A magnified image of the sample will be observed by the CCD, with incoherent white light, and a picture is taken to determine the position of the I.T.O. interdigitated electrodes for modelling purposes. Without any signal applied, a range of fringes appears. Another picture is taken, that will allow us to determine the shift generated by the sample itself and not due to the phenomenon studied. Then the desired signal is applied and when the sample reaches the steady state, a short movie is recorded by the CCD camera to cover the whole period of the applied signal. The frame rate for image acquisition is 30 fps. In Figure 3.3, it is possible to observe the position of the electrodes on

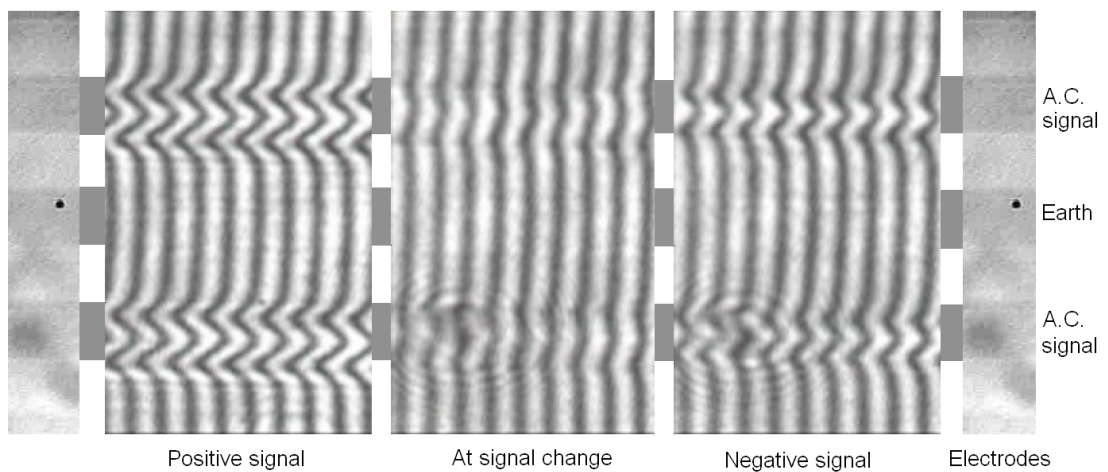


Figure 3.3: Picture observed from the CCD camera in the interferometer

both sides, to acquire this picture the laser source is turned off and a white light source is placed behind the sample. The end part of the interferometer is now used as a microscope which also allows the cell to be positioned in focus. Without moving the sample, the incoherent light source is removed and the laser is fired again and the interference fringes appear. The signal is turned on and the fringes are distorted according to the variation in the optical path. The centre-left and the centre-right pictures in Figure 3.3 show the maximum distortion for positive and negative signals respectively. The middle Figure (see Figure 3.3) shows the

distortion at zero voltage.

3.2.3 Extraction of results

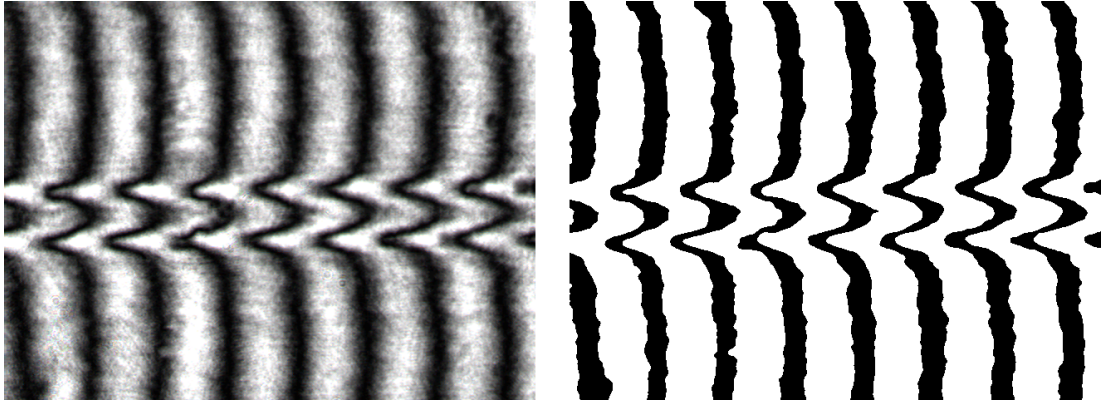


Figure 3.4: Picture of raw data (left) and threshold data (right) from interferometer observations

Each recorded movie is then treated to extract the required information. They are opened using the image analysis software “ImageJ” [70] which converts the movie into a stack of 300 images. The following process is applied to each of the images taken from the individual frames. First the images are converted from an RGB colour picture to a 8-bit black and white picture. Then it undergoes a smoothing process, included in the software, to reduce the background noise. The threshold is then set to get a 2-level representation of the fringes (see Figure 3.4 and 3.6) or the distortion can be plotted as function of the position in the x-direction and time as shown in Figure 3.5. The final results are saved as a text image which is composed only of 0’s and 255’s. The text file can be analysed by a C program, compiled by Mr. R Morris, which counts the number of 0’s and 255’s and transforms the file into the position of the fringes at their mid-point. The obtained data is treated by a MathLab[®] program kindly provided by Mr. D. Willmer, to calculate the distortion and also remove any distortion induced by the non liquid crystal material in the cell. The images without interference are used at this stage and give the relative position of electrodes to locate the

3.2. Device geometry and data acquisition

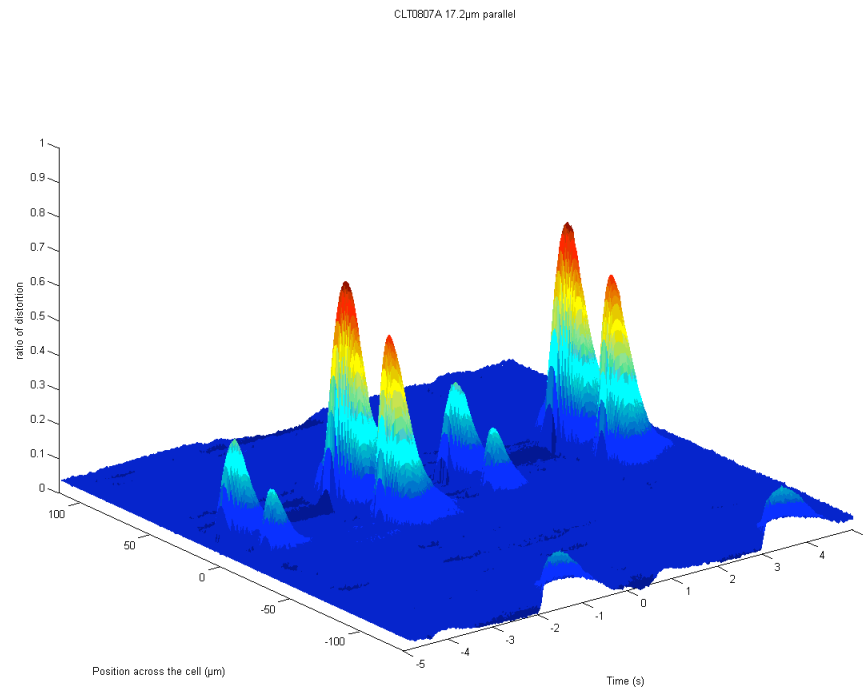


Figure 3.5: 3D plot of the distortion across the cell and as a function of time

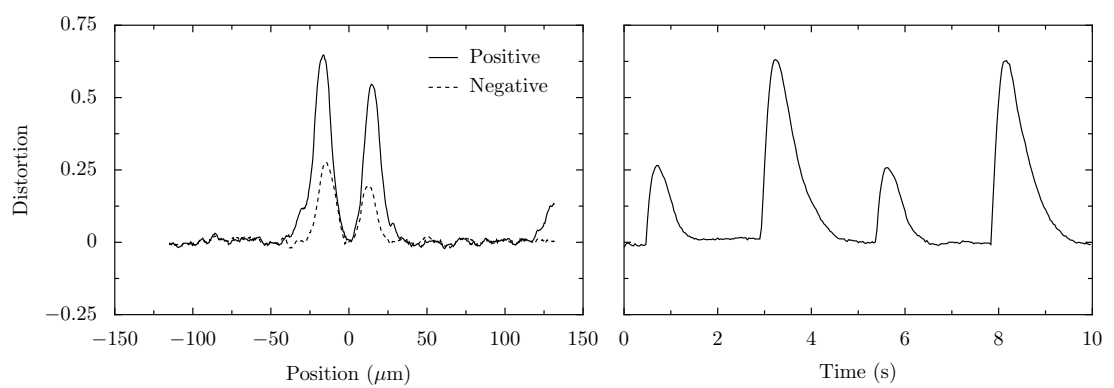


Figure 3.6: Plots of the distortion across the cell and as a function of time

distortion effects.

3.3 Experimental results on a dual frequency material

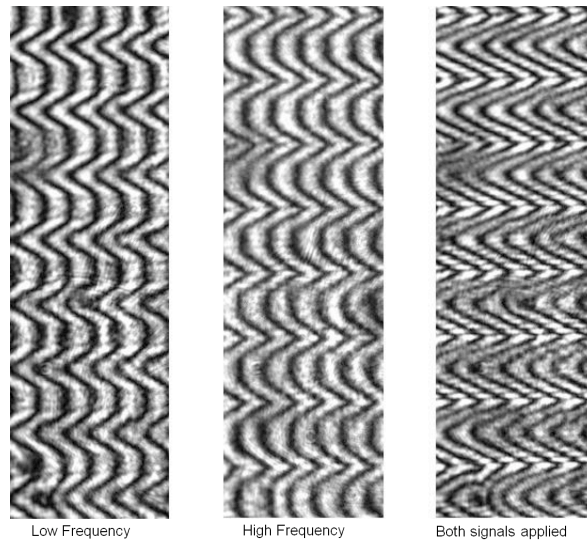


Figure 3.7: Fringe movement induced by 2-frequency material when different frequencies signals are applied

The original purpose of the experiment was to improve the efficiency of the phase grating system by using 2 frequency material and applying signals at two different frequencies to give regions of planar and homeotropic alignment [36]. The aim was to try to reduce the major source which degrades the efficiency of a phase grating system, the “fly-back” region, the zone where the orientation of the director is gradually changing from one direction to another. If the two orientations could stand close to each other, the definition of the 1D array of diffracted spots would be clearer. Forcing the orientation by applying two different signals allows us to get two perpendicular orientations, planar and homeotropic states, using a material which permittivity depends on the frequency of the signal applied. In Figure 3.7, the left side is an interdigitated cell where a set of electrodes is connected to a low frequency generator (AC 6.8V pk-pk 1kHz). The central

3.4. Nematic continuum theory in 2 dimensions

image shows the same cell, where the first set of electrodes is now connected to earth and the second is connected to a high frequency signal (AC 6.8V pk-pk 100Khz). The right part shows the behaviour when the previous two signals are applied simultaneously in order to observe, as written in the previous paragraph, a reduction in size of the “fly-back” region. The fringes do not have the square shape which was expected. The fields and the alignment in the regions in the plane between the interdigitated electrodes are complicated and further research and modelling is required to clarify this behaviour.

3.4 Nematic continuum theory in 2 dimensions

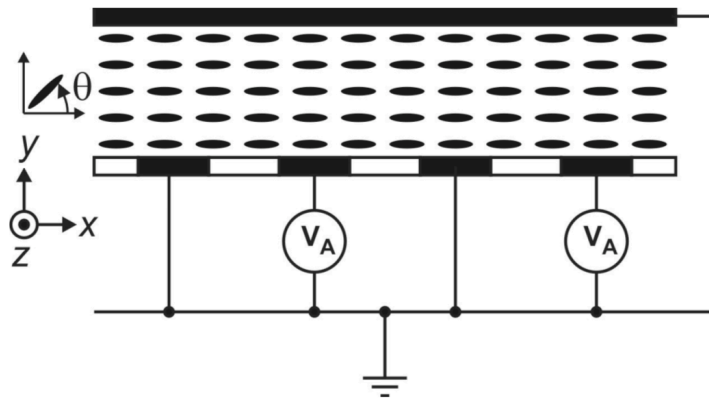


Figure 3.8: Schematic cross-section of the cell with nematic liquid crystal used for modelling

In the actual model and experiment, the studied alignment of the director is planar and experimentally achieved by rubbing the polyvinyl alcohol (P.V.A.) layer perpendicularly to the orientation of the interdigitated electrodes, as shown in x-direction in Figure 3.8. With this alignment it was considered that no z-component existed in the model equations and they were only dependant on x- and y-factors. In the model all characteristics which affect the behaviour of the nematic liquid crystal have to be inserted, as well as the ones describing the orientation of its director. The first statement for the model is that Maxwell’s

3.4. Nematic continuum theory in 2 dimensions

equations must be satisfied :

$$\nabla \cdot \underline{D} = 0 \quad (3.2)$$

$$\nabla \times \underline{E} = 0 \quad (3.3)$$

The angle of the director is θ , the angle between the orientation of the director and the x-direction. The director is defined by \underline{n} where:

$$\underline{n} = [\cos \theta, \sin \theta, 0] \quad (3.4)$$

The electric field (\underline{E}) experienced by the nematic layer is also defined in 2-dimensions without any z-component:

$$\underline{E} = -\nabla U = \left[-\frac{\partial U}{\partial x}, -\frac{\partial U}{\partial y}, 0 \right] \quad (3.5)$$

The total energy is given by:

$$\begin{aligned} \omega = & \frac{1}{2}K_{11}(\nabla \cdot \underline{n})^2 + \frac{1}{2}K_{22}(\underline{n} \cdot \nabla \times \underline{n})^2 + \frac{1}{2}K_{33}(\underline{n} \times \nabla \times \underline{n})^2 \\ & - \frac{1}{2}(\varepsilon_0 \varepsilon_{\perp} \underline{E} + \varepsilon_0 \Delta \varepsilon (\underline{n} \cdot \underline{E}) \underline{n}) \cdot \underline{E} - (e_{11}(\nabla \cdot \underline{n}) \underline{n} + e_{33}(\nabla \times \underline{n} \times \underline{n})) \cdot \underline{E} \end{aligned} \quad (3.6)$$

It is noticeable that there is no K_{22} elastic constant, which corresponds to a twist distortion. This can not occur in a 2-D model with planar orientation and no z-component. The total energy includes the elastic energy ω_N , the dielectric energy ω_D and the flexoelectric polarisation ω_F for nematic liquid crystal. After

3.4. Nematic continuum theory in 2 dimensions

rearranging, the total energy equation becomes:

$$\begin{aligned}
\omega = & \frac{1}{2}K_{11}(\sin\theta\frac{\partial\theta}{\partial x} - \cos\theta\frac{\partial\theta}{\partial y})^2 + \frac{1}{2}K_{33}(\cos\theta\frac{\partial\theta}{\partial x} + \sin\theta\frac{\partial\theta}{\partial y})^2 \\
& - \frac{1}{2}\varepsilon_0[(\varepsilon_{\parallel}\cos^2\theta + \varepsilon_{\perp}\sin^2\theta)(\frac{\partial U}{\partial x})^2 + (\varepsilon_{\parallel}\sin^2\theta + \varepsilon_{\perp}\cos^2\theta)(\frac{\partial U}{\partial y})^2 \\
& + 2(\varepsilon_{\parallel} - \varepsilon_{\perp})\sin\theta\cos\theta\frac{\partial U}{\partial x}\frac{\partial U}{\partial y}] + (e_{11}\cos^2\theta - e_{33}\sin^2\theta)\frac{\partial\theta}{\partial y}\frac{\partial U}{\partial x} \\
& - (e_{11} + e_{33})\sin\theta\cos\theta\frac{\partial\theta}{\partial x}\frac{\partial U}{\partial x} + (e_{33}\cos^2\theta - e_{11}\sin^2\theta)\frac{\partial\theta}{\partial x}\frac{\partial U}{\partial y} \\
& + (e_{11} + e_{33})\sin\theta\cos\theta\frac{\partial\theta}{\partial y}\frac{\partial U}{\partial y}
\end{aligned} \tag{3.7}$$

More of this calculation can be found in Appendix A.1. It is also assumed for this particular model that there is no flow

$$\underline{v} = (0, 0, 0) \tag{3.8}$$

which implies that the rate of strain tensor is:

$$A_{ij} = \frac{1}{2}(v_{i,j} + v_{j,i}) = 0 \tag{3.9}$$

and the vorticity tensor:

$$\omega_{ij} = \frac{1}{2}(v_{i,j} - v_{j,i}) = 0 \tag{3.10}$$

The co-rotational time flux of the director is defined as:

$$N_i = \dot{n}_i - \omega_{ij}n_j \equiv \dot{n} \tag{3.11}$$

The viscous dissipation inequality is calculated by:

$$D = \alpha_1(n_i A_{ij} n_j)^2 + 2\gamma_2 N_i A_{ij} n_j + \alpha_4 A_{ij} A_{ij} + (\alpha_5 + \alpha_6) n_i A_{ij} A_{jk} n_k + \gamma_1 N_i N_i \geq 0 \tag{3.12}$$

$$D = \gamma_1 N_i N_i \geq 0 \tag{3.13}$$

3.4. Nematic continuum theory in 2 dimensions

$$D = \gamma_1 \dot{n}_i \dot{n}_i \geq 0 \quad (3.14)$$

$$D(A_{ij}, N_i, n_i) = 2\hat{D}(v_{i,j}, \dot{\theta}, \theta) \quad (3.15)$$

The balance of angular momentum can be expressed as:

$$\left(\frac{\partial \omega}{\partial(\frac{\partial \theta}{\partial x})}\right)_x + \left(\frac{\partial \omega}{\partial(\frac{\partial \theta}{\partial y})}\right)_y - \frac{\partial \omega}{\partial \theta} - \frac{\partial \hat{D}}{\partial \dot{\theta}} = 0 \quad (3.16)$$

Which can be also written as:

$$\begin{aligned} & \frac{\partial}{\partial x} \left[K_{11} \left(\sin \theta \frac{\partial \theta}{\partial x} - \cos \theta \frac{\partial \theta}{\partial y} \right) \sin \theta + K_{33} \left(\cos \theta \frac{\partial \theta}{\partial x} + \sin \theta \frac{\partial \theta}{\partial y} \right) \cos \theta \right. \\ & \quad \left. - (e_{11} + e_{33}) \sin \theta \cos \theta \frac{\partial U}{\partial x} + (e_{33} \cos^2 \theta - e_{11} \sin^2 \theta) \frac{\partial U}{\partial y} \right] \\ & + \frac{\partial}{\partial y} \left[-K_{11} \left(\sin \theta \frac{\partial \theta}{\partial x} - \cos \theta \frac{\partial \theta}{\partial y} \right) \cos \theta + K_{33} \left(\cos \theta \frac{\partial \theta}{\partial x} + \sin \theta \frac{\partial \theta}{\partial y} \right) \sin \theta \right. \\ & \quad \left. + (e_{11} \cos^2 \theta - e_{33} \sin^2 \theta) \frac{\partial U}{\partial x} + (e_{11} + e_{33}) \sin \theta \cos \theta \frac{\partial U}{\partial y} \right] \\ & - \frac{1}{2} (K_{11} - K_{33}) \sin(2\theta) \left[\left(\frac{\partial \theta}{\partial x} \right)^2 - \left(\frac{\partial \theta}{\partial y} \right)^2 \right] + (K_{11} - K_{33}) \cos(2\theta) \frac{\partial \theta}{\partial x} \frac{\partial \theta}{\partial y} \\ & + \frac{1}{2} \varepsilon_0 (\varepsilon_{\parallel} - \varepsilon_{\perp}) \sin(2\theta) \left[\left(\frac{\partial U}{\partial y} \right)^2 - \left(\frac{\partial U}{\partial x} \right)^2 \right] + \varepsilon_0 (\varepsilon_{\parallel} - \varepsilon_{\perp}) \cos(2\theta) \frac{\partial U}{\partial x} \frac{\partial U}{\partial y} \\ & + (e_{11} + e_{33}) \sin(2\theta) \left[\frac{\partial \theta}{\partial x} \frac{\partial U}{\partial y} + \frac{\partial \theta}{\partial y} \frac{\partial U}{\partial x} \right] \\ & + (e_{11} + e_{33}) \cos(2\theta) \left[\frac{\partial \theta}{\partial x} \frac{\partial U}{\partial x} + \frac{\partial \theta}{\partial y} \frac{\partial U}{\partial y} \right] - \gamma_1 \frac{\partial \theta}{\partial t} = 0 \end{aligned} \quad (3.17)$$

This last equation will be used to solve the angle (θ) of the director in the model.

In the COMSOL software this equation must be rearranged and written in the following form:

$$da \frac{\partial U}{\partial t} + \nabla \cdot \underline{\Gamma} = F \quad (3.18)$$

Where the terms are defined in Appendix A.1. The energy must also be minimised with respect to U' , the Euler-Lagrange equation is:

$$\left(\frac{\partial \omega}{\partial(\frac{\partial U}{\partial x})}\right)_x + \left(\frac{\partial \omega}{\partial(\frac{\partial U}{\partial y})}\right)_y - \frac{\partial \omega}{\partial U} = 0 \quad (3.19)$$

which can also be formulated as:

$$\begin{aligned}
 & \frac{\partial}{\partial x} \left\{ -\frac{1}{2} \varepsilon_0 [2(\varepsilon_{\parallel} \cos^2 \theta + \varepsilon_{\perp} \sin^2 \theta) \left(\frac{\partial U}{\partial x} \right) + 2(\varepsilon_{\parallel} - \varepsilon_{\perp}) \sin \theta \cos \theta \frac{\partial U}{\partial y}] \right. \\
 & + (e_{11} \cos^2 \theta - e_{33} \sin^2 \theta) \frac{\partial \theta}{\partial y} - (e_{11} + e_{33}) \sin \theta \cos \theta \frac{\partial \theta}{\partial x} \left. \right\} \\
 & + \frac{\partial}{\partial y} \left\{ -\frac{1}{2} \varepsilon_0 [2(\varepsilon_{\parallel} \sin^2 \theta + \varepsilon_{\perp} \cos^2 \theta) \left(\frac{\partial U}{\partial y} \right) + 2(\varepsilon_{\parallel} - \varepsilon_{\perp}) \sin \theta \cos \theta \frac{\partial U}{\partial x}] \right. \\
 & \left. + (e_{33} \cos^2 \theta - e_{11} \sin^2 \theta) \frac{\partial \theta}{\partial x} + (e_{11} + e_{33}) \sin \theta \cos \theta \frac{\partial \theta}{\partial y} \right\} = 0
 \end{aligned} \tag{3.20}$$

This last equation is the expression of the potential in the model which defines the electric field experienced by the liquid crystal material in the cell [71, 72].

Equations 3.17 and 3.20 were solved self-consistently using commercial PDE solver software [73, 74]. The time evolution of the 2 dimensional n-director profile through the liquid crystal layer, $h(x, z, t)$, was calculated in response to a squarewave voltage waveform applied to the electrodes at $z=0$ and $z=d$. The use of finite elements to solve the nematic continuum equations can lead to a loss of the nematic n-director symmetry, $n \equiv -n$, as a result of the discretisation of the equation onto the finite element grid [75–77]. This difficulty does not arise in the current work because the fringing field geometry removes any ambiguity between the θ orientations in neighbouring positions on the finite element grid and also low switching voltages are employed which do not cause large gradients in the n-director.

To realise the fitting, some parameters were kept constant as they are inner properties of the material used (E7 in this case shown in Table 4.1). The parameters inputted as constant in the COMSOL model and Matlab data processing program, are the elastic constants (K_{11} and K_{33}), the different refractive indices (n_e and n_o) and the permittivities (ε_{\perp} and ε_{\parallel}). One of the parameters used for fitting was only the pretilt depend only upon the process used to rub the cell substrate and were assume to be identical on each one. The pretilt is related to the asymmetry of the peaks across the cell as illustrated on Figure 3.9 (A). The second one was the exponential decay factor of the applied signal represented

3.4. Nematic continuum theory in 2 dimensions

on Figure 3.11 (b) which is related to the shielding effect from the ions in the material illustrated on Figure 3.9 (C). Finally, the most important parameter to be use for this study is the sum of the flexoelectric coefficients ($e_1 + e_3$) which control the asymmetry of the peak response to positive and negative signal as illustrated on Figure 3.9 (B). The model was run until the results fit at the best the experimental data across the cell as illustrated by the solid line in Figure 3.10 and simultaneous as a function of time as illustrated by the solid line in Figure 3.11 (a). The data obtained from the model are the director angle regrouped in a matrix across and through the cell and as a function of time for a given applied signal. From these data, the variation of optical path through the cell is calculated and is compared with to the distortion of the fringes in the experimental data.

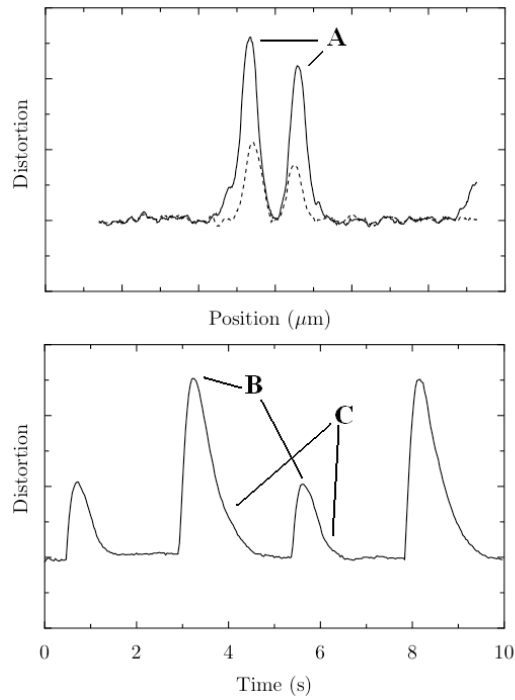


Figure 3.9: Illustration of the effects from the parameter used for the fitting (A: pretilt; B: flexoelectricity and C: ions)

3.5 Experimental results on a non-dispersive nematic liquid crystal (E7)

Table 3.1: Characteristics of cells used during interferometric investigations of the sum of flexoelectric coefficients ($e_1 + e_3$)

Cell's code	Material	Cell thickness	Alignment	Electrodes width & gap
CLT08-07 A	E7	17.2 μ m	Antiparallel	37 μ m & 43 μ m
CLT08-07 B	E7	17.8 μ m	Parallel	37 μ m & 43 μ m
CLT08-07 C	E7	8.9 μ m	Antiparallel	N/A
CLT08-07 D	E7	8.1 μ m	Parallel	N/A

The following experiments were carried out using the commercial nematic material E7 [57]. Table 3.1 presents the characteristics of each cell built for these experiments.

3.5.1 Thick cell with antiparallel alignment

The signal applied to cell CLT08-07A is a square wave of amplitude 1.17V rms. and a frequency of 0.2Hz. The results of the positive and negative distortion (see Figures 3.10 and 3.12) are the ones at the maximum of the fringe movement during each respective period. The asymmetry on both edges of the electrodes is situated at $\pm 17\mu$ m, this is due to the antiparallel orientation. Another characteristic of the results is the decay of the distortion which can be observed in Figures 3.11 and 3.12. The distortion reaches its maximum around 250ms after the change of polarity of the applied signal, it is thought to be due to the ionic migration which shields the applied signal.

3.5.2 Thick cell with parallel Alignment

The same signal has been applied to the cell CLT08-07B and the time dependent fringe displacement data was analysed as discussed previously.

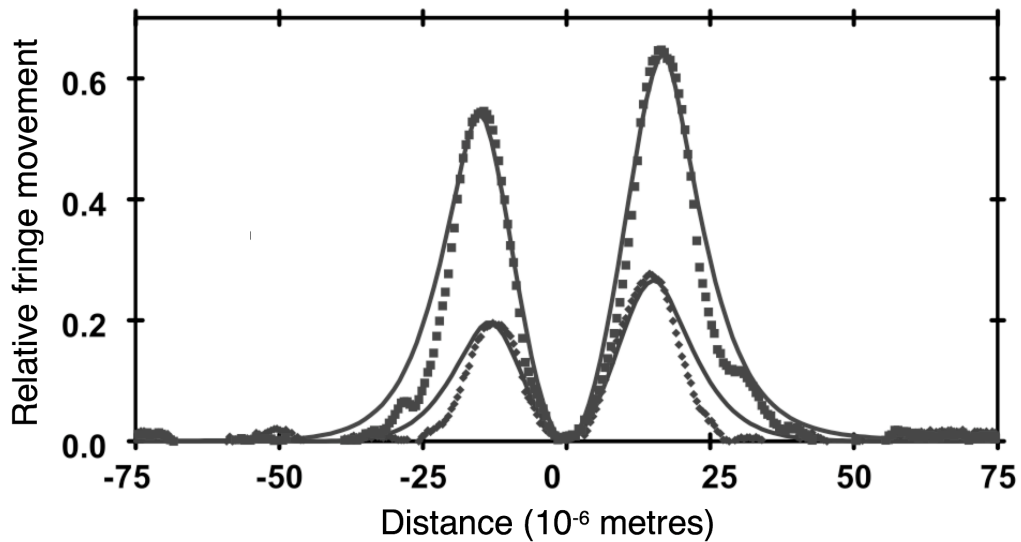


Figure 3.10: Maximum distortion during positive applied signal (squares) and negative applied signal (diamonds) for the antiparallel thick geometry and the model data represented by the line. With 0 representing the centre of the electrode where the signal is applied.

In Figure 3.13 of the maximum distortion as a function of time the same particularities which can be observed in both the parallel and antiparallel orientations. The major difference is on the positive and negative maximum distortion (Figure 3.14) where there is a small asymmetry for the positive signal in one direction and in another direction for the negative signal (see Figure 3.14). For modelling purposes, it was impossible to fit this behaviour and, as a compromise, the fit has no asymmetry for positive or negative signals. The fringe movement is localised at the regions toward the edge of the centre electrode, mainly due to the fringing fields being highest in these regions.

3.5.3 Cell thickness dependence

Another approach of the investigation was to look at the effect of the thickness dependence. This was done using cell CLT08-07C which is approximately half the thickness of cell CLT08-07A, but sharing the same orientation (see Table

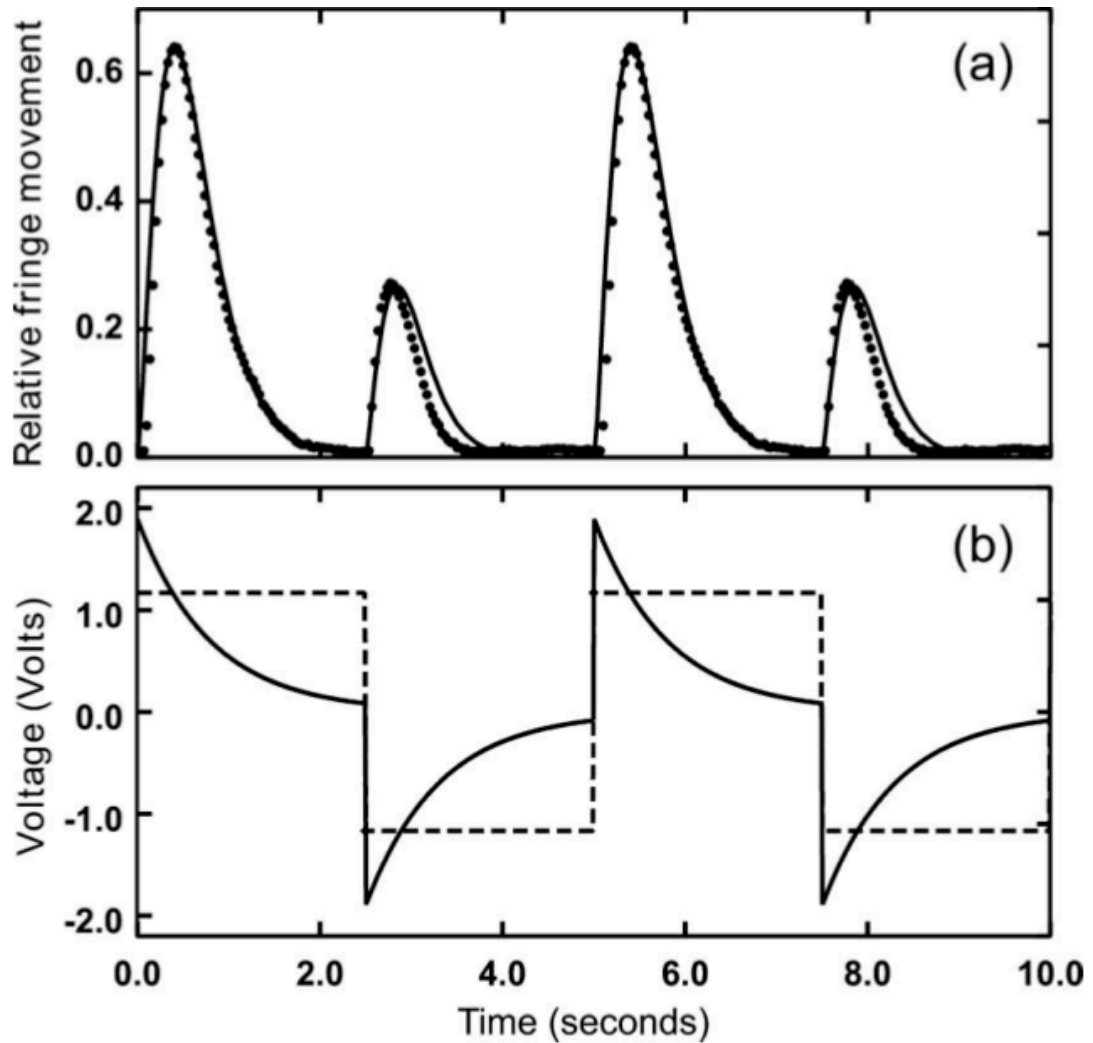


Figure 3.11: (a) The filled circles show experimental data for the relative fringe movement as a function of time at the position $x=15\mu\text{m}$. (b) The applied voltage wave form is shown as the dotted line. The solid line shows the voltage waveform that was used to obtain the fit to the data shown by the solid line in (a).

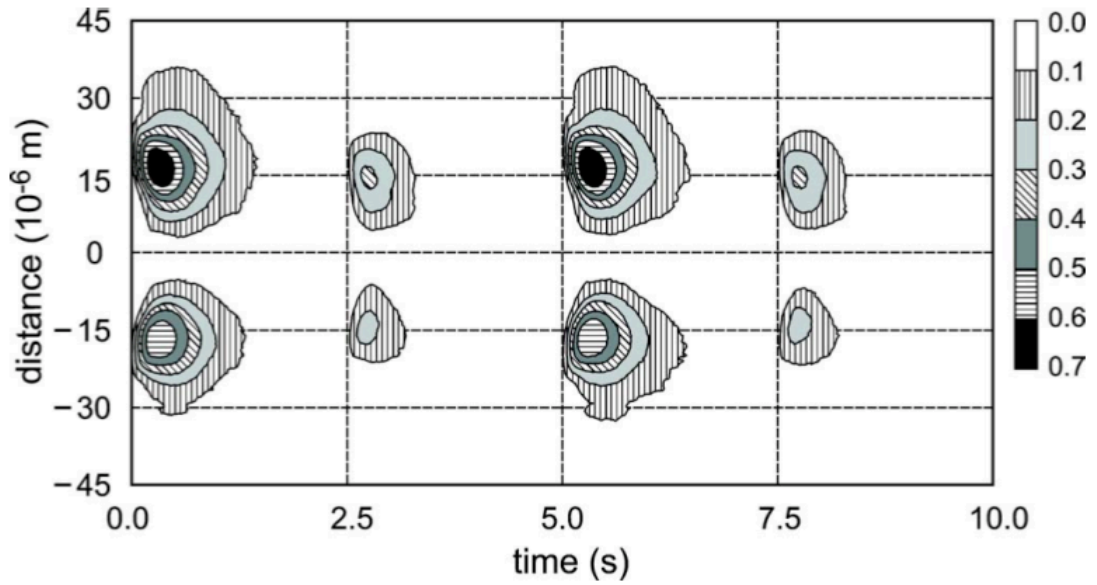


Figure 3.12: Contour plot of the relative fringe movement with time as a function of the distance in the x-direction across cell CLT08-07A. From 0.0-2.5 and 5.0-7.5 s +1.17V is applied to the central electrode, and from 2.5-5.0 and 7.5-10.0 s the applied voltage is -1.17V

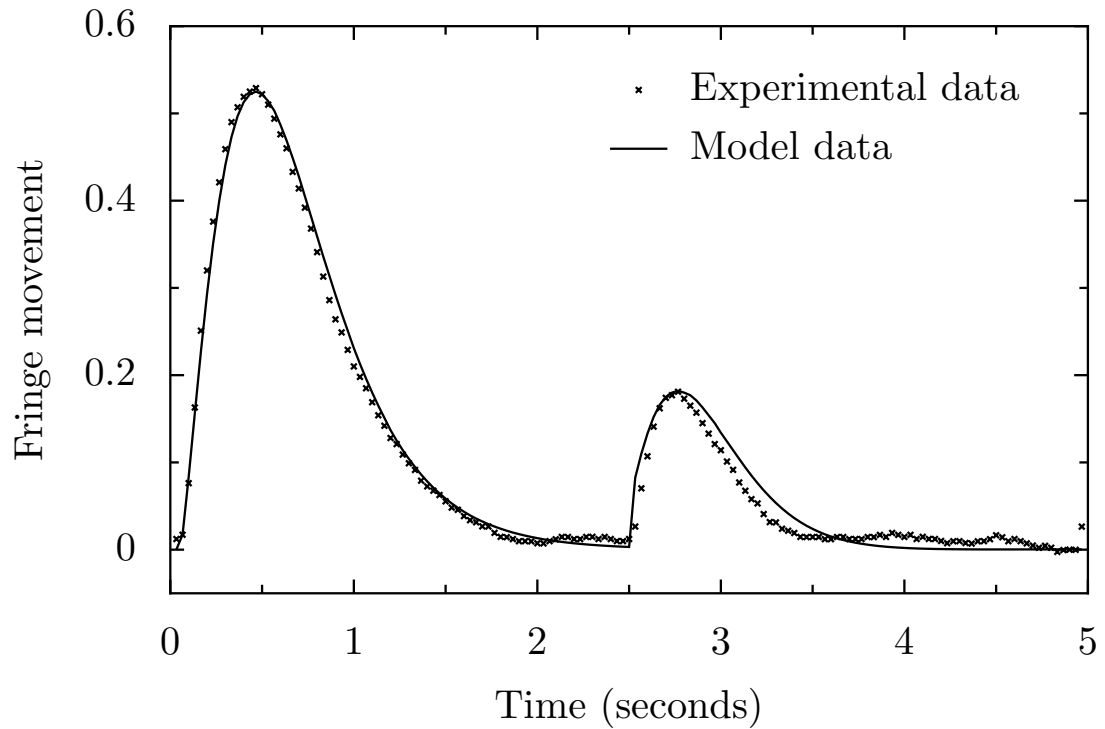


Figure 3.13: Results of the relative fringe movement as a function of time in a parallel alignment cell

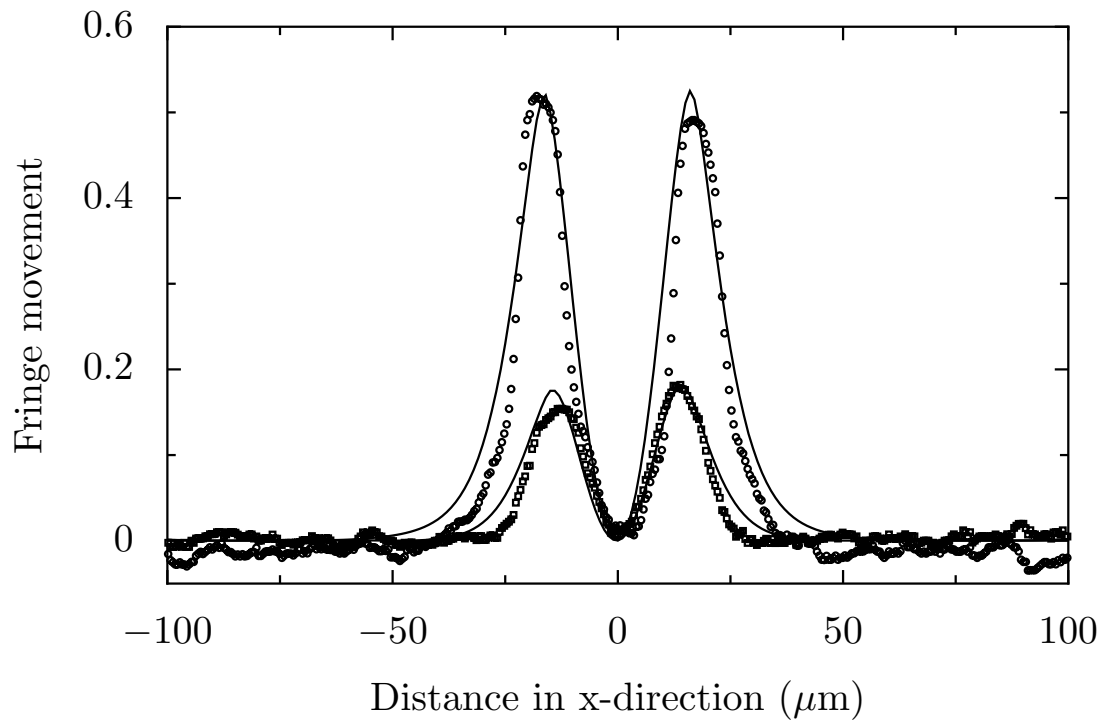


Figure 3.14: Maximum distortion during positive applied signal (circles) and negative applied signal (squares) in a parallel alignment cell

3.1). The same signal was applied and the distortion observed in the thinner cell was greater than in the thicker one (see Figure 3.16). The reason being that the electric field experienced by the nematic material was greater. This is traded against having a thinner layer and so there is more refractive index difference between the distorted and undistorted regions in the thin cell. It is also interesting to note in the same figure, that the antiparallel orientation gives the same asymmetry as the one observed in the same orientation thick cell. In Figure 3.15 it can be observed that the reorientation of the director occurs faster after reaching the maximum distortion due to a greater effect from the surface anchoring. No further investigations have been done with this sample but this could be explored in future work.

3.5. Experimental results on a non-dispersive nematic liquid crystal (E7)

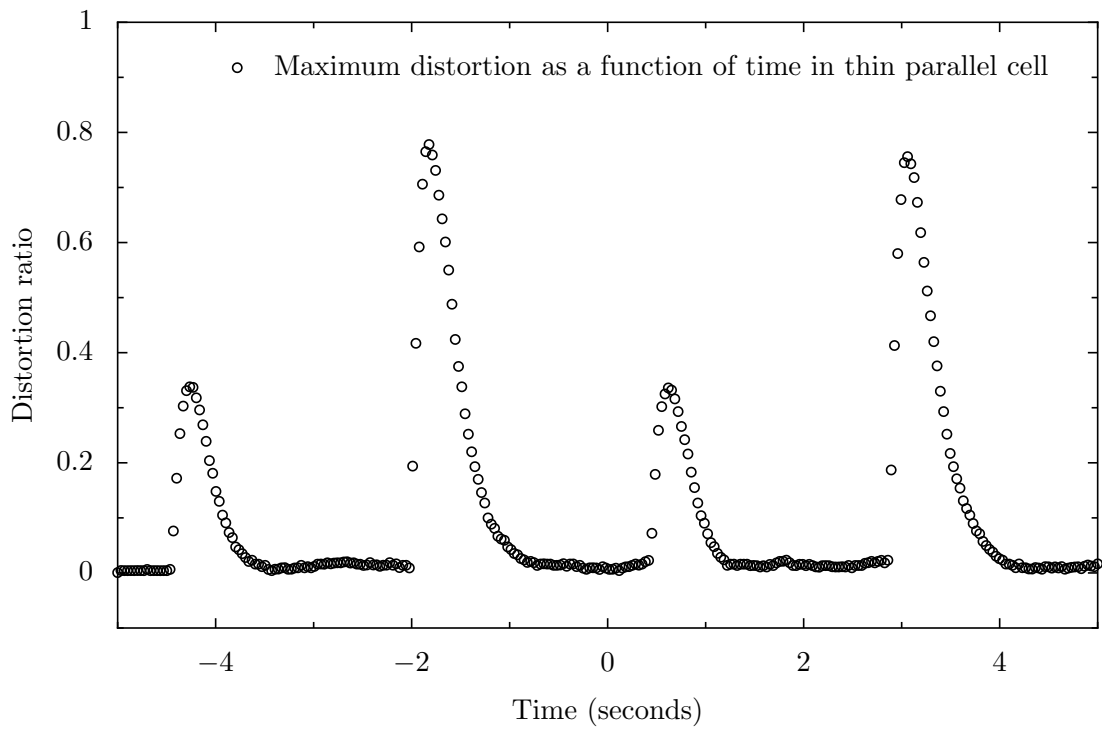


Figure 3.15: Results of the relative fringe movement as a function of time in thin antiparallel alignment cell

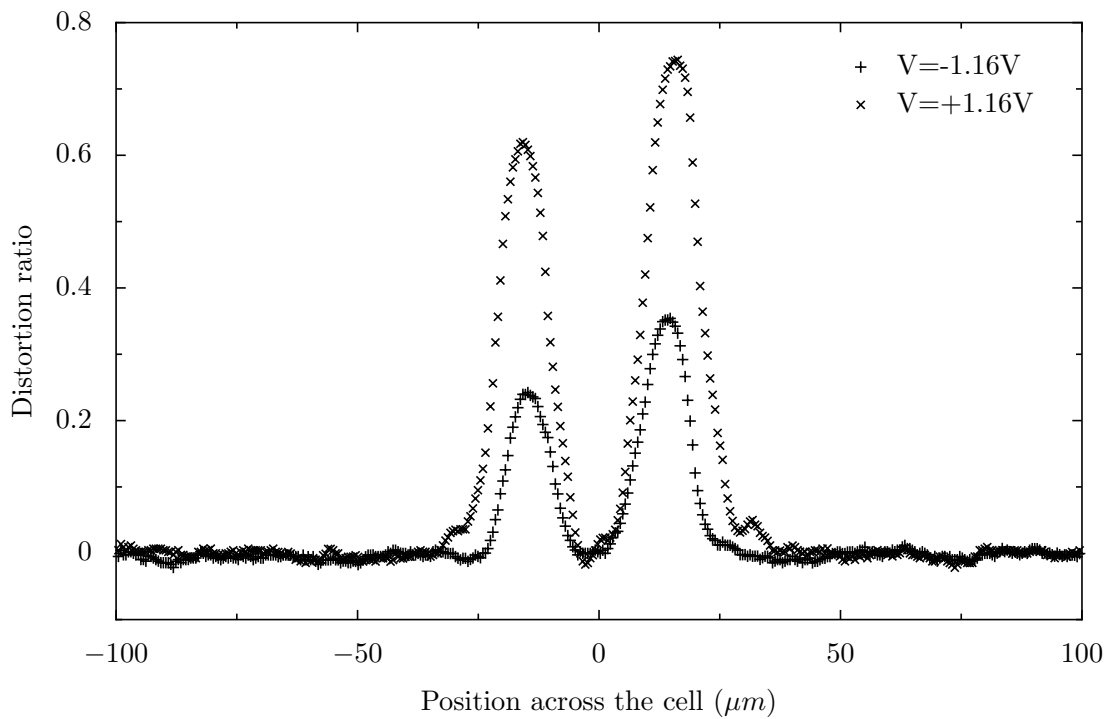


Figure 3.16: Maximum distortion during positive and negative applied signal for the thin antiparallel geometry cell

3.6 Implementation of the model

3.6.1 Assumption in the numerical modelling

To fit the observed fringe distortion, an assumption needed to be made to simulate the voltage shielding effect induced by the charge free carriers (ions) and their migration. So the effective voltage experienced by the nematic layer was modified and it was assumed that the applied voltage was enhanced by a reversed ion-field after each polarity reversal and then decayed exponentially with time during each half period as represented in Figure 3.11(b).

3.6.2 Transient capacitance measurements and simulations

Measures

To support the assumptions made about the shielding effect of the applied signal by the free charge carriers, a study of the evolution of permittivity as a function of time when the same type of signal is applied was done using the transient capacitance experiment (Figure 2.12). Details of cells used during this measure can be seen in Figure 2.9 and 2.10 with parallel orientation based on the principle developed in Section 2.2. The data was recorded at a temperature of 20°C and presented in Figure 3.17. The Fréedericksz threshold voltage [25] has previously been measured as 0.93 V in the same cell geometry and on the same batch of E7 material with a 1 kHz a.c. applied voltage at 24°C [43]. In the absence of ionic contamination this value would also give the threshold for the amplitude of a squarewave voltage above which reorientation of the nematic director in the bulk of the layer would occur. If the squarewave voltage having an amplitude above the threshold is applied for a sufficient time that the permittivity of the layer should rise to a constant value corresponding to the value that would be obtained from static measurements using a capacitance bridge [25, 78]. In Figure 3.17 there is little change in the permittivity up to 1.21 V and above this voltage there

is a peak in the permittivity within each half period of the 0.2 Hz squarewave voltage. This switching behaviour can be explained by the presence of ionic contamination in the liquid crystal material. During the application of a d.c. voltage in each half period the ionic species migrate by drift under the action of the electric field towards the electrodes. As the ions accumulate in the region of the electrodes they shield the external voltage, since a positive ion will drift to a negative electrode and vice versa. This “ionic-field” reduces the voltage that is experienced by the liquid crystal layer [79, 80]. When the polarity of the applied voltage is instantaneously reversed the ions are initially adjacent to electrodes that have the same polarity, i.e., a positive ion is now adjacent to a positive electrode. There is a reverse “ionic field” which adds to the field from the electrodes which causes an initial reorientation of the nematic n-director during each half period. The increasing tilt angle leads to the increase in permittivity. A peak in the permittivity occurs because this is followed by the reduction in the director tilt angle again as the ions move to shield the applied voltage.

Simulations

The simulations of the transient capacitance of a nematic layer containing mobile ionic species was investigated using dynamic nematic continuum theory with a single viscosity, γ_1 [22, 81]. The continuum theory equation, the non-equilibrium charge transport equations, and the appropriate Maxwell equations in 1 dimension were solved self-consistently using commercial PDE solver software [73, 74]. The time evolution of the n-director profile through the liquid crystal layer, $h(z, t)$, was calculated in response to a squarewave voltage waveform applied to the electrodes at $z = 0$ and $z = d$. The potential profile through the layer, $V(z, t)$, and the densities of positive ions, $n_p(z, t)$, and negative ions, $n_n(z, t)$, were solved simultaneously. The simulation does not model the surface trapping of ions [82, 83] and the surfaces were treated as being electrically blocking. The permittivity as a function of the position within the layer, $\varepsilon[\theta(z, t)]$, was calculated using the

3.6. Implementation of the model

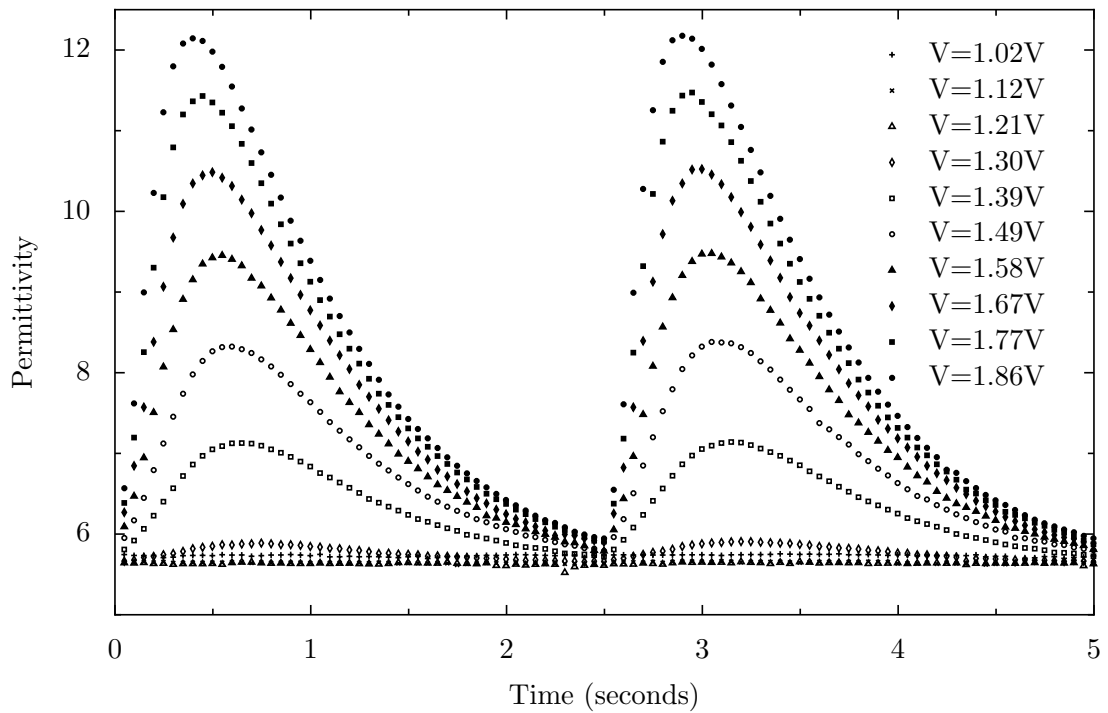


Figure 3.17: Transient capacitance response of a $22 \mu\text{m}$ planar layer of the nematic liquid crystal E7 to an applied squarewave voltage waveform with frequency 0.2 Hz and amplitude between 1.02 V and 1.86 V.

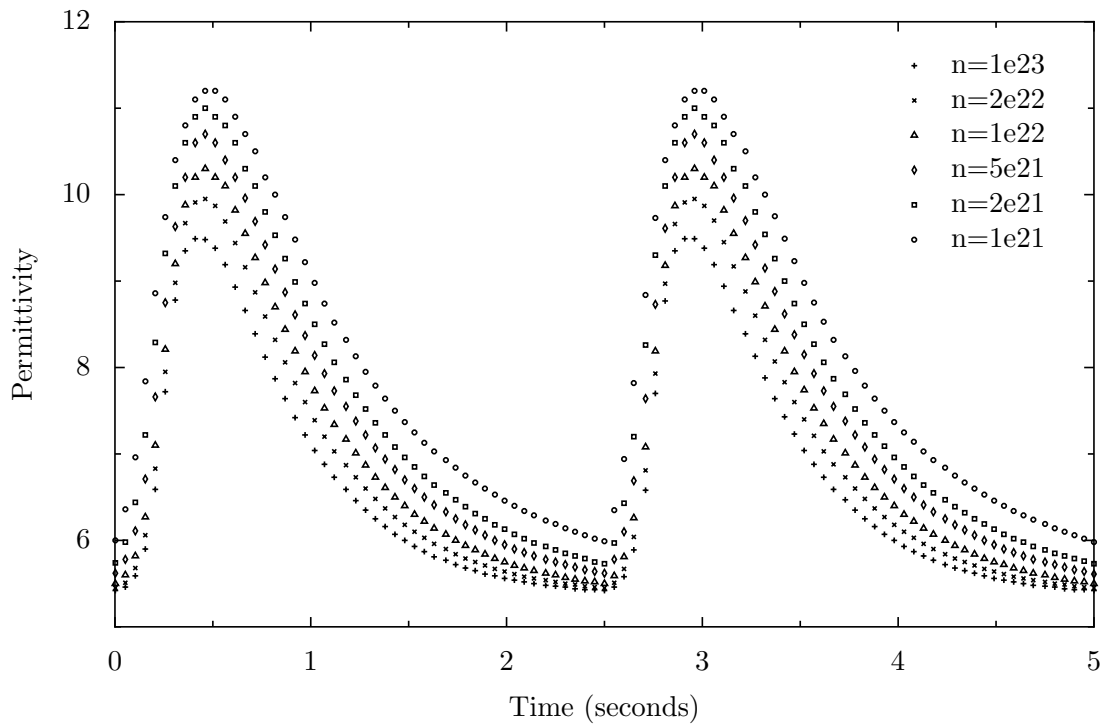


Figure 3.18: Theoretical prediction of the transient capacitance in response to a squarewave voltage waveform with frequency 0.2 Hz and amplitude 1.5 V with concentration of charged mobile ionic species shown in the legend.

3.6. Implementation of the model

values $\varepsilon_{\parallel} = 19.1$ and $\varepsilon_{\perp} = 5.2$. The permittivity of the nematic layer was then calculated by dividing the layer into slices and treating it as an array of capacitors in series. The values of the physical parameters were as follows [43]: splay elastic constant $K_{11} = 10.5pN$; bend elastic constant $K_{33} = 15.2pN$; and viscosity $\gamma_1 = 0.18N.s.m^2$.

Figure 3.18 shows a theoretical prediction of the transient capacitance in response to a squarewave voltage with frequency 0.2 Hz and amplitude 1.5 V. The equilibrium ion densities of positively and negatively charged mobile ionic species were set to be equal, $n_{n_0} = n_{p_0} = n_0$ with values between $n_0 = 1.0 \times 10^{21}m^{-3}$ and $n_0 = 1.0 \times 10^{23}m^{-3}$, as shown in the legend for Figure 3.18. The value of the mobility was chosen to obtain curves with peak values in similar positions to the experimental curves shown in Figure 3.17. For both the charged species the mobility μ was set as $\mu = \mu_n = \mu_p = 1 \times 10^9 m^2 V^{-1} s^{-1}$ and the value of the diffusion constant was fixed via the Einstein relation, $D = (k_B T / |q|) \mu = 0.026 \mu$ for singly charged species at room temperature. Figure 3.19 shows the value of the

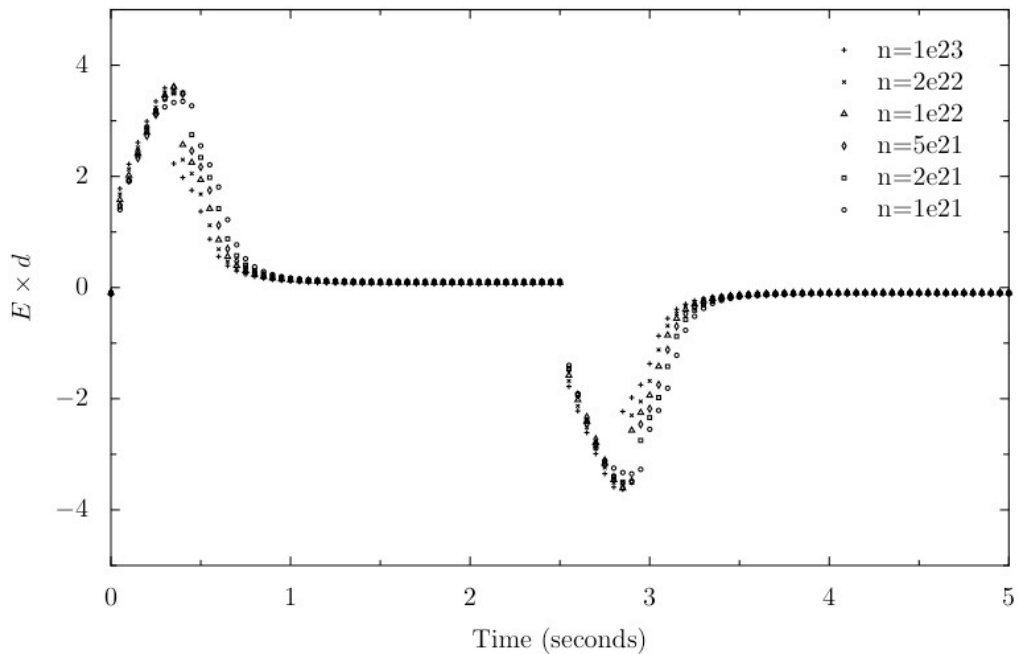


Figure 3.19: Theoretical predictions for the electric field in the centre of the cell multiplied by the cell thickness corresponding to the transient capacitance curves shown in the previous figure.

gradient of the potential in the centre of the cell multiplied by the cell thickness, $d \times \nabla V(z = d/2, t)$. This gives an indication of the potential that is experienced by the bulk region of the nematic liquid crystal layer after the shielding effects of the mobile ionic charge. It is an indication, rather than a quantitative measure, because the charge distribution is only localised close to the electrodes at the boundaries towards the end of a half period of the applied waveform. In addition, the potential profile through the layer, $V(z, t)$, is a solution of the Maxwell equation $\nabla \times D = |e|(n_p - n_n)$ and this is highly distorted away from being a linear profile due to the dielectric anisotropy of the liquid crystal and the presence of the ionic species. However, given these caveats, the numerical work indicates that a voltage waveform similar to that shown in Figure 3.19 can be used as an appropriate simplified model to simulate the effects of charge migration and shielding without solving the full non-equilibrium charge transport equations. The simulation will be used in the 2 dimensional simulations in Section 3.8.

3.7 Optical diffraction measurements

The sample can be used as a phase grating component using the same setup as the one shown in Figure 3.20. To investigate the flexoelectric coefficients ($e_1 + e_3$), the same signal waveform and the same potential were applied to the sample. If successful this will allow the comparison of the interferometric method with the diffractive one.

3.7.1 Sample and processing details

To study the phase grating system, the sample geometry is an important factor. The size of the electrodes determine the periodicity and by the Bragg diffraction relation $2d \sin \theta = m\lambda$ [11], it also gives the angle of diffraction. The sample structure was discussed in Section 2.1.5.

3.7.2 Diffraction measurements

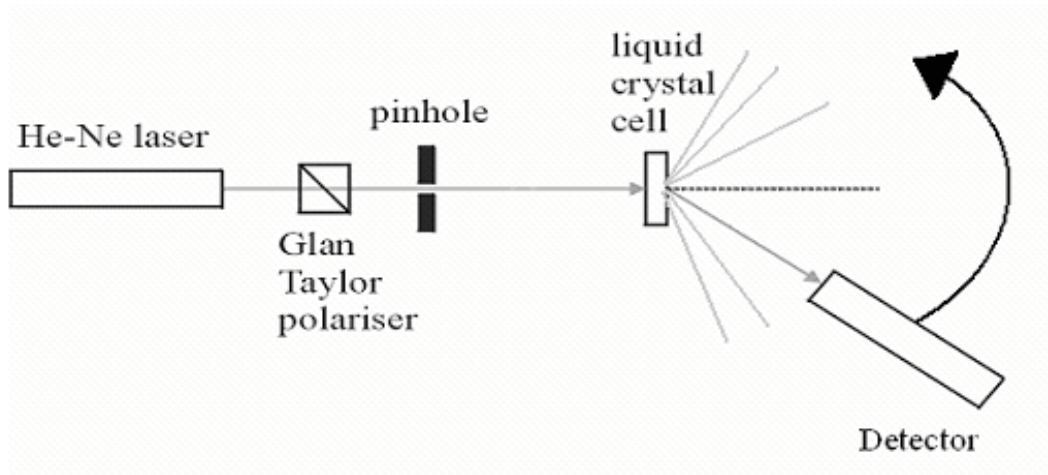


Figure 3.20: Schematic representation of the setup for the diffraction experiment

To achieve the diffraction measurements, the diffractive sample is mounted into a setup which is composed of a laser source and a polariser on one side of the sample. On the other side of a photo detector held on a rotating arm to measure the output power of the different diffraction orders as shown in Figure 3.20 [35]. The electric signal applied to the sample is increased by steps and the diffracted power is recorded for each visible diffraction spot.

3.7.3 Static optical diffraction patterns

Static far field diffraction patterns are shown in Figure 3.21 when the device was illuminated with collimated He-Ne laser light of wavelength 632.8 nm. In Figure 3.21(a) all of the electrodes were connected to earth potential. The diffraction pattern is due to the indium tin oxide striped electrodes on the substrate. The second diffraction orders correspond to the electrode period of 80 μm . The periodic striped electrodes act as a squarewave transmission grating and so only the even diffraction orders ($\pm 2, \pm 6, \pm 10$) appear in Figure 3.21(a) and the odd orders are missing.

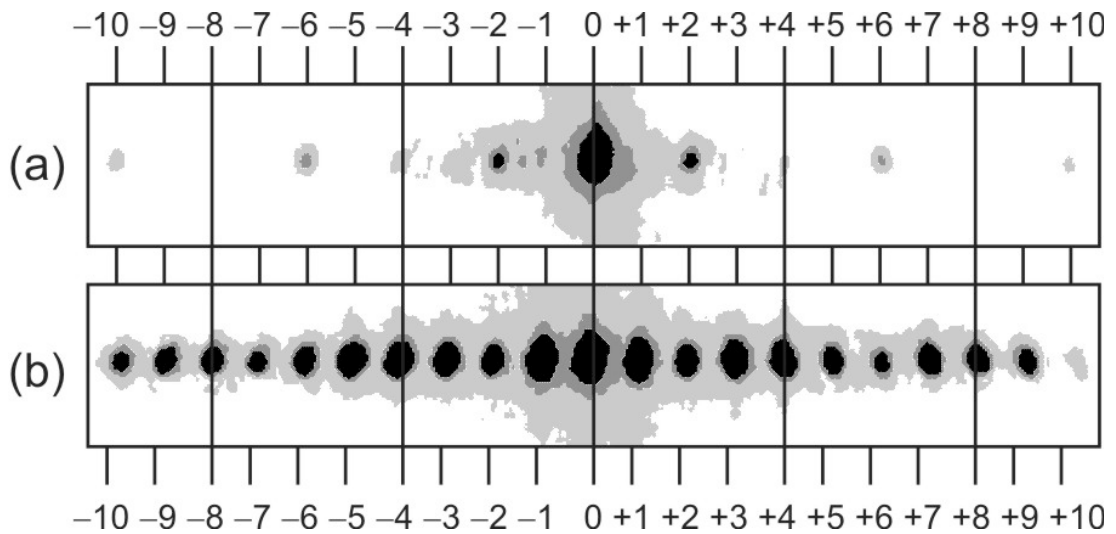


Figure 3.21: Diffraction pattern induced by the $40\mu m$ interdigitated electrode sample with a signal of $1.16V_{rms}$ and $1kHz$

A sinewave voltage with frequency 1.0 kHz and amplitude $V=1.17V_{rms}$ was applied to produce the far field diffraction pattern shown in Figure 3.21(b). A distortion of the nematic liquid crystal occurs in the regions of the alternate electrodes to which the voltage was applied. The laser light was polarised in the x-direction and so it experienced the spatially periodic lowering of the refractive index associated with the distortion regions. This gives rise to the ± 1 first diffraction orders corresponding to twice the electrode period, i.e. $160\mu m$. A range of higher order diffraction spots occurs in Figure 3.21(b) and the intensity envelope of the diffraction orders is determined, to the first approximation, from the profile of the average refractive index due to the distortion in the nematic material as a function of the x coordinate.

3.7.4 Time dependent optical diffraction patterns

The far field optical diffraction patterns were next measured during the application of a squarewave voltage of frequency 0.2 Hz and amplitude $V_a = 1.17 V$ to alternate electrodes in the striped interdigitated electrode array. The resultant

3.7. Optical diffraction measurements

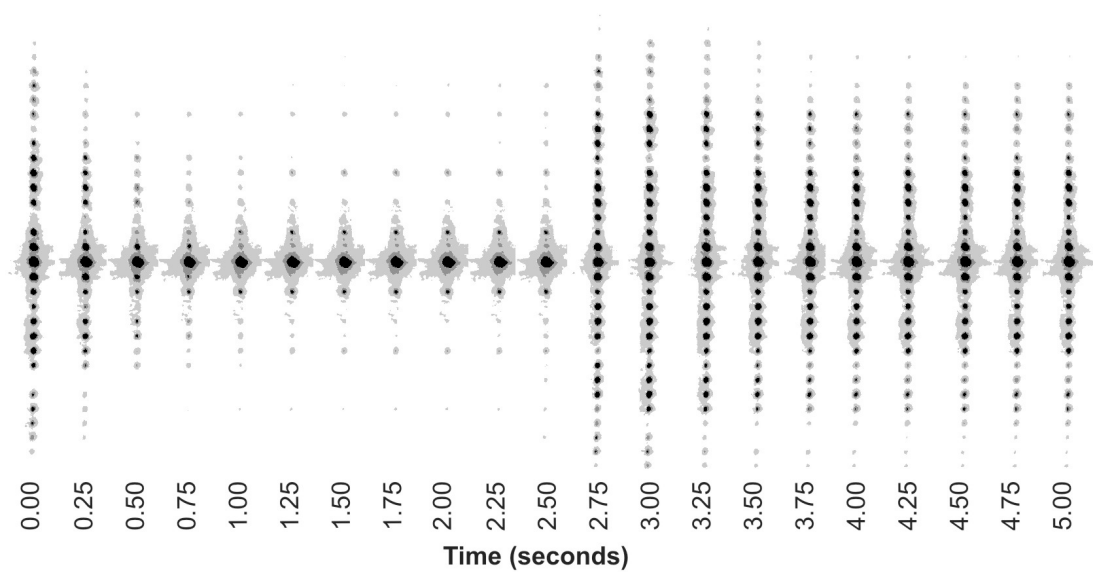


Figure 3.22: Time dependent observation of the diffraction pattern induced by the $40\mu\text{m}$ interdigitated electrode sample (negative signal from 0 to 2.5 seconds and positive signal from 2.5 to 5 seconds)

diffraction patterns are shown in Figure 3.22 at 0.25 sec intervals and the voltage was negative ($V_a = -1.17\text{V}$) during the time interval $0.0 < t < 2.5$ sec and positive ($V_a = +1.17\text{ V}$) during the time interval $2.5 < t < 5.0$ sec. The images have been digitized to show 16 grey-levels and the darker color corresponds to a diffraction spot having higher intensity. Immediately after the application of the positive voltage ($t > 2.50$ sec) a series of strong diffraction spots appear up to order ± 15 . The highest orders reduce in intensity within 1.25 sec but the lower orders persist throughout the duration of the positive voltage. After the change in polarity to the negative voltage ($t > 0$ sec in Figure 3.22) the diffracted orders up to ± 8 are strong but there is a fast decay within 0.25 - 0.5 sec. By 1.25 sec after the change to negative polarity the diffraction pattern is similar to the diffraction pattern in Figure 3.21(a) which is solely due to the diffraction from the electrodes. These observations are consistent with the maximum fringe distortion shown in Figure 3.10 where there is a larger distortion after the application of the positive pulse than after the application of the negative pulse. There is still a significant distortion across the nematic layer 2.5 sec after the positive pulse which continues to

diffract light. The time dependent intensity the first 4 diffracted orders is shown in Figure 3.23. The labelling system is the same as that shown in Figure 3.21, i.e. the ± 1 orders correspond to diffraction from a spatial period of $160 \mu m$. Figure 3.23(a) shows the time dependent intensities of the zero (solid line), ± 1 (squares) and ± 2 (diamonds) orders and Figure 3.23(b) shows the time dependent intensities of the ± 3 (squares) and ± 4 (diamonds) orders, both with a logarithmic intensity scale. For both of the graphs the filled symbols show data for the positive orders and the empty symbols for the negative diffracted orders. For the ± 1 , ± 3 and ± 4 orders shown there is a peak in the intensity after a change in polarity of the applied voltage and this is followed by a decay of the intensity. This decay is greater after the change from positive to negative polarity. It was discussed in Section 3.5 that although the applied voltage was a 0.2 kHz square-wave with a constant amplitude of 1.17 V, the data from the measurements performed on the Mach-Zehnder interferometer could only be fitted using nematic continuum theory if the voltage actually experienced by the liquid crystal layer was assumed to be exponentially decaying in each half of the waveform cycle due to the shielding effect of mobile ionic charges in the liquid crystal medium. The same effect is observed in the optical diffraction measurements. The ± 2 orders show an increase in intensity with time after the initial decay. It should be noted, however that the even orders are influenced by diffraction from the periodic striped electrodes that have a slightly lower transmission than the uncoated glass substrate.

3.8 Fit to experimental data using the continuum theory model

Table 3.2 compares the values obtained from fitting the interferometric data for the parallel and the antiparallel geometry. The values used to obtain a fit for the two different cells were the same, and the values for the sum of the flexoelectric

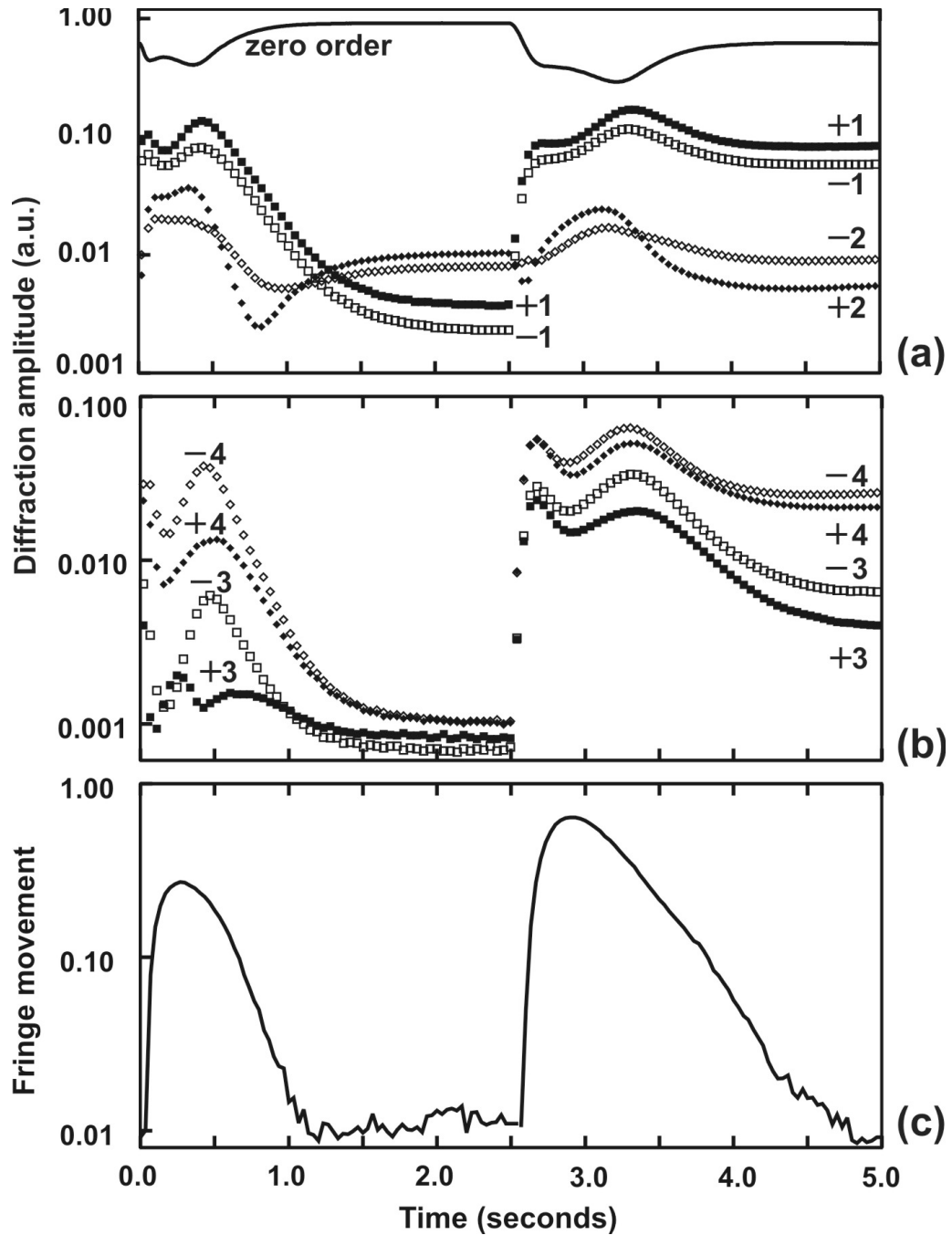


Figure 3.23: (a) and (b) show the time dependent intensity of different orders in the far field diffraction pattern. (c) shows the displacement of fringes in a Mach-Zehnder interferometer as a function of time.

3.9. Conclusion

coefficients (e_1+e_3) are also in agreement to within statistical errors. These results are also consistent with an analysis of results of Fréedericksz measurements on the same material, E7 [57], in Reference [84], and compare well with the value (e_1+e_3)= 15 ± 2 pC.m⁻¹ found for the same material in References [66, 85]. The comparison between the experimental and the model data can be observed for the antiparallel geometry as a function of the x-direction in Figure 3.10, and as a function of time in Figure 3.11. The results for the parallel geometry can be observed as a function of the x-direction in Figure 3.14 and as a function of time in Figure 3.13.

Table 3.2: Parameters obtained from the fit to the interferometric data for the phase grating device with parallel and anti parallel alignment

Parameter	Parallel	Antiparallel
Ion enhanced voltage, V_{pk}	1.89 V	1.89 V
Voltage decay time, τ	0.8 sec	0.8 sec
Surface pretilt, θ_p	0.4°	0.4°
Viscosity, γ_1	0.18 N.s.m ⁻²	0.18 N.s.m ⁻²
(e_1+e_3)	14 ± 1 pC.m	15 ± 2 pC.m

3.9 Conclusion

The interferometric method is used to determine the flexoelectric coefficient of a ionic nematic liquid crystal. This method gave satisfying results 14 ± 1 pC.m⁻¹ for the antiparallel alignment cell and 15 ± 2 pC.m⁻¹ values which are comparable to the accepted value for E7 material [66, 85] but differ from other results [67]. In future work, the new model including the presence of free charge carriers will have to be used to fit the interferometric data. Another direction for future work will be to analyse the evolution of the power of the different spots of the diffraction pattern and to find a way to link it to the flexoelectric parameters. The last possible direction at the present time would be to investigate the variation

3.9. Conclusion

of the director's angle across the sample and as a function of time.

Chapter 4

Transient capacitance in the presence of ionic contamination

4.1 Introduction

The previous chapter described a novel method to determine the sum of the flexoelectric coefficients using an interferometric method with liquid crystal phase grating samples. To achieve this, assumptions have been made about the free charge carrier behaviour and their interaction with the applied field. Ions contained in a nematic liquid crystal can originate from the production process as impurities, or can be generated by the liquid crystal dissociation induced by the large dielectric anisotropy or by the applied DC electric field. The free charge carriers can have effects including the shielding of applied field [79, 80] as mentioned earlier or the alteration of liquid crystal performance by creation of internal electric fields from ions [86] and Freederickz transition [74]. They are responsible for the conductivity in samples [87–89] and can degrade display characteristics [89, 90]. Hybrid Aligned Nematic (HAN) samples cells have been used to determine the flexoelectric coefficients. They have been used with different techniques such as half [59–61] or fully [66] leaky guided mode, in plane fields [59–61, 68], or with magnetic fields [91]. The principle behind all these experiments is the splay-bend distortion of the director (n) creates an “In-built” flexoelectric polarisation (see Section: 1.5.6) [27]. In many of these references, the interaction with free charge carriers is cited especially in the work done by Cornford et al. [92] or by Ponti et al. [68] who studied the effect induced by ions in a HAN cell.

The purpose of this investigation is to explore an alternative method to measure the flexoelectricity coefficients in nematic liquid crystals by switching a HAN cell. The study is based on the measure of the capacitance of a nematic liquid crystal cell as a function of time [43, 93]. The set up of the experiment, shown in Figure 2.11 and 2.12, is using the principle of transient capacitance based on the effect of variation of the permittivity of the liquid crystal according to the orientation of the director [94]. The presence of an asymmetric response to D.C. voltage in the HAN cell gives information about flexoelectricity in the material.

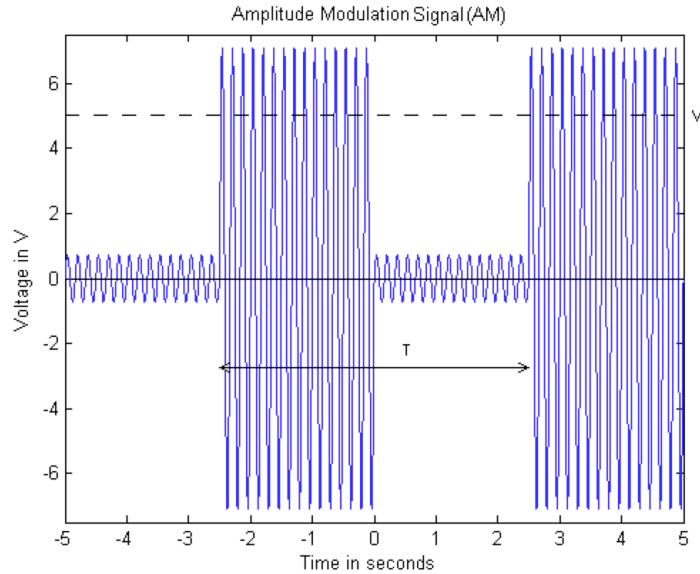


Figure 4.1: Illustration of the Amplitude Modulation (A.M.) signal sample used in this investigation

Unfortunately, high flexoelectric coefficients seems to go together with high ionic concentration. The materials used during this experiment, are one with high ionic concentration and flexoelectric properties (E7) and the other presenting virtually no ions or flexoelectricity (TL216). The second one is used as a control, it will allow fitting of parameters and will be used as a baseline for the appreciation of the flexoelectric or ionic effect in the first material. To carry out these different investigations on flexoelectricity and ions, three different signal will be applied to the samples. The first one is an amplitude modulation signal (A.M.) of 10 kHz, as shown in Figure 4.1, which should allow us to the observe the switching time of the material in the planar cells and the flexoelectric effect in the HAN without generating any ionic migration within the sample. This signal has already been used previously to achieve parameter fitting [43].

The second one is a quasi-continuous D.C. voltage (square), represented in Figure 4.2, which will generate an ionic migration in the material shielding the applied signal.

Finally, the last signal is also a quasi-continuous D.C. voltage which, instead of

4.1. Introduction

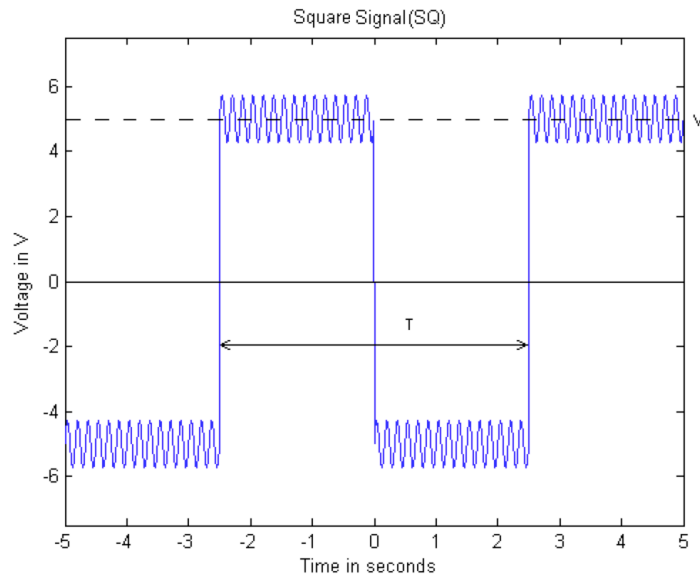


Figure 4.2: Illustration of the Square signal sample (S.Q.) used in this investigation

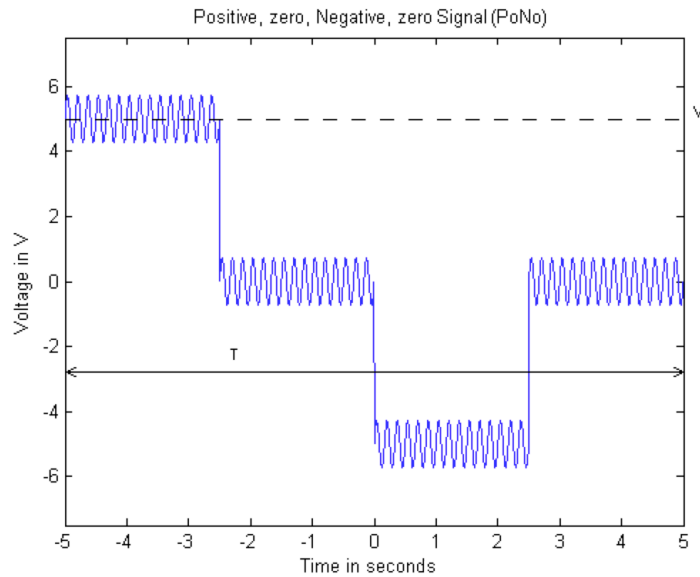


Figure 4.3: Illustration of the combined positive, zero and negative signal sample (PoNo) used in this investigation

changing directly from positive to negative, possesses a period of time when the signal is null between each sign changing of the signal (PoNo), as illustrated in Figure 4.3. These extra periods may allow an estimation of the shielding effect induced by the ions and the field they generate when they are plated on both surfaces of the samples. Added to these signals was a reference signal small enough with an high enough frequency (10 kHz) and low voltage (50 mV) so as not to interfere with the parameters investigated (ions and flexoelectricity). The extrac-

Table 4.1: Characteristics of the liquid crystal materials used in the transient capacitance experiment.

Quantity	E7	TL216	Units
Type	Nematic	Nematic	
Nematic-Isotropic transition			
temperature (T_{N-I})	59.8	80.0	$^{\circ}C$
Solid-Nematic transition			
temperature (T_{S-N})	-2	+4	$^{\circ}C$
Threshold voltage (V_c)	0.93	1.73	V
Extraordinary refractive index (n_e)	1.7378	1.7288	($\lambda = 633nm$)
Ordinary refractive index (n_o)	1.5188	1.5208	($T = 20^{\circ}C$)
Splay elastic constant (K_{11})	11.2	15.3	$10^{-12}N$
Bend elastic constant (K_{33})	15.7	18.0	$10^{-12}N$
Rotational viscosity (γ_1)	0.18	-	$N.s.m^{-1}$
Parallel permittivity (ϵ_{\parallel})	19.1	4.1	no unit
Perpendicular permittivity (ϵ_{\perp})	5.2	9.5	no unit
Permittivity anisotropy ($\Delta\epsilon$)	13.9	5.4	no unit
Sum of flexoelectric coefficients			
($e_{11} + e_{33}$)	15 ± 2	$\sim 1 \pm 0.5$	$10^{-12}C.m^{-1}$
Ions mobility (μ_i)	$\sim (1 - 10)$	~ 0	$10^{-6}m^2V^{-1}s^{-1}$
Charge number density (n_0)	$\sim (1 - 10^5)$	~ 0	$10^{18}m^{-3}$

tion of the flexoelectric coefficients from the HAN cell measurement requires the elastic constants, the viscosity and the different permittivities to be known. In the case of E7 it requires information on the free charge carriers such as the ionic density and mobility (see Table 4.1). This will be done using different planar

4.2. Experimental results

cells of the same thicknesses ($5\mu m$) to compare the results between the ionic and non-ionic material. Different thickness ($5\mu m$ and $22\mu m$) will be used with E7. This variation of thickness will reduce the number ions involve in the material and also reduce the distance these carrier have to travel. The characteristics of the different cell used during the experiments are regrouped in Table 4.2. To go further these different experiments were done at different temperatures to highlight any relation between this parameter and the concentration of ions in the materials.

Table 4.2: Characteristics of cells used for transient capacitance experiments

Cell's code	Material	Thickness	Orientation	Empty cell capacitance (C_o)
CLT 0606 B	E7	$22\mu m$	Planar	45.1 pF
JMH 0606 A	E7	$5\mu m$	Planar	204.68 pF
CVB Jun 0503	E7	$5\mu m$	HAN	188.1 pF
CVB 0601 C	TL216	$5\mu m$	Planar	212.2 pF
CVB 0601 D	TL216	$5\mu m$	HAN	187.0 pF

4.2 Experimental results

4.2.1 Results from the amplitude modulation signal

(A.M.)

Thick $22\mu m$ planar cell and E7 material

For all the following measures, the period was kept at 5 seconds. The rising time (τ_{on}) is related to the rotational viscosity (γ_1), to the thickness of the sample (d) and to the applied (V) and threshold voltage (V_c) by the Equation 4.1 [26, 43, 95, 96].

$$\tau_{on} = \frac{\gamma_1 d^2}{\varepsilon_0 \Delta \varepsilon (V^2 - V_c^2)} \quad (4.1)$$

4.2. Experimental results

During the first half, when the burst A.C. voltage signal is on, the director orientates itself increasing the permittivity, then when the signal is removed, the relaxation phase occurs and the director returns to its original orientation. The speed of reorientation is also related to the rotational viscosity (γ_1), to the thickness of the sample (d) but also to the elastic constant (K) by the Equation 4.2 [26, 43, 95, 96].

$$\tau_{off} = \frac{\gamma_1}{K} \left(\frac{d}{\pi} \right)^2 \quad (4.2)$$

The frequency of the signal (10 kHz) is high enough not to generate any significant migration of ions. The insignificance of the ionic effects comes from the loss of the cell and the frequency dependence of the permittivity. This is explained in more detail in Chapter 5. The variation of the responses as a function of temperature can only be related to the variation of the rotational viscosity (see the top part of Figures 4.4 and 4.5).

Comparing the bottom part of Figures 4.4 and 4.5, the relation between the

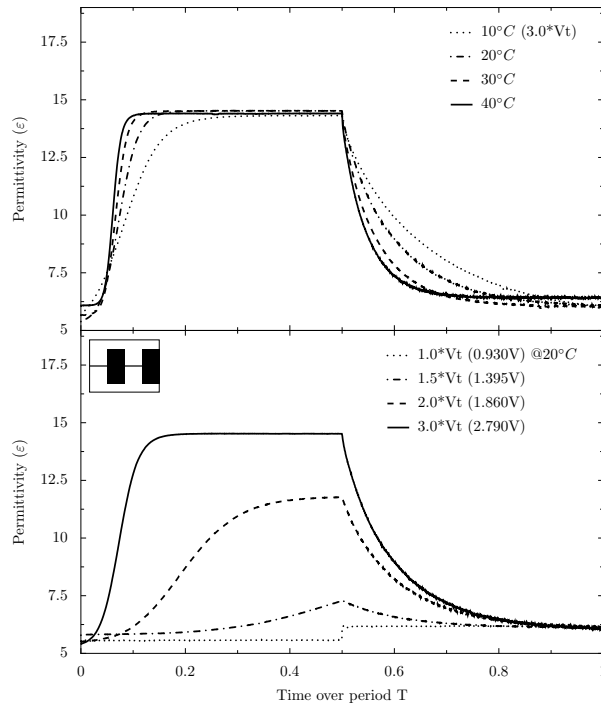


Figure 4.4: Measure of permittivity in the thick planar E7 cell with the AM signal as a function of temperature (top) and as function of the applied voltage (bottom)

4.2. Experimental results

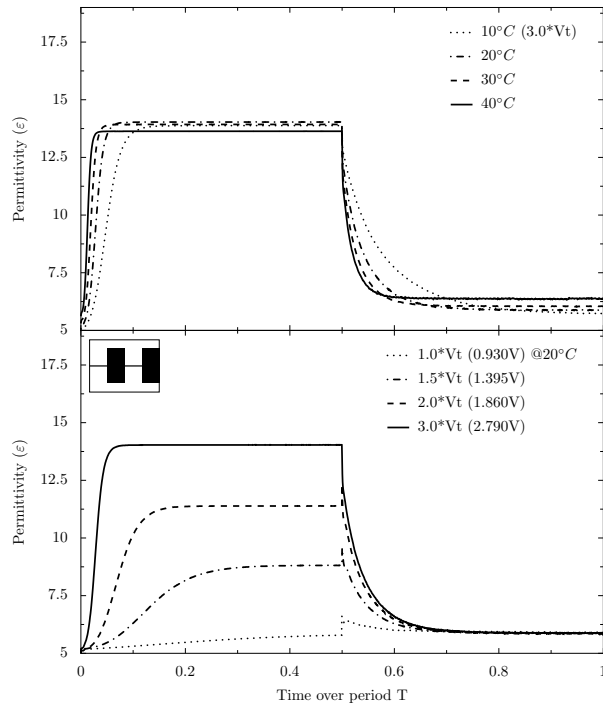


Figure 4.5: Measure of permittivity in the thin planar E7 cell with the AM signal as a function of temperature (top) and as function of the applied voltage (bottom)

rising time as well as the relaxation phase with the thickness (d) can be observed. They are both faster in the thinner sample illustrated in Figure 4.5. The rising time for an applied voltage of three times the threshold voltage ($3 \times V_t$) in the thick cell is occurring at $0.2T$ whereas for the thin cell it occurs at $0.08T$. The relaxation phase is $0.4T$ for the thick cell and only $0.2T$ for the thin cell. Observing the top part of Figures 4.4, 4.5 and 4.6, especially the relaxation phase, a relation between the temperature and the rotational viscosity can be seen if the elastic constants are considered not to vary with the temperature.

By comparing now the same thickness cell but with different orientation (planar and HAN) it is possible to observe that the rise time is much shorter for the HAN cell (see bottom part of Figure 4.6) compared to the planar orientation. The relaxation phase is similar for both orientations. The other observation is about the different values of permittivity reached after the rise time or the relaxation phase, this is due only to the geometry of the samples. The same kind of observations can be made between the two geometry cells filled with the

4.2. Experimental results

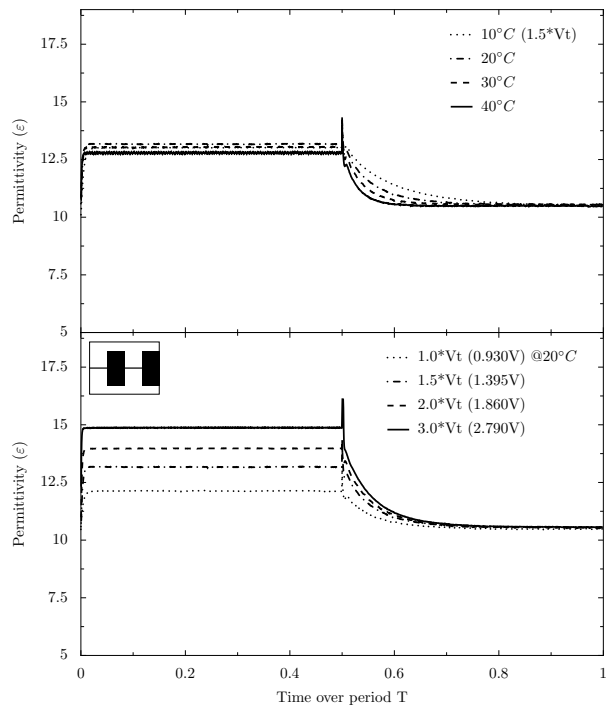


Figure 4.6: Measure of permittivity in the thin HAN E7 cell with the AM signal as a function of temperature (top) and as function of the applied voltage (bottom)

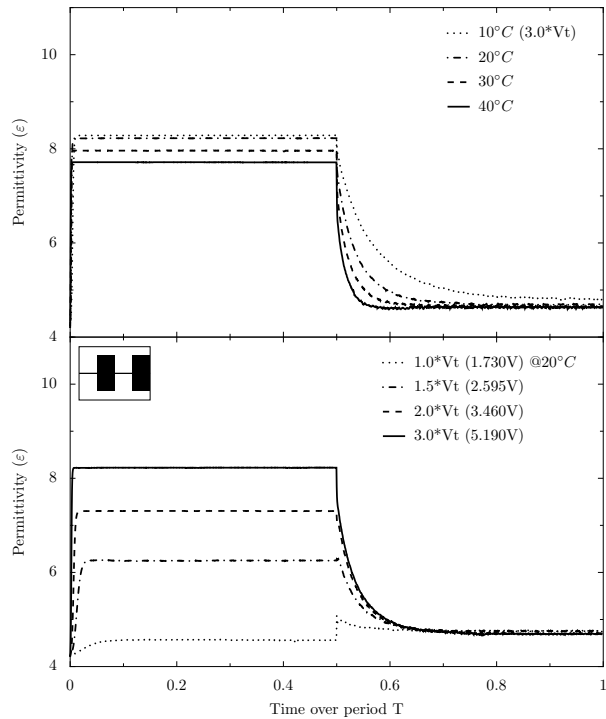


Figure 4.7: Measure of permittivity in the thin planar TL216 cell with the AM signal as a function of temperature (top) and as function of the applied voltage (bottom)

4.2. Experimental results

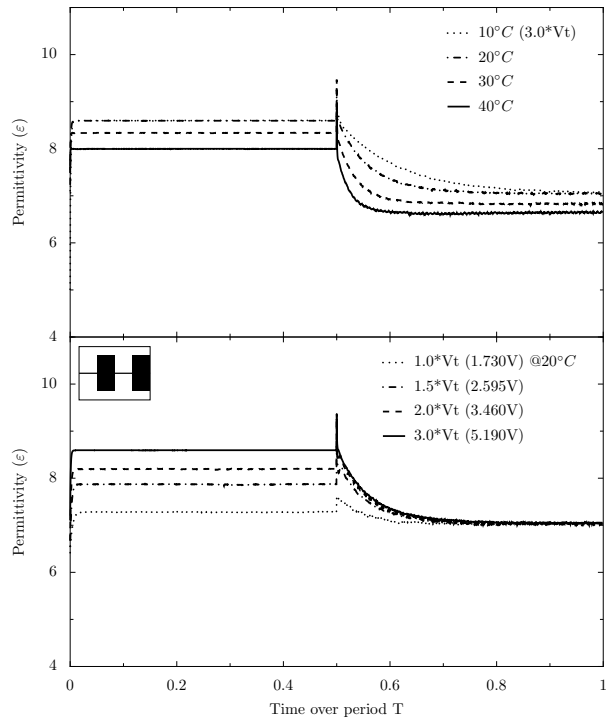


Figure 4.8: Measure of permittivity in the thin HAN TL216 cell with the AM signal as a function of temperature (top) and as function of the applied voltage (bottom)

low ionic material (TL216) as the cells of similar thickness filled with highly ionic material (E7) (see Figures 4.7 and 4.8). The rise time can not be compared between the different materials from the different Figures, this is due to the fact that the applied voltage is also higher because it is a function of the transition voltage which is higher for TL216 (1.730V at 20°) as compared to E7 (0.930V at 20°).

However, the relaxation time gives information about the rotational velocity (γ_1) of TL216. Considering that the elastic constants of the two materials are of the same order of magnitude (see Table 4.1) as well as the thickness and the relaxation time being similar; the rotational velocity should also be nearly identical.

4.2. Experimental results

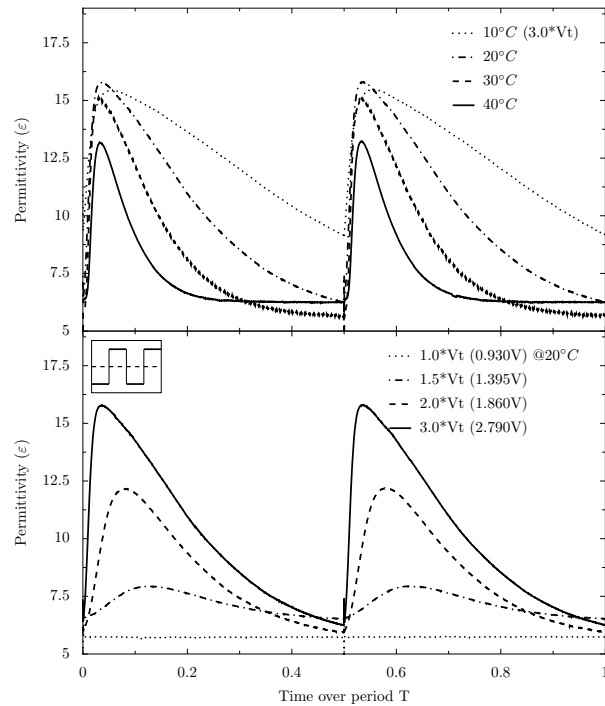


Figure 4.9: Measure of permittivity in the thick planar E7 cell with the SQ signal as a function of temperature (top) and as function of the applied voltage (bottom)

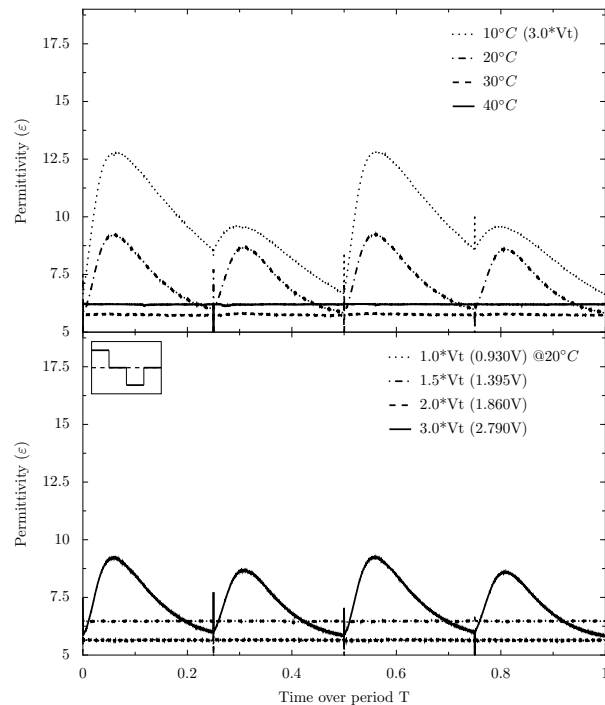


Figure 4.10: Measure of permittivity in the thick planar E7 cell with the PoNo signal as a function of temperature (top) and as function of the applied voltage (bottom)

4.2.2 Investigation of the ionic contamination and effects

Ionic effect in E7

The signal applied now is a square signal (SQ) with a period of 5 s illustrated in Figure 4.2. In the presence of free charge carriers in the material, this quasi-continuous signal should generate a migration of ions toward the electrode of the opposite sign. The build-up of ionic charge concentration as a layer over the ITO electrodes creates a surface charge density which tends to cancel out the applied signal. As a result of this effect, a reorientation of the director should be observed as a decrease of the permittivity during the positive or negative continuous half period. In Figure 4.9, during both periods the permittivity is showing a sharp increase during a short period followed by a slow decay. As a function of voltage (bottom part of Figure 4.9), the reorientation is nearly completed in the half period, the value of permittivity being virtually equal to the value of the perpendicular permittivity (see Table 4.1). At the top of Figure 4.9, it is possible to observe the evolution of this phenomenon as a function of temperature. In Figure 4.4 in the previous Section 4.2.1, the rotational velocity is suspected to vary with temperature as the relaxation phase become shorter as the temperature increases. It appears to be the same here but there are other parameters to take into account such as the concentration of the ions in the sample and their mobility. The shielding occurs earlier and stronger as the temperature increases which reveal that the ionic properties increase as well. It is important to note that when the applied signal change signs, the voltage experienced by the material within the cell is not similar to the one provided by the waveform generator. The ions are at the end of the half period plated on the electrode of the opposite sign of the charge they carry. When the signal suddenly changes, and before the ions start dispersing and migrate toward the opposite electrode, the material experiences the applied voltage and also the potential generated by the ions. This kind of approach has been illustrated in the assumptions made in

Section 3.6.1 and shown by the solid line in Figure 3.11(b).

It is hard to see the contribution of the free charge carriers with a square (SQ) signal. To reveal the ionic effect, another signal was applied to the same sample, PoNo. It is important to keep in mind that the signal PoNo is null during the second and fourth quarter of period T as represented in Figure 4.3. The results of the high ionic concentration material in the thick cell shows a similar response as the square signal one (see Figure 4.9), the decay reveals, in the first and third quarter of the period, the shielding of the applied signal by the charge build-up of the ions of the surface of the electrodes. On the top of Figure 4.10 at 10°C and at 20°C , it is important to notice that a second small response occurs when the signal goes from a positive or negative value to the null state. It behaves as if a second voltage was applied. The explanation can be found in the ionic migration which shields the external applied signal but acts like an internal signal when the external signal is removed. As the temperature increases the response from the material becomes similar for the external signal and the ionic induced field before both effects disappear completely at higher temperatures, which also means at higher levels of ionic concentration. At 20°C the reorientation produced by the waveform generator is similar to the one induced by the field whereas at 10°C it appears to be only half the size. At higher temperatures the concentration appears so high that it completely cancels any possible reorientation from the applied signal. Also at the bottom of Figure 4.10 the only voltage which induces a response is three times ($3 \times V_t$) the threshold voltage.

Applying the same signal to a thinner sample with similar geometry and filled with the same material can give information about the behaviour of the ions. Which regards to mobility as the sample is more than four times (4.4) thinner, the free charge carriers had less distance to cover from one electrode to the other. The other information extracted from these new measures is that the concentration of ions was not changed, being the same material in the cell, but that their number is also reduced by more than four times. To have appreciable results as

4.2. Experimental results

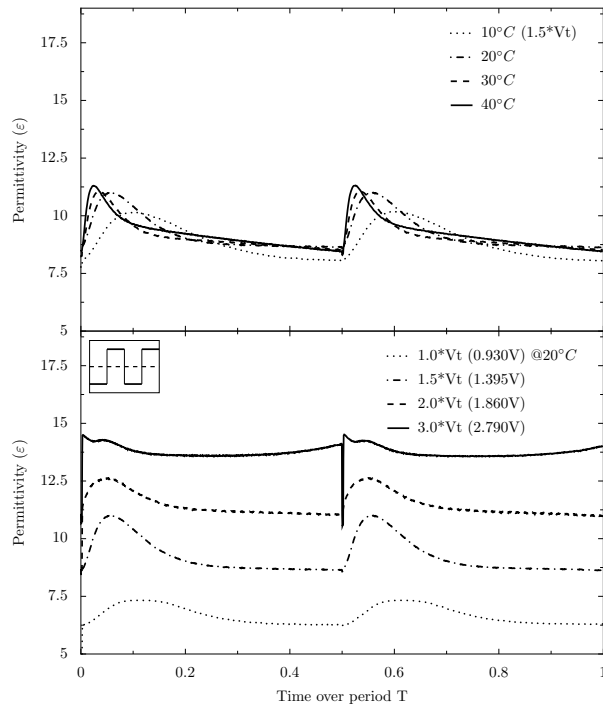


Figure 4.11: Measure of permittivity in the thin planar E7 cell with the SQ signal as a function of temperature (top) and as function of the applied voltage (bottom)

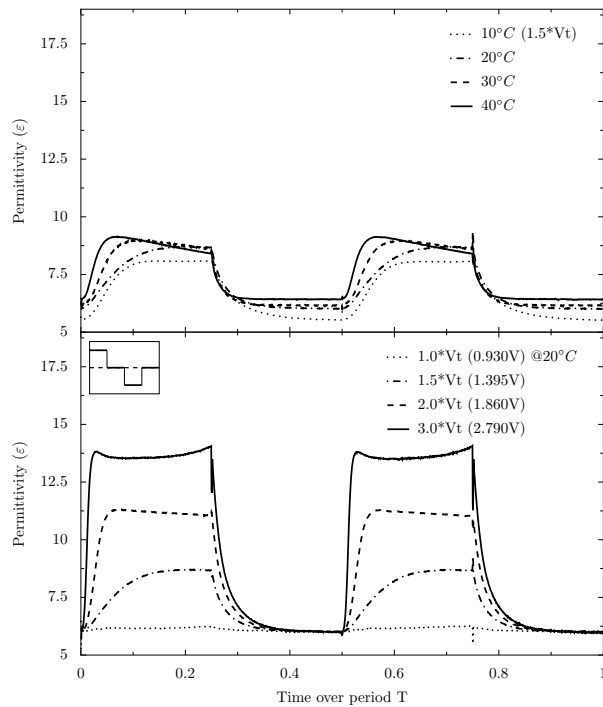


Figure 4.12: Measure of permittivity in the thin planar E7 cell with the PoNo signal as a function of temperature (top) and as function of the applied voltage (bottom)

4.2. Experimental results

a function of the temperature, the voltage applied on the cell has been reduced, it is now one and a half the threshold voltage ($1.5 \times V_t$). Similar behaviour can be observed in the thin cell with the square signal (see Figures 4.11 and 4.9) but the shielding is not complete as the measured permittivity is not equal to the perpendicular permittivity, so there is not a total reorientation to the resting position. As with the PoNo signal (see Figures 4.12 and 4.10), the number of ions is not large enough to build up a electric field capable to generate a response from the nematic material.

By comparing the results from the square signal in Figure 4.11 and in Figure 4.9, especially when the relaxation phase starts, it is possible to note that the mobility of the ions dictates when the reorientation happens.

Ionic effect in TL216

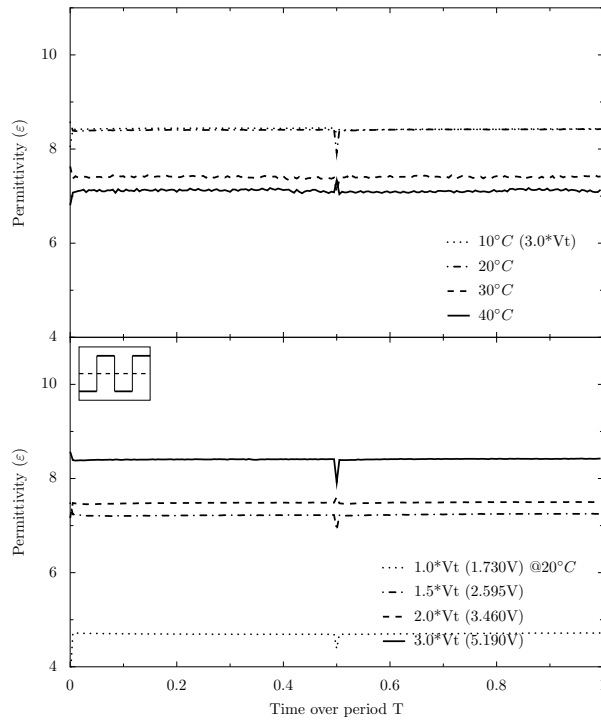


Figure 4.13: Measure of permittivity in the thin planar TL216 cell with the SQ signal as a function of temperature (top) and as function of the applied voltage (bottom)

Applying the square signal onto a thin sample filled with TL216, low ionic

4.2. Experimental results

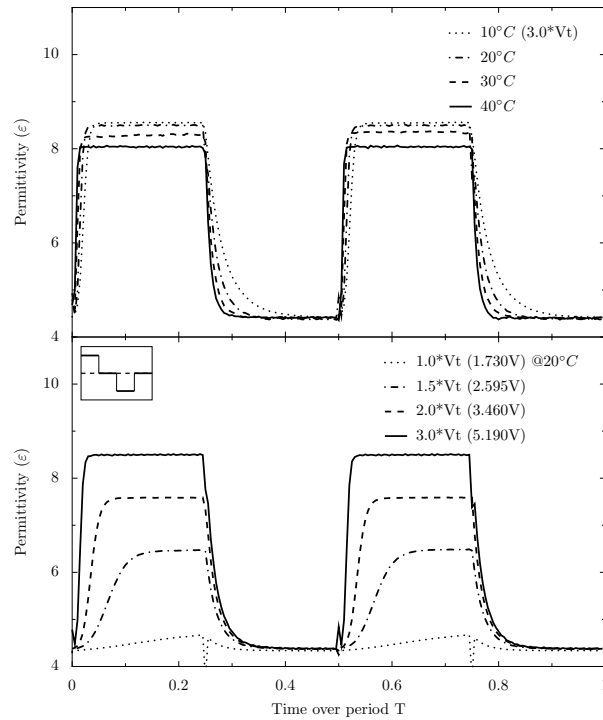


Figure 4.14: Measure of permittivity in the thin planar TL216 cell with the PoNo signal as a function of temperature (top) and as function of the applied voltage (bottom)

material, it is noticeable that the value of the permittivity does not change as a function of time. Also it appears insensitive to the orientation of the applied voltage (see Figure 4.13: Bottom half). The first conclusion which could be drawn is that the material contains virtually no ions. It is also possible to observe the evolution of the permittivity value as a function of the temperature (see the top of Figure 4.13). The discontinuity at the beginning and middle of the period are only artefacts due to the lock-in amplifier losing the reference signal when the overall sign of the voltage is changing.

The planar thin cell with low ionic material TL216 shows identical responses to the PoNo signal (see Figure 4.14) as the AM signal (see Figure 4.7). This result supports the idea that TL216 contains virtually no ions. The other conclusions which can be extracted from this part of the experiment is that the evolution of the rotational viscosity and the permittivities occur as a function of temperature (see top of Figure 4.14).

4.2.3 Investigation of the flexoelectric effect in E7 and TL216

Flexoelectric effect in E7

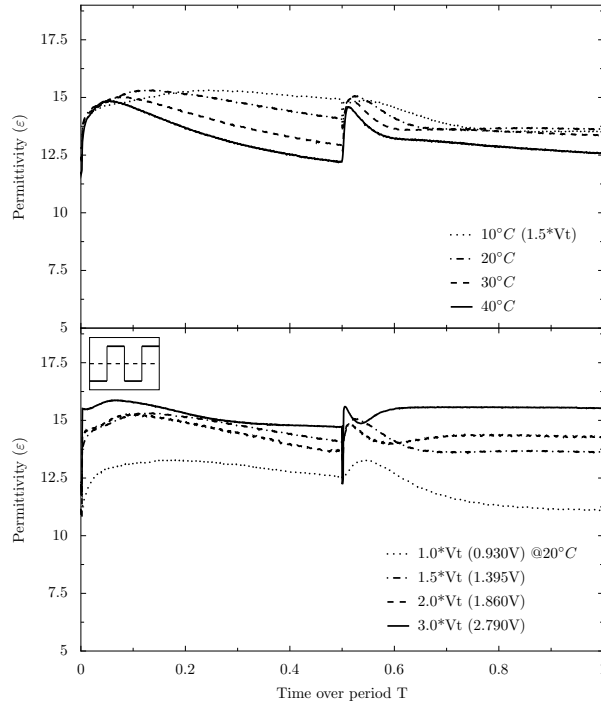


Figure 4.15: Measure of permittivity in the thin HAN E7 cell with the SQ signal as a function of temperature (top) and as function of the applied voltage (bottom)

In Figure 4.15, the applied signal was positive during the first half of the period and negative during the second half. The first characteristic of the measure of permittivity is the different response of the material at different orientations of voltage; this indicates flexoelectric properties. The material used here is E7, the sum of flexoelectric coefficients being determined to be equal to $15 \pm 2 \text{ pC.m}^{-1}$ (see Table 4.1) in Chapter 3 [66, 97–99]. It can also be noted that there is a shielding due to ions in the material but as it already be observed in Figure 4.11 which partially only cancel the applied signal.

When the PoNo signal is applied to the same sample (see Figure 4.16), it is still possible to see the asymmetric response from the material which supports the idea of a flexoelectric effect. But as already pointed out the ions were not in large

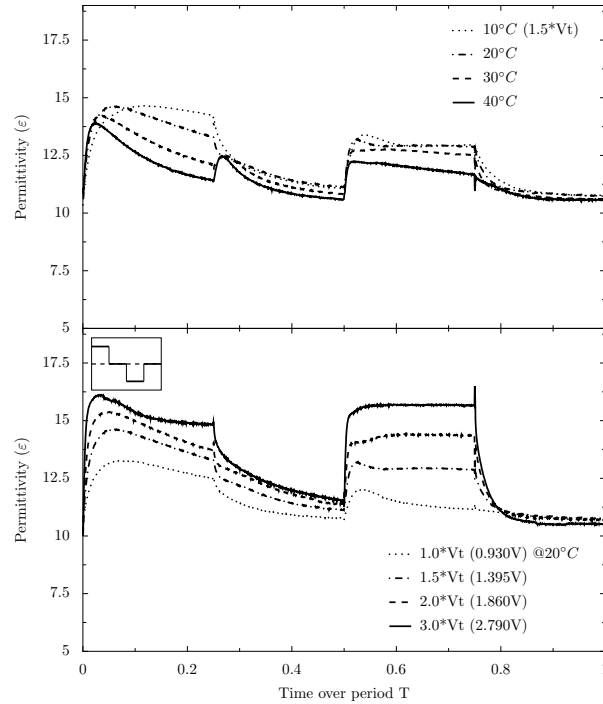


Figure 4.16: Measure of permittivity in the thin HAN E7 cell with the PoNo signal as a function of temperature (top) and as function of the applied voltage (bottom)

enough numbers to produce an induced voltage capable of generating a response from the liquid crystal material contained in the cell. However, at the top of Figure 4.16, at the highest temperature (30°C and 40°C) when the signal goes from a positive to a null value, the liquid crystal seems to be experiencing an induced voltage. This voltage disappears as quickly as the ions disperse in the material so any conclusion about the possible orientation of this induced signal is virtually impossible to achieve. To get a possible answer, this experiment should be reproduced on the same cell geometry but a thicker cell where it seems the free charge carriers are in large enough numbers to induce a voltage capable to generate a response from the material as illustrated in Figure 4.10.

Flexoelectric effect in TL216

Contrary to the asymmetry which has been observed in the E7 filled HAN cell, illustrated in Figure 4.15, the thin HAN cell filled with TL216 under a square

4.2. Experimental results

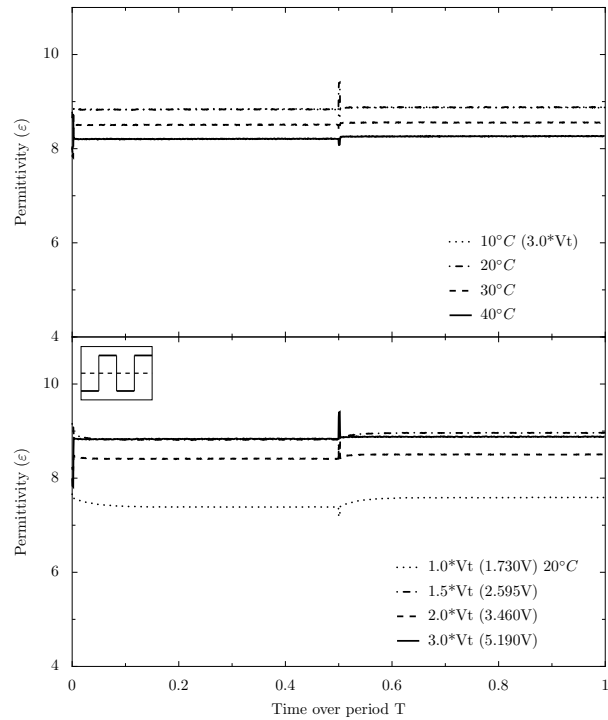


Figure 4.17: Measure of permittivity in the thin HAN TL216 cell with the SQ signal as a function of temperature (top) and as function of the applied voltage (bottom)

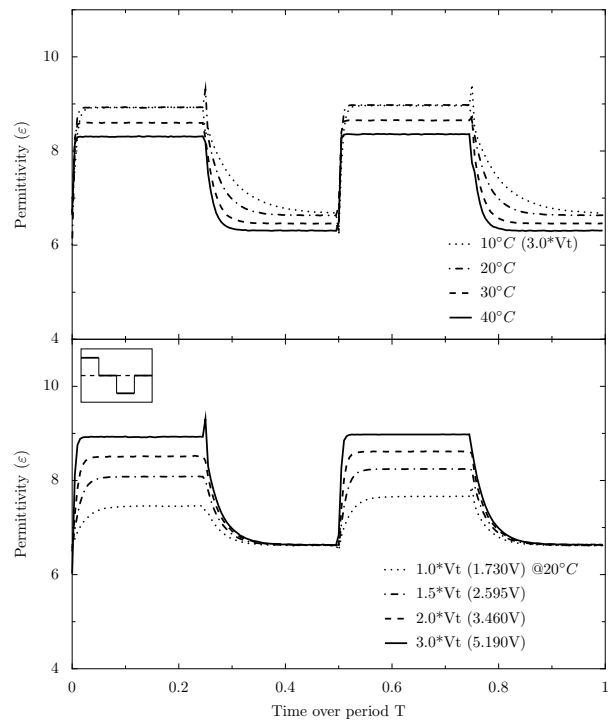


Figure 4.18: Measure of permittivity in the thin HAN TL216 cell with the PoNo signal as a function of temperature (top) and as function of the applied voltage (bottom)

signal does not show large asymmetry. Nevertheless in the bottom of Figure 4.17 at low voltage ($1.0, 1.5$ and $2.0 \times V_t$) a small variation of the permittivity can be notice. This support the idea of a very small sum of flexoelectric coefficients ($e_1 + e_3$), as shown in Table 4.1. It is also to notable that is not possible to observe this characteristic when the cell in submitted to the PoNo signal, as shown in Figure 4.18.

4.2.4 Other observations during the transient capacitance investigation

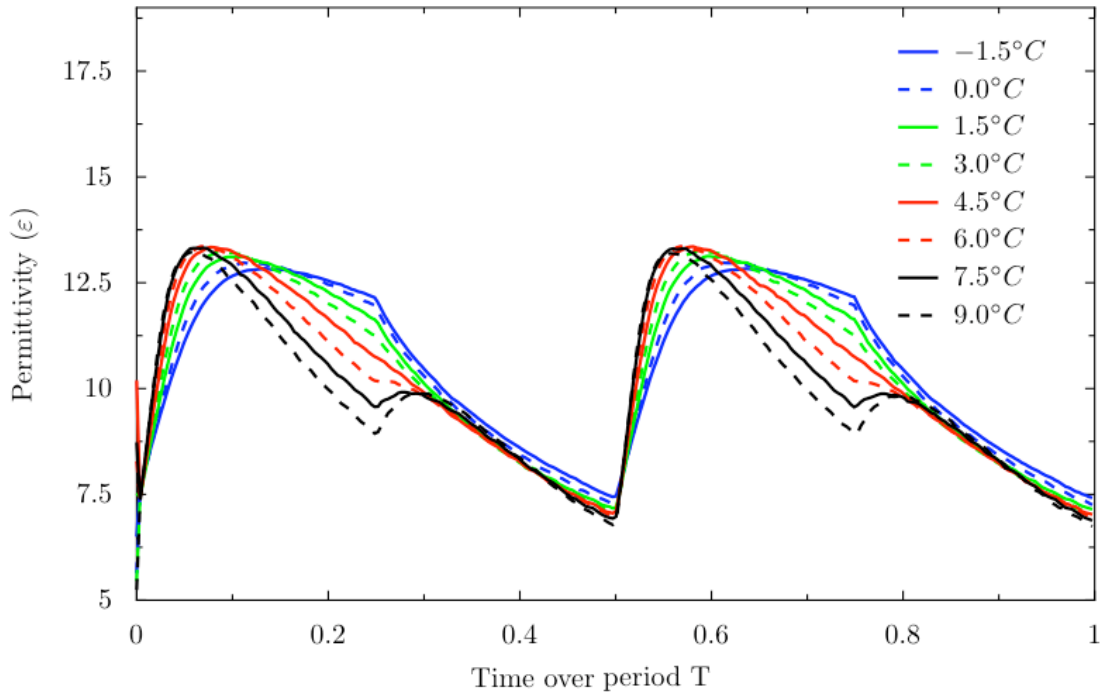


Figure 4.19: Results for the investigation of the evolution of the ion effect at low temperatures on a thick ionic planar cell

Aside from the main investigation done in Section 4.2.2 (thick planar cell filled with E7), an interesting behaviour of the permittivity at low to very low temperatures close to the solid-nematic transition temperature was observed. The rotational viscosity increased, which is shown in Figure 4.19, by a longer rising time. Another aspect can be observed which supports the hypothesis raised in

Section 4.2.2 (thin planar cell filled with E7), which is that the concentration is low enough to not be able to totally shield the external applied signal and also too low to build a large enough internal field to get any response from the liquid crystal. It appears that the critical temperature for this cell geometry, thickness and material is around 4.5°.

4.3 Modelling and fitting

To corroborate the experimental data with the continuum theory for nematic liquid crystal in 2 dimensions, the use of a modelling program was required. This has also been done in Chapter 3, Section 3.6. This model's results which can be seen in Figure 3.18, use an anti-parallel planar geometry with a square wave signal. It is important to note that the evolution of the permittivity in this case is similar to that which can be observed in the experimental data in the bottom part of Figure 4.9. The sharp rise is followed by the decay (suspected to be induced by ionic shielding), which confirms the observations made during this investigation. Unfortunately the model considers the ions in the material to be point like and not having dimensions. The shielding is not modelled as the experimental work might suggest. Another limitation of the model was dealing with a too large numbers of ions within the sample. No further investigations were achieved to look at different materials or geometry. The modelling work was primarily to support the assumptions made in Section 3.6.

4.4 Conclusion

This investigation gives results on the flexoelectric and ionic effects in two different nematic materials. The ionic effect has been shown in E7 with quasi continuous signals (SQ and PoNo). The first of these signals gave information on the flexoelectricity the liquid crystal may have. The second one (PoNo) shows that if

4.4. Conclusion

the ions are in large numbers they can create an induced voltage sufficient to generate a response from the nematic material when an external signal has been removed. Temperature is also an important factor in the production of ions from a material with high dielectric anisotropy. No further modelling has been done due to the difficulty of properly reproducing the behaviour and characteristics of the free charge carriers contained in the material.

Chapter 5

Effects of ionic contamination and flexoelectricity on the Fréedericksz transition

5.1 Principle

Originally observed by R. Meyer in 1969 [27] it was first explained as the relation between the distortion of the director and an electric polarisation in the liquid crystal due to permanent electric dipole and asymmetric shape [28–32]. Subsequently it has been suggested that flexoelectricity has an effect on the Fréedericksz transition in homogeneous nematic liquid crystal, whatever, the external source applied to reorient the director [84, 100]; either magnetic [32] or electric [101]. More recently, it has been suggested that the flexoelectric polarisation interacts with free charge carriers [74, 80]. The present experiment is designed to confirm the hypothesis presented theoretically by A. Smith et al.[74]. Electric fields interact with liquid crystals due to their electric susceptibility ($\chi_E \sim 10$) and dielectric permittivity ($\epsilon_r \sim 10$). The presence of polarisation in a liquid crystal sample can influence the electric field. With the opposite, liquid crystals at equilibrium virtually unaffected applied magnetic fields due to their diamagnetic susceptibility ($\chi_M \sim 10^{-5}$) and magnetic permeability ($\mu_r \cong 1$) [26]. The first approach was to use a material which has virtually no flexoelectricity nor ionic contamination and then increase the concentration of free charge carriers within the sample and observe the evolution of the Fréedericksz transition magnetically and electrically stimulated. The material used for this part of the investigation is TL216 [102] which is known to be non-ionic and does not display flexoelectric behaviour. To increase the concentration of free charge carriers, hexadecyltrimethylammonium bromide (or HmAB ($CH_3(CH_2)_{15}N(Br)(CH_3)_3$)) is added in specific quantities (1% mol.). The results of this first attempt in the investigation did not reveal the expected outcome due to the fact that the added component did not dissolve properly into the liquid crystal, and therefore no information about the evolution of the ionic concentration could be extracted. Another attempt was made using the same nematic liquid crystal (TL216 [102]) and mixing it with another nematic liquid crystal (E7 [57]) in a specific quantity (2% wt.). This was done in order to

bring ions and flexoelectricity into the sample as the later material is known to show those characteristics. Using this method, no promising results to support the theory were revealed and none of them will be presented in the following sections. The most interesting results were observed on an aged sample of the material E7 which had high ionic contamination and from literature studies is known to have high flexoelectric coefficients [58, 66, 67, 97–99].

5.2 Experimental setup

5.2.1 Magnetic field experiment

Experiment principle

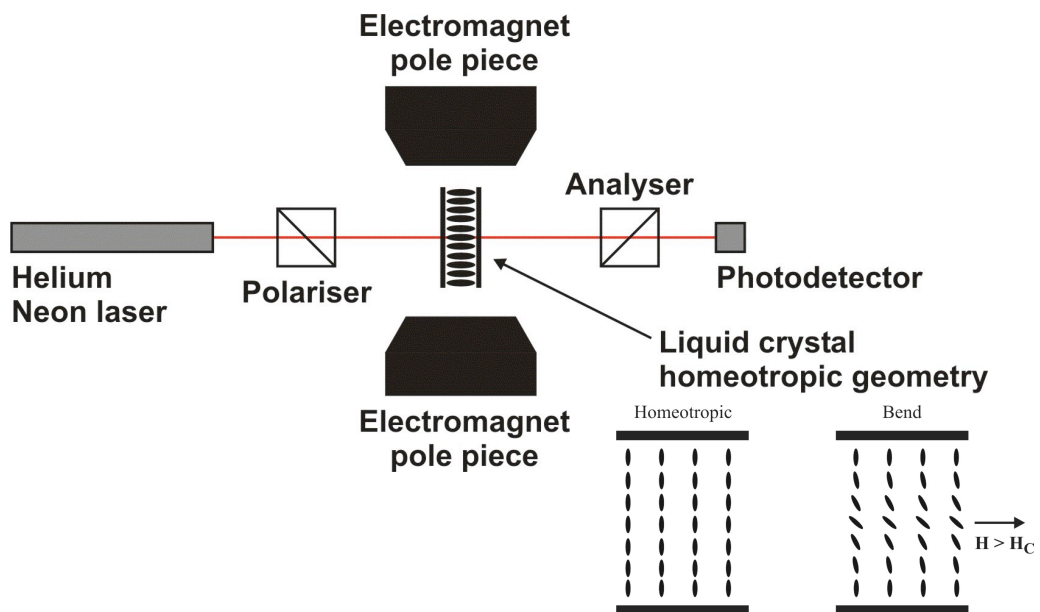


Figure 5.1: Experimental setup for the magnetic measure of bend distortion

To reorient liquid crystal using a magnetic field, the sample material needs to be in a uniform field of the correct orientation. Figures 5.1 and 5.2 show the set-up for the bend and splay distortions with a homeotropic and planar cell. The value of the elastic constants can be derived from the magnetic Fréedericksz

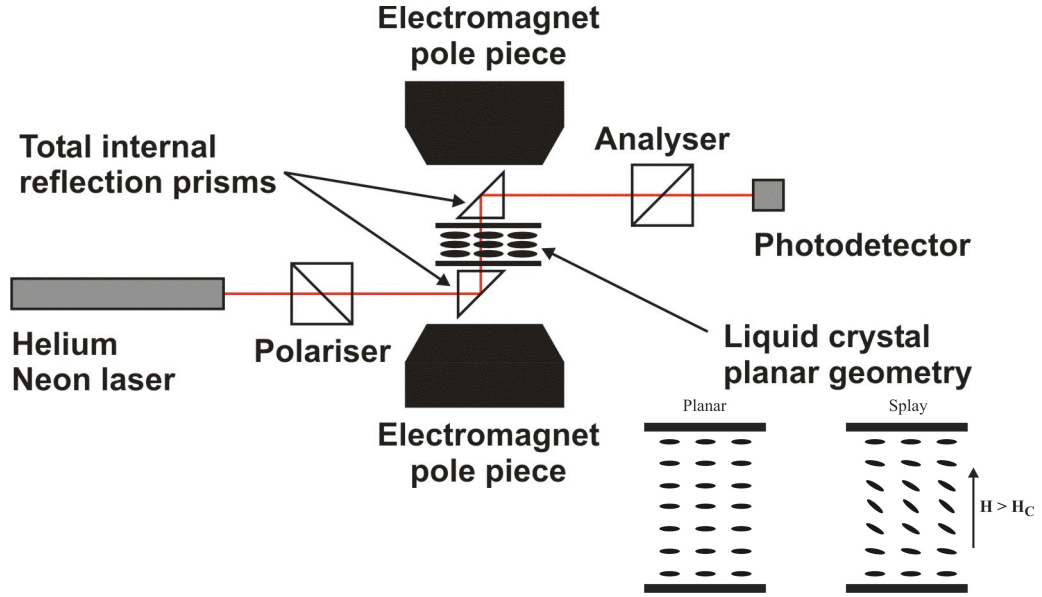


Figure 5.2: Experimental setup for the magnetic measure of splay distortion

threshold [26]:

$$H_c = \left(\frac{\pi}{d}\right) \sqrt{\frac{K_{xx}}{\mu_0 \Delta_\chi}} \quad (5.1)$$

The current, provided by the power supply (Model SCT-45-15 from KSM), running through the coil of the electromagnet (Model EM747 from Mullard), is recorded and can be related to the magnetic field via a calibration factor. This is determined using a Hall probe placed between the two poles and the magnetic field is calibrated for several values of current running in the coils (Data and regression analysis in Section A.3).

Magnetic determination of K_{11}

To determine the value of K_{11} a planar cell filled with the material to be studied is placed perpendicular to the magnetic field as shown in Figure 5.2. When the magnetic field is greater than the critical magnetic field, the director in the centre of the cell starts reorienting which creates splay distortions related to the K_{11} elastic constant. To detect when the angle of the director changes, a polarised laser beam is shone through the sample after being reflected perpendicular to the

sample by a total internal reflection prism which does not affect the magnetic field uniformity. The prisms are needed because ideally there would be holes in the pole pieces affecting the uniformity of the field. Another polariser and the photo-detector are present to detect any variation in the light transmission due to any variations within the sample characteristics. The two polariser are set at right angle orientation and are both 45° to the liquid crystal director. The transmission is determined by the Equation 5.2 [9–13] where I is the intensity of the beam at the photo-detector, I_0 the intensity without the liquid crystal, Δn is the optical anisotropy of the liquid crystal material, d is the thickness of the cell, λ is the wavelength of the beam and α is the angle between the orientation of the first polariser and the orientation of the liquid crystal director.

$$I = I_0 \sin 2\alpha \sin^2 \left(\frac{\pi \Delta n d}{\lambda} \right) \quad (5.2)$$

Magnetic determination of K_{33}

Based on the same principle of the determination of K_{11} , the investigation of K_{33} only differs in the sample geometry which is now homeotropic. Also the orientation between the electromagnet poles, is placed along the magnetic field as shown in Figure 5.1. When the magnetic field is over the critical value, the distortion generated is the bend one in relation to the K_{33} elastic constant. These orientations for the determination of the elastic constants were used because the material investigated (E7) possesses a positive diamagnetic anisotropy ($\Delta\chi > 0$).

5.2.2 Electric field experiment

Experiment principle

To measure permittivity, the measurement of the static capacitance is achieved using an Agilent 4284A LCR meter. The cell is placed into a temperature controlled device, Linkam LTS350 driven by the controller Linkam TMS94, allowing

5.2. Experimental setup

the temperature to be controlled within $\pm 0.1^\circ \text{C}$ [103]

$$\varepsilon = \frac{C}{C_0} \quad (5.3)$$

Permittivity is related to the orientation of the director of the nematic liquid crystal, any variation of permittivity as a function of the applied voltage will be related to a reorientation of the director. When the applied voltage is over the critical or threshold value, the director orientation starts to change and a variation of permittivity is recorded. If the cell is planar, the distortion within the sample is a splay related to K_{11} .

$$V_c = \pi \sqrt{\frac{K_{11}}{\varepsilon_0 \Delta \varepsilon}} \quad (5.4)$$

From the equation 5.4, K_{11} can be determined if $\Delta \varepsilon$ is known. On the ideal plot in Figure 5.3, the evolution of permittivity value just above the threshold can also be related to the second elastic constant by the ratio $\frac{K_{33}}{K_{11}}$.

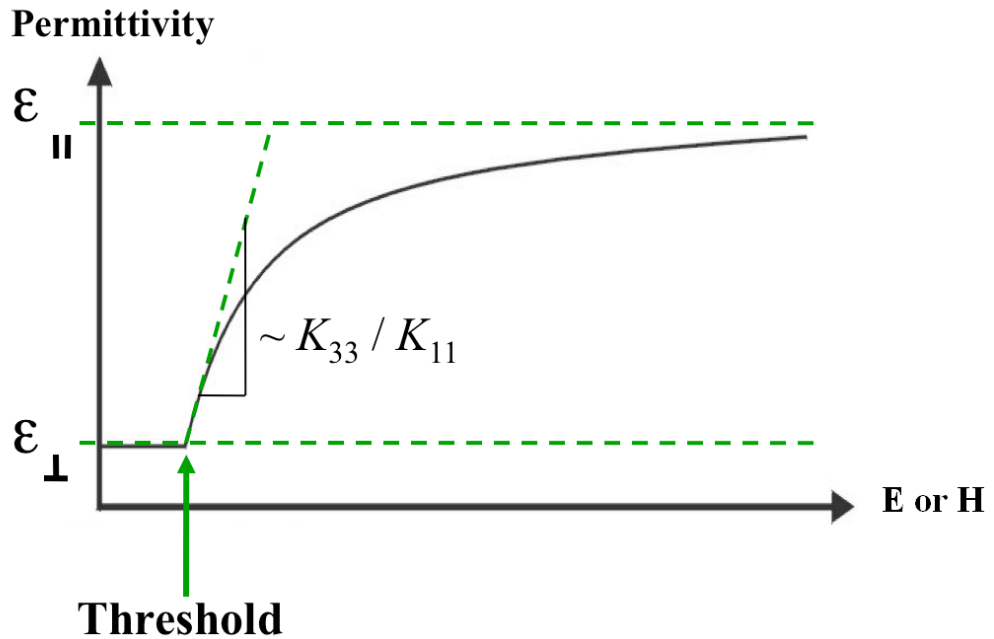


Figure 5.3: Idealised results for permittivity measurements

5.2.3 Experimental parameters

Frequencies

By studying the evolution of complex permittivity of a sample as a function of frequency, it is possible to reveal the loss behaviour of a material. At high values of frequency, the cell shows mainly plate capacitor characteristics acting like an electric circuit of an ideal capacitor and resistor. If low values of frequency are applied, the ionic material reveals more resistive properties due to free charge carrier motion. The loss rises at high and low frequencies with a characteristic $\frac{1}{f}$ dependence at low frequency.

Temperature

In the electric experiment the sample was placed in the temperature controlled stage. At the opposite, for experimental reasons, the control over the temperature could not be controlled and could rise over the time scale of the experiment. Each initial and final temperatures were recorded, if the deviation was more than 5°C over the room temperature the results were disregarded. The electric experiment was then set to the mean temperature to allow meaningful comparison.

Thickness

The thickness of the samples is 22 μ m, the electric determination of elastic constants is independent of the thickness but it can be noted in equation 5.1 that the strength of the magnetic field is inversely proportional to the thickness of the sample. A choice was made between 5 and 22 μ m samples, the thicker one was chosen as it allows measurements to be made just within the maximum field of 0.5 T provided by the electromagnet with pole pieces at 35 mm spacing. Both thicknesses have been used for the electric signal to look at properties related to the size of the nematic layer.

5.3 Experimental results

5.3.1 Magnetic determination of elastic constants

Splay elastic constant K_{11}

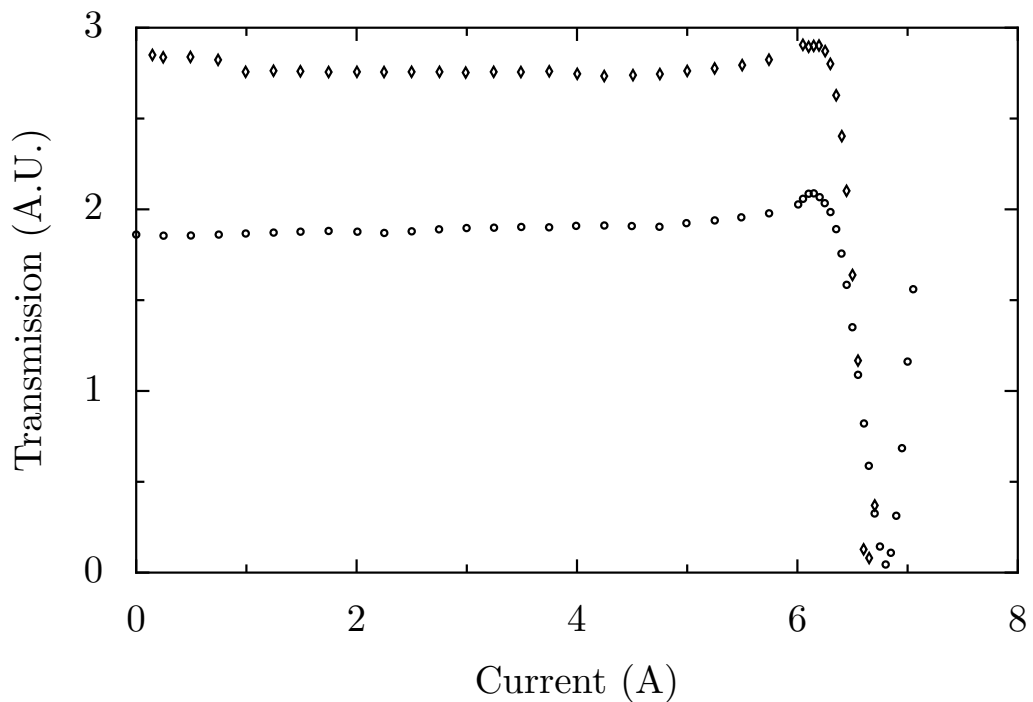


Figure 5.4: Experimental results for K_{11} determination

The determination of K_{11} using magnetic fields gives consistent results for two repeated measurements, this can be observed in the Figure 5.4. The reorientation of the director is revealed by a change in the transmittance of the sample measure by a variation of magnet current which occurs around 6.25 ± 0.08 A for this particular sample filled with nematic liquid crystal E7 [57] containing ions and presenting flexoelectric behaviour. No calculations were done using the equation 5.1 since $\Delta\chi$ is unknown, the value of K_{11} will be determined instead using the electric signal. The current running through the coils was not converted in magnetic field for reasons discussed in Section 5.3.3. In Figure 5.4, the transmission value is nearly constant up a current of 6 A but several attempts show variation due to a misalignment of the cell or a large temperature variation. When the

variation was too large the results were disregarded.

Bend elastic constant K_{33}

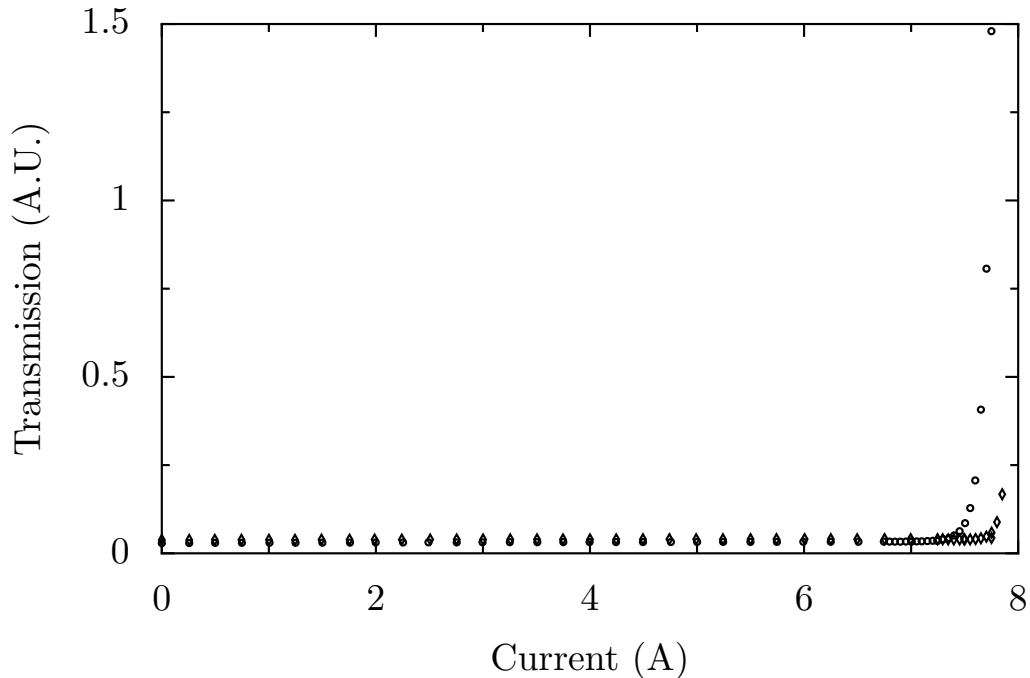


Figure 5.5: Experimental results for K_{33} determination

The setup of this experiment (see Figure 5.2) has many variables that may affect the final results. The orientation of the cell is 45° to the vertical and also the setup requires the use of two total internal reflection prisms. The set up of the experiment makes it harder to get the sample at the exact orientation every time. The two results in Figure 5.5, are the best achievable and give a threshold current of 7.37 ± 0.15 A. Only the circle measurements were kept, the second set represented by diamonds in Figure 5.5 were only done to confirm the values but the temperature recorded was too high. Also this experiment raises awareness of the fact that large electrical currents running through coils generate a lot of heat, which was difficult to control.

5.3.2 Electric determination of elastic constants

Permittivity vs. applied voltage

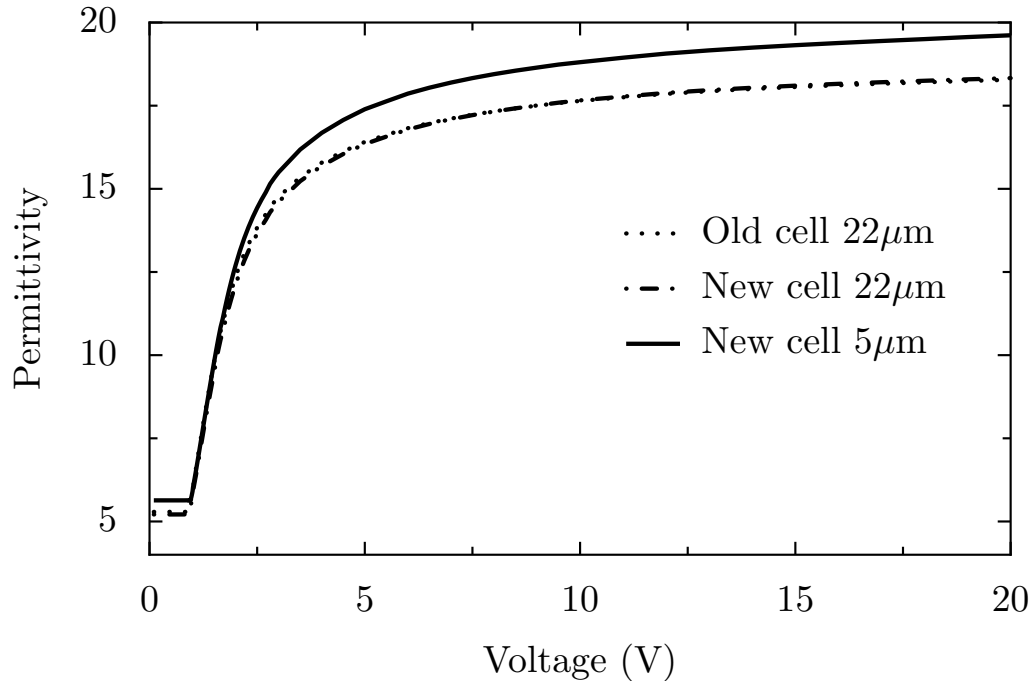


Figure 5.6: Permittivity comparison between old and new sample and different thickness'

From the applied signal, the value of the threshold voltage is around 0.93V for the 5 and 22 μm cell as expected. What is also interesting to note is the difference between the thick (22 μm) and the thin (5 μm) cells at high voltage which may be exacerbated by having non-infinite surface anchoring. If the section around the threshold value is expanded and if only the two thick cells (old & new) are plotted as shown in Figure 5.7, it is interesting to observe that, a slight difference occurs. The difference is only noted above the Fréedericksz transition and not under it or towards high values of applied signal. The old cell was used a lot and often with D.C. voltage applied, it is thought that the ionic concentration might have been altered and become higher with time from ionic dissociation. The effect suspected is an ionic screening on the transition. The opposite movement will be the flexoelectric stiffening.

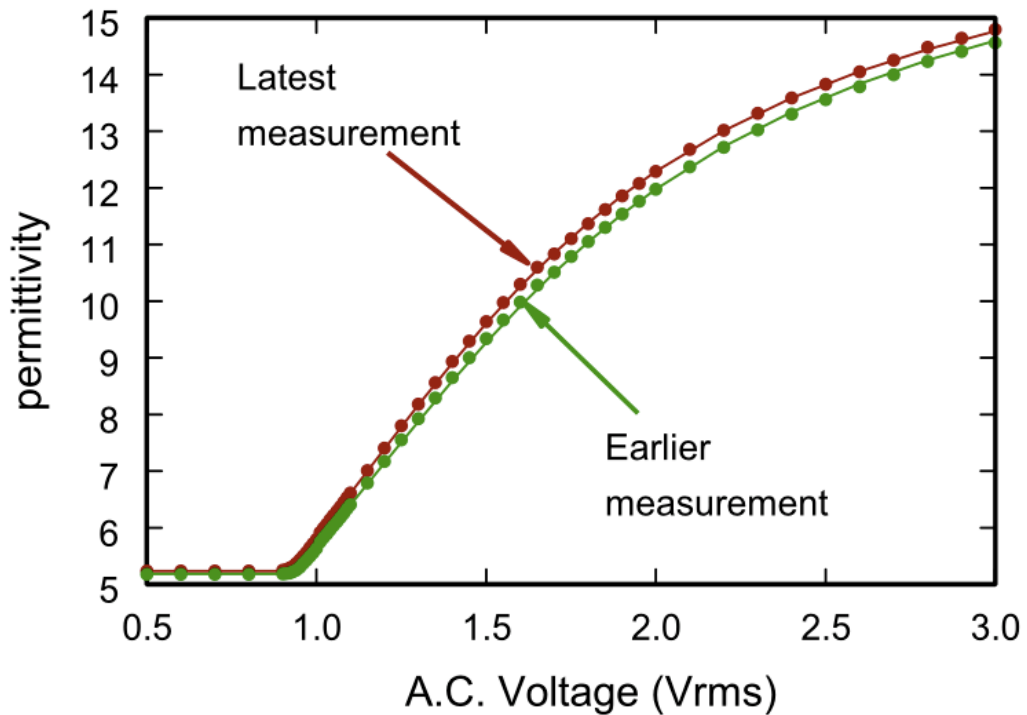


Figure 5.7: Permittivity comparison between old (latest measurement) and new (earlier measurement) sample of $22\mu\text{m}$, the solid line is the fit for each cell

Permittivity vs. frequency

To investigate the idea of ionic dissociation in an aged cell, the measure of permittivity is done as a function of the frequency applying a signal below the transition or critical value of 0.1 V rms. The loss represented by the dashed lines in Figure 5.8 gives information about the conductivity of the cell. At high frequencies the cell is behaving like a plate capacitor and a resistor; and as the frequency is increased the loss does the same. It is of note that at high frequency that both cells show similar response. More interestingly is that at low frequency, the new cell shows a lower conductivity compared to the later measurements done with the old cell. This discovery supports the idea that there are more free charges carriers in the old cell than in the new one. Both results show $\frac{1}{f}$ dependence which is expected for a “leaky capacitor”.

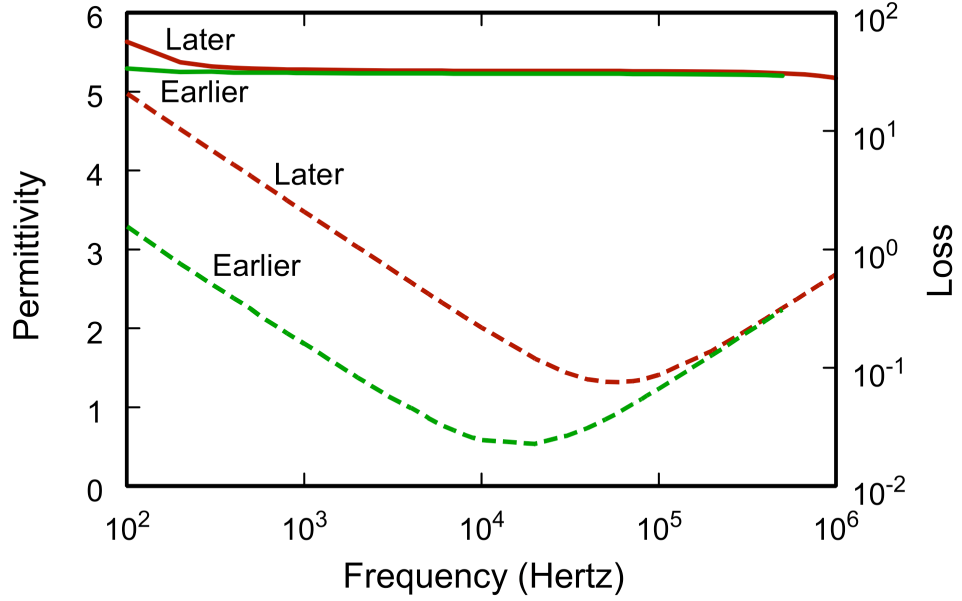


Figure 5.8: Permittivity (solid line) and loss (dashed line) as a function of the signal frequency for E7 material in old (later) and new (earlier) cell

5.3.3 Analysis and comparison of K_{33}/K_{11} from different methods

Analysing the results from the magnetic measures, will use equation 5.1.

For a splay distortion:

$$H_{c1} = \frac{\pi}{d} \sqrt{\frac{K_{11}}{\Delta\chi}} \propto I_{c1} \quad (5.5)$$

For a bend distortion:

$$H_{c3} = \frac{\pi}{d} \sqrt{\frac{K_{33}}{\Delta\chi}} \propto I_{c3} \quad (5.6)$$

Which leads to:

$$\sqrt{\frac{K_{33}}{K_{11}}} = \frac{I_{c3}}{I_{c1}} \quad (5.7)$$

Using the experimental results:

$$\frac{K_{33}}{K_{11}} = \left(\frac{I_{c3}}{I_{c1}}\right)^2 \Rightarrow \frac{K_{33}}{K_{11}} = \left(\frac{7.37 \pm 0.15}{6.25 \pm 0.08}\right)^2 = 1.4 \pm 0.1 \quad (5.8)$$

5.3. Experimental results

To analyse the results from the electric signal, the formulae it is based on is more complex because it needs to undergo a fitting using the linear nematic Fréedericksz theory.

$$\frac{V}{V_c} = \frac{2}{\pi} (1 + \gamma \sin^2 \theta_m)^{1/2} \int_0^{\theta_m} d\theta \left(\frac{(1 + K \sin^2 \theta)}{(1 + \gamma \sin^2 \theta) (\sin^2 \theta_m - \sin^2 \theta)} \right)^{1/2} \quad (5.9)$$

And also using:

$$\frac{\varepsilon}{\varepsilon_{\perp}} = \frac{\int_0^{\theta_m} d\theta \left(\frac{(1+K \sin^2 \theta)(1+\gamma \sin^2 \theta)}{(\sin^2 \theta_m - \sin^2 \theta)} \right)^{1/2}}{\int_0^{\theta_m} d\theta \left(\frac{(1+K \sin^2 \theta)}{(1+\gamma \sin^2 \theta)(\sin^2 \theta_m - \sin^2 \theta)} \right)^{1/2}} \quad (5.10)$$

Where:

$$V_c = \pi \left(\frac{K_{11}}{\varepsilon_0 \Delta \varepsilon} \right)^{1/2} \quad (5.11)$$

Also:

$$\gamma = (\varepsilon_{\parallel} - \varepsilon_{\perp}) / \varepsilon_{\perp} = \Delta \varepsilon / \varepsilon_{\perp} \quad (5.12)$$

And:

$$K = (K_{33} - K_{11}) / K_{11} \quad (5.13)$$

The two equations (5.9 and 5.10) are solved by using θ_m as a parameter for each voltage. By using a 1D model and considering the boundary region, it can be considered that the profile of θ_m across the cell for the applied signal just above the critical value $V > V_c$ can be written as $\theta_z \approx \theta_m \sin\left(\frac{\pi z}{d}\right)$ for $0 \leq z \leq d$ [78]. This can then be used to determine permittivity (ε) across the cell. Using the interval bisection method, V_c can be fitted first, which allow us to determine the values of K_{11} and $\Delta \varepsilon$. The determination of the ratio $\frac{K_{33}}{K_{11}}$, is achieved by finding a minima (also called “golden minima”). The final parameter is ε_{\parallel} to get the asymptote for large values of applied signal. The results of the fittings earlier and later ones can be seen in Table 5.1. It is important to note that the ratio $\frac{K_{33}}{K_{11}}$ in the two right columns is unchanged, the only important changed parameter is

Table 5.1: Results of fitting parameter for E7 material illustrated in Figure 5.7

Parameters	Fit 1 to earlier measurement	Fit 2 to earlier measurement	Fit to later measurement
K_{11}	11.2 pN	11.2 pN	10.9 pN
$\frac{K_{11}}{K_{33}}$	1.57 ± 0.06	1.40 ± 0.06	1.40 ± 0.06
K_{33}	17.6 pN	15.7 pN	15.7 pN
ε_{\perp}	5.18	5.18	5.23
$\Delta\varepsilon$	13.92	13.92	13.86
$e_{11}+e_{33}$	0.0 pC.m^{-1}	1.6 pC.m^{-1}	0.0 pC.m^{-1}

the value of flexoelectricity which is cancelled by the ionic screening.

5.4 Model results

The model was used only for the magnetic solution, none was done on the electric signal. Using the model provided by Dr. A.A.T Smith, some investigations were done to observe the behaviour of nematic liquid crystals and the effect on the Fréedericksz transition. In Figure 5.9, three curves can be seen, one which is the transition without any flexoelectricity or ions within the material. The second has only flexoelectric properties, a stiffening of the trend of permittivity just above the critical value of magnetic field can be observed. The last curve shows where ionic contamination has been added, the effect appears to be an ionic screening against the previous effect. The permittivity evolution just above the threshold is getting closer to the one without flexoelectricity and free charge carriers in the material. These observations generally support the idea of the effects of flexoelectricity above the threshold, but also show that ions can counterbalance this effect.

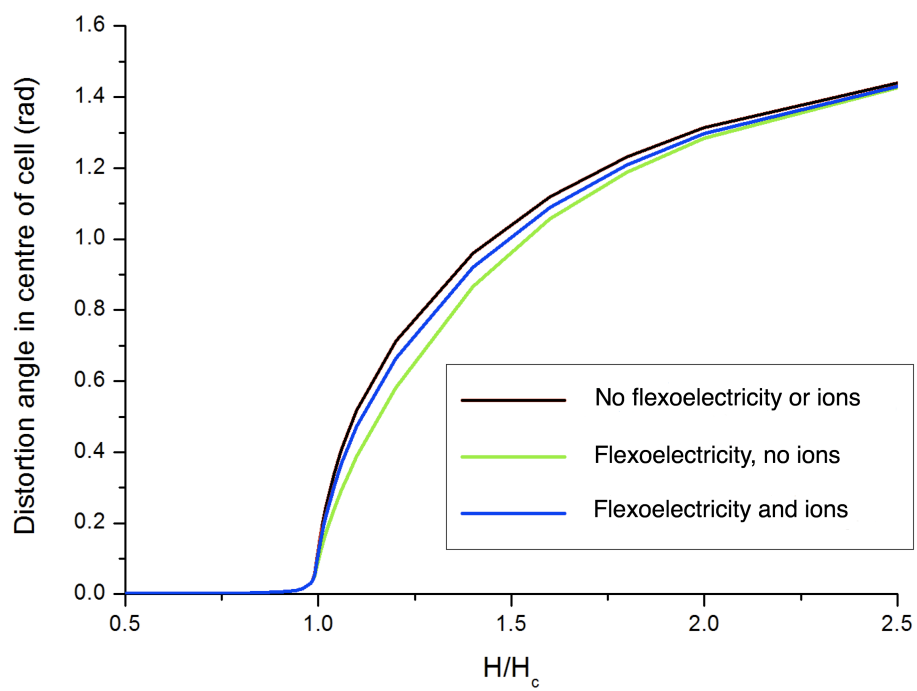


Figure 5.9: Theoretical results for the magnetic experiment highlighting the effect of flexoelectricity and ions on the Fréedericksz transition

5.5 Discussion and further work

From the results in Table 5.1 and Figures 5.7 and 5.8 it can be seen that in a nematic liquid material with flexoelectric properties, free charge carriers have an effect over the Fréedericksz transition. The comparison between E7 [57] as a new material which include a certain quantity of ions and the aged one which possesses a greater ionic concentration, shows a screening effect from the free charge carriers which tends to cancel the stiffening effect of the Fréedericksz transition due to the flexoelectric characteristic. This assumption is supported by the magnetic model, for future investigations a model based on the electric signal could bring a clearer answer to this conundrum.

Chapter 6

Bistability in nematic liquid crystals controlled by sidewall morphology

6.1 Principle of bistability

Zenithal or azimuthal bistable and multistable orientations are often induced by the surface morphology of the nematic liquid crystal cell [1, 5, 104, 105]. It can be generated by post [106], wells [107], a surface step [108], periodic gratings [109, 110], or surface grating generated by rubbing on a nanoscale [111, 112]. Bistability can be defined as a toggle switch which can stay in one of two stable positions without necessitating being held by an external source of energy [113, 114]. The principle makes it interesting for displays that are required to show static images without the requirement for an external source of power. All the above types of bistable geometries are called mechanical bistable display structures [113]. Some can be controlled by applying thermal or electric variations and these are called thermodynamical liquid crystal bistable systems. Recently, an increasing interest in bistable [115, 116] or multi-stable orientation [117] depending on the the surface profile has emerged regarding commercial uses of such a device [118].

The work conducted for this investigation is in support of a submitted publication [119]. This work consists of identifying, and quantifying the different defects and alignment states in a sawtooth geometry cell. The work also aims to establish if the defects do or do not reappear at the same location after thermal annealing. This is to check that they are only due to the geometry of the sidewall and not from pinning on any unwanted defect in the photo-resist resin used to produce the cell geometry.

6.2 Geometries of test cells

Usually the geometry of a bistable cell is created by engraving or depositing the structure onto one or both of the glass substrates which make up the sample. In this work the approach is different, in that the study is based on the effect of the sidewall as shown in Figure 6.1.

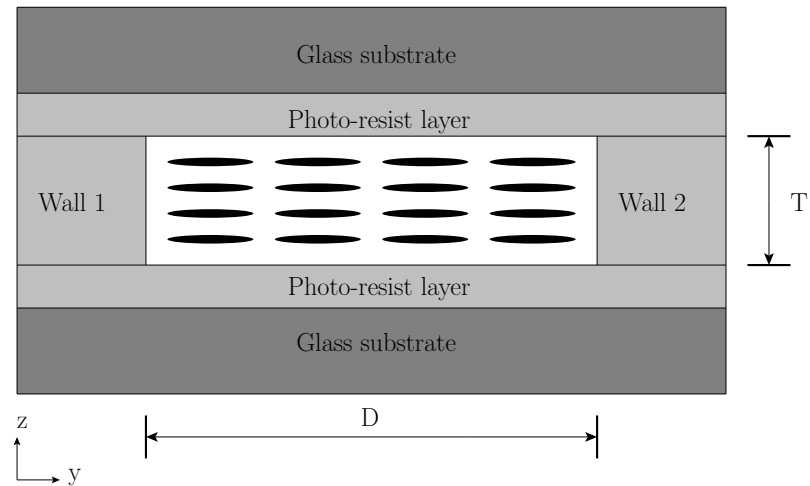


Figure 6.1: Schematic cross-section of sawtooth sample

The geometry of the samples can be classified into three categories. The first composed of two sawtooth in opposite phase (Figure 6.2), the second also of two sawtooth but in-phase (Figure 6.3) and the last of only one sawtooth facing a flat wall (Figure 6.4). The distance between the sawtooth mid-position is kept constant at $D=80\mu\text{m}$ and the thickness of the nematic liquid crystal is $T=15\mu\text{m}$. The height of the teeth is kept constant, $h=20\mu\text{m}$ and the pitch (p) varies from 10 to $100\mu\text{m}$. All the statistical investigations are done as a function of the pitch (p). The samples are filled with commercial nematic material E7 [57]. Due to

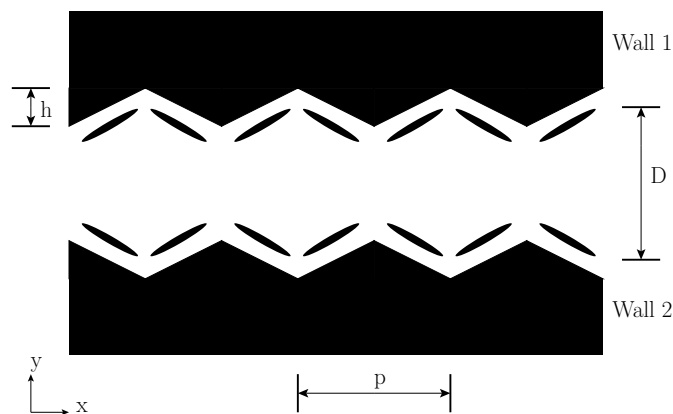


Figure 6.2: Schematic top view of anti-phase sawtooth sample

the nature of the SU8 photoresist [120], the director of the nematic liquid crystal tends to orientate as a planar structure along the sidewall as shown in Figures

6.2, 6.3 and 6.4. To produce the samples, the photolithography method was used. The cleaning process is the same than the one described in Section 2.1.2. One of the glass substrate was coated with a layer of SU8 negative photoresist and then cured at 155°C. Another layer of SU8 was then spread on and then exposed to UV light. The new layer is developed and baked at 100°C to cure. The second glass substrate is coated with a layer of photoresist and the two substrates, patterned and flat one, are assembled together and heated up to 150°C. The cell is then capillary filled with the liquid crystal material at a temperature just above the nematic-isotropic transition.

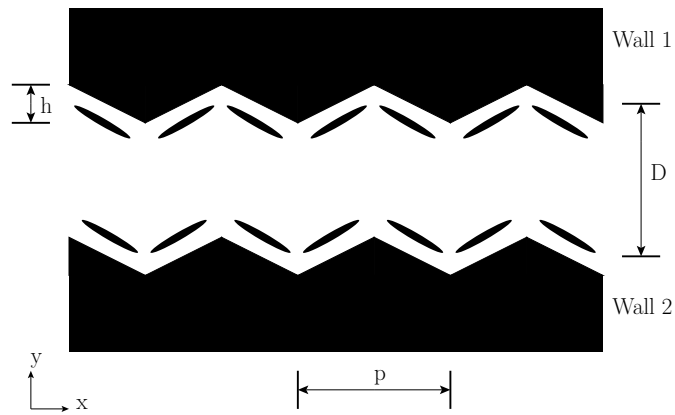


Figure 6.3: Schematic top view of in-phase sawtooth sample

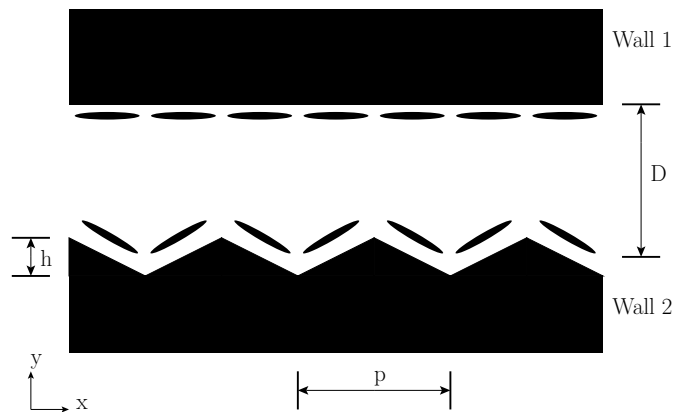


Figure 6.4: Schematic top view of sawtooth flat sample

6.3 Different type of director orientation across the cell

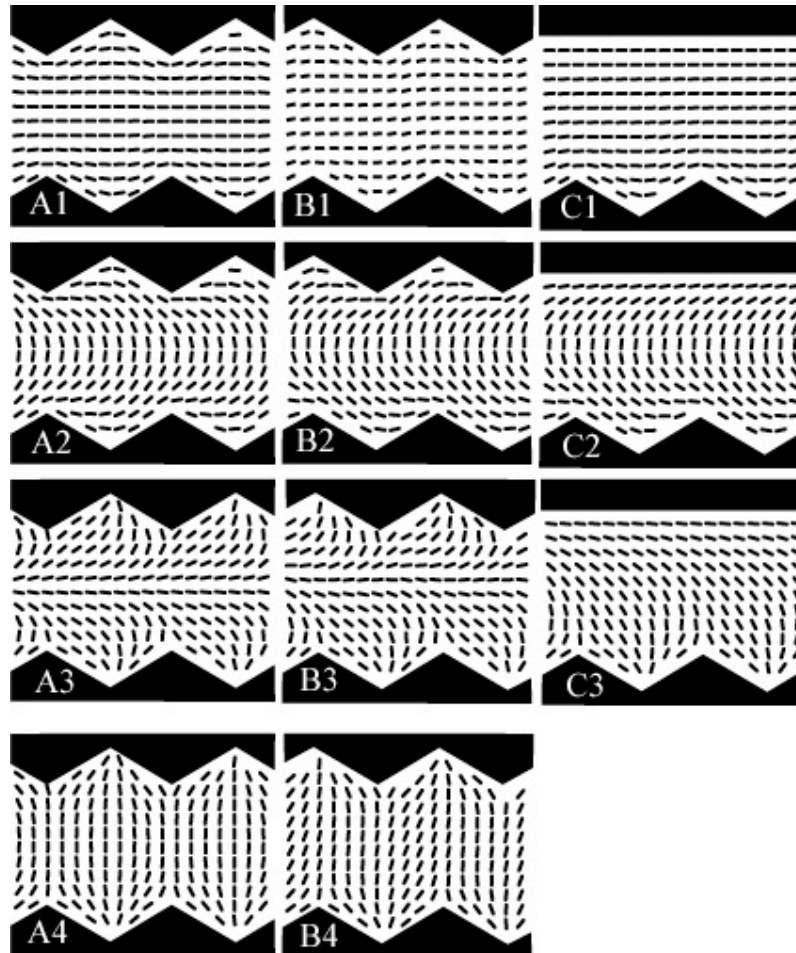


Figure 6.5: Schematic cross-section of sawtooth/flat samples (A: anti-phase, B: In-phase and C: sawtooth/flat)

The purpose of this work is to quantify the different states as a function of the geometry of the sawtooth and of the cell before and after annealing. Additionally to control that defects do not reappear at the same position throughout the sample. In Figure 6.5, A1, A2, A3 and A4 are anti-phase geometry, B1, B2, B3 and B4 are in-phase geometry and C1, C2 and C3 are flat/sawtooth geometry. In geometry A1, B1 C1, the distortion disappears smoothly into the bulk and the central region is horizontally orientated which is a planar orientation. In A2, B2 and C2, the director rotates by π radians across the structure and is vertically

aligned in the central region. This is a bend state as can be observed in pi-cell structures. In structure A3 and B3, the orientation of the director also rotates by π radians but the central region is horizontally aligned which is related to a splay state. In structure C3, the director rotates only by $\pi/2$ radians which is similar to a HAN alignment. In structure A4 and B4, the distortion also disappears smoothly into the bulk but the central region is now vertically orientated.

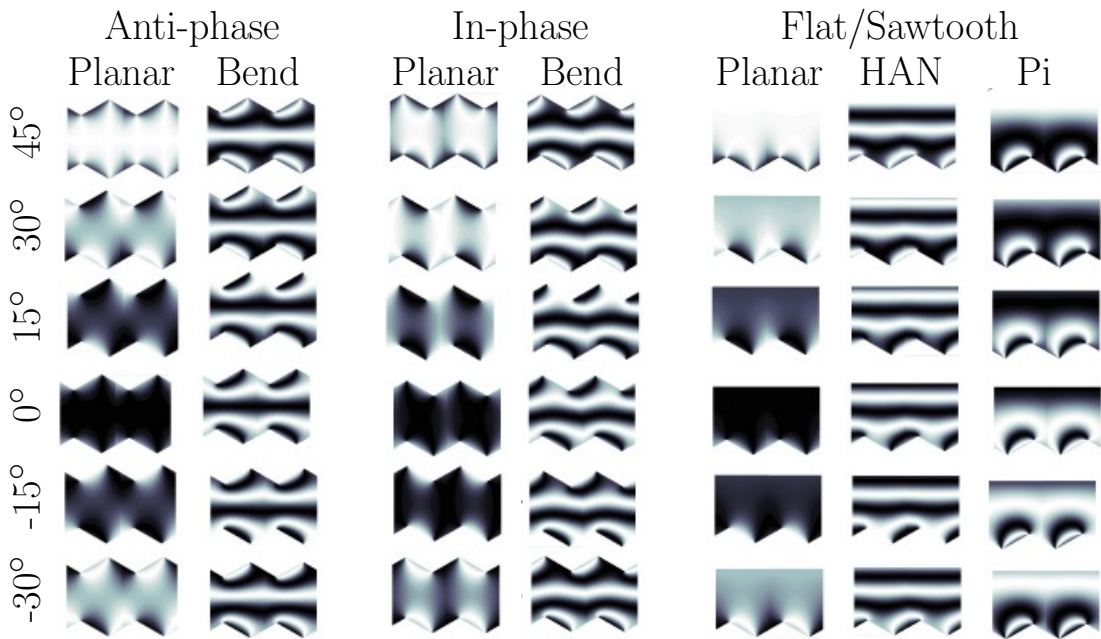


Figure 6.6: Theoretical optical textures across the cell of the different states in samples

Figure 6.6 represents the theoretical optical textures from the possible director configurations illustrated in Figure 6.5. The theoretical optical texture in Figure 6.6 were produced using the Q -tensor method in the software package COMSOL Multiphysics [73] which was provided by Dr. A. Davidson and Prof. N. Mottram. Experimental microscope observations done under crossed polariser in Figure 6.7 can be related to the theory in Figure 6.6. A1 & A4 being the anti-phase planar state, A2 & A3 anti-phase bend. B1 & B4 is the in-phase planar and B2 & B3 the bend. In the flat/sawtooth C1 is the planar state, C2 Pi and HAN being C3.

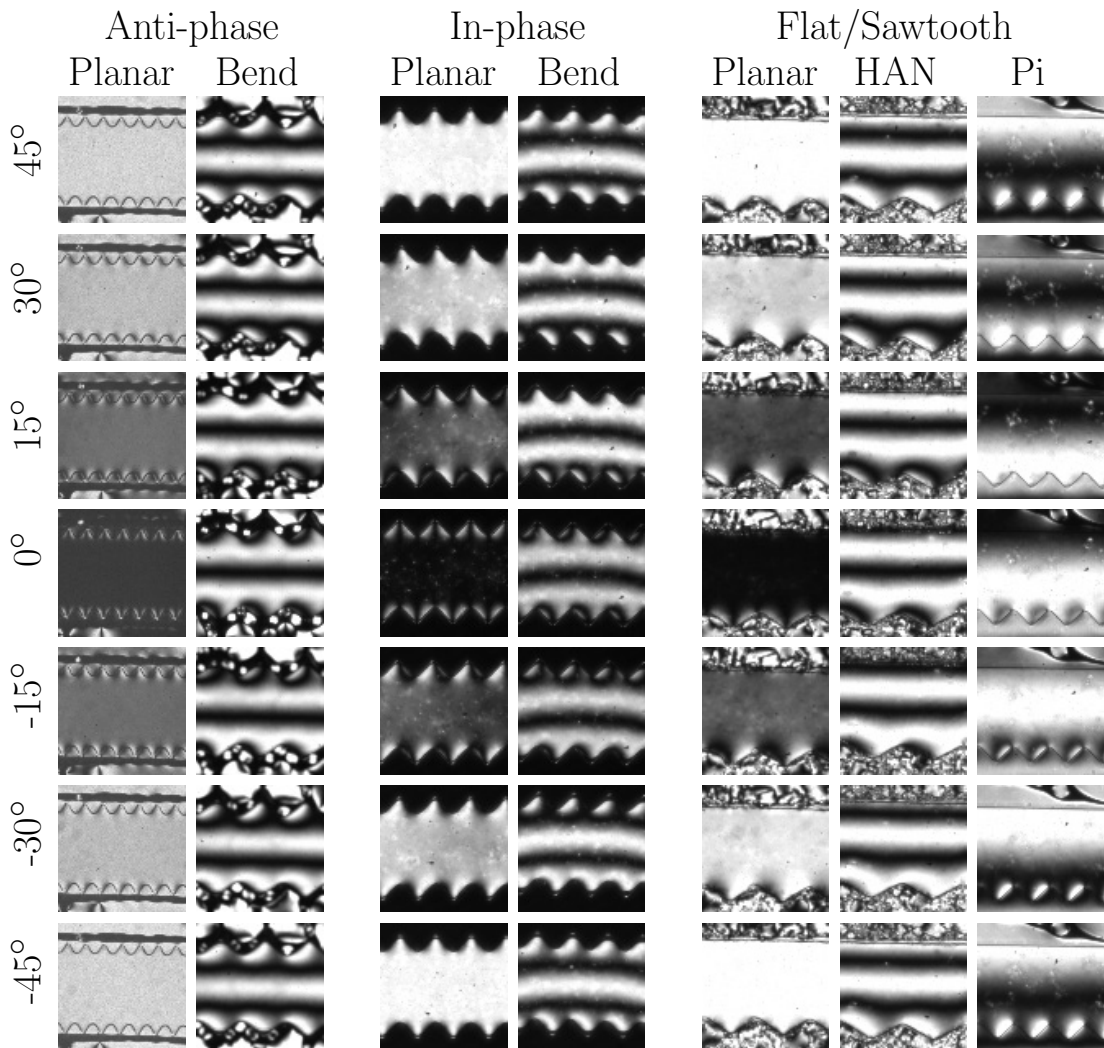


Figure 6.7: Experimental observations of the different states in samples from theoretical predictions shown in Figure 6.6

6.4 Observations and results

6.4.1 Observations

Based on the principle explained in Section 5.2 and the Equation 5.2, the orientation of the director of the liquid crystal relative to the orientation of the first polariser (α) dictates the brightness observed across the structure. If the director is aligned or at a right angle with respect to the orientation of the first polariser ($\alpha = 0$ or $\alpha = \pi/2$) the liquid crystal appears dark under the microscope. At the opposite, if the angle is half-way between the two ($\alpha = \pi/4$), the material appears relatively bright. The brightness is dictated by the wavelength of the light (λ), the refractive index anisotropy (Δn) and the thickness of the sample (d) which is a multiple of the wavelength. The bend defect in an anti-phase sample is illustrated in Figure 6.5(A2). Figure 6.8 is an experimental observation of such a defect. Both side walls have similar brightness because the director orientation is rotated by π radians. The central part orientation is at a $\pi/2$ radians angle and appears having an identical brightness sandwiched by the brighter bands. By rotating the sample the director profile across the sample is confirmed. The bottom part of Figure 6.8 illustrated a state which has not be theoretically considered in Section 6.3. Another part of these observations was to make sure that defects

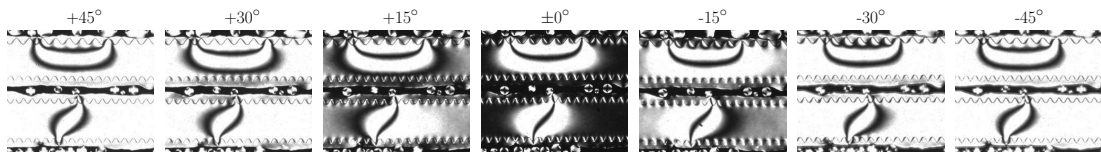


Figure 6.8: Microscope observations of a bend defect in an anti-phase sample under crossed polarised light at different angles from $+45^\circ$ (left) to -45° (right) by steps of 15°

were not pinned due to unwanted defects in the sidewall geometry. To investigate this, the sample was thermally annealed, slowly heated at a rate of 1° per min up to 70° , well above the nematic-isotropic transition, the temperature was held for 15 mins, then the sample was left to cool down over a period of 12 hours to

ensure no more reorientation would occur.

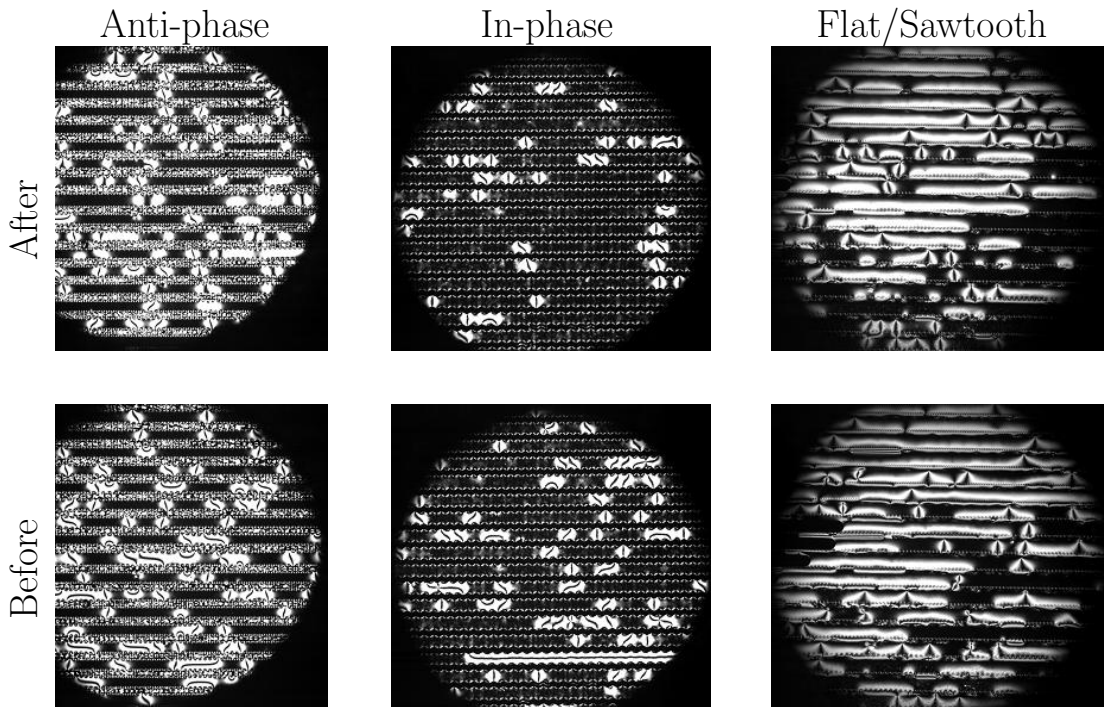


Figure 6.9: Microscope control before and after annealing for defects not occurring at different position

In Figure 6.9, all the observations made for all of the samples are shown and it is clear after a closer look that the defects do not reappear at the same location. The sample can be used for statistical investigation with confidence that the defects are permanently pinned to certain imperfections on the sidewall photo-resist resin.

6.4.2 Statistic and results

Anti-phase sample

In Figure 6.10, the sample is anti-phase sawtooth, the results of the annealing show that the proportion of both planar and bend state changes. This supports the idea that the defects do not reappear at the same place but also shows that this configuration is mainly favourable to the planar state. The proportion of the planar state was over 60% before the thermal annealing and above 70% after it

6.4. Observations and results

occurs, whereas the bend state is approximately 20% before and less than 10% after.

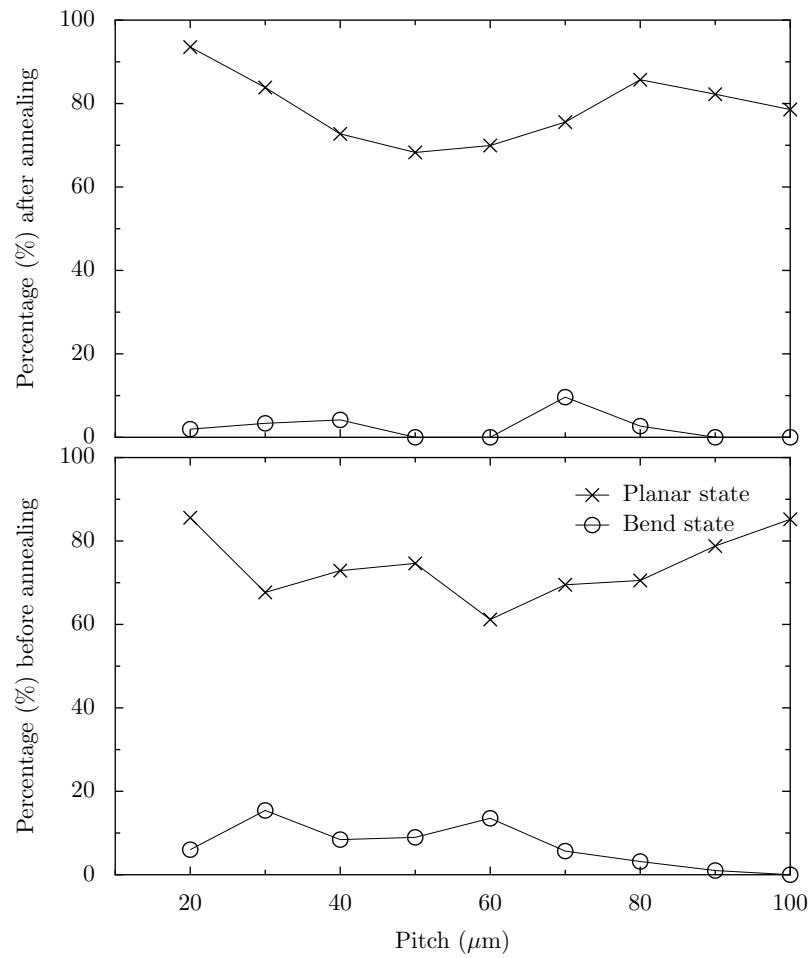


Figure 6.10: Statistical results of presence of bend and planar states in the anti-phase sample as a function of the pitch

In-phase sample

In Figure 6.11, the same observations as for the anti-phase sample can be made. The nematic material shows a predisposition to orientate to a planar state more than the bend configuration. After annealing, the planar state proportion is even more apparent with a presence of around 90% over the whole range and pitches whereas the bend state remains on average below 10%. The planar state is the state without distortion, it is the energetically more favourable.

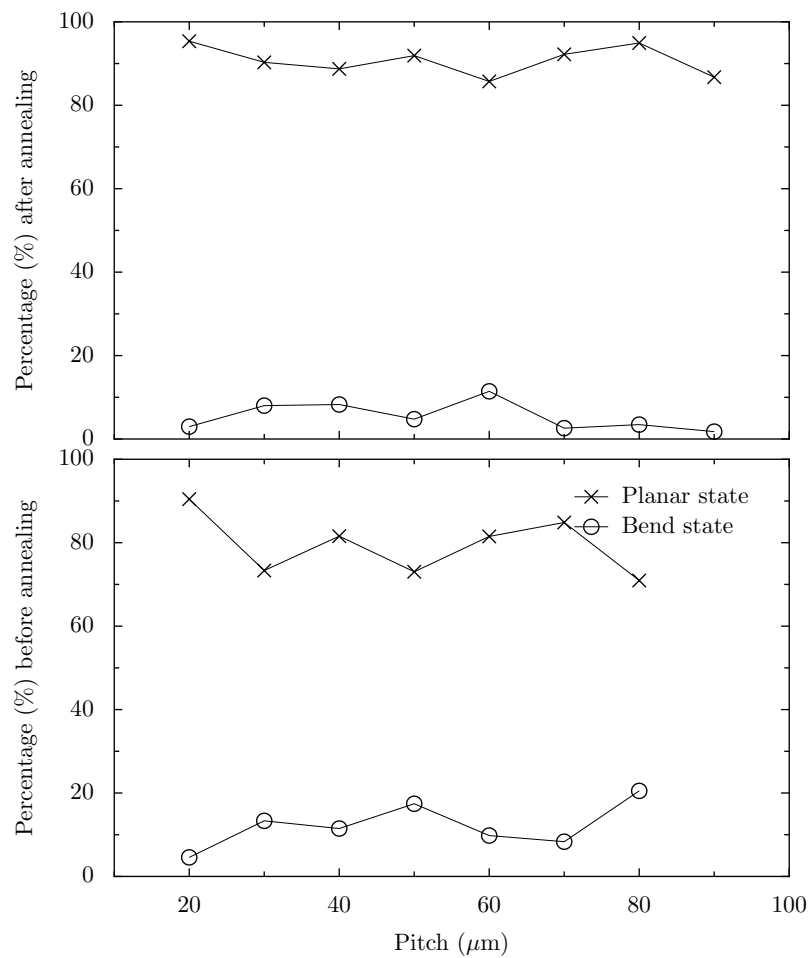


Figure 6.11: Statistical results of presence of bend and planar states in the in-phase sample as a function of the pitch

Flat/sawtooth sample

Finally in Figure 6.12, the evolution of the proportion of the states evolves according to the size of pitch across the sample. The planar state is nearly absent for the small size pitches and leans toward a domination in presence at large pitches. At the opposite, the two states (HAN and π) tend to disappear as the size of the pitch increases. At small pitch sizes the HAN state seems to overcome the π -state, this can find its origin in the fact that it is less distorted with only $\pi/2$ radian rotation of the director angle compared to the full π radian rotation in Pi state.

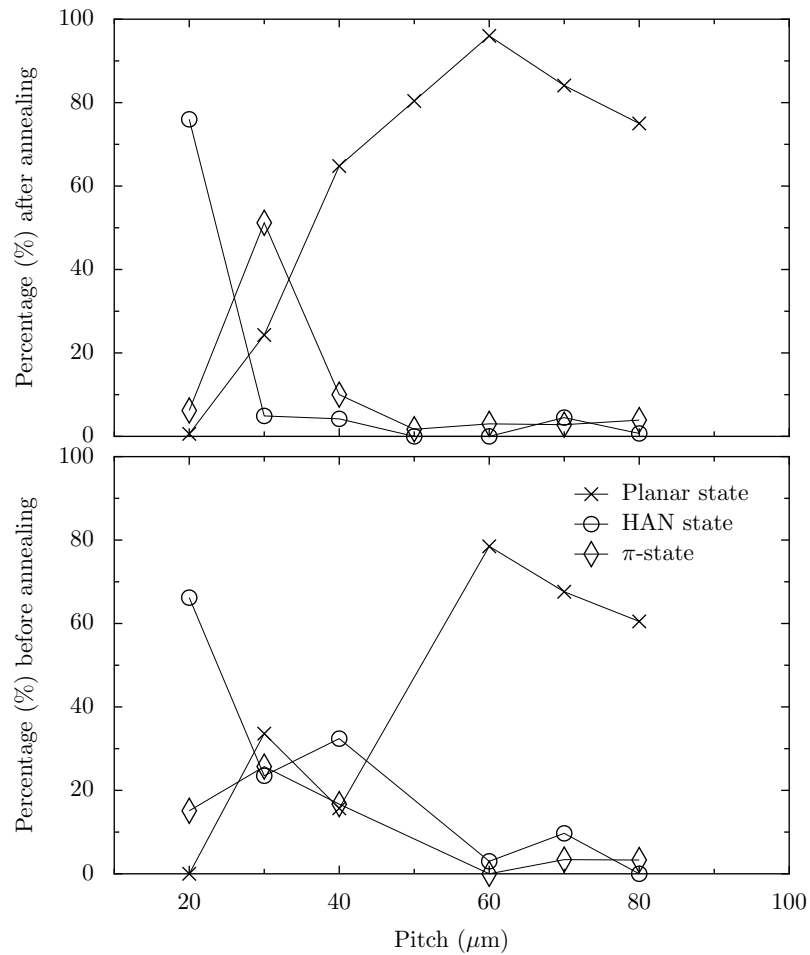


Figure 6.12: Statistical results of presence of bend, planar and Pi states in the flat/sawtooth sample as a function of the pitch

6.5 Conclusion

The first part of this investigation did produce the expected results, supporting the submitted publication by Ladak et al [119]. This publication demonstrates that the different defect states were occurring at different positions before and after annealing and were not the result of pinning by unwanted defects in the photoresist resin geometry of the sidewall of the sample.

The second part shows the evolution of the proportion of these different states according to the size and the geometry of the samples as anti, in-phase or flat/sawtooth design. The planar state appears to be the most commonly present even if it has been explained in the publication by Ladak et al [119] that according to the energy in the different states, the distribution might have been different. To extend this work, the distance (D) between the two sidewalls can be changed to determine the relation between this and the presence of states. Another parameter which has been kept constant is the thickness (T) which could also undergo investigation to understand its effect on the presence of different states.

Chapter 7

Other investigations using interferometric methods

7.1 Foreword

The following two sections are two separate research projects where interferometry helped to give a better understanding of the physical phenomenon involved and also allow for data acquisition. Section 7.2 investigates liquid dielectrophoresis using the Mach-Zhender interferometer [44, 45] setup. Section 7.3 investigates the resonance frequency of insects using the Michelson setup [121] with the same laser source as in Section 2.4.

7.2 Liquid dielectrophoresis

7.2.1 Principle

Known for over a century, the effect of non-uniform electric fields upon liquids such as water or oils can appear as a force which moves the liquid and reshapes the meniscus [122]. At the end of the 19th century, H. Pellat demonstrated that the force can pull a liquid upward when a voltage is applied between two electrodes [123–126]. He also discovered a relation between the height (h) and the applied electric field (E).

$$h \approx \frac{(\varepsilon_1 - 1) \epsilon_0 E^2}{2\rho_1 g} \quad (7.1)$$

In the equation 7.1, ε_1 is the dielectric constant of the liquid with a density equal to ρ_1 ; ϵ_0 is the permittivity of free space (8.854×10^{-12} F.m⁻¹); g is the gravity (9.81 m.s⁻² earth acceleration) and E is the electric field, approximated at $E \approx \frac{V}{d}$ where d is the distance separating the two electrodes.

In Pellat's experiment the setup was vertical and the field uniform between the electrodes [123]. The current experiment is horizontal, with a non-uniform electric field, created by applying a voltage through co-planar electrodes. The liquid sitting on the top of the electrodes will tend to accumulate where the electric field density is the greatest [127–130], at the edges of the conducting strips, this will

reshape the profile of the liquid. This phenomena has been used to manipulate small droplets of liquid. In a lot of previous experiments involving liquid manipulation on a microscopic scale, the setup has only involved a set of two parallel electrodes. Instead of using this setup, replacing this by a 1-D periodic array of electrodes and the droplets by a thin film. When the voltage is applied to this, the liquid being deformable, will reshape as a periodic fluctuation of the thickness [131]. The force exerted by the electric field (f_e) is called the dielectrophoresis (DEP) force and is proportional to the square value of the applied voltage (V), ($f_e = K \times V^2$) [122, 127, 130, 132, 133]. The surface of the liquid will tend to align roughly parallel to the electric field lines [134].

7.2.2 Preliminary investigation and data

The setup used to investigate the effect of electric fields on thin film of oils, is the same Mach-Zehnder interferometer [44, 45] as described in Figure 2.16 in section 2.4. The sample is also an interdigitated electrode as shown in Figure 2.2. The signal is applied to both sets of electrodes but the major difference is that it is an open sample coated with a dielectric layer ($15\mu\text{m}$ of SU8 [120]). As the sample is not capped (see Figure 7.1), the setup was altered slightly and rotated by a right angle for the sample arm to be vertical which allows the sample to sit in it horizontally and not have the oil (*hexadecane* $\text{C}_{16}\text{H}_{34}$) running down under the effect of gravity.

The acquisition of data is done in the same way as the experiment described

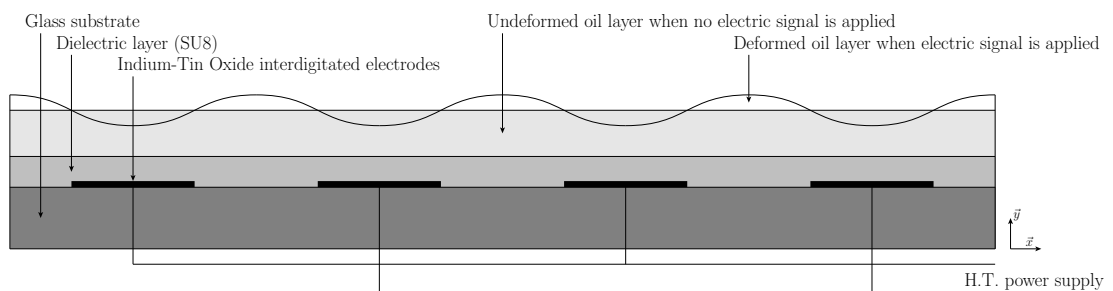


Figure 7.1: Schematic cross-section of dielectrophoresis sample

in Section 2.4, except instead of a variation of the refractive index inducing the fringe movement, it is now related to a variation in the thickness of the oil layer as shown in Figure 7.2 which gives a periodic variation in the optical path length. It moves under the influence of the non-uniform electric field generated by the co-planar ITO interdigitated electrodes.

7.2.3 Experimental results and conclusion

After plotting the results of the fringe distortion as a function of the electrodes size and the oil thickness (see Figures 7.3, 7.4, 7.5, 7.6) and tabulating the results of the gradient and the standard error of the gradient (see Table 7.1), the relation between the movement of the fringes and the square of the applied voltage can not be demonstrated without doubt. It is still interesting to note the relationship which appears to link the thickness of hexadecane and the intensity of the distortion, plus the influence of the separation between the electrodes.

From Figures 7.3, 7.4, 7.5 and 7.6, it is possible to observe a linear relation between the amplitude of fringes distortion and the square of the rms. of the applied voltage ($A \propto V^2$). The relation of the amplitude (A) on the square of the applied voltage (V^2) can be calculated with few approximations: the amplitude is small in comparison to the electrodes size ($A \ll d$), the electrodes produce a periodic potential profile and the profile is unperturbed by the air-oil interface. This leads to the relation:

$$A = \left[\frac{16\varepsilon_0}{3\gamma\pi^4} (\varepsilon_{oil} - \varepsilon_{air}) \exp\left(-\frac{4\pi h}{d}\right) \right] V^2 \quad (7.2)$$

Where (ε_{oil}) and (ε_{air}) are respectively the permittivity of the oil and air, (ε_0) is

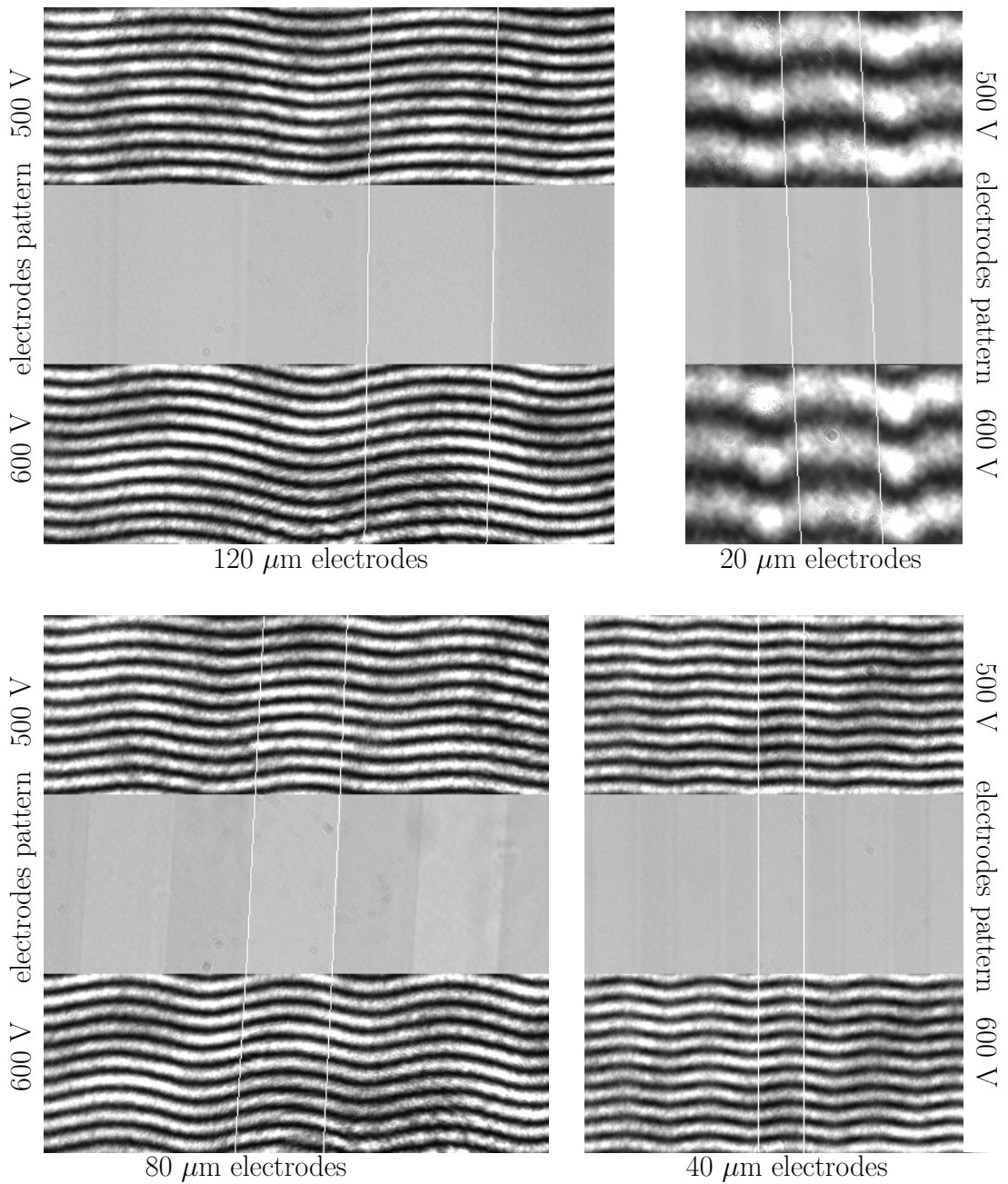


Figure 7.2: Observation of the fringe movement related to thickness variation across the oil layer, the size of the electrodes and the voltage applied

7.2. Liquid dielectrophoresis

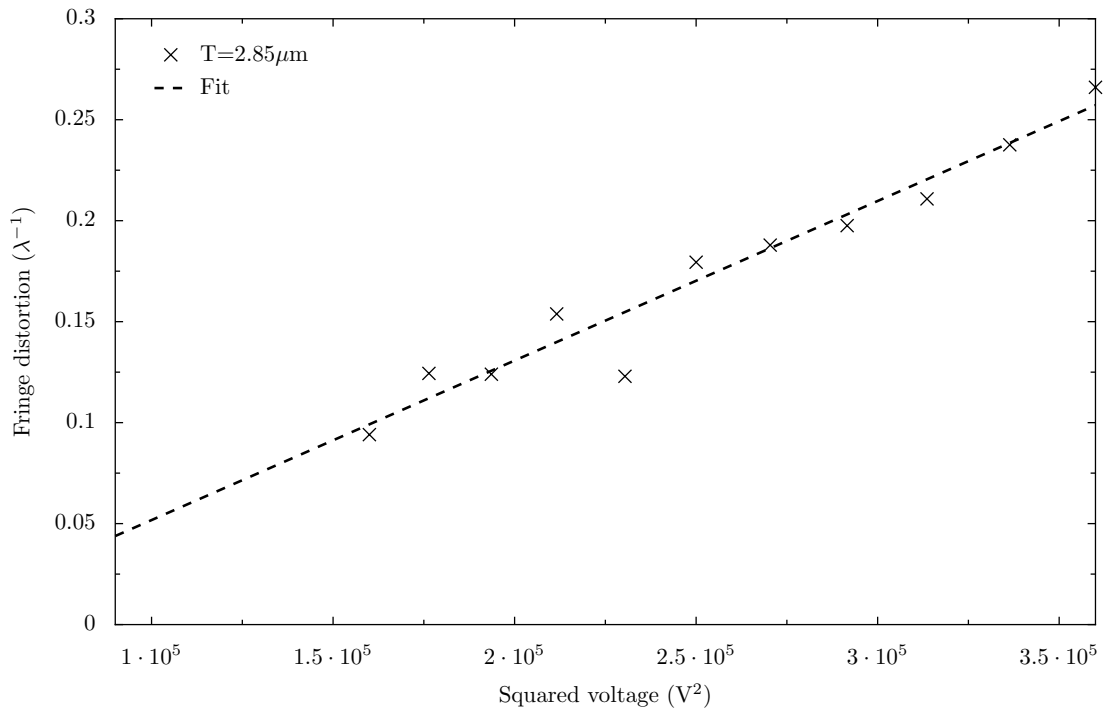


Figure 7.3: Results for $20\mu\text{m}$ electrodes with $2.85\mu\text{m}$ thick oil layer

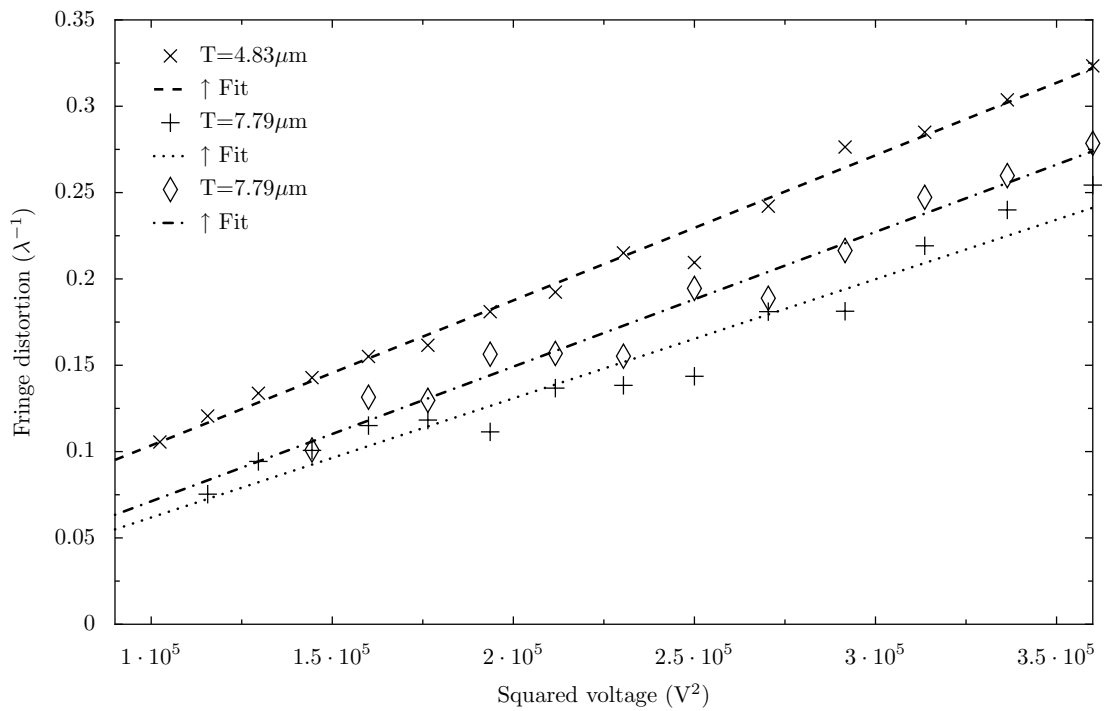


Figure 7.4: Results for $40\mu\text{m}$ electrodes with $4.83\mu\text{m}$ and $7.79\mu\text{m}$ thick oil layers

7.2. Liquid dielectrophoresis

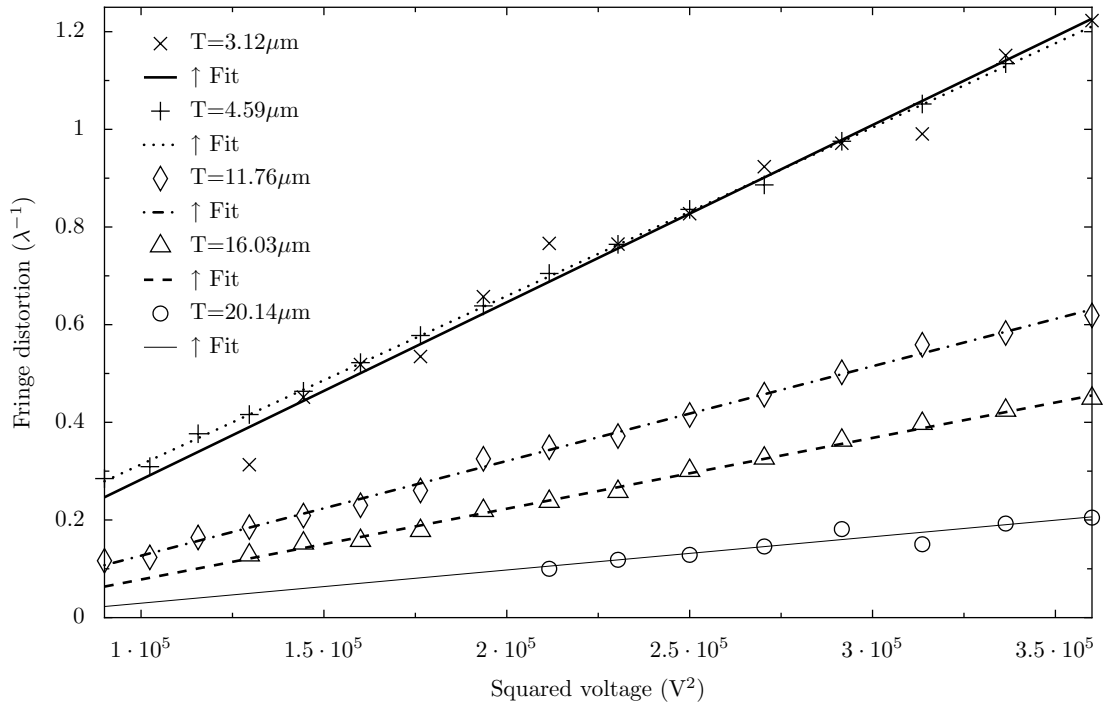


Figure 7.5: Results for $80\mu\text{m}$ electrodes for different oil layer thickness

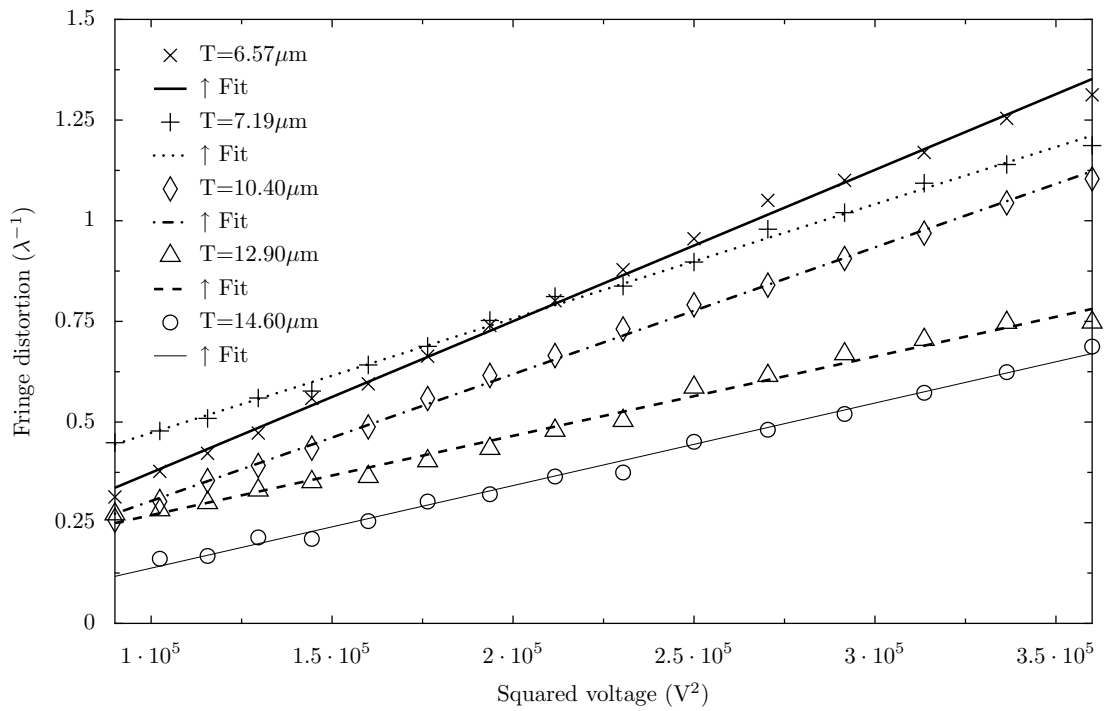


Figure 7.6: Results for $120\mu\text{m}$ electrodes for different oil layer thickness

Table 7.1: Results of fringe distortion as a function of electrodes size and oil thickness

Electrodes size (d) (μm)	Oil thickness (h) (μm)	Gradient ($\propto A/V^2$) ($10^{-6} \lambda^{-1} V^{-2}$)	Standard error of gradient (10^{-6})
20	2.85	0.79	0.06
	4.83	0.84	0.02
40	7.79	0.69	0.04
	7.79	0.78	0.04
80	3.12	3.63	0.16
	4.59	3.45	0.02
	11.80	1.94	0.03
	16.00	1.45	0.03
	20.10	0.68	0.10
120	6.57	3.76	0.06
	7.19	2.84	0.04
	10.40	3.15	0.04
	12.90	1.97	0.06
	14.60	2.05	0.04

the free space permittivity and (γ) is the surface tension of the oil. Equation 7.2 can be rewritten as:

$$A \sim V^2 \exp\left(-\alpha \frac{h}{d}\right) \quad (7.3)$$

$$\ln(A) \sim \ln(V^2) + \left(-\alpha \frac{h}{d}\right) \quad (7.4)$$

$$\ln\left(\frac{A}{V^2}\right) \sim -\alpha \frac{h}{d} \quad (7.5)$$

Using the data from Table 7.1, represented in Figure 7.7, the relation in Equation 7.5 between (A/V^2) and (h/d) or (α) come from the regression analysis (see Appendix A.4) at a value of (8.74) which is far from (4π) in Equation 7.2. This deviation might be due to the relatively thick ($15\mu\text{m}$) dielectric layer (SU8). Further research has already been undertaken to reduce it and observe its influence [135].

7.3. Investigation of resonance modes in insects

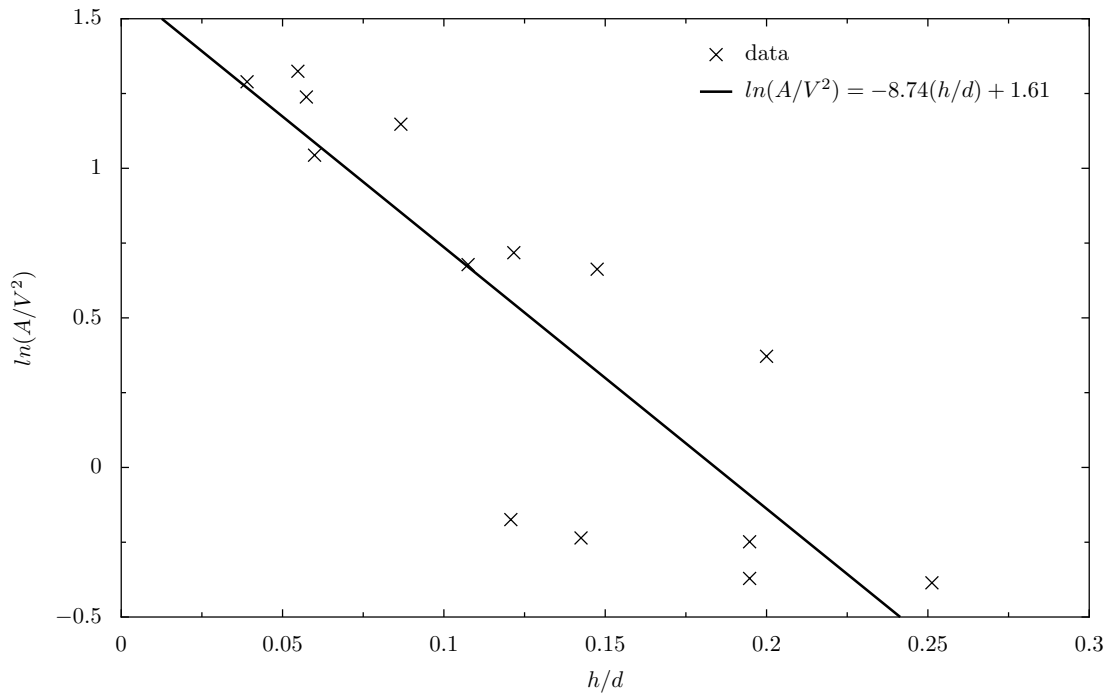


Figure 7.7: Plot of the relation between $\ln(A/V^2)$ vs. h/d

7.3 Investigation of resonance modes in insects

7.3.1 Introduction on honeybees and the *Varroa destructor* mite



Figure 7.8: Pictures of *Varroa destructor*

Honey bees are important and beneficial insects to mankind for food but not only as such. Bees are the vector in the pollination of many plants and are

essential in the production of many crops and fruit. If bees were not here it would put many species in danger [136]. Bees belong to the *Apidae* family species which contains seven species of honey bees. The species which is mainly based in Europe, Africa, America and part of Western Asia is the *Apis mellifera* [137, 138]. The *Varroa destructor* mite is spread worldwide apart central Africa and Australia [139–145]. Today's bees are affected by the parasite *Varroa jacobsoni* which was first observed in Java in 1904 and named after Marcus Terentius Varro [146]. The parasite affecting the western bees (*Apis mellifera*) is another species of the *Varroa* parasite, the *Varroa destructor* (see Figure 7.8). There is no physical distinction the two types *Varroa jacobsoni* and *Varroa destructor* [145]. However, the colonies of bees affected by the *Varroa destructor* parasite if left without proper treatment, will probably be wiped out in a few years [138].

The *Varroa Destructor* is a small mite measuring 1.1 mm long by 1.5 mm wide with a roughly oval curved body [142, 145]. The main threat is not the mite itself but the fact that it is a vector of virus [147–149] directly affecting the health of honey bees which are injected during mite feeding [141].

The purpose of this investigation is to determine the resonance frequency of the hard back shell of the *Varroa*, in a attempt to upset the intruder to the beehive and force it to leave. No work on hard shell insect resonance frequency has previously conducted, the only investigation similar to this was a study on the bioacoustics by Gopfert and Robert in 2002 [150] using Doppler vibrometry.

7.3.2 Outline of the investigation

This investigation plan is as follows, the preliminary work was conducted on polymethylmethacrylate (PMMA) or Perspex[®] [151] disks to corroborate the value measured by the interferometer with the one recorded by an accelerometer. The second part was to use a ground beetle (*Carabus problematicus*) and determine the resonance frequencies of its hard back shell, comparing the results with an

alternative method, optical coherence tomography (OCT). The final part of the experiment, which has yet to be undertaken, is to move to the *Varroa destructor* and determine the frequencies at which its shell resonates.

Experimental setup

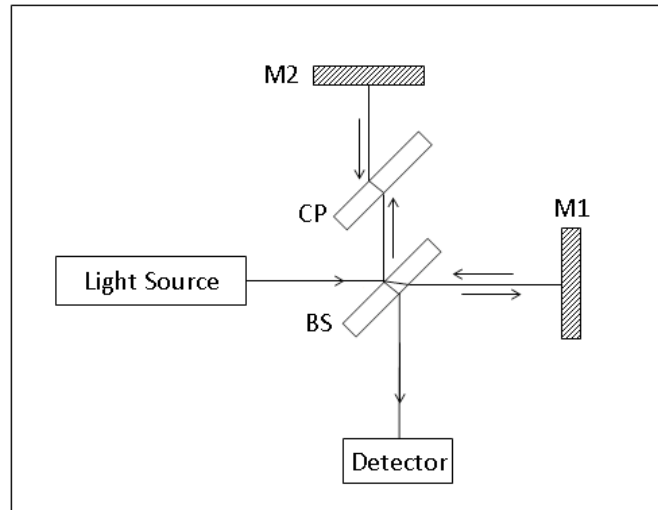


Figure 7.9: Schematic representation of the Michelson interferometer setup

In the work conducted with the common fruit fly (*Drosophila melanogaster*) by Gopfert and Robert [150], the principle was based on laser Doppler vibrometer (manufactured by Polytec). This was not a viable option for this project due to the fact it was very expensive. Instead, the investigation will be based on the Michelson interferometer [121]. This setup (see Figure 7.9) offers a contact-free measure, which gives a complete resonance freedom to the sample and does not affect the resonance modes of very small samples.

The studied sample will be used as one of the reflective mediums at the end of one of the arms of the interferometer. To compensate for any curvature of the sample, a convergent lens will be placed on the sample arm to concentrate the laser beam at the same point as the centre of curvature of the sample and allow a normal incidence of the converging beam. When the sample resonates the optical path of the sample arm is changed, as is the interference pattern over the detector.

7.3.3 Preliminary study to validate the method

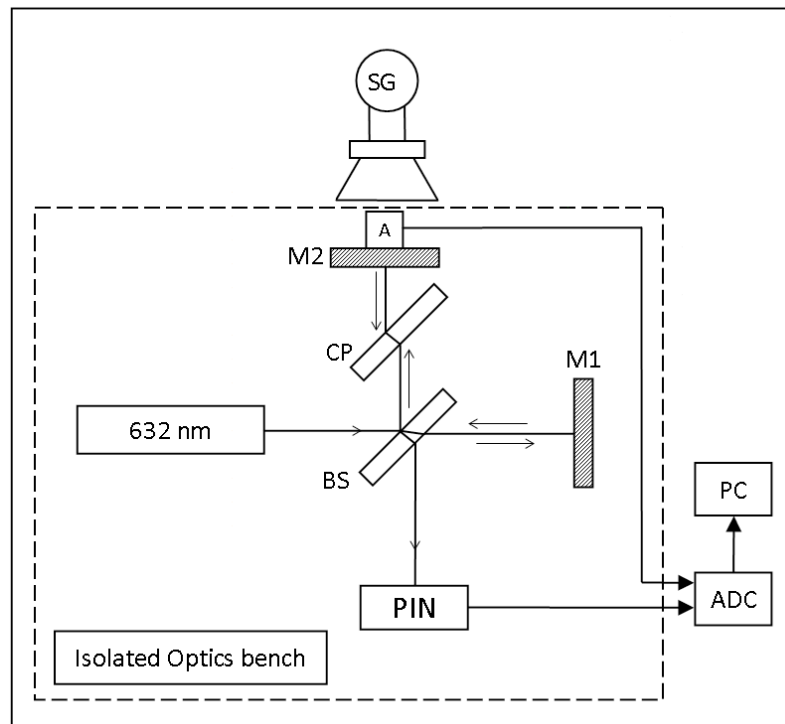


Figure 7.10: Experimental setup for interferometry and accelerometer data acquisition

To validate the principle of using interferometry to measure vibration, a decision was taken to use PMMA material with a square form. The square shape was used to correlate measures recorded from the accelerometer and the interferometer detector. The square is 10^4mm^2 by 6 mm thick and was held by one edge, perpendicular to the incoming laser beam. The accelerometer was secured on the back of the PMMA sample and the speaker placed behind it. The accelerometer was an Endevco Isotron Model 7259B-10 capable of monitoring acceleration from 20Hz up to 250 kHz, with a sensitivity of $1.059 \text{ mV}/(\text{m}\cdot\text{s}^{-2})$ [152], and an accuracy of $\pm 1.5\%$ [153]. The speaker was held by a stand, placed off the vibrations isolated optical bench as shown on the picture 7.10. The photo-detector used was a Menlo Systems FPD510 PIN photo-detector with a spectral range from 400 to 1000 nm, a frequency range from 0 Hz up to 250MHz and a rising time of 2 ns [154]. To reduce the main parasites, the detector was plugged to a 12V

battery. The signals from the PIN detector and the accelerometer were sent to an analogue-to-digital (ADC) converter to transmit the data to a computer for post-processing.

For the results shown in Figure 7.11, it can be concluded that there are high lev-

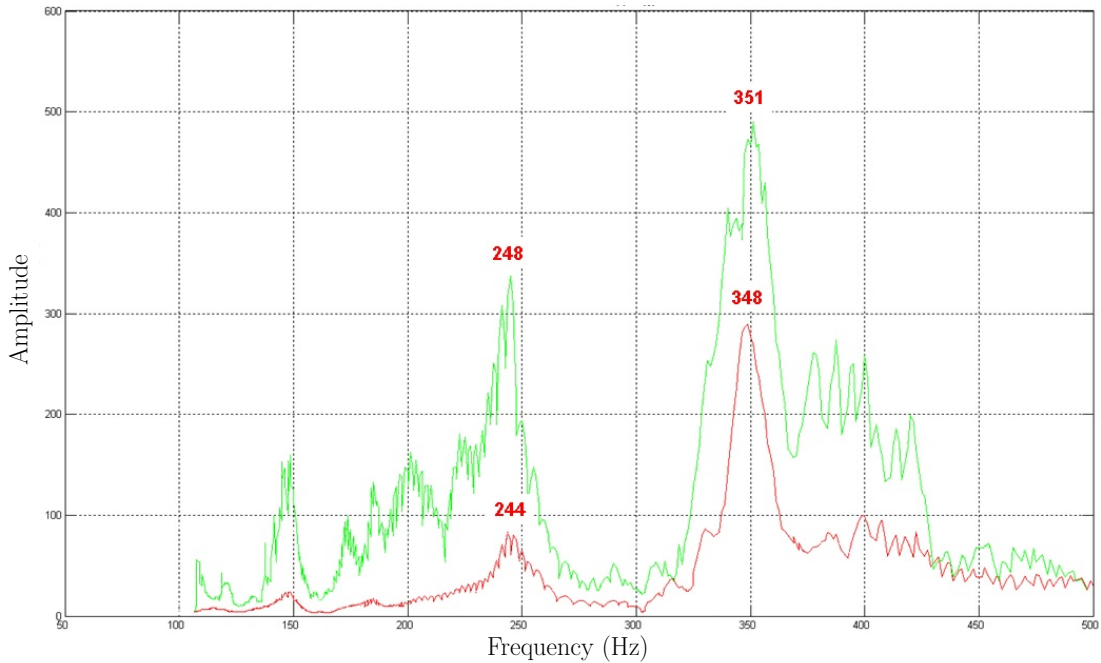


Figure 7.11: Comparison between interferometry (high) and accelerometer (low) results

els of agreement between the two methods. The amount of discrepancy between the two methods is relatively small $\sim 2\%$ which tends to support the argument that interferometry can be used for vibration measures.

7.3.4 Investigation of resonance of a large insect: *Carabus problematicus*

Before passing directly to a small insect, an intermediate investigation was undertaken with a ground beetle; (*Carabus problematicus*) (see Figure 7.12). This was done in order to determine the resonance frequencies and corroborate the results with an alternative method. The first alternative attempted was an interferometric surface profiler did not show any conclusive results. Another alternative



Figure 7.12: View of the *Carabus problematicus*

was to use optical coherence tomography (OCT). The principle of OCT is based on interferometry, the method is non-invasive and contact free. It allows high definition imaging in 3D but for the purpose of investigating insect resonance 2D was used for faster acquisition. The setup of OCT is based on Michelson interferometry with a fast moving mirror for the depth scan but using a low-coherence light source [155]. The method used is the Fourier domain optical coherence tomography (FD-OCT) which analyses the spectrogram of the reflected beam interfering with the reference one when recombined, to determine the position of the reflecting interface [156, 157].

The results obtained show the amplitude of displacement as a function of frequency. In Figure 7.13, it is interesting to note that the experiment with the *Carabus problematicus* exhibits resonance at different frequencies. The first one occurs around 3.25 kHz, then another mode appears just after 4 kHz, a massive displacement occurs at 4.5 kHz, and a last one appears to occur around 5.75 kHz. These frequencies can be matched in the two series of results obtained using the OCT method.

In the interferometry method the same setup was used as for the validation shown in Figure 7.10 but to date no satisfying results have been obtained. The noise

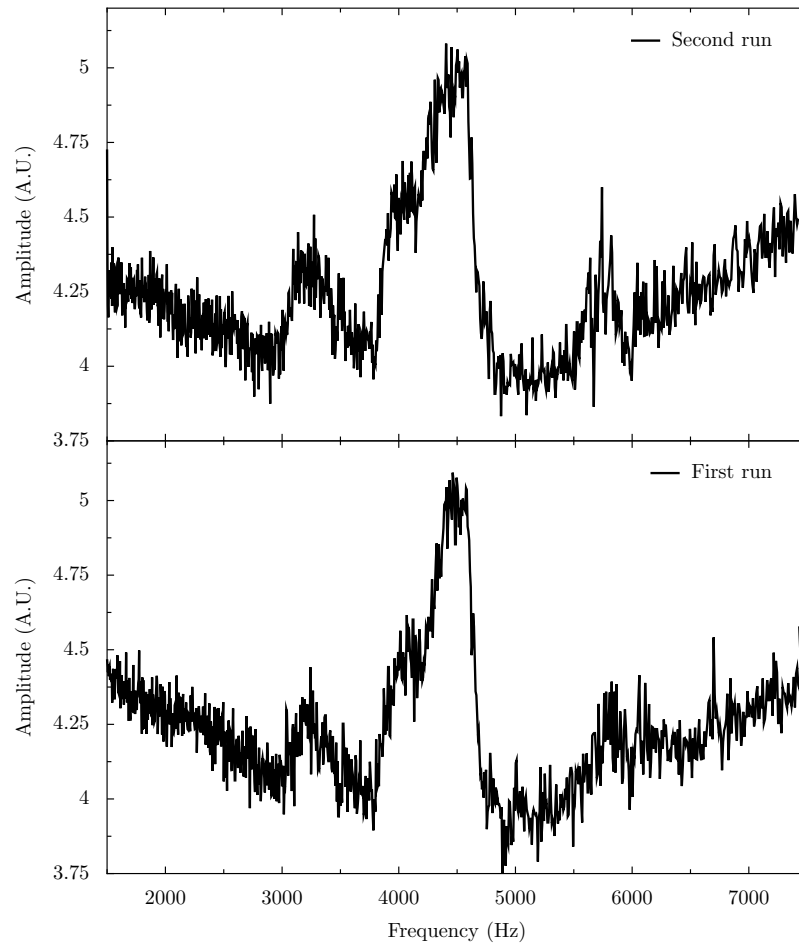


Figure 7.13: Results from the Optical Coherence Tomography

to signal ratio is too high due to light scattering from the grooved back of the *Carabus problematicus*.

7.3.5 Investigation on the *Varroa destructor*

The next step will be to investigate the resonance frequencies of the *Varroa destructor* which is the main purpose of this study, but at the present time this work has not been undertaken. The investigation will resume when a better corroboration between interferometry and the OCT method has been achieved.

7.3.6 Conclusion

After obtaining a satisfying corroboration between the interferometer and the accelerometer using the smooth surface of the PMMA sample, work was moved on towards large insects using a gold coated *Carabus problematicus*. The results were then corroborated using an alternative method (OCT). The roughness of the back of the ground beetle creates a light scattering pattern which affects the recording of the resonance frequencies obtained by the interferometric method. This problem has to be overcome, in order to reduce the noise to signal ratio. This problem may not occur with the insect of interest. The *Varroa Destructor*'s back does not appear to be grooved like the ground beetle, see Figures 7.8 and 7.12.

Chapter 8

Conclusion

8.1 Ionic contamination

8.1.1 Effects on the Fréedericksz transition

As a follow up of previous work on the effect of flexoelectricity over the Fréedericksz transition [74], this study investigated the effect of free charges carriers on the same transition. The previous study had shown that flexoelectricity tends to stiffen the transition. This research showed the opposite effect, revealing that the ions tend to screen the stiffening of the transition. When these two effects can be found within the same material it is interesting to note that one tends to cancel the other out. The primary method of carrying out this research was to compare the results over the Fréedericksz transition using both an electric and a magnetic field. The investigation using electric fields should have generated a reaction over the free charge carriers and revealed the ionic effect. Whereas using the magnetic force to reorientated the director should not generate the same response from free charge carriers and outline only the flexoelectric effect over the Fréedericksz transition. Later it was noted that there were differences between new and ageing cells. It has been revealed that the ageing cell contained more free charge carriers and the effect which ions may have over the Fréedericksz transition has been shown by comparing the permittivity plots of the two cells.

8.1.2 Transient capacitance measures

During this part of the research program only experimental data was collected to reveal the effect ions generate in nematic liquid crystal materials. A comparison between highly ionic (E7 [57]) and a non-ionic (TL216 [102]) material has been made. It is interesting to observe the plotted results of the evolution of the transient capacitance for different material, different thickness and different applied signal in detail. Some of the results revealed the presence of ions in the sample by showing a shielding effect, the most revealing result was the reaction of the

nematic material when no signal was applied and only induced by the free charge carriers. It can be concluded that is only due from the ions because the same signal applied to the non-ionic material did not show the same effect. Also by comparing the different signals applied more information can be extracted from this investigation on ions in nematic material. The amplitude modulation (A.M.) does not generate ionic reaction where as the two other applied signals do; the square one (SQ.) and the positive-zero-negative-zero (PoNo). The comparison between all of these signals may additionally give more information about flexoelectricity. The ions motion and shielding has been approximate but not quantify whereas the ions-director-flexoelectric coupling has been elucidated using the continuum theory.

8.2 Bistability

The work undertaken in this report was to support the finding of the submitted article by Ladak [119]. It consisted of an investigation of the influence of the sidewall geometry over the orientation of the director of nematic liquid crystal material. To demonstrate the bistability of the sample the first part was to show that defects were random and not related to a strong pinning with unwanted defects in the photo-resist resin. This was achieved by thermally annealing the sample and observing where the defects appear then comparing those locations with the ones before annealing. None of the defects observed reappeared at the same place which confirms the randomness of the phenomenon. The second part of this work was to study the appearance of certain defects in different geometry; anti-phase sawtooth, in-phase sawtooth and sawtooth geometry facing a flat wall. The investigation was based on the pitch of the sawtooth geometry. This showed the relation between the presence of states and the size of the pitch.

8.3 Flexoelectricity

One of the achievements of this project was to design a new technique to investigate the flexoelectricity effect and measure it using interdigitated electrodes samples with signals applied across the sample as well as “in plane” electric field. The material used during this was highly ionic which generated a shielding of the applied signal. The asymmetric response between positive and negative applied signals gives an indication of the extent of the flexoelectric strength. The Mach-Zhender interferometer was used to study the optical properties of liquid crystal and the refractive index anisotropy as a function of the orientation of the director. The variation of optical path can be linked to the rotation of alignment related to the applied field and how it evolves through time as the flexoelectric force increases and then the ions migrate and reduce the electric field. Using a commercial nematic liquid crystal, E7 [57], which is a well known and studied material, the values found were $(e_1 + e_3) = 14 \pm 1 pC.m^{-1}$ for an antiparallel alignment and $(e_1 + e_3) = 15 \pm 1 pC.m^{-1}$ for the parallel alignment. These values are comparable to the value found by Prost and Perchan [58] and also comparable to the one found for the same material by Jewell [66]. They are very different to the one found by Kruschka [67] but their approach has been recognised to be in need of further investigation and not totally reliable [158].

8.4 Other studies

Liquid dielectrophoresis

The work achieved in this part shows encouraging results in the use of the dielectrophoresis phenomena as a diffraction system. It also opens the field for further investigations into the relation between the applied field and the extent of the distortion of the oil layer. The relation is based on the square value of the applied electric field as has been suggested by previous publications [123, 124, 127, 132]

in the same area. However previous publications did not reveal this relation on the diffractive system, this relationship has not been confirmed but is suggested from the plotting of the fringe distortion as a function of the applied voltage

Insects resonance modes

Only one other group, Gopfert and Robert [150], has previously studied the effect of acoustic waves on insects. The purpose of this investigation was to determine the resonance frequency of hard back insects in particular one of the bee parasites *Varroa Destructor*. This was to find a way to upset them in infected hives and force them to leave using either acoustic waves or electric fields, as the back of these insects appears to show dielectric responses. The first insect used for the preliminary study was a *Carabus problematicus*, or ground beetle, the results are very encouraging for reducing the size of the insect and reaching the dimensions of the *Varroa*.

8.5 Further Works

To complete the work commenced in this report a lot more could be done. The investigations on the flexoelectric effect needs further research, mainly modelling, to explore the transient capacitance and the effect on the Fréedericksz transition to achieve a match for the experimental results with any new theories. This implies a better modelling of the size and effect of the ions contained in the material. The interferometric method needs more modelling, the implemented version of the model used in the report is already available including free charge carriers but it requires a little reworking to include the surface effect too. The method can also be extended to investigate other materials with different characteristics. To push forward the work on bistability, investigations can be orientated towards a study of the influence of variation of the thickness of the sample and also the distance between the two sidewalls. In addition observing how the pattern of the

same sidewall affects the distribution of different orientations.

For the dielectrophoresis, the main work which can be done has already been undertaken, it is about reducing the layer of the dielectric resin between the layer of oil and the interdigitated electrodes. Using the new set of samples a quantitative relationship between the distortion and the applied fields should be getting closer to the theory. This study could also be extended to other materials with different parameters.

The final part of this thesis was the study of the bee parasites, to advance this work, a way to improve the signal to noise ratio in the interferometry investigation on the ground beetle has to be found. When this is achieved, investigations need to be conducted on smaller insects and especially the *Varroa Destructor*. When the frequencies are determined a further investigation may be required to using live specimens and observing the reaction when exposed to those frequencies, and perhaps using electric field to make the back on the insects resonate.

Appendix A

Appendix

A.1 Interdigitated electrodes model

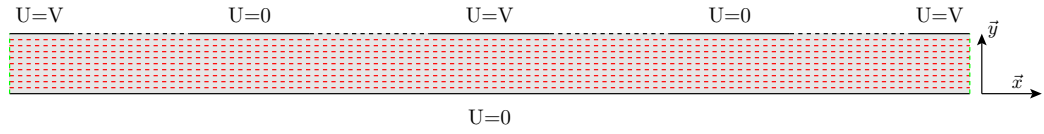


Figure A.1: Schematic cross-section of a planar alignment interdigitated cell with nematic liquid crystal

Orientation :

$$\theta = \theta(x, y) \quad (\text{A.1})$$

Electric field :

$$U = U(x, y) \quad (\text{A.2})$$

The orientation and the electric field only depend on x and y, no z component, only splay and bend distortion no twist in the 2-dimensions model.

Planar director :

$$\underline{n} = [\cos \theta, \sin \theta, 0] \quad (\text{A.3})$$

Maxwell's equations must be satisfied :

$$\nabla \cdot \underline{D} = 0 \quad , \quad \nabla \times \underline{E} = 0 \quad (\text{A.4})$$

Electric field :

$$\underline{E} = -\nabla U = \left[-\frac{\partial U}{\partial x}, -\frac{\partial U}{\partial y}, 0 \right] \quad (\text{A.5})$$

Elastic energy :

$$\omega_N = \frac{1}{2} K_1 (\nabla \cdot \underline{n})^2 + \frac{1}{2} K_2 (\underline{n} \cdot \nabla \times \underline{n})^2 + \frac{1}{2} K_3 (\underline{n} \times \nabla \times \underline{n})^2 \quad (\text{A.6})$$

Electric displacement :

$$\underline{D}_{Dielectric} = \varepsilon_0 \varepsilon_{\perp} \underline{E} + \varepsilon_0 \Delta \varepsilon (\underline{n} \cdot \underline{E}) \underline{n} \quad (\text{A.7})$$

$$\underline{D}_{Flexoelectric} = \underline{P}_{Flexoelectric} = e_{11} (\nabla \cdot \underline{n}) \underline{n} + e_{33} (\nabla \times \underline{N} \times \underline{n}) \quad (\text{A.8})$$

$$\omega_{Dielectric} = -\frac{1}{2} \underline{D}_{Dielectric} \cdot \underline{E} = -\frac{1}{2} (\varepsilon_0 \varepsilon_{\perp} \underline{E} + \varepsilon_0 \Delta \varepsilon (\underline{n} \cdot \underline{E}) \underline{n}) \cdot \underline{E} \quad (\text{A.9})$$

$$\omega_{Dielectric} = -\underline{D}_{dielectric} \cdot \underline{E} = -(e_{11} (\nabla \cdot \underline{n}) \underline{n} + e_{33} (\nabla \times \underline{N} \times \underline{n})) \cdot \underline{E} \quad (\text{A.10})$$

Total energy :

$$\begin{aligned} \omega = & \frac{1}{2} K_1 (\nabla \cdot \underline{n})^2 + \frac{1}{2} K_2 (\underline{n} \cdot \nabla \times \underline{n})^2 + \frac{1}{2} K_3 (\underline{n} \times \nabla \times \underline{n})^2 \\ & - \frac{1}{2} (\varepsilon_0 \varepsilon_{\perp} \underline{E} + \varepsilon_0 \Delta \varepsilon (\underline{n} \cdot \underline{E}) \underline{n}) \cdot \underline{E} - (e_{11} (\nabla \cdot \underline{n}) \underline{n} + e_{33} (\nabla \times \underline{N} \times \underline{n})) \cdot \underline{E} \end{aligned} \quad (\text{A.11})$$

$$\nabla \cdot \underline{n} = -\sin \theta \frac{\partial \theta}{\partial x} + \cos \theta \frac{\partial \theta}{\partial y} \quad (\text{A.12})$$

$$\nabla \times \underline{n} = \begin{vmatrix} \underline{i} & \underline{j} & \underline{k} \\ \frac{\partial}{\partial x} & \frac{\partial}{\partial y} & \frac{\partial}{\partial z} \\ \cos \theta & \sin \theta & 0 \end{vmatrix} = \underline{i}(0) - \underline{j}(0) + \underline{k}(\cos \theta \frac{\partial \theta}{\partial x} + \sin \theta \frac{\partial \theta}{\partial y}) \quad (\text{A.13})$$

$$\nabla \times \underline{n} = (0, 0, \cos \theta \frac{\partial \theta}{\partial x} + \sin \theta \frac{\partial \theta}{\partial y}) \quad (\text{A.14})$$

$$\underline{n} \cdot \nabla \times \underline{n} = (\cos \theta, \sin \theta, 0) \cdot (0, 0, \cos \theta \frac{\partial \theta}{\partial x} + \sin \theta \frac{\partial \theta}{\partial y}) = 0 \quad (\text{A.15})$$

$$\begin{aligned} \underline{n} \times \nabla \times \underline{n} &= \begin{vmatrix} \underline{i} & \underline{j} & \underline{k} \\ \cos \theta & \sin \theta & 0 \\ 0 & 0 & \cos \theta \frac{\partial \theta}{\partial x} + \sin \theta \frac{\partial \theta}{\partial y} \end{vmatrix} \\ &= \underline{i}(\sin \theta \cos \theta \frac{\partial \theta}{\partial x} + \sin^2 \theta \frac{\partial \theta}{\partial y}) - \underline{j}(\cos^2 \theta \frac{\partial \theta}{\partial x} + \sin \theta \cos \theta \frac{\partial \theta}{\partial y}) + \underline{k}(0) \end{aligned} \quad (\text{A.16})$$

$$\underline{n} \times \nabla \times \underline{n} = (\sin \theta \cos \theta \frac{\partial \theta}{\partial x} + \sin^2 \theta \frac{\partial \theta}{\partial y}, -\cos^2 \theta \frac{\partial \theta}{\partial x} - \sin \theta \cos \theta \frac{\partial \theta}{\partial y}, 0) \quad (\text{A.17})$$

$$\omega_N = \frac{1}{2}K_1\left(\cos\theta\frac{\partial\theta}{\partial y} - \sin\theta\frac{\partial\theta}{\partial x}\right)^2 + \frac{1}{2}K_3\left[\left(\sin\theta\cos\theta\frac{\partial\theta}{\partial x} + \sin^2\theta\frac{\partial\theta}{\partial y}\right)^2 + \left(-\cos^2\theta\frac{\partial\theta}{\partial x} - \sin\theta\cos\theta\frac{\partial\theta}{\partial y}\right)^2\right] \quad (\text{A.18})$$

$$= \frac{1}{2}K_1\left(\sin\theta\frac{\partial\theta}{\partial x} - \cos\theta\frac{\partial\theta}{\partial y}\right)^2 + \frac{1}{2}K_3\left[\sin^2\theta\left(\cos\theta\frac{\partial\theta}{\partial x} + \sin\theta\frac{\partial\theta}{\partial y}\right)^2 + \left(\cos^2\theta\left(\cos\theta\frac{\partial\theta}{\partial x} - \sin\theta\frac{\partial\theta}{\partial y}\right)^2\right)\right] \quad (\text{A.19})$$

$$\omega_N = \frac{1}{2}K_1\left(\sin\theta\frac{\partial\theta}{\partial x} - \cos\theta\frac{\partial\theta}{\partial y}\right)^2 + \frac{1}{2}K_3\left(\cos\theta\frac{\partial\theta}{\partial x} + \sin\theta\frac{\partial\theta}{\partial y}\right)^2 \quad (\text{A.20})$$

$$\omega_{Dielectric} = -\frac{1}{2}\left[\varepsilon_0\varepsilon_\perp\left(-\frac{\partial\theta}{\partial x}, -\frac{\partial\theta}{\partial y}, 0\right) + \varepsilon_0\Delta\varepsilon\left(-\cos\theta\frac{\partial\theta}{\partial x} - \sin\theta\frac{\partial\theta}{\partial y}, \cos\theta, \sin\theta, 0\right)\right] \cdot \left(-\frac{\partial\theta}{\partial x}, -\frac{\partial\theta}{\partial y}, 0\right) \quad (\text{A.21})$$

$$= -\frac{1}{2}\left[\left(-\varepsilon_0\varepsilon_\perp\frac{\partial U}{\partial x}, -\varepsilon_0\varepsilon_\perp\frac{\partial U}{\partial y}, 0\right) - \varepsilon_0\Delta\varepsilon\left(\cos\theta\frac{\partial U}{\partial x} + \sin\theta\frac{\partial U}{\partial y}, \cos\theta, \sin\theta, 0\right)\right] \cdot \left(-\frac{\partial U}{\partial x}, -\frac{\partial U}{\partial y}, 0\right) \quad (\text{A.22})$$

$$= -\frac{1}{2}\left[\left(-\varepsilon_0\varepsilon_\perp\frac{\partial U}{\partial x}, -\varepsilon_0\varepsilon_\perp\frac{\partial U}{\partial y}, 0\right) - \varepsilon_0\Delta\varepsilon\left(\cos^2\theta\frac{\partial U}{\partial x} + \sin\theta\cos\theta\frac{\partial U}{\partial y}, \sin\theta\cos\theta\frac{\partial U}{\partial x} + \sin^2\theta\frac{\partial U}{\partial y}, 0\right)\right] \cdot \left(-\frac{\partial U}{\partial x}, -\frac{\partial U}{\partial y}, 0\right) \quad (\text{A.23})$$

$$= -\frac{1}{2}\left[\left(-\varepsilon_0\varepsilon_\perp\frac{\partial U}{\partial x}, -\varepsilon_0\varepsilon_\perp\frac{\partial U}{\partial y}, 0\right) - \left(\varepsilon_0\Delta\varepsilon\cos^2\theta\frac{\partial U}{\partial x} + \varepsilon_0\Delta\varepsilon\sin\theta\cos\theta\frac{\partial U}{\partial y}, \varepsilon_0\Delta\varepsilon\sin\theta\cos\theta\frac{\partial U}{\partial x} + \varepsilon_0\Delta\varepsilon\sin^2\theta\frac{\partial U}{\partial y}, 0\right)\right] \cdot \left(-\frac{\partial U}{\partial x}, -\frac{\partial U}{\partial y}, 0\right) \quad (\text{A.24})$$

A.1. Interdigitated electrodes model

$$\begin{aligned} \omega_{Dielectric} = & -\frac{1}{2}\varepsilon_0[(\varepsilon_{\perp} \sin^2 \theta + \varepsilon_{\parallel} \cos^2 \theta)\left(\frac{\partial U}{\partial x}\right)^2 + (\varepsilon_{\perp} \cos^2 \theta + \varepsilon_{\parallel} \sin^2 \theta)\left(\frac{\partial U}{\partial y}\right)^2 \\ & + 2(\varepsilon_{\parallel} - \varepsilon_{\perp}) \sin \theta \cos \theta \frac{\partial U}{\partial x} \frac{\partial U}{\partial y}] \end{aligned} \quad (\text{A.33})$$

$$(\nabla \cdot \underline{n}) \times \underline{n} = \begin{vmatrix} \underline{i} & \underline{j} & \underline{k} \\ 0 & 0 & \cos \theta \frac{\partial \theta}{\partial x} + \sin \theta \frac{\partial \theta}{\partial y} \\ \cos \theta & \sin \theta & 0 \end{vmatrix} \quad (\text{A.34})$$

$$\begin{aligned} & = \underline{i}(-\sin \theta \cos \theta \frac{\partial \theta}{\partial x} - \sin^2 \theta \frac{\partial \theta}{\partial y}) - \underline{j}(-\cos^2 \theta \frac{\partial \theta}{\partial x} - \sin \theta \cos \theta \frac{\partial \theta}{\partial y}) + \underline{k}(0) \\ & = (-\sin \theta \cos \theta \frac{\partial \theta}{\partial x} - \sin^2 \theta \frac{\partial \theta}{\partial y}, \cos^2 \theta \frac{\partial \theta}{\partial x} + \sin \theta \cos \theta \frac{\partial \theta}{\partial y}, 0) \end{aligned} \quad (\text{A.35})$$

$$\omega_{flexoelectric} = -(e_{11}(\nabla \cdot \underline{n})\underline{n} + e_{33}(\nabla \times \underline{n} \times \underline{n})) \cdot \underline{E} \quad (\text{A.36})$$

$$\begin{aligned} & = -[e_{11}(-\sin \theta \frac{\partial \theta}{\partial x} + \cos \theta \frac{\partial \theta}{\partial y})(\cos \theta, \sin \theta, 0) \\ & + e_{33}(-\sin \theta \cos \theta \frac{\partial \theta}{\partial x} - \sin^2 \theta \frac{\partial \theta}{\partial y}, \cos^2 \theta \frac{\partial \theta}{\partial x} + \sin \theta \cos \theta \frac{\partial \theta}{\partial y}, 0)] \\ & \quad \cdot (-\frac{\partial U}{\partial x}, -\frac{\partial U}{\partial y}, 0) \end{aligned} \quad (\text{A.37})$$

$$\begin{aligned} & = -[e_{11}(-\sin \theta \cos \theta \frac{\partial \theta}{\partial x} + \cos^2 \theta \frac{\partial \theta}{\partial y}, -\sin^2 \theta \frac{\partial \theta}{\partial x} + \sin \theta \cos \theta \frac{\partial \theta}{\partial y}, 0) \\ & + (-e_{33} \sin \theta \cos \theta \frac{\partial \theta}{\partial x} - e_{33} \sin^2 \theta \frac{\partial \theta}{\partial y}, e_{33} \cos^2 \theta \frac{\partial \theta}{\partial x} + e_{33} \sin \theta \cos \theta \frac{\partial \theta}{\partial y}, 0) \\ & \quad \cdot (-\frac{\partial U}{\partial x}, -\frac{\partial U}{\partial y}, 0) \end{aligned} \quad (\text{A.38})$$

$$\begin{aligned} & = -[(-e_{11} \sin \theta \cos \theta \frac{\partial \theta}{\partial x} + e_{11} \cos^2 \theta \frac{\partial \theta}{\partial y}, -e_{11} \sin^2 \theta \frac{\partial \theta}{\partial x} + e_{11} \sin \theta \cos \theta \frac{\partial \theta}{\partial y}, 0) \\ & + (-e_{33} \sin \theta \cos \theta \frac{\partial \theta}{\partial x} - e_{33} \sin^2 \theta \frac{\partial \theta}{\partial y}, e_{33} \cos^2 \theta \frac{\partial \theta}{\partial x} + e_{33} \sin \theta \cos \theta \frac{\partial \theta}{\partial y}, 0) \\ & \quad \cdot (-\frac{\partial U}{\partial x}, -\frac{\partial U}{\partial y}, 0) \end{aligned} \quad (\text{A.39})$$

$$\begin{aligned} & = -[-e_{11} \sin \theta \cos \theta \frac{\partial \theta}{\partial x} + e_{11} \cos^2 \theta \frac{\partial \theta}{\partial y} - e_{33} \sin \theta \cos \theta \frac{\partial \theta}{\partial x} - e_{33} \sin^2 \theta \frac{\partial \theta}{\partial y}, \\ & \quad -e_{11} \sin^2 \theta \frac{\partial \theta}{\partial x} + e_{11} \sin \theta \cos \theta \frac{\partial \theta}{\partial y} + e_{33} \cos^2 \theta \frac{\partial \theta}{\partial x} + e_{33} \sin \theta \cos \theta \frac{\partial \theta}{\partial y}, 0] \\ & \quad \cdot (-\frac{\partial U}{\partial x}, -\frac{\partial U}{\partial y}, 0) \end{aligned} \quad (\text{A.40})$$

A.1. Interdigitated electrodes model

$$\begin{aligned}
&= [(e_{11} \cos^2 \theta - e_{33} \sin^2 \theta) \frac{\partial \theta}{\partial y} - (e_{11} + e_{33}) \sin \theta \cos \theta \frac{\partial \theta}{\partial x}, \\
&+ (e_{33} \cos^2 \theta - e_{11} \sin^2 \theta) \frac{\partial \theta}{\partial x} + (e_{11} + e_{33}) \sin \theta \cos \theta \frac{\partial \theta}{\partial y}, 0] \\
&\quad \cdot \left(\frac{\partial U}{\partial x}, \frac{\partial U}{\partial y}, 0 \right)
\end{aligned} \tag{A.41}$$

$$\begin{aligned}
\omega_{flexoelectric} &= [(e_{11} \cos^2 \theta - e_{33} \sin^2 \theta) \frac{\partial \theta}{\partial y} \frac{\partial U}{\partial x} - (e_{11} + e_{33}) \sin \theta \cos \theta \frac{\partial \theta}{\partial x} \frac{\partial U}{\partial x} \\
&+ (e_{33} \cos^2 \theta - e_{11} \sin^2 \theta) \frac{\partial \theta}{\partial x} \frac{\partial U}{\partial y} + (e_{11} + e_{33}) \sin \theta \cos \theta \frac{\partial \theta}{\partial y} \frac{\partial U}{\partial y}
\end{aligned} \tag{A.42}$$

$$\begin{aligned}
\omega &= \frac{1}{2} K_1 \left(\sin \theta \frac{\partial \theta}{\partial x} - \cos \theta \frac{\partial \theta}{\partial y} \right)^2 + \frac{1}{2} K_3 \left(\cos \theta \frac{\partial \theta}{\partial x} + \sin \theta \frac{\partial \theta}{\partial y} \right)^2 \\
&- \frac{1}{2} \varepsilon_0 [(\varepsilon_{\perp} \sin^2 \theta + \varepsilon_{\parallel} \cos^2 \theta) \left(\frac{\partial U}{\partial x} \right)^2 + (\varepsilon_{\perp} \cos^2 \theta + \varepsilon_{\parallel} \sin^2 \theta) \left(\frac{\partial U}{\partial y} \right)^2 \\
&+ 2(\varepsilon_{\parallel} - \varepsilon_{\perp}) \sin \theta \cos \theta \frac{\partial U}{\partial x} \frac{\partial U}{\partial y}] + [(e_{11} \cos^2 \theta - e_{33} \sin^2 \theta) \frac{\partial \theta}{\partial y} \frac{\partial U}{\partial x} \\
&- (e_{11} + e_{33}) \sin \theta \cos \theta \frac{\partial \theta}{\partial x} \frac{\partial U}{\partial x} + (e_{33} \cos^2 \theta - e_{11} \sin^2 \theta) \frac{\partial \theta}{\partial x} \frac{\partial U}{\partial y} \\
&\quad + (e_{11} + e_{33}) \sin \theta \cos \theta \frac{\partial \theta}{\partial y} \frac{\partial U}{\partial y}
\end{aligned} \tag{A.43}$$

Assume no flow:

$$\mathbf{v} = (0, 0, 0) \tag{A.44}$$

Rate of strain tensor:

$$A_{ij} = \frac{1}{2} (v_{i,j} + v_{j,i}) = 0 \tag{A.45}$$

Vorticity tensor:

$$\omega_{ij} = \frac{1}{2} (v_{i,j} - v_{j,i}) = 0 \tag{A.46}$$

Co-rotationnal time flux of the director:

$$Ni = \dot{n}_i - \omega_{ij} n_j \equiv \dot{n} \tag{A.47}$$

Viscous dissipation inequality:

$$D = \alpha_1(n_i A_{ij} n_j)^2 + 2\gamma_2 N_i A_{ij} n_j + \alpha_4 A_{ij} A_{ij} + (\alpha_5 + \alpha_6) n_i A_{ij} A_{jk} n_k + \gamma_i N_i N_i \geq 0 \quad (\text{A.48})$$

$$\Rightarrow D = \gamma_i N_i N_i \geq 0 \Rightarrow D = \gamma_i \dot{n}_i \dot{n}_i \quad (\text{A.49})$$

$$\underline{n} = \underline{n}(\theta) \quad (\text{A.50})$$

$$\omega = \omega(\theta, \theta_i) \quad (\text{A.51})$$

$$D = (A_{ij}, N_i, n_i) = 2\hat{D}(v_{ij}, \dot{\theta}, \theta) \quad (\text{A.52})$$

Balance of angular momentum becomes:

$$\left(\frac{\partial \omega}{\partial \theta_i} \right)_i - \frac{\partial \omega}{\partial \theta} - \frac{\partial \hat{D}}{\partial \dot{\theta}} = 0 \quad (\text{A.53})$$

$$\Rightarrow \left(\frac{\partial \omega}{\partial \left(\frac{\partial \theta}{\partial x} \right)} \right)_x + \left(\frac{\partial \omega}{\partial \left(\frac{\partial \theta}{\partial y} \right)} \right)_y - \frac{\partial \omega}{\partial \theta} - \frac{\partial \hat{D}}{\partial \dot{\theta}} = 0 \quad (\text{A.54})$$

$$\begin{aligned} \frac{\partial \omega}{\left(\frac{\partial \theta}{\partial x} \right)} = & K_1 \left(\sin \theta \frac{\partial \theta}{\partial x} - \cos \theta \frac{\partial \theta}{\partial y} \right) \sin \theta + K_3 \left(\cos \theta \frac{\partial \theta}{\partial x} + \sin \theta \frac{\partial \theta}{\partial y} \right) \cos \theta \\ & - (e_{11} + e_{33}) \sin \theta \cos \theta \frac{\partial \theta}{\partial x} + (e_{33} \cos^2 \theta - e_{11} \sin^2 \theta) \frac{\partial \theta}{\partial y} \end{aligned} \quad (\text{A.55})$$

$$\begin{aligned} \frac{\partial \omega}{\left(\frac{\partial \theta}{\partial y} \right)} = & K_1 \left(\sin \theta \frac{\partial \theta}{\partial x} - \cos \theta \frac{\partial \theta}{\partial y} \right) (-\cos \theta) + K_3 \left(\cos \theta \frac{\partial \theta}{\partial x} + \sin \theta \frac{\partial \theta}{\partial y} \right) (\sin \theta) \\ & + (e_{11} \cos^2 \theta - e_{33} \sin^2 \theta) \frac{\partial \theta}{\partial x} + (e_{11} + e_{33}) \sin \theta \cos \theta \frac{\partial \theta}{\partial y} \end{aligned} \quad (\text{A.56})$$

$$\begin{aligned}
\frac{\partial \omega}{\partial \theta} &= K_1 \left(\sin \theta \frac{\partial \theta}{\partial x} - \cos \theta \frac{\partial \theta}{\partial y} \right) \left(\cos \theta \frac{\partial \theta}{\partial x} + \sin \theta \frac{\partial \theta}{\partial y} \right) \\
&\quad + K_3 \left(\cos \theta \frac{\partial \theta}{\partial x} + \sin \theta \frac{\partial \theta}{\partial y} \right) \left(-\sin \theta \frac{\partial \theta}{\partial x} + \cos \theta \frac{\partial \theta}{\partial y} \right) \\
&\quad - \frac{1}{2} \varepsilon_0 [(-2\varepsilon_{\parallel} \cos \theta \sin \theta + 2\varepsilon_{\perp} \sin \theta \cos \theta) \left(\frac{\partial U}{\partial x} \right)^2 \\
&\quad + (2\varepsilon_{\parallel} \sin \theta \cos \theta + 2\varepsilon_{\perp} \cos \theta \sin \theta) \left(\frac{\partial U}{\partial y} \right)^2 + 2(\varepsilon_{\parallel} - \varepsilon_{\perp}) \cos(2\theta) \frac{\partial U}{\partial x} \frac{\partial U}{\partial y} \\
&\quad + (-2e_{11} \cos \theta \sin \theta - 2e_{33} \sin \theta \cos \theta) \frac{\partial \theta}{\partial y} \frac{\partial U}{\partial x} - (e_{11} + e_{33}) \cos(2\theta) \frac{\partial \theta}{\partial x} \frac{\partial U}{\partial x} \\
&\quad + (-2e_{33} \cos \theta \sin \theta - 2e_{11} \sin \theta \cos \theta) \frac{\partial \theta}{\partial x} \frac{\partial U}{\partial y} + (e_{11} + e_{33}) \cos(2\theta) \frac{\partial \theta}{\partial y} \frac{\partial U}{\partial y} \\
\Rightarrow &= K_1 \left(\sin \theta \cos \theta \left(\frac{\partial \theta}{\partial x} \right)^2 + \sin^2 \theta \frac{\partial \theta}{\partial x} \frac{\partial \theta}{\partial y} - \cos^2 \theta \frac{\partial \theta}{\partial x} \frac{\partial \theta}{\partial y} - \sin \theta \cos \theta \left(\frac{\partial \theta}{\partial y} \right)^2 \right) \\
&\quad + K_3 \left(-\sin \theta \cos \theta \left(\frac{\partial \theta}{\partial x} \right)^2 + \cos^2 \theta \frac{\partial \theta}{\partial x} \frac{\partial \theta}{\partial y} - \sin^2 \theta \frac{\partial \theta}{\partial x} \frac{\partial \theta}{\partial y} + \sin \theta \cos \theta \left(\frac{\partial \theta}{\partial y} \right)^2 \right) \\
&\quad - \frac{1}{2} \varepsilon_0 [-2(\varepsilon_{\parallel} - \varepsilon_{\perp}) \sin \theta \cos \theta \left(\frac{\partial U}{\partial x} \right)^2 + 2(\varepsilon_{\parallel} - \varepsilon_{\perp}) \sin \theta \cos \theta \left(\frac{\partial U}{\partial y} \right)^2 \\
&\quad + 2(\varepsilon_{\parallel} - \varepsilon_{\perp}) \cos(2\theta) \frac{\partial U}{\partial x} \frac{\partial U}{\partial y}] - 2(e_{11} + e_{33}) \sin \theta \cos \theta \frac{\partial \theta}{\partial y} \frac{\partial U}{\partial x} \\
&\quad - (e_{11} + e_{33}) \cos(2\theta) \frac{\partial \theta}{\partial x} \frac{\partial U}{\partial x} - 2(e_{11} + e_{33}) \sin \theta \cos \theta \frac{\partial \theta}{\partial x} \frac{\partial U}{\partial y} \\
&\quad + (e_{11} + e_{33}) \cos(2\theta) \frac{\partial \theta}{\partial y} \frac{\partial U}{\partial y} \\
\end{aligned} \tag{A.57}$$

$$\begin{aligned}
\Rightarrow &= K_1 \left(\sin \theta \cos \theta \left[\left(\frac{\partial \theta}{\partial x} \right)^2 - \left(\frac{\partial \theta}{\partial y} \right)^2 \right] - \cos(2\theta) \frac{\partial \theta}{\partial x} \frac{\partial \theta}{\partial y} \right) \\
&\quad + K_3 \left(\sin \theta \cos \theta \left[\left(\frac{\partial \theta}{\partial y} \right)^2 - \left(\frac{\partial \theta}{\partial x} \right)^2 \right] - \cos(2\theta) \frac{\partial \theta}{\partial x} \frac{\partial \theta}{\partial y} \right) \\
&\quad - \frac{1}{2} \varepsilon_0 [-(\varepsilon_{\parallel} - \varepsilon_{\perp}) \sin(2\theta) \left(\frac{\partial U}{\partial x} \right)^2 + (\varepsilon_{\parallel} - \varepsilon_{\perp}) \sin(2\theta) \left(\frac{\partial U}{\partial y} \right)^2 \\
&\quad + 2(\varepsilon_{\parallel} - \varepsilon_{\perp}) \cos(2\theta) \frac{\partial U}{\partial x} \frac{\partial U}{\partial y}] - (e_{11} + e_{33}) \sin(2\theta) \frac{\partial \theta}{\partial y} \frac{\partial U}{\partial x} \\
&\quad - (e_{11} + e_{33}) \cos(2\theta) \frac{\partial \theta}{\partial x} \frac{\partial U}{\partial x} - (e_{11} + e_{33}) \sin(2\theta) \frac{\partial \theta}{\partial x} \frac{\partial U}{\partial y} \\
&\quad + (e_{11} + e_{33}) \cos(2\theta) \frac{\partial \theta}{\partial y} \frac{\partial U}{\partial y} \\
\end{aligned} \tag{A.59}$$

$$\begin{aligned}
&\Rightarrow = (K_1 - K_3) \sin \theta \cos \theta \left[\left(\frac{\partial \theta}{\partial x} \right)^2 - \left(\frac{\partial \theta}{\partial y} \right)^2 \right] - (K_1 - K_3) \cos(2\theta) \frac{\partial \theta}{\partial x} \frac{\partial \theta}{\partial y} \\
&- \frac{1}{2} \varepsilon_0 \left[(\varepsilon_{\parallel} - \varepsilon_{\perp}) \sin(2\theta) \left[\left(\frac{\partial U}{\partial y} \right)^2 - \left(\frac{\partial U}{\partial x} \right)^2 \right] + 2(\varepsilon_{\parallel} - \varepsilon_{\perp}) \cos(2\theta) \frac{\partial U}{\partial x} \frac{\partial U}{\partial y} \right] \\
&- (e_{11} + e_{33}) \sin(2\theta) \left[\frac{\partial \theta}{\partial x} \frac{\partial U}{\partial y} + \frac{\partial \theta}{\partial y} \frac{\partial U}{\partial x} \right] - (e_{11} + e_{33}) \cos(2\theta) \left[\frac{\partial \theta}{\partial x} \frac{\partial U}{\partial x} - \frac{\partial \theta}{\partial y} \frac{\partial U}{\partial y} \right]
\end{aligned} \tag{A.60}$$

$$\begin{aligned}
\frac{\partial \omega}{\partial \theta} &= \frac{1}{2} (K_1 - K_3) \sin(2\theta) \left[\left(\frac{\partial \theta}{\partial x} \right)^2 - \left(\frac{\partial \theta}{\partial y} \right)^2 \right] - (K_1 - K_3) \cos(2\theta) \frac{\partial \theta}{\partial x} \frac{\partial \theta}{\partial y} \\
&- \frac{1}{2} \varepsilon_0 (\varepsilon_{\parallel} - \varepsilon_{\perp}) \sin(2\theta) \left[\left(\frac{\partial U}{\partial y} \right)^2 - \left(\frac{\partial U}{\partial x} \right)^2 \right] - \varepsilon_0 (\varepsilon_{\parallel} - \varepsilon_{\perp}) \cos(2\theta) \frac{\partial U}{\partial x} \frac{\partial U}{\partial y} \\
&- (e_{11} + e_{33}) \sin(2\theta) \left[\frac{\partial \theta}{\partial x} \frac{\partial U}{\partial y} + \frac{\partial \theta}{\partial y} \frac{\partial U}{\partial x} \right] - (e_{11} + e_{33}) \cos(2\theta) \left[\frac{\partial \theta}{\partial x} \frac{\partial U}{\partial x} - \frac{\partial \theta}{\partial y} \frac{\partial U}{\partial y} \right]
\end{aligned} \tag{A.61}$$

$$\begin{aligned}
\frac{\partial \hat{D}}{\partial \dot{\theta}} &= \frac{\partial}{\partial \dot{\theta}} \frac{1}{2} D = \frac{1}{2} \frac{\partial}{\partial \dot{\theta}} (\gamma_1 \dot{n}_i \dot{n}_i) = \frac{1}{2} \frac{\partial}{\partial \dot{\theta}} \left(\gamma_1 \left[(-\sin \theta \dot{\theta})^2 + (\cos \theta \dot{\theta})^2 \right] \right) \\
&\Rightarrow = \frac{1}{2} \frac{\partial}{\partial \dot{\theta}} \left(\gamma_1 \left[-\sin^2 \theta \dot{\theta}^2 + \cos^2 \theta \dot{\theta}^2 \right] \right) = \frac{1}{2} \gamma_1 \frac{\partial}{\partial \dot{\theta}} (\dot{\theta}^2) = \gamma_1 \dot{\theta} = \gamma_1 \frac{\partial \theta}{\partial t}
\end{aligned} \tag{A.62}$$

So the balance of the angular momentum becomes:

$$\begin{aligned}
&\frac{\partial}{\partial x} \left[K_1 \left(\sin \theta \frac{\partial \theta}{\partial x} - \cos \theta \frac{\partial \theta}{\partial y} \right) \sin \theta + K_3 \left(\cos \theta \frac{\partial \theta}{\partial x} + \sin \theta \frac{\partial \theta}{\partial y} \right) \cos \theta \right. \\
&\quad \left. - (e_{11} + e_{33}) \sin \theta \cos \theta \frac{\partial U}{\partial x} + (e_{33} \cos^2 \theta - e_{11} \sin^2 \theta) \frac{\partial U}{\partial y} \right] \\
&\frac{\partial}{\partial y} \left[-K_1 \left(\sin \theta \frac{\partial \theta}{\partial x} - \cos \theta \frac{\partial \theta}{\partial y} \right) \cos \theta + K_3 \left(\cos \theta \frac{\partial \theta}{\partial x} + \sin \theta \frac{\partial \theta}{\partial y} \right) \sin \theta \right. \\
&\quad \left. + (e_{11} \cos^2 \theta - e_{33} \sin^2 \theta) \frac{\partial U}{\partial x} + (e_{11} + e_{33}) \sin \theta \cos \theta \frac{\partial U}{\partial y} \right] \\
&- \frac{1}{2} (K_1 - K_3) \sin(2\theta) \left[\left(\frac{\partial \theta}{\partial x} \right)^2 - \left(\frac{\partial \theta}{\partial y} \right)^2 \right] + (K_1 - K_3) \cos(2\theta) \frac{\partial \theta}{\partial x} \frac{\partial \theta}{\partial y} \\
&+ \frac{1}{2} \varepsilon_0 (\varepsilon_{\parallel} - \varepsilon_{\perp}) \sin(2\theta) \left[\left(\frac{\partial U}{\partial y} \right)^2 - \left(\frac{\partial U}{\partial x} \right)^2 \right] + \varepsilon_0 (\varepsilon_{\parallel} - \varepsilon_{\perp}) \cos(2\theta) \frac{\partial U}{\partial x} \frac{\partial U}{\partial y} \\
&+ (e_{11} + e_{33}) \sin(2\theta) \left[\frac{\partial \theta}{\partial x} \frac{\partial U}{\partial y} + \frac{\partial \theta}{\partial y} \frac{\partial U}{\partial x} \right] + (e_{11} + e_{33}) \cos(2\theta) \left[\frac{\partial \theta}{\partial x} \frac{\partial U}{\partial x} - \frac{\partial \theta}{\partial y} \frac{\partial U}{\partial y} \right] \\
&\quad - \gamma_1 \frac{\partial \theta}{\partial t} = 0
\end{aligned} \tag{A.63}$$

A.1. Interdigitated electrodes model

This is the expression for theta in the model but it need to be in the form of:

$$da \frac{\partial U}{\partial t} + \nabla \cdot \underline{\Gamma} = F \quad (\text{A.64})$$

The energy must also be minimised with respect to U: Euler-Lagrange equation

$$\left(\frac{\partial \omega}{\partial \left(\frac{\partial U}{\partial x} \right)} \right)_x + \left(\frac{\partial \omega}{\partial \left(\frac{\partial U}{\partial y} \right)} \right)_y - \frac{\partial \omega}{\partial U} = 0 \quad (\text{A.65})$$

$$\nabla \cdot \underline{D} = 0 \quad (\text{A.66})$$

$$D = D_{elect} + D_{flexo} \quad (\text{A.67})$$

$$[\nabla \cdot (D_{elect} + D_{flexo})] = 0 \quad (\text{A.68})$$

$$\begin{aligned} \left(\frac{\partial \omega}{\partial \left(\frac{\partial U}{\partial x} \right)} \right) &= -\frac{1}{2} \varepsilon_0 \left[2 (\varepsilon_{\parallel} \sin^2 \theta + \varepsilon_{\perp} \cos^2 \theta) \left(\frac{\partial U}{\partial x} \right) + 2 (\varepsilon_{\parallel} - \varepsilon_{\perp}) \sin \theta \cos \theta \frac{\partial U}{\partial y} \right] \\ &\quad + (e_{11} \cos^2 \theta - e_{33} \sin^2 \theta) \frac{\partial \theta}{\partial y} - (e_{11} + e_{33}) \sin \theta \cos \theta \frac{\partial \theta}{\partial x} \end{aligned} \quad (\text{A.69})$$

$$\begin{aligned} \left(\frac{\partial \omega}{\partial \left(\frac{\partial U}{\partial y} \right)} \right) &= -\frac{1}{2} \varepsilon_0 \left[2 (\varepsilon_{\parallel} \cos^2 \theta + \varepsilon_{\perp} \sin^2 \theta) \left(\frac{\partial U}{\partial y} \right) + 2 (\varepsilon_{\parallel} - \varepsilon_{\perp}) \sin \theta \cos \theta \frac{\partial U}{\partial x} \right] \\ &\quad + (e_{33} \cos^2 \theta - e_{11} \sin^2 \theta) \frac{\partial \theta}{\partial x} - (e_{11} + e_{33}) \sin \theta \cos \theta \frac{\partial \theta}{\partial y} \end{aligned} \quad (\text{A.70})$$

$$\frac{\partial \omega}{\partial U} = 0 \quad (\text{A.71})$$

The expression for the potential becomes:

$$\begin{aligned}
& \frac{\partial}{\partial x} \left(-\frac{1}{2} \varepsilon_0 \left[2 (\varepsilon_{\parallel} \sin^2 \theta + \varepsilon_{\perp} \cos^2 \theta) \left(\frac{\partial U}{\partial x} \right) + 2 (\varepsilon_{\parallel} - \varepsilon_{\perp}) \sin \theta \cos \theta \frac{\partial U}{\partial y} \right] \right. \\
& \quad \left. + (e_{11} \cos^2 \theta - e_{33} \sin^2 \theta) \frac{\partial \theta}{\partial y} - (e_{11} + e_{33}) \sin \theta \cos \theta \frac{\partial \theta}{\partial x} \right) \\
& + \frac{\partial}{\partial y} \left(-\frac{1}{2} \varepsilon_0 \left[2 (\varepsilon_{\parallel} \cos^2 \theta + \varepsilon_{\perp} \sin^2 \theta) \left(\frac{\partial U}{\partial y} \right) + 2 (\varepsilon_{\parallel} - \varepsilon_{\perp}) \sin \theta \cos \theta \frac{\partial U}{\partial x} \right] \right. \\
& \quad \left. + (e_{33} \cos^2 \theta - e_{11} \sin^2 \theta) \frac{\partial \theta}{\partial x} - (e_{11} + e_{33}) \sin \theta \cos \theta \frac{\partial \theta}{\partial y} \right) = 0
\end{aligned} \tag{A.72}$$

A.2 Regression analysis for the spectrometer data

Regression Analysis: Wave number (N) versus n

The regression equation is
 Wave number (N) = - 70.4 + 0.000057 n

Predictor	Coef	SE Coef	T	P
Constant	-70.3931	0.0304	-2319.12	0.000
n	0.00005704	0.00000002	2948.54	0.000

S = 0.0211392 R-Sq = 100.0% R-Sq(adj) = 100.0%

Analysis of Variance

Source	DF	SS	MS	F	P
Regression	1	3885.0	3885.0	8693867.19	0.000
Residual Error	34	0.0	0.0		
Total	35	3885.0			

Unusual Observations

Obs	n	Wave number (N)	Fit	SE Fit	Residual	St Resid
1	1252427	1.0000	1.0507	0.0069	-0.0507	-2.54R

R denotes an observation with a large standardized residual.

Figure A.2: Regression analysis from the spectrometer data for the determination of the sample thickness

A.3 Regression analysis for determination of the calibration factor of the electromagnet

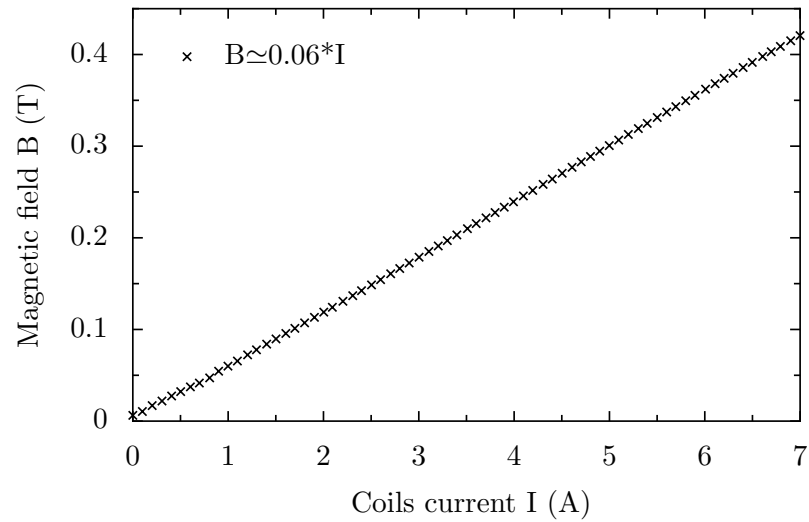


Figure A.3: Calibration curve for the magnetic field as function of the current in the coils

A.4 Regression analysis for the $\ln(A/V^2)$ vs. h/d

A.4. Regression analysis for the $\ln(A/V^2)$ vs. h/d

Regression Analysis: B (T) versus I (A)

The regression equation is
 $B \text{ (T)} = 0.000170 + 0.0601 \text{ I (A)}$

Predictor	Coef	SE Coef	T	P
Constant	0.0001698	0.0003729	0.46	0.650
I (A)	0.0600563	0.0000919	653.37	0.000

S = 0.00158669 R-Sq = 100.0% R-Sq(adj) = 100.0%

Analysis of Variance

Source	DF	SS	MS	F	P
Regression	1	1.0747	1.0747	426896.77	0.000
Residual Error	69	0.0002	0.0000		
Total	70	1.0749			

Unusual Observations

Obs	I (A)	B (T)	Fit	SE Fit	Residual	St Resid
1	0.00	0.006268	0.000170	0.000373	0.006098	3.95R
2	0.10	0.010492	0.006175	0.000365	0.004317	2.80R
3	0.20	0.016934	0.012361	0.000357	0.004573	2.96R
4	0.31	0.021930	0.018547	0.000349	0.003383	2.19R

R denotes an observation with a large standardized residual.

Figure A.4: Regression analysis for the determination of the factor between the current in the coils and the magnetic field generated

A.4. Regression analysis for the $\ln(A/V^2)$ vs. h/d

Regression Analysis: Gradient (A/V^2) versus (h/d)

The regression equation is
Gradient (A/V^2) = 1.61 - 8.74 (h/d)

Predictor	Coef	SE Coef	T	P
Constant	1.6144	0.2194	7.36	0.000
(h/d)	-8.740	1.549	-5.64	0.000

S = 0.363201 R-Sq = 72.6% R-Sq(adj) = 70.4%

Analysis of Variance

Source	DF	SS	MS	F	P
Regression	1	4.2009	4.2009	31.85	0.000
Residual Error	12	1.5830	0.1319		
Total	13	5.7839			

Unusual Observations

Obs	(h/d)	Gradient (A/V^2)	Fit	SE Fit	Residual	St Resid
2	0.121	-0.1744	0.5590	0.0976	-0.7334	-2.10R

R denotes an observation with a large standardized residual.

Figure A.5: Regression analysis for the $\ln(A/V^2)$ vs. h/d

References

- [1] P.G. de Gennes and J. Prost. *The physics of Liquid Crystals*. Oxford Science Publications, 2nd edition, 1993.
- [2] P.J. Collings. *Liquid Crystal, Nature's Delicate Phase of Matter*. IOP Publishing Ltd, 1990.
- [3] F. Reinitzer. Contribution to the knowledge of cholesterol (translation from the original german article from 1888). *Liquid Crystals*, 5:7–18, 1989.
- [4] P.J. Collings and J.S. Patel, editors. *Handbook of Liquid Crystal Research*. Oxford University Press, 1997.
- [5] S. Chandrasekhar. *Liquid Crystals*. Cambridge University Press, 1977.
- [6] J. Cognard. *Molecular Crystals and Liquid Crystals: Supplement 1 Alignment of nematic liquid crystals and their mixture*. Gordon and Breach Sciencw Publishers, 1982.
- [7] I.-C. Khoo. *Liquid Crystals: Physical Properties and Nonlinear Optical Phenomena*. John Wiley & sons, Inc., 1995.
- [8] P.J. Collings and M. Hird. *Introduction to Liquid Crystals, Chemistry and Physics*. Taylor & Francis, 1997.
- [9] W.H. De Jeu. *Physical Properties of Liquid Crystalline Materials*. Gordon and Breach Sciencw Publishers, 1980.

- [10] F.L. Pedrotti, L.S. Pedrotti, and L.M. Pedrotti. *Introduction to Optics 3rd edition*. Pearson International Edition, 2007.
- [11] E. Hecht. *Optics 4th Edition*. Addison Wesley, 2002.
- [12] F.A. Jenkins and H.E. White. *Fundamentals of Optics*. Mc Graw-Hill International Editions, 1981.
- [13] M. Born and E. Wolf. *Principle of Optics 7th edition: Electromagnetic Theory of Propagation, Interference and Diffraction of light*. Cambridge University Press, 1999.
- [14] L.M. Blinov. *Electro-Optical and Magneto-Optical Properties of Liquid Crystals*. John Wiley & sons, Inc., 1983.
- [15] E.A. Wood. *Crystals and Light, an introduction to optical crystallography*. Dover Publication Inc., 2nd edition, 1977.
- [16] D.R. Lide. Crc handbook of chemistry and physics, internet version 2005.
- [17] C.V. Brown. Msc lectures notes, 2003.
- [18] C.W. Oseen. Beitrage zur theorie der anisotropen flussigkeiten. *Arkiv for Matematik, Astronomi och Fysik*, 19A(9):1–19, 1025.
- [19] C.W. Oseen. The theory of liquid crystals. *Transmission Faraday Society*, 29:883–889, 1933.
- [20] H. Zocher. Uber die einwirkung magnetischer, elektrischer und mechanischer krafte auf mesophasen. *Physik. Zietschr*, 28:790–796, 1927.
- [21] F.C. Frank. On the theory of liquid crystals. *Discussion Faraday Society*, 25:19–28, 1958.
- [22] J. L. Eriksen. Conservation laws for liquid crystals. *Transaction of the Society of Rheology*, 5:23–24, 1961.

- [23] Guest Ed. H. Stegemeyer. *Topics in Physical Chemistry vol.3: Liquid Crystals*. Steinkopff Darmstadt Springer New York, 1994.
- [24] J.F. Stromer, E.P. Raynes, and C.V. Brown. Study of elastic constant ratios in nematic liquid crystals. *Applied Physics Letters*, 88(5), 2006.
- [25] V. Freedericksz and V. Zolina. Force causing the orientational of an anisotropic liquid. *Transmission Faraday Society*, 29:919–930, 1993.
- [26] Iain W. Stewart. *The static and dynamic continuum theory of liquid crystals: A mathematical introduction*. Taylor & Francis, 2004.
- [27] R.B.Meyer. Piezoelectric effects in liquid crystals. *Physical Review Letters*, 22(18):918, May 1969.
- [28] Jeffrey L. Billeter and Robert A. Pelcovits. Molecular shape and flexoelectricity. *Liquid Crystals*, 27(9):1151–1160, 2000.
- [29] Alberta Ferrarini. Shape model for molecular interpretation of flexoelectric effect. *Physical Review E*, 64:021710, 2001.
- [30] P. Rudquist and S.T. Lagerwall. On the flexoelectric effect in nematics. *Liquid Crystals*, 23(4):503–510, 1997.
- [31] H.J. Deuling. The piezo-electric effect in nematic layers. *Molecular Crystals and Liquid Crystals*, 26:281–284, 1973.
- [32] H.J. Deuling. On a method to measure the flexoelectric coefficients of nematic liquid. *Solid State Communications*, 14:1073–1074, 1974.
- [33] Merck kgaa, darmstadt, germany.
- [34] Y. Yin, S.V. Shiyakovskii, A.B. Golovin, and O.D. Lavrentovich. Dielectric torque and orientation dynamics of liquid crystals with dielectric dispersion. *Physical Review Letters*, 95(8), August 2005.

- [35] R.G. Lindquist, J.H. Kulick, G.P. Nordin, J.M. Jarem, S.T. Kowel, and M. Friends. High-resolution liquid-crystal phase grating formed by fringing fields from interdigitated electrodes. *Optics Letters*, 19(9):670, May 1994.
- [36] E.E. Kriezis and C.V. Brown. *Handbook of Organic Electronics and Photonics, Chap 27: Liquid Crystal Diffractive Optical Elements*. American Scientific Publishers, 2006.
- [37] J.C. Kirsch, D.A. Gregory, M.W. Thie, and B.K. Jones. Modulation characteristics of the epon liquid crystal television. *Optical Engineering*, 31(5):963, May 1992.
- [38] V. Laude, S. Maze, P. Chavel, and Ph. Refregier. Amplitude and phase coding measurements of a liquid crystal television. *Optics Communications*, 103:33–38, 1993.
- [39] S.M. Sze. *Physics of semiconductor devices*. John Wiley & sons, Inc., 1981.
- [40] A.V. Zakharov and Ronald Y. Dong. Surface polarization and effective anchoring energy in liquid crystals. *Physical Review E*, 64:042701, 2001.
- [41] S.G. Hahm, T.J. Lee, S.W. Lee, J. Yoon, and M. Ree. Detailed investigation on factor governing liquid crystal alignment on rubbed polystyrene film. *Materials Science and Engineering B*, 2006.
- [42] J.A. Ekhoﬀ, M.J. Farrow, D.M. Walba, and K.L. Rowlen. Molecular orientation of a model liquid crystal alignment layer. *Talanta*, 60:801–808, 2003.
- [43] J.M. Hind, A.A.T. Smith, and C.V. Brown. Transient capacitance study of switching in the nematic fredericksz geometry. *Journal of applied Physics*, 100:094109, November 2006.
- [44] L Mach. Ueber einen interferenzrefraktor. *Zeitschrift Fur Instrumentenkunde*, 12:89, March 1892.

- [45] L. Zehnder. Ein neuer interferenzrefraktor. *Zeitschrift für Instrumentenkunde*, 11:275–285, 1891.
- [46] V. Shaoulov and J. Rolland. Compact relay lenses using microlenslet arrays. *International Optical Design Conference 2002 Proceeding of SPIE*, 4832(588):74–79, 2002.
- [47] M.S.L. Lee, Ph Lalanne, J.C. Rodier, P. Chavel, E. Cambril, and Y. Chen. Imaging with blazed-binary diffractive elements. *Journal of Optics A: Pure and Applied Optics*, 4:119–124, 2002.
- [48] M.S.L. Lee, P. Pichon, Ch Sauvan, Ph Lalanne, M. Hutley, D. Joyeux, P. Chavel, E. Cambril, and Y. Chen. Transmission blazed-binary grating for visible light operation: performances and interferometric characterization. *Journal of Optics A: Pure and Applied Optics*, 5:244–249, 2003.
- [49] M.V. Klein and T.E. Furtak. *Optics*, volume 2nd edition. Wiley, 1986.
- [50] W.A. Crossland and T.D. Wilkinson. *Nondisplay Applications of Liquid Crystals*, [*Handbook of Liquid Crystals*]. Wile-VCH, Weinhem, 1998.
- [51] U. Efron, B. Apter, and E. Bahat-Treidel. Fringing-field effect in liquid-crystal beam-steering devices: an approximate analytical model. *Journal of the Optical Society of America A-Optics Image Science and Vision*, 21(10):1996–2008, 2004.
- [52] E. Bahat-Treidel, B. Apter, and U. Efron. On the fringing-field effect in liquid-crystal beam-steerring devices. *Applied Optics*, 43(1):11–19, January 2004.
- [53] E. Hallstig, J. Stigwall, T. Martin, L. Sjoqvist, and M. Lindgren. Fringing fields in a liquid crystal spatial light modulator for beam steering. *Journal of Modern Optics*, 51(8):1233–1247, 2004.

- [54] D.P. Resler, D.S. Hobbs, R.C. Sharp, L.J. Friedman, and T.A. Dorschner. High-efficiency liquid-crystal optical phased-array beam steering. *Optics Letters*, 21(9):689–691, 1996.
- [55] A. Tanone, Z. Zhang, C.-M. Uang, and F.T.S. Yu. Optical beam-steering using a liquid-crystal television panel. *Microwave and Optical Technology Letters*, 7(6):285–289, April 1994.
- [56] R.M. Matic. Blazed phase liquid-crystal beam-steering. *SPIE Proceedings Laser Beam Propagation and Control*, 2120:194–205, January 1994.
- [57] Merck KGaA, Darmstadt, Germany.
- [58] J. Prost and P.S. Pershan. Flexoelectricity in nematic and smectic-A liquid crystals. *Journal of Applied Physics*, 47(6):2298–2312, June 1976.
- [59] A. Mazzulla, F. Ciuchi, and J.R. Sambles. Optical determination of flexoelectric coefficients and the surface polarization in a hybrid aligned nematic cell. *Physical Review E*, 64:021708, 2001.
- [60] G. Barbero and L.R. Evangelista. Comment on "optical determination of flexoelectric coefficients and surface polarization in hybrid aligned nematic cell". *Physical Review E*, 68:023701, 2003.
- [61] A. Mazzulla, F. Ciuchi, and J.R. Sambles. Reply to "comment on 'optical determination of flexoelectric coefficients and surface polarization in a hybrid aligned nematic cell'". *Physical Review E*, 68:023702, 2003.
- [62] N.V. Madhusudana and G. Durand. Linear flexo-electro-optic effect in a hybrid aligned nematic crystal cell. *Journal Physique Lettres*, 46:195–200, 1985.
- [63] B. Valenti, C. Bertoni, G. Barbero, P. Taverna-Valabrega, R. Bartolinortoni, G. Barbero, P. Taverna-Valabrega, and R. Bartolino. Flexoelectricity in

- the hybrid aligned nematic cell. *Molecular Crystals and Liquid Crystals*, 146:307–320, 1987.
- [64] L.M. Blinov, G. Durand, and S.V. Yablonsky. Curvature oscillations and linear electro-optical effect in a surface layer of a nematic liquid crystal. *Journal Physique II France*, 2:1287–1297, May 1992.
- [65] S.R. Warriar and N.V. Madhusudana. An ac electrooptic technique for measuring the flexoelectric coefficient (e_1+e_3) and anchoring energies of nematics. *Journal Physique II France*, 7:1789–1803, December 1997.
- [66] S.A. Jewell and J.R. Sambles. Fully leaky guided mode study of the flexoelectric effect and surface polarization in hybrid aligned nematic cells. *Journal of applied Physics*, 92(1):19, July 2002.
- [67] C. Kischka, L.A. Parry-Jones, S.J. Elston, and E.P. Raynes. Measurement of the sum ($e(1) + e(3)$) of the flexoelectric coefficients $e(1)$ and $e(3)$ of nematic liquid crystals using a hybrid aligned nematic (han) cell. *Molecular Crystals and Liquid Crystals*, 480:103, 2008.
- [68] S. Ponti, P. Zihlerl, and C. Ferrero. Flexoelectro-optic effect in a hybrid nematic cell. *Liquid Crystals*, 26(8):1171–1177, August 1999.
- [69] Taiju Takahashi, Shigeru Hashidate, Hirokazu Nishijou, Makio Usiu, Munehiro Kimura, and Tadashi Akahane. Novel measurement method for flexoelectric coefficients of nematic liquid crystals. *Jpn Journal of Applied Physics*, 37(4):1865–1869, April 1998.
- [70] Public Domain. Imagej image processing and analysis in java.
- [71] A.A.T. Smith. Private communications, 2007.
- [72] N.J. Mottram. Private communications, 2007.

- [73] Comsol multiphysics, comsol ltd, uh innovation centre, college lane, hatfield, hertfordshire al10 9ab, u.k.
- [74] A.A.T. Smith, C.V. Brown, and N.J. Mottram. Theoretical analysis of the magnetic freedericksz transition in the presence of flexoelectricity and ionic contamination. *Physical Review E*, 75(041704), 2007.
- [75] A. Kilian and S. Hess. Derivation and application of an algorithm for the numerical-calculation of the local orientation of nematic liquid-crystals. *Zeitschrift Fur Naturforschung Section A-A Journal of Physical Sciences*, 44(8):693–703, August 1989.
- [76] S. Dickmann, J. Eschler, O.Cossalter, and D.A. Mlynski. Simulation of lds including elastic anisotropy and inhomogeneous field. Technical report, Society for information Display International Symposium, 1993.
- [77] H. Miro, E.C. Gartland, J.R. Kelly, and P.J. Bos. Multidimensional director modeling using q tensor representation in a liquid crystal cell and its application to the pi cell with patterned electrodes. *Japanese Journal of Applied Physics*, 38(1A):135–146, January 1999.
- [78] M.J. Bradshaw and E.P. Raynes. Electric permittivities and elastic-constants of the cyano bi-cyclohexanes (cch). *Molecular Crystals and Liquid Crystals*, 72(2-3):35, 1981.
- [79] H. Mada and K. Osajima. Time response of a nematic liquid-crystal cell in a switched dc electric-field. *Journal of applied Physics*, 60(9):3111–3113, 1986.
- [80] M. Scalerandi, P. Pagliusi, G. Cipparrone, and Barbero G. Influence of the ions on the dynamical reponse of a nematic cell submitted to a dc voltage. *Physical Review E*, 69(051708), 2004.

- [81] F. M. Leslie. Continuum theory for nematic liquid-crystals. *Continuum Mechanics and Thermodynamics*, 4(3):167–175, August 1992.
- [82] L.M. Blinov, A.Y. Kabayenkov, and A.A. Sonin. Experiment studies of the anchoring energy of nematic liquid-crystals. *Liquid Crystals*, 5(2):645–661, 1989.
- [83] G. Barbero, A.K. Zvezdin, and L.R. Evangelista. Ionic adsorption and equilibrium distribution of charges in a nematic cell. *Physical Review E*, 59(2):1846–1849, February 1999.
- [84] C.V. Brown and N.J. Mottram. Influence of flexoelectricity above the nematic fredericksz transition. *Physical Review E*, 68(3), 2003.
- [85] R.A. Ewings, C. Kischka, L.A. Parry-Jones, and S.J. Elston. Measurement of the difference in flexoelectric coefficients of nematic liquid crystals using a twisted nematic geometry. *Physical Review E*, 73, 2006.
- [86] S.H. Perlmutter, D. Doroski, and G. Moddel. Degradation of liquid crystal device performance due to selective adsorption of ions. *Applied Physics Letters*, 69(9):1182–1184, August 1996.
- [87] M. Schadt and C. Von Planta. Conductivity relaxation in positive dielectric liquid crystals. *The Journal of Chemical Physics*, 63(10):4379, November 1975.
- [88] H. Seiberle and M. Schadt. Lc-conductivity and cell parameters; their influence on twisted nematic and supertwisted nematic liquid crystal displays. *Molecular Crystals and Liquid Crystals*, 239:229–244, 1994.
- [89] Z. Zou, N.A. Clark, and M.A. Handschy. Ionic transport effects in ssflc cells. *Ferroelectrics*, 121:147–158, 1991.

- [90] E. De Ley, V. Ferrara, C. Colpaert, B. Maximus, A. De Meyere, and F. Bernardini. Influence of ionic contaminations on ssfled addressing. *Ferroelectrics*, 178:1–16, 1996.
- [91] Grzegorz Derfel and Mariola Felczak. Polarized states of hybrid aligned nematic layers. *Liquid Crystals*, 29(7):889–897, 2002.
- [92] S.L. Cornford, T.S. Taphouse, and J.R. Sambles. Analysis of the sign-dependent switching observed in a hybrid aligned nematic cell. *New Journal of Physics*, 11:013045, January 2009.
- [93] S.K. Kwok and Y. Liao. Transient phenomena of relaxation from electric-field-induced nematic phase to cholesteric phase. *Journal of applied Physics*, 49(7):3970–3975, July 1978.
- [94] C.V. Brown, T. Muller, J.M. Hind, and A.A.T. Smith. Static and transient dielectric response of a nematic two frequency material. Unpublished, July 2007.
- [95] F. Brochard, P. Pieranski, and E. Guyon. Dynamics of the orientation of a nematic-liquid-crystal film in a variable magnetic field. *Physical Review Letters*, 28(26):1681–1683, June 1972.
- [96] P. Pieranski, F. Brochard, and E. Guyon. Static and dynamic behavior of a nematic liquid crystal in a magnetic field part ii: Dynamics. *Le Journal de Physique*, 34:35–48, January 1973.
- [97] C.L. Trabi, C.V. Brown, A.A.T. Smith, and N.J. Mottram. Interferometric method for determining the sum of the flexoelectric coefficients (e_1+e_3) in an ionic material. *Applied Physics Letters*, 92(22):223509, June 2008.
- [98] C.L. Trabi, A.A.T. Smith, and C.V. Brown. Interferometric method for the measurement of the flexoelectric polarisation using nematic liquid crystal phase grating. *Molecular Crystals and Liquid Crystals*, 509:378–392, 2009.

- [99] C.L. Trabi, A.A.T. Smith, N.J. Mottram, and C.V. Brown. Flexoelectric polarisation effects in nematic liquid crystal phase gratings. *Liquid Crystals XII Proceedings of the Society of Photo-Optical Instrumentation Engineers (SPIE)*, 7050:R500, 2008.
- [100] U.D. Kini. Magnetic and electric field induced periodic deformations in planar oriented nematics. *Liquid Crystals*, 24(2):177–199, 1998.
- [101] C.V. Brown, Em. E. Kriezis, and S.J. Elston. Optical diffraction from a liquid crystal phase grating. *Journal of applied Physics*, 91(6):3495, March 2002.
- [102] Merck kga, darmstadt, germany.
- [103] User’s manual.
- [104] J. Cheng. Surface pinning of disclinations and the stability of bistable nematic storage displays. *Journal of applied Physics*, 52(2):724, February 1981.
- [105] A. Majumdar, C.J.P. Newton, J.M Robbins, and M. Zyskin. Topology and bistability in liquid crystal devices. *Physical Review E*, 75, 2007.
- [106] S. Kitson and A. Geisow. Controllable alignment of nematic liquid crystals around microscopic posts: Stabilization of multiple states. *Applied Physics Letters*, 80(19):3635–3637, 2002.
- [107] C. Tsakonas, A.J. Davidson, C.V. Brown, and N.J. Mottram. Multistable alignment states in nematic liquid crystal filled wells. *Applied Physics Letters*, 90:111913, 2007.
- [108] C. Uche, S.J. Elston, and L.A. Parry-Jones. Microscopic observation of zenithal bistable switching in nematic devices with different surface relief structures. *Journal of Physics D: Applied Physics*, 38:2283–2291, 2005.

- [109] R. Barberi, J.J. Bonvent, M. Giocondo, M. Iovane, and A.L. Alexe-Ionescu. Bistable nematic azimuthal induced by anchoring competition. *Journal of applied Physics*, 84(3):1321–1324, August 1998.
- [110] C.V. Brown, M.J. Towler, V.C. Hui, and G.P. Bryan-Brown. Numerical analysis of nematic liquid crystal alignment on asymmetric surface grating structures. *Liquid Crystals*, 27(2):233–242, 2000.
- [111] J-H Kim, M. Yoneya, J. Yamamoto, and H. Yokoyama. Surface alignment bistability of nematic liquid crystals by orientationally frustrated surface patterns. *Applied Physics Letters*, 78(20):3055–3057, May 2001.
- [112] J-H Kim, M. Yoneya, J. Yamamoto, and H. Yokoyama. Nano-rubbing of a liquid crystal alignment layer by an atomic force microscope: a detailed characterization. *Nanotechnology*, 13:133–137, 2002.
- [113] R.N. Thurston, J. Cheng, and G.D. Boyd. Mechanically bistable liquid-crystals display structures. *IEEE Transactions on Electron Devices*, 27(11):2069–2080, November 1980.
- [114] G.D. Boyd, J. Cheng, and P.D.T Ngo. Liquid crystal orientational bistability and nematic storage effects. *Applied Physics Letters*, 36(7):556–558, April 1980.
- [115] D.W. Berreman and W.R. Heffner. New bistable cholesteric liquid crystal display. *Applied Physics Letters*, 37(1):109–111, July 1980.
- [116] L.A. Parry-Jones, S.J. Elston, and C.V. Brown. Zenithal bistability in a nematic liquid crystal device with a monostable surface condition. *Molecular Crystals and Liquid Crystals*, 410:427–433, 2004.
- [117] R. Barberi, M. Giocondo, Ph. Martinot-Lagarde, and G. Durand. Intrinsic multiplexability of surface bistable nematic displays. *Applied Physics Letters*, 62(25):3270–3272, June 1993.

- [118] G.P. Bryan-Brown, C.V. Brown, and J.C. Jones. Gb2318422. UK Patent, 16 October 1995.
- [119] S. Ladak, A.J. Davidson, C.V. Brown, and N.J. Mottram. Sidewall control of static azimuthal bistable nematic alignment states. *Journal of Physics D: Applied Physics*, 42, December 2009. Submitted.
- [120] Microchem corp. ma, usa.
- [121] A.A. Michelson and E.W. Morley. On the relative motion of the earth and the luminiferous ether. *The American Journal of Science*, 34(203):333–345, November 1887.
- [122] T.B. Jones. On the relationship of dielectrophoresis and electrowetting. *Langmuir*, 18:4437–4443, 2002.
- [123] H. Pellat. Mesure de la force agissant sur les dielectriques liquides non electrises places dans un champ électrique. *Comptes Rendus hebdomadaires des seances de l'Academie des Sciences Paris*, 123(18):691–694, November 1896.
- [124] T.B. Jones, M.P. Perry, and J.R. Melcher. Dielectric siphons. *Sciences*, 174(4015):1232–1233, December 1971.
- [125] T.B. Jones, M. Gunji, M. Washizu, and M.J. Feldman. Dielectrophoretic liquid actuation and nanodroplet formation. *Journal of applied Physics*, 89(3):1441–1448, February 2001.
- [126] K.-L. Wang and T.B. Jones. Saturation effect in dynamic electrowetting. *Applied Physics Letters*, 86(054104), 2005.
- [127] H.A. Pohl. *Dielectrophoresis, The behaviour of neutral matter in nonuniform electric fields*. Cambridge Monographs on Physics, Cambridge, 1978.

- [128] M. Gunji, T.B. Jones, and M. Washizu. Dielectrophoresis microfluidic devices. *Proceeding of IEJ/ESA Joint Symposium on Electrostatics, Kyoto, Japan*, pages 78–87, September 2000.
- [129] T.B. Jones, T. Ito, H. Yoo, and R. Ahmed. Factor influencing response time of dep microfluidic actuation. MicroTAS 2002 Conference, Nara, Japan, November 2002.
- [130] R. Ahmed, D. Hsu, C. Bailey, and T.B. Jones. Dispensing picoliter droplets using dielectrophoresis (dep) micro-actuation. *Microscale Thermophysical Engineering*, 8:271–283, 2004.
- [131] R. Ahmed, T.N. Tombs, T.B. Jones, and P. Leas. Dispensing thin liquid film using dielectrophoresis. Fifth international meeting on electrowetting, Rochester, NY (USA), June 2006.
- [132] H.H. Woodson and J.R. Melcher. *Electromechanical Dynamics: Part II: Fields, Forces, and motion*. John Wiley & sons, Inc., 1968.
- [133] R. Ahmed and T.B. Jones. Dispensing picoliter droplets on substrates using dielectrophoresis. *Journal of Electrostatics*, 64:543–549, 2006.
- [134] T.B. Jones. Liquid dielectrophoresis. *Journal of Electrostatics*, 51-52:290–299, 2001.
- [135] C.V. Brown, G.G. Wells, M.I. Newton, and G. McHale. Voltage-programmable liquid optical interface. *Nature Photonics*, 3:403–405, July 2009.
- [136] J.R. Ongus. *Varroa destructor virus 1: A new picorna-like virus in Varroa mites as well as honey bees*. PhD thesis, Wageningen University (The Netherlands), 2006.

- [137] B.P. Oldroyd. Coevolution while you wait: *Varroa jacobsoni*, a new parasite of western honeybees. *Trends in Ecology and Evolution*, 14(8):312–315, August 1999.
- [138] D. De Jong, R.A. Morse, and G.C. Eickwort. Mite pests of honey bees. *Annual Review of Entomology*, 27:229–252, 1982.
- [139] M. Marin. World spread of varroa disease. *Apiacta*, 13:163–166, 1978.
- [140] D. De Jong. *Varroa jacobsoni* does reproduce in worker cells of *apis cerana* in south korea. *Apidologie*, 19(3):241–244, 1988.
- [141] S. Martin, A. Hogarth, J. Van Breda, and J. Perrett. A scientific note on *varroa jacobsoni* oudemans and the collapse of *apis mellifera* l. colonies in the united kingdom. *Apidologie*, 29:360–370, 1998.
- [142] H.A. Denmark, H.L. Cromroy, and L. Cutts. *Varroa* mite, *varroa jacobsoni* oudemans (acari: Varroidae). *Entomology Circular*, 347, October 1991.
- [143] P. Akrotanankul and M. Burgett. *Varroa jacobsoni*: A prospective pest of honeybees in many parts of the world. *Bee World*, 56:119–121, 1975.
- [144] K. Koivulehto. *Varroa jacobsonii* - a new mite infesting honeybees in europe. *British Bee Journal*, 104:16–17, 1976.
- [145] D.L. Anderson and J.W.H. Trueman. *Varroa jacobsoni* (acari: Varroidae) is more than one species. *Experimental and Applied Acarology*, 24:165–189, 2000.
- [146] A.C. Oudemans. Acarological notes xiii. *Entomologische berichten uitgegeven door de Nederlansche Entomologische Vereeniging*, 1:169–174, September 1904.
- [147] L. Bailey, A.J. Gibbs, and R.D. Woods. Two viruses from adult honey bees (*apis mellifera* linnaeus). *Virology*, 21:390–395, 1963.

- [148] L. Bailey, A.J. Gibbs, and R.D. Woods. Sacbrood virus of the larval honey bee (*apis mellifera linnaeus*). *Virology*, 23:425–429, 1964.
- [149] L. Bailey, B.V. Ball, and J.N. Perry. Association of viruses with two protozoal pathogens of the honey bee. *Annals of Applied Biology*, 103:13–20, 1983.
- [150] M.C. Gopfert and D. Robert. The mechanical basis of drosophila audition. *The journal of experimental biology*, 205:1199–1208, 2002.
- [151] Ineos Acrylics UK Limited. Product: Xt perspex. Product Specification.
- [152] Endevco Corp. Product: 7259b-10. Product Specification.
- [153] Endevco Corp. Model 7259b-10. Certificate of standardization-calibration.
- [154] Menlo Systems GmbH. Product: Fpd510-fv. Product Specification.
- [155] A.F. Fercher, W. Drexler, CK Hitzenberger, and T Lasser. Optical coherence tomography - principles and applications. *Institute of Physics Publishing - Reports on Progress in Physics*, 66:239–303, 2003.
- [156] B.E. Bouma and G.J. Tearney, editors. *Handbook of Optical coherence tomography*. Marcel Dekker, Inc., 2002.
- [157] M. Brezinski. *Optical coherence tomography - Principles and applications*. Elsevier, 2006.
- [158] C. Kischka. Flexoelectricity investigation communication. Private communication, March 2008.